Development of an integrated, portable DNA amplification and detection system based on electrohydrodynamic aggregation

Bastien Venzac

▶ **To cite this version:**

Bastien Venzac. Development of an integrated, portable DNA amplification and detection system based on electrohydrodynamic aggregation. Micro and nanotechnologies/Microelectronics. Université Pierre et Marie Curie - Paris VI, 2016. English. NNT : 2016PA066720 . tel-01617817

HAL Id: tel-01617817

https://theses.hal.science/tel-01617817v1

Submitted on 17 Oct 2017

HAL is a multi-disciplinary open access archive for the deposit and dissemination of scientific research documents, whether they are published or not. The documents may come from teaching and research institutions in France or abroad, or from public or private research centers.

L'archive ouverte pluridisciplinaire **HAL**, est destinée au dépôt et à la diffusion de documents scientifiques de niveau recherche, publiés ou non, émanant des établissements d'enseignement et de recherche français ou étrangers, des laboratoires publics ou privés.

Institut Curie – Laboratoire Physico-Chimie Curie

Ecole doctorale Physique en Ile-de-France

Development of an integrated, portable DNA amplification and detection system based on electrohydrodynamic aggregation.

Bastien Venzac

Thèse de doctorat de Physique de l'Université Pierre et Marie Curie

Dirigée par Laurent Malaquin et Jean-Louis Viovy

Présentée et soutenue publiquement le 7 décembre 2016 devant un jury composé de :

M. Jan Eijkel, Professeur	Rapporteur
M. Mats Nilsson, Professeur	Rapporteur
Mme Olivia Duroure, Chargée de Recherche	Examinatrice
M. Jean-Louis Viovy, Directeur de Recherche	Directeur de thèse
M. Laurent Malaquin, Chargé de Recherche	Co-directeur de thèse, invité
M. Guilhem Larigauderie, DGA	Invité

Except where otherwise noted, this work is licensed under
http://creativecommons.org/licenses/by-nc-nd/3.0/

Table of contents

Preface 1

Chapter 1: Introduction to molecular diagnosis and microfluidics 5

Chapter 2: Conductometric detection of DNA aggregates triggered by electrohydrodynamic instabilities. 37

Chapter 3: Amplification-elongation reaction for the detection of small DNA biomarkers..... 87

Chapter 4: The sliding wall technology 135

Conclusion 161

Appendix 165

Preface

Epidemic and biological threats

Communicable infections are one of the leading health problems around the world, and it also remains a potential bioterrorism threat. According to the World Health Organization (WHO), infectious diseases like respiratory infections, HIV, parasitic or bacterial contaminations are responsible for 9.1 million deaths in 2012, or 16% of deaths worldwide[1]. These diseases are divided into a first category of well-established illnesses, of which the number of infected persons and the incidence rate - or the number of new cases - are roughly constant over time (HIV, tuberculosis, malaria, for example). A second category comprises epidemic diseases, with a temporally-limited spread but a high contamination rate, like the H1N1 fever during 2009 or Ebola fever outbreak in West Africa during 2014-2015. Against these threats, the World Health Organization has allocated programs and resources in order to decrease the incidence and mortality rate of AIDS, tuberculosis, malaria, hepatitis, waterborne and neglected tropical diseases, within the framework of the Sustainable Development Goals (SDGs). The goals list challenges to take up before 2030, and replace the former United Nations Millennium Development Goals (MDGs).

In parallel to the fight against natural epidemics, from which developed and developing countries have to be prepared, many countries are also concerned by the growing risk of bioterrorism. Pathogenic microorganisms have already been used for terrorist attacks, even if casualties have fortunately been limited so far. Anthrax powder has been sent in postal letters across the USA in 2001, killing 5 people. In Oregon, the Rajneeshee group poisoned food with salmonella and caused 45 hospitalizations and 751 poisoning. In 1993, the Aum Shinrikyo sect aerosolized anthrax suspension in Tokyo[2]. Fortunately, the used strain was attenuated for vaccines purposes and no victims have been counted. Indeed, pathogen strains of microorganisms could be easier to obtain than nuclear or mass destruction weapons. In addition, even with limited lethality, an uncontrollable outbreak would make the country's economy fall and would create panic among population. Western countries, as Europe or the USA are taking the risk of bioterrorist attack in their ground or against military forces deployed during foreign operation more and more seriously[3] and is preparing counter-measures against pandemics.

Counter-measures

Concerning natural and well-implanted diseases, the World Health Organization has almost completed the Millennium Development Goal 6. The original aims were an inversion of the HIV, malaria and other major diseases incidences and universal access to AIDS treatment. During the period 2000-2015, HIV incidence dropped from 160 cases for a population of 100 000 persons to 135 cases, malaria incidence rate decreased by 37% and tuberculosis new cases were 18% lower at the end of the period as seen on the following figure. Also, the medical coverage has been significantly

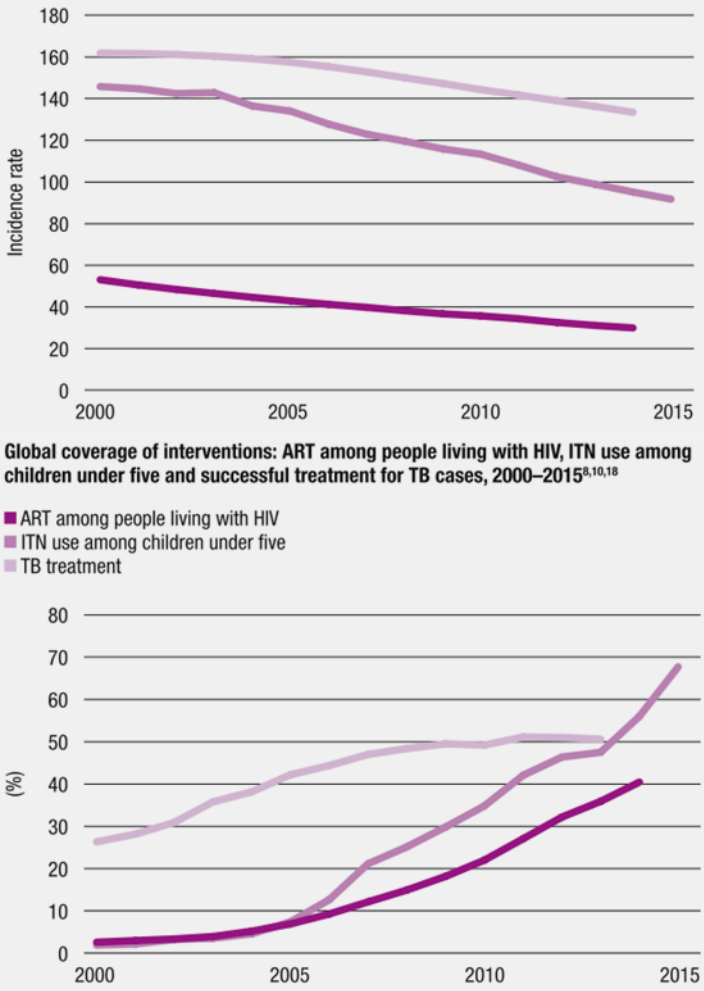

Taken from the reference 1. The original sources of the data, noted 8,9,10,15,18 are reproduced as 4, 5, 6, 7, 8.

improved. For example, access to Antiretroviral Therapy (ART) for the AIDS patients increased from 2 to 40% of the cases, thanks to drastic decreasing in treatment price and complexity, and a world-wide funding initiative. Prevention also played a strong role in changing behaviour and diminishing the HIV transmission. In the case of tuberculosis, improved disease detection (from 38 to 64% of cases), thanks to new and cheaper diagnosis protocols, and treatment coverage (from 50% in 2000 to 85% in 2015), led to a two-fold dividing of the mortality rate. Without any unexpected future difficulties, like a severe antibiotic or antiviral resistance, the combination of prevention, disease monitoring, rapid diagnosis and treatment coverage should significantly reduce the incidence of these major global diseases.

Counter-measures against epidemics are way less easy to plan. First, the World Health Organization has set up a global network of disease monitoring, the International Health Regulations, in order to gather and share information coming from the 196 UN members and 200 technical institutions. Other networks like the Global Outbreak Network or the Global Influenza Surveillance and Response System also have the capabilities to monitor epidemic spread thought data collection, analysis in harbours, airports, frontiers, and to coordinate the access of resources and experts in the case of international outbreak. Besides this monitoring, technology development also has a major role to play, in order to slow down and stop epidemics. Concerning outbreaks of fast-mutating microorganisms, like viruses, one of the most crucial points is the time necessary for the preparation of a vaccine specific to the new strain. Also, when the disease has a fast propagation, an early detection of the new cases in the patient's place is a key to avoid transmission of the pathogen.

Concerning the bioterrorist risk, as deliberate pathogen dissemination has the same behaviour as a natural outbreak, countries have also set up their own monitoring network. The USA has the Real-time Outbreak and Disease Surveillance (RODS), a real-time automated detection system. Data is collected from sources all around the country, from clinical centers, laboratories and

over-the-counter drug sales records[9]. Equivalent system has been created in Europe (ECDC, European Centre for Disease prevention and Control). Drug stocks and vaccination against smallpox and anthrax for army forces are also an easy way to prepare troops deployed in foreign countries against biological attacks. On the technological side, the Defense Advances Research Projects Agency (DARPA) in the USA and national armies in Europe have funded projects on protection equipments for the first responders to outbreak, on faster and more portable diagnosis devices, or on more rapid vaccine manufacturing. As future pathogens used in terrorist attacks could even be engineered to have a higher drug resistance, to make vaccines inefficient, or to enhance the virulence or transmissibility of the pathogen, the time delay from discovery of the disease, complete characterization of the pathogen and drug/vaccine production has to be as short as possible.

Diagnosis devices

As seen above, one of the tools used to counter the advance of an outbreak, or to avoid further transmission of pathogens is an early detection and characterization of the microorganisms responsible for the disease. Even if some diseases could be diagnosed directly by a physician according to the different symptoms, the use of detection devices is essential:

- to confirm a first diagnosis,
- when symptoms would not be sufficient to discriminate between different diseases,
- when no educated staff would be available close to the patient's area,
- and/or to achieve as early as possible the most accurate and reliable characterization of the strain at play.

Depending on the use, diagnostic device characteristics would be completely different. In urban areas of developed countries, diagnostic devices are gathered into clinical centres, hospitals or laboratories. Sensitivity, specificity, reproducibility and robustness are the main specifications of interest. Examples of protocols are HIV testing with ELISA and Western Blot, or molecular diagnosis with the Xpert system (Cepheid), smear microscopy and sputum culture for tuberculosis detection. In a number of cases, however, such centralized system does not exist. In developing countries, the lack of modern laboratories, difficulties with reagent storage, unavailability of educated staff, high prices of some technologies or even difficulties to reach urban areas do not allow the generalization of the previous protocols. A second class of diagnostic device has to be used for a first and rapid test. They must be portable, low cost, and work without any electricity supply. The protocol has to be simple enough to be understood by minimally-trained users. As they would be used for first tests, to be confirmed, if positive, by a more robust protocol, specificity and/or precision don't need to be as high as for the hospitals “gold standards”. One example is the malaria immunochromatography cassette (ICT) from ICT Diagnostics (South Africa)[10], used as a malaria rapid diagnostic test in Nigeria. It is important to note that the developed countries' armies have exactly the same needs. As bioterrorism would also target American troops mobilized in foreign countries, the DARPA began to fund during the late 90's miniaturized diagnostic devices to allow fast pathogen detection on the field.

This is the context of my PhD research. The aim of my PhD project is to develop, based on a DNA detection method developed in the MMBM team, a new diagnostic device for on-field use. Our objective is to propose a quick, sensitive and efficient method for pathogen detection based on a universal genomic detection in a microfluidic format. This manuscript is divided into four chapters. First, I will introduce the different pathogens and the technologies used for their diagnosis, with an emphasis on genetic bacteria detection, and I will highlight the contribution of microfluidics technologies. In the second chapter, I will introduce the conductometric DNA detection, based on electrohydrodynamic instabilities, the core of the technology used during my PhD. The third chapter is dedicated to the DNA amplification method used and developed to increase the sensitivity of the detection. Finally, a new technology called "sliding wall" and used for the integration of the DNA amplification and preconcentration on-chip is presented in the fourth chapter.

1. World Health Organization report: "Health in 2015: from MDGs to SDGs"

2. Takahashi, H. *et al.* Bacillus anthracis Incident, Kameido, Tokyo, 1993. *Emerg. Infect. Dis.* **10,** 117–120 (2004).

3. http://archive.defense.gov/news/newsarticle.aspx?id=65852

4. How AIDS changed everything. MDG 6: 15 years, 15 lessons of hope from the AIDS response. Geneva: UNAIDS; 2015

5. Global tuberculosis report 2015. Geneva: World Health Organization;

6. Achieving the malaria MDG target: reversing the incidence of malaria 2000–2015. Geneva and New York (NY): World Health Organization and United Nations Children's Fund; 2015

7. WHO/UNAIDS estimates; 2015.

8. Estimated TB treatment coverage calculated from: Global tuberculosis report 2015. Geneva: World Health Organization; 2015

9. https://www.rods.pitt.edu/site/

10. Garcia, M., Kirimoama, S., Marlborough, D., Leafasia, J. & Rieckmann, K. H. Immunochromatographic test for malaria diagnosis. *Lancet*, **224,** 871–872 (2000).

CHAPTER 1: Introduction to molecular diagnosis and microfluidics.

Table of contents

1 Traditional pathogen detection 7
1.1 Pathogens and micro-organisms 7
1.2 Visual detection of pathogen 8
1.3 Quantification of a test performances 10
1.4 Molecular diagnostic test 11
1.4.1 Protein detection 12
1.4.2 Genomic detection 14
2 Microfluidics for molecular diagnostics 24
2.1 Definition 24
2.2 Microchip and microfabrication 25
2.3 Microfluidics for molecular diagnosis 27
2.3.1 Improvement of DNA amplification 27
2.3.2 Integrated Point-of-Care system with DNA amplification 28
2.3.3 DNA direct read on microfluidic systems 29
2.3.4 Protein detection 30
2.4 PhD project: conductometric detection of electro-hydrodynamic aggregates of DNA 30
References 32

1 Traditional pathogen detection

1.1 Pathogens and micro-organisms

Communicable diseases are always provoked by pathogenic micro-organisms: bacteria, unicellular parasites (protozoa), multicellular parasites, fungus or viruses; even if the latter was sometimes considered as a non-living object.

Viruses are the simplest ones: outside of a host cell, a virus is called virion. Its usual size ranges from 30 to 200nm and it consists of a protein membrane which encapsulates genetic material, DNA or RNA (Figure 1). It can't self-reproduce and needs to infect a host cell and to use its genetic machinery. Duplication of the genome of the virus and production of new viral proteins allows the formation of new virions, which could then infect new host cells. During virus replication, host cell functions are altered by viral proteins, going from a slower metabolism, malignant proliferation to death by apoptosis. In human, viruses are responsible for AIDS, influenza, rubella, yellow fever, measles, mumps or even cancer in the case of papillomavirus. No general treatment is available for viruses, contrary to bacteria, as the virus diversity is larger. Moreover, mutations occur quickly in viral genome because of the lack of repair mechanism. As an example, the influenza vaccine has to be changed every year.

Bacteria are small prokaryotic cells, from 0.5 to 5µm in length. They are composed of a cell wall (mainly peptidoglycan) doubled by a double lipid membrane, enclosing gel-like medium called cytoplasm, proteins and genomic DNA. Bacterial DNA is a single circular chromosome, folded into the cytoplasm without any compartmentalization. Unlike virus, bacteria are able to reproduce without any external help. Asexual reproduction occurs after DNA replication by a division of the bacterium between two identical daughters. Bacteria have a relatively short replication cycle, 20 minutes for Escherichia Coli.

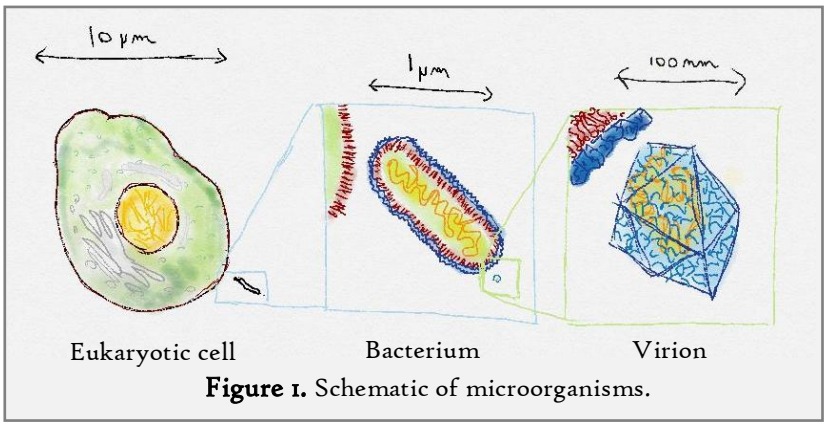

Figure 1. Schematic of microorganisms.

Bacterium is the most diverse branch of the tree of life, both in term of total biomass or number of different species. All the ecological niches are occupied by bacteria: from the high pressure of abysses, to the high atmosphere, with extremophile bacteria living up to 80°C or below 700 meters of ice in Antarctica. Also, more than 1000 species of bacteria are found inside human gut and digestive track[1].

Fortunately, only a few numbers of bacteria are pathogenic for human compared to the whole domain. Oral ingestion of pathogenic bacteria, via contaminated food or droplets expelled by infected human, can lead to pneumonia or tuberculosis. Gastroenteritis occurs when the normal,

harmless gut flora is partly replaced by pathogenic bacteria. Sometimes, even gut bacteria could be responsible for infection, in the case of opportunistic species which become harmful only in the case of an immunosuppresion. Skin infection can occur when skin is injured and can be caused either by normal skin microbiota - which correspond to the bacteria which live on healthy skin - or by outer species. In general, diseases linked to bacterial infection have two main causes. First, bacteria can produce toxins which are released into the organs or the blood circulation after the bacteria's death and lysis. This is the case for *Clostridium tetani*, responsible for tetanus. A second possibility is illustrated by tuberculosis. *Mycobacterium tuberculosis* is a bacteria protected by a waxy coating which makes it resistant to phagocytosis by macrophages. The bacteria can survive into the immune cell and use its nutrients to grow and multiply, causing cell death and tissue necrosis.

Pathogenic bacteria could be targeted by specific treatments. The antibiotics are molecules which disrupt the bacterial membrane or inhibit bacteria's enzymes specifically without any effect on host metabolism. Treatment could either kill the microorganisms or block their growth. However, bacteria also have a high mutation rate, to a lesser extent compared to viruses. Experiments demonstrated that under starvation, bacteria can have a phenotypic change linked to a genomic mutation in less than 6 days[2]. This property, coupled with a high capacity of horizontal gene transfer between different bacteria strains and the over-use of antibiotic, increases the drug resistance of pathogenic bacteria.

Some diseases are also provoked by other types of microorganisms. Fungi are mainly responsible for non-lethal skin infection. Parasites, unicellular protozoa and multicellular eukaryotes are the sources of various diseases, sometimes really severe in the case of malaria, induced by the *Plasmodium* protozoa. The main difference with bacteria and viruses are the size of the pathogen, which is the same or larger than typical human cells. Complete review of the transmission and pathogenic action of these microorganisms won't be made here because of the huge diversity of different cases and diseases.

1.2 Visual detection of pathogen

Historically, the first microorganisms were discovered via microscopic observations. Antonie van Leeuwenhoek identified the first protozoa and the first bacteria in 1674 and 1676 thanks to a rudimentary microscope. As viruses were too small to be observed at the time with microscope, the existence of pathogens smaller than bacteria has been stated in 1892 by Dmitri Ivanovsky and confirmed by Martinus Beikirinck in 1898 by using a filtering system that removed all the bacteria from a sample. The tobacco mosaic virus, that infects tobacco plants, was able to pass through the filter and to re-infect new cells. It is only since 1937 that direct observation of viruses has been possible with electron microscopy.

Culturing microorganisms became quickly the best way to visualize, amplify and count them. The use of agar plate, composed of a thick layer of agar (a compound extracted from seaweed) and growth media in a Petri dish, is now the main protocol for detection and isolation of bacteria. Sample is deposed uniformly on agar plate and incubated at the good temperature for bacteria growth. As bacteria number is doubled every division cycle, which is fast compared to the eukaryotic one, a visible colony could appear after 1 day for *Escherichia Coli* and 4 to 9 days for *Campylobacter*. All the

bacteria from the same colony would be generated from a single bacterium, if the initial concentration was low enough. Thus, counting the colonies on an agar plate allows a direct quantification of the initial bacteria concentration.

Agar plates are also used to identify the different bacteria on a sample. First, the size, colour and morphology of colonies are different for each species. A skilled microbiologist can differentiate bacteria and strains only with these clues. Agar plate can also be modified in order to only let some species grow. The plate can be selective, with a specific media or nutrient that can be metabolized only by a specific bacteria strain, or restrictive, with the addition of antibiotics in order to kill unwanted contaminants while keeping alive and culturing bacteria insensible to the drug. This last example allows also the labelling of unknown bacteria, when a single plate is submitted to the action of different antibiotics. On this antibiogram, antibiotic disks are placed on agar, and bacteria sensitive to this drug died around the disk (Figure 2). As the antibiotic diffuses in the gel, the size of the empty ring is proportional to the maximum concentration tolerated by the microorganism. Using several antibiotics, the result can be specific enough to obtain the specie and the strain of the unknown bacteria.

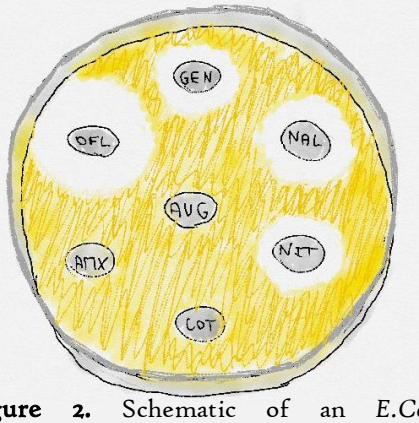

Figure 2. Schematic of an *E.Coli* antibiogram. The antibiotic are AUG: augmentin, OFL: ofloxacin, GEN: gentamicin, NAL: nalidixic acid, NIT: nitrofurantoin, COT: cotrimoxazole and AMX: amoxicillin.

An equivalent approach also exists for viral culture. As they can't survive without hosts, viruses are cultured in association with host cells in a classic cell culture protocol[3]. Indirect visualization of viruses is possible by two different methods. Host cells undergo a visible, phenotypic change called cytophasic effect when infected, specific for different strains. Cytophasic effect occurs after 2 days for herpes virus, and from 1 to 3 weeks for cytomegalovirus. Viruses could also be detected by "plaguing"[4]. Agar is mixed with host cells and viral sample and polymerized. As the host cells are immobile in the gel, but the viruses can move, virus propagation is seen by the growing of a clear disk of killed cells as the viruses multiply and infect new hosts. Finally, direct visualization of viruses is also possible with fluorescent DNA or RNA label, and a counting of the resulting bright spot with an epifluorescence microscope.

The plating method has major limitations for bacteria pathogen detection. The sample-to-result time can be several days, especially when a two-step protocol (culture, isolation and identification via an antibiogram) is needed. Lab space for the plate storage, security reinforcement to avoid pathogen spreading and highly-educated staff for the pathogen identification are essential. Moreover, only a fraction of the total bacteria can be cultured *in-vitro*. For example, only 50% of the microflora associated with human oral infections is culturable[5]. However, the simplicity, the sensitivity and the low cost of a microbial culture (around 35$[6] for a complete diagnosis) explain the leading position of this detection method. All these limitations also apply to viral culture, and this method, used in the early 2000's for herpes, cytomegalovirus, varicella-zoster virus, adenovirus,

rhinoviruses, influenza and enteroviruses detection is now mainly replaced by molecular diagnostic test.

1.3 Quantification of a test performances

Before the presentation of the main diagnostic techniques used to complement, confirm or replace visual detection of pathogens, the main parameters used to describe the performance of a medical test have to be described.

- Limit of detection: minimal amount of target detectable by the method. For bacteria or fungus, LOD is often given in Colony Forming Unit (CFU) per ml, which corresponds to the number of viable microorganisms able to divide to form a colony during culture.

- Specificity: also named false-positive rate, specificity corresponds to the proportion of positively-labelled objects which are effectively the searched objects.

- Repeatability / reproducibility: repeatability is the measure of the precision of a specific device. To determine it, the same experiment is repeated multiple times with the same parameters, the same experimentalist and the same instrument in a short amount of time, and the standard deviation of the results is calculated. This method provides a measure of the precision of the device under the best possible conditions. Reproducibility is the precision of a method. The experiment is duplicated with different instruments, in different independent laboratories, and results are gathered and standard deviation is calculated. For example, in the case of centralized medical diagnostic instrument, a coefficient of variation (standard deviation / mean of the results) of 2% is sometime considered as the larger acceptable variation for commercialization.

- Testing time / sample-to-result time / hands-on time: the first term corresponds to the time used by the diagnostic instrument. The second term corresponds to the time necessary between sample collection and result delivery. For example, a DNA amplification and detection can be finished in less than 2 hours, but the sample-to-result time, including sample purification, reagent preparation, analysis of the results and sometimes a second testing for confirmation would be half a day. In the case of developing countries or remote rural area, transportation time of the sample or patient have also to be counted when comparing a point-of-care and a traditional method. The third term corresponds to the actual time used for manual operation and quantifies the degree of automation of a system.

- Cost: price is an important parameter of a diagnostic test. When comparing different technique, not only the prices of the consumables and the instrument, divided by the total number of runs, have to been counted. Hidden costs also comprise the salary of the staff, the transportation of sample or patient to a medical centre, etc...

- Cost per QALY (Quality Adjusted Life Year): one QALY corresponds to one year of living in perfect health. If the health of the patient isn't perfect, the QALY can take any number between 1 (perfect health) to 0 (death). Associated with a specific medical action, the cost

per QALY is the price to pay for one supplementary year in perfect shape compared to a control group. This criterion is used to compare the cost / utility ratio of two techniques in order to allocate health resources to the cheapest and most beneficial technique, and is frequently applied to diagnostic tests[7].

- Portability: some diagnostic tests are commercialized as Point-Of-Care (POC) devices. That means that the test is made close to the patient habitation or, in the case of hospitalization, close to the patient's bed. The usual examples of POC diagnostic are glucose monitoring test for diabetic and pregnancy tests. Weight, dimensions and need for an electricity supply are the main handicap for portability.

- Simplicity: simplicity is an important but hard to quantify parameter. The decreasing of manual operations, sample pre-treatment and human interventions could enable the use of the diagnostic test by uneducated staff without decreasing reproducibility and sensitivity of the method, allowing a larger diffusion of the technology.

- Adaptability to "extreme" conditions: in developing countries, the range of temperature and humidity can be higher than in the country where a diagnostic test has been developed. The lack of good storage condition can be detrimental to sensitive reagents like enzymes.

- Multiplexing / versatility: multiplexing is the possibility to run, with a single sample, different tests with the same diagnostic device. For example, multiplexed PCR can detect up to five different DNA targets with only one sample and reaction kit. A diagnostic device is called versatile when the same technology can detect a large number of pathogen different just by changing reagents or consumables.

No perfect diagnosis device exists and compromises have to be made in order to adapt the diagnostic test to a specific use along the different possibilities, ranging from a bulky, super-sensitive, reproducible device installed on a modern laboratory to a portable, low-cost, resistant and multiplexed test for the on-field testing of pathogens.

1.4 Molecular diagnostic test

As seen before, rapid identification of pathogens is not obtained with traditional culture techniques, whereas time is the main parameter to limit the spread of an infectious disease. In addition, before the pathogen identification, an antibiotic or antiviral cocktail is prescribed in most cases before switching to the right drug, leading to antibiotic resistance. Faster methods are needed, but their performances in particular in terms of sensitivity, reproducibility and simplicity have to be as good as the ones obtained by culturing microorganisms, or better.

Another way to detect a pathogen is to probe a specific molecular marker to this micro-organism instead of detecting the whole pathogen. Thus, molecular diagnostic tests can be classified according to the target, which could be genomic (DNA or RNA) or proteomic, to the technology used (optical, electrochemical...), to the presence of a signal or target amplification step which is

sometimes needed to compensate the low sensitivity of the sensor or because the initial target concentration is too low.

1.4.1 Protein detection

Instead of detecting a whole pathogen, some molecular tests recognize structural elements of microorganisms: proteins. Protein is a polypeptide, composed of a linear chain of amino-acids chosen between 21 different molecules. Proteins have a specific 3D structure due to the folding of the linear chain, stabilized by hydrogen bonds, disulfide bonds or hydrophobic-hydrophobic interactions between non-consecutive amino-acids.

Molecular tests take advantage of existing specific interactions between proteins. Part of the 3D conformation of the probing protein is complementary to part of the target protein and the association is stabilized by non-covalent molecular interactions between amino-acids. When the two proteins bind together, this could trigger enzymatic reactions or conformational changes. But some specific proteins of the immune system, called antibodies, are specifically produced to recognize and bind part of foreign protein called antigen with a strong affinity. This antibody/antigen interaction is extremely specific and this property is massively used in molecular test. Moreover, antibodies for a specific antigen are now easier to produce, using inoculated animals or immortalized lymphocyte cultures. These antibodies can be polyclonal, if they recognize different part (or epitope) of the antigen. In that case, it's a mix of several different antibodies. Antibodies can also be monoclonal, that means they are all identical and target the same epitope.

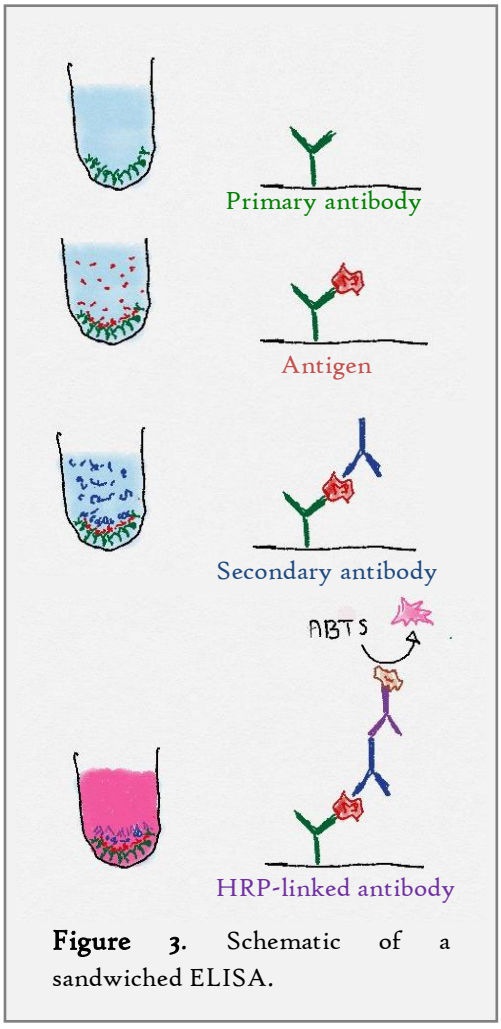

Figure 3. Schematic of a sandwiched ELISA.

As a first example, antibody is often used to characterize viruses in viral culture in an easier way that waiting for the cytophasic effect. Antibodies linked to a fluorophore, directed against a virion protein, allow the identification and the counting of the searched pathogen directly under an epifluorescent microscope[4]. But protein recognition enables direct detection of target pathogen in a sample, without culturing them before. The enzyme-linked immunosorbent assay, or ELISA, created in 1971, is one of most used assay for antigen detection[8]. As shown on the Figure 3, the protocol for sandwiched ELISA is:

1. Antibody specific to the searched antigen is immobilized on a solid surface, for example the bottom of a 96-wells plate.
2. Sample is added to the wells. If the antigen is present, it binds to the primary antibody.
3. Washing step is used to remove the unbound antigen.
4. Secondary antibodies, specific to a second epitope of the antigen are added in the wells and bind to the attached antigens.

5. A second washing step is used to remove the unbound secondary antigen.
6. A third antibody, specific to the secondary antibody, is added. This third antibody is linked to an enzyme, often a horseradish peroxidase enzyme (HRP).
7. A third washing step is used to remove the unbound third antibodies.
8. The substrate for the enzyme is added to the wells. In the case of HRP the substrate is ABTS (or 2,2'-azino-bis(3-ethylbenzothiazoline-6-sulphonic acid)). The enzymatic reaction transforms the substrate into a coloured molecule. The absorbance of the solution is finally proportional to the initial concentration of antigens.

ELISA has been widely used for pathogen detection. For example, this method is able to detect *E. Coli* bacteria (LOD: 1.3×10^3 CFU/ml), *Campylobacter* (LOD: 10^5 - 10^6 CFU/ml), *Salmonella* (LOD: 10^6 CFU/ml)[9], viruses - ELISA is also the reference test for HIV screening -, toxins... However, classical ELISA stays a non-portable, lab-based assay. Even if one bacterium carries more than one searched antigen, probably thousands of them, the ELISA sensitivity doesn't allow the detection of a single pathogen. Contrary to DNA amplification methods, described in a further section, that results in exponential signal amplification, the enzymatic reaction involved in ELISA induces a linear increase of the absorbance with time which might be insufficient for the detection. However, ELISA can benefit from automated liquid handling robots are often used in large clinical facilities, decreasing the cost and hands-on time, increasing the throughput of this test.

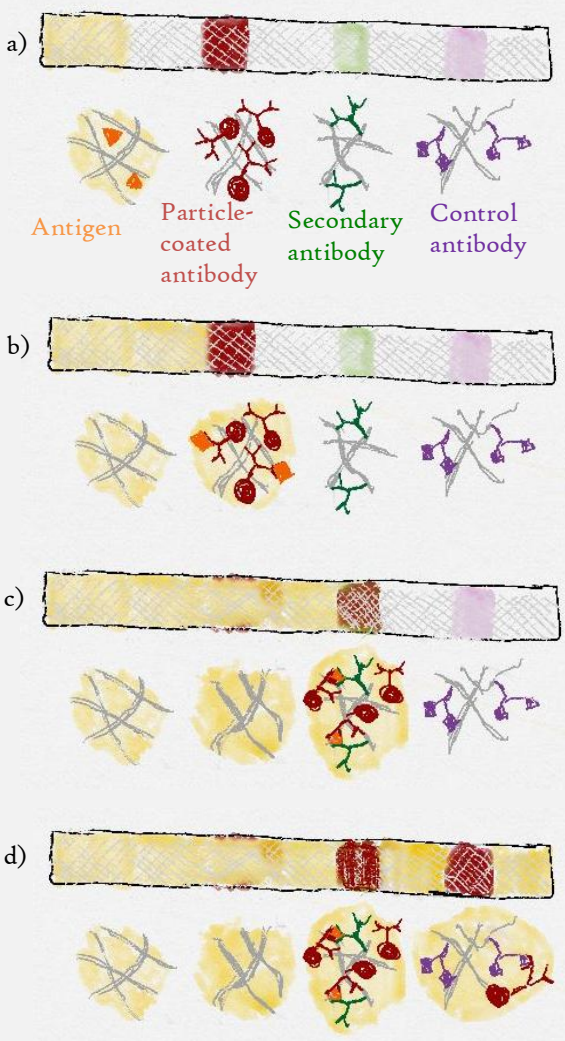

Figure 4. Schematic of a lateral flow assay. **a)** Impregnation of the extremity of the paper strip with the sample and the searched antigen. **b)** Capture of the antigen by the particle-coated antibodies. **c)** Capture of the particle by the secondary antibodies. **d)** Capture of the free particle by the control antibodies.

An alternative to the microtitre plate ELISA is the lateral flow immunochromatic assay (Figure 4). Its most spread application is the pregnancy test.

1. First, the sample containing the antigen to be detected is disposed at the extremity of a strip of a porous material (paper or polymer) which acts as a sponge. If the sample is a swab, diluting buffer can be added.

2. The porous material is then pumping the sample by capillarity. The searched antigen is displaced through a first line of antibody-coated and coloured particles, mostly latex beads or gold nanoparticles.
3. Sample and particles move to a second line of immobilized secondary antibodies, also directed against the antigen. If antigens were captured by particles, they would be trapped by the secondary antibodies. As particles are captured on the line, visible colour appears slowly and indicates a positive test.
4. A control line is always added to avoid false negatives. In this third line, antibodies directed against the primary antibodies capture the sample-free, displaced particles, proving that the test worked correctly.

Lateral flow assay is now a mature technology, used and validated by the World Health Organization for the detection of infectious diseases like malaria in developing countries at concentration as low as 200 parasites per microliters[10]. Indeed, the assay is cheap, fast (around 15min), really portable, easy to use, the reagents are pre-stored inside the consumable, and the result is easy to interpret. Moreover, as seen in the Table 1, commercialized lateral flow assays are directed against a wide range of pathogens: bacteria, viruses or parasites. However, each assay can generally be used for one sample and one pathogen only, while other multiplexed analysis could recognize a higher number of pathogens or differentiate between different strains in order to obtain more information about the perfect treatment to give. Lastly, the sensitivity is worse than the ELISA sensitivity, because the signal is not amplified other time.

1.4.2 Genomic detection

1.4.2.1 Genomic material

The second main target for molecular test is genomic material, DNA or RNA. DNA is a long biopolymer, composed of nucleotides. For example, *E.Coli* genome is 4.6 million nucleotides long. Each nucleotide contains a base chosen between adenine, guanine, cytosine and thymine. Single-stranded DNA (or ssDNA) hybridizes via hydrogen bonds to its complementary DNA: adenine binds to thymine and guanine binds to cytosine. *In-vivo*, double-stranded DNA (dsDNA) is the main form of genomic material, except during DNA replication. For some viruses, genomic material is composed of RNA. RNA skeleton is more flexible than DNA. As a consequence, RNA is mostly found in a folded single-stranded state, as the polymer would self-hybridize with itself if complementary sequences were present. A deeper physical description of the DNA molecule will be present in the next chapter.

Genomic material is different from one organism to the other. DNA is divided in coding sequences, separated by non-coding parts. A coding sequence, called gene, is duplicated into RNA messenger (or mRNA) during transcription, which is then translated into protein. Even if differences are observed between individuals of the same species, a pool of common gene is always shared by all the members of the same strain. This "core genome" can be as large as 99.5% of total genome in the human species[11], whereas an individual from the *E.Coli* group has only an estimate of 20% of its genome that is found in all the other genomes of the group[12]. These conserved sequences of the "core genome" are good candidates for detection of pathogen using DNA recognition as they are shared by all the individuals of the same species. However, in order to ensure a good specificity, the

chosen sequence has to be only present in the genome of the searched species. Indeed, the same gene can be shared by different microorganism, because they descend from the same common ancestor, or because the gene has been acquired from another microorganism thanks to the horizontal gene transfer phenomenon, mostly for bacteria. Another possibility of non-specificity arises when a short sequence is used for the detection. There are around 1 million possibilities for a DNA sequence composed of 10 nucleotides (10nt) chosen between adenine, guanine, thymine and cytosine (4^{10}). This sequence has a high probability to exist in one genome among the rough estimate of 100 millions of species on Earth (an 8.7 million estimation of eukaryotic species number have been given[13]), each of them is at least larger than 1 million base-pair. Even with a wild guess that only 1% of each genome is fully original, the total number of sequences available in the world is 10^{12}. A 10nt long sequence should be found in a large number of genomes. For comparison, a 25 nucleotide-long DNA has 10^{15} different possible sequence. In practical, this probe size is specific enough for most diagnostic test.

1.4.2.2 Genomic amplification

At first glance, compared to protein detection, direct genomic detection has limitations. First, a DNA sequence is rarely present at more than one copy in the cell, decreasing the number of searched target. RNA messenger can be targeted for pathogen detection to increase the number of targets, because a specific mRNA is present in larger quantity in the cell cytoplasm than the initial DNA sequence. However, the molecule is very fragile - RNase enzymes are present everywhere thus limiting strongly the lifetime of a circulating molecule - and the mRNA amount is also highly variable and dependant on gene expression, leading to a difficult conversion to the absolute number of pathogen.

Polymerase Chain Reaction

To overcome these limitations, genomic amplification is widely used to increase the quantity of targets. The first and main technique is the Polymerase Chain Reaction, or PCR, invented on 1983 by Kary Mullis[14]. During PCR, a first short oligonucleotide (artificial DNA), complementary of the searched ssDNA sequence and called forward primer hybridizes to the 3' end of the target at 65°C (see Figure 5). A thermostable polymerase extends the primer from its 3' extremity and creates a dsDNA. The temperature is then increased until the melting temperature of the dsDNA, around 95°C. The thermal energy overcomes the hybridization energy of the two complementary strands that are separated. When decreasing temperature down to 65°C, a new forward primer anneals to the first ssDNA while a second primer, called reversed primer, anneals to 3' end of the newly created ssDNA. This process is repeated several times. At each cycle, the number of amplified sequence is doubled. PCR is thus an exponential amplification, and optimized protocol can even amplify a single DNA to millions of copies. The specificity of the PCR is due to the two primers used. The length of the primers, around 20nt, insures a good specificity for the hybridization of a single primer. The association of the two primers increases this specificity because the two primed sequences have to be close enough to allow the amplification. However, primer design has to be carefully done, because dimers of partially complementary primers can be highly efficiently amplified and results in non-specific amplification. Concerning the duration of the amplification, traditional PCR amplification

can last from 30 minutes to 3h, depending on the size the target. This duration is short enough to be added on a diagnostic scheme.

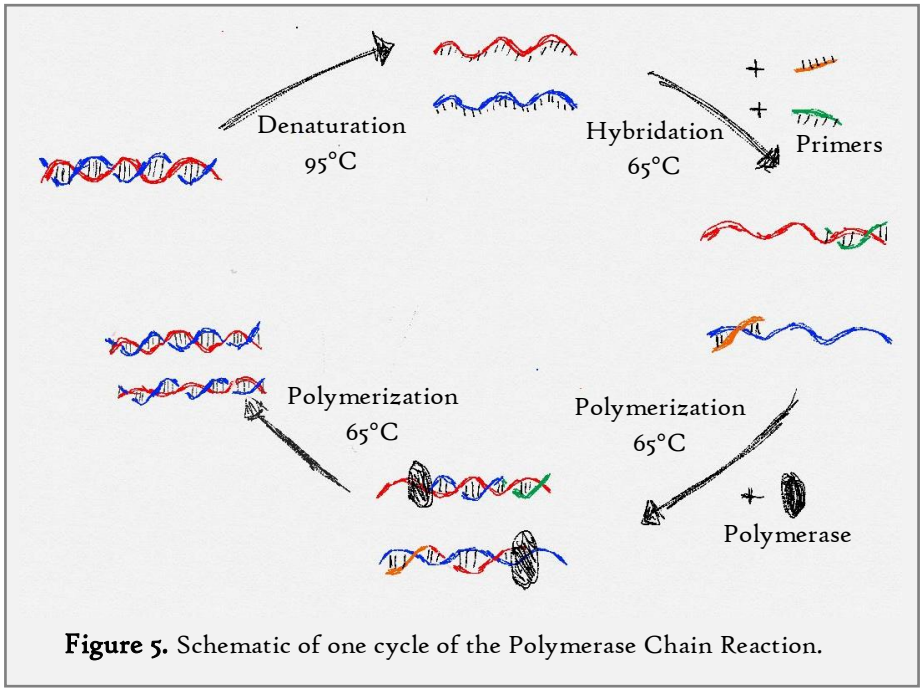

Figure 5. Schematic of one cycle of the Polymerase Chain Reaction.

PCR products can be directly detected using nucleic acid stains. These molecules (SyBr Green, ethidium bromide...) are molecules which are fluorescent when bounded to nucleic acid. Without any parasite reaction, checking the fluorescence of the PCR products with SyBr Green I, specific to dsDNA, is enough to assess the initial presence of the target. For more precision, gel electrophoresis is the main method to determine the result of a PCR. Products are put in an agarose or poly-acrylamide gel, and DNA is moved and separated through the gel pore by electrophoresis. The molecule velocity toward the cathode is proportional to the product size. After a fixed separation time, the stained products are observed and the final positions give the DNA sizes. DNA electrophoresis enables to discriminate between target copies and primer-dimers or non-specific products because of the different sizes of these nucleic acids. But this technique adds time to the PCR duration and doesn't allow a quantification of the target initial concentration, or the determination of the exact sequence of the products, which is useful in the case of mutation detection.

Real-time PCR, also called quantitative PCR (qPCR), is an alternative to the traditional end-point PCR. During qPCR, product accumulation is monitored at the end of each thermal cycle with fluorescent probes[15]. The probes can be non-specific, like SyBr Green I that detects any dsDNA, or specific to a given sequence. For example, Taqman probes are oligonucleotides complementary to a central region of the PCR products. A fluorophore and a quencher are linked to each side of the probe. After hybridization of the probe with the PCR product at the beginning of each cycle, the exonuclease activity of the Taq polymerase digests the probe and separates the quencher and the fluorophore: the fluorescence intensity increases[16]. The resulting fluorescence curve corresponds to the exponential amplification of products and can be fitted to obtain the initial concentration of target, with a dynamic range covering 5 orders of magnitude and going down to a single molecule.

qPCR is also compatible with other improvements of the initial PCR. First, RNA can be detected through PCR using a prior reverse-transcription reaction, which allows the creation of a complementary DNA (cDNA) to RNA thanks to a reverse-transcriptase enzyme. Secondly, PCR can be multiplexed to amplify multiple targets during the same reaction, using one set of primers for each product. Primer-dimer reaction and discrepancy in the amplification rate between different products limit in practical the multiplexing up to 9 different targets, after extensive optimization[17]. In the case of multiplexed-qPCR, the number of amplified sequence is often limited to 4, which is the usual number of optical channels on qPCR devices. Nested PCR is an alternative to multiplex PCR, in order to increase the specificity of the system with a 2 steps-reaction. A large sequence is first amplified by PCR, aliquoted into separate reservoirs, and a second PCR is run with different primer pairs, targeting different sub-sequence in the first PCR product, located in the different reservoirs. For a complete review of the PCR techniques, the reader could search for Michael J.McPherson and Simon Geir Møller's book[18].

Lab-based PCR is already used for a large number of pathogen detection. For viruses, the choice of qPCR over ELISA and viral culture (or RT-qPCR for retroviruses) has already been done in the early 2000's for a large number of pathogens: HSV, Enterovirus, Rabbies, Papillomavirus...[3]. For bacteria, PCR often shows a smaller LOD and higher specificity[19]. LOD for PCR is around 1 CFU/mL for *Legionella pneumophilia*, 5 cells for *E.Coli* and 1000 CFU/mL for *Listeria*[9]. Nevertheless, PCR has also limitations:

- The amplification reaction is inhibited by a large number of compounds: sample treatments and nucleic acid purification are often necessary steps. They are sometimes not generalizable to all samples and remain time-consuming in traditional laboratories.
- Its high sensitivity makes the reaction prone to contamination problems. Without special precautions, as the use of different rooms for the PCR mix preparation and the PCR thermocycling, products of previous run could contaminate the new reaction and cause false positive result as they could be amplified again.
- The PCR is really sensitive to the temperature of the different steps of the thermal cycling. Temperature precision and homogeneity, along with a high speed of heating and cooling make the thermocycler expensive, and difficult to miniaturize.
- The denaturation and polymerization steps are really fast. The limiting factor is actually the necessary time to heat or cool the sample between the different steps.

Isothermal amplification

More recently, other DNA amplification techniques have been developed to avoid the thermal cycling steps inherent to the PCR. These new methods work at a fixed temperature, so they are called isothermal amplification. Thermal denaturation has to be replaced, either by a different primer design or by an association between the polymerase and a second enzyme.

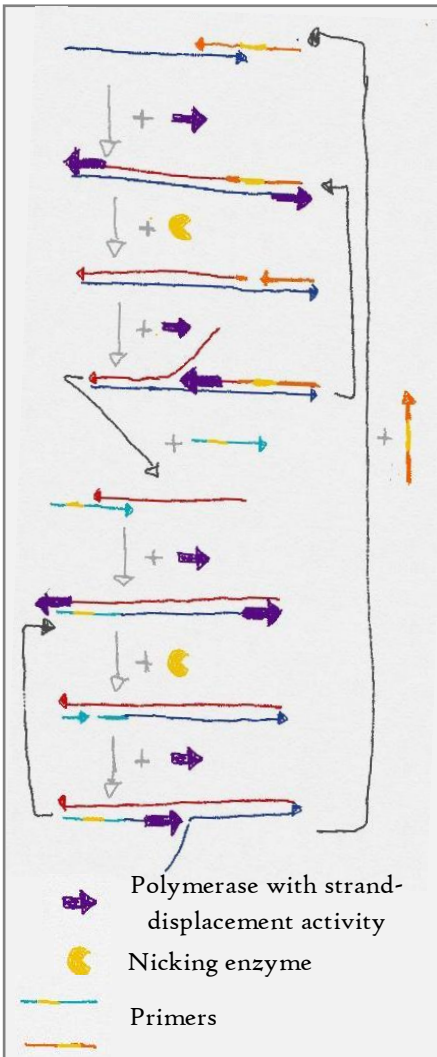

Figure 6. SDA scheme. 3' ends are indicated with arrows.

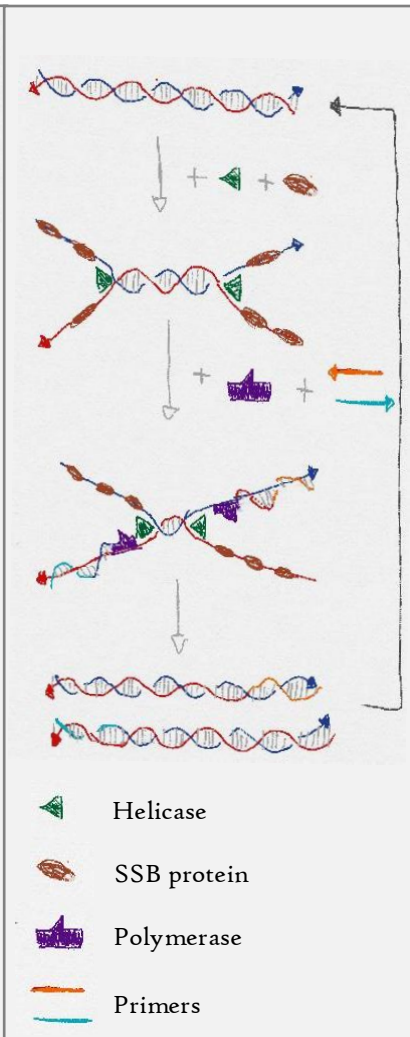

Figure 7. HDA scheme

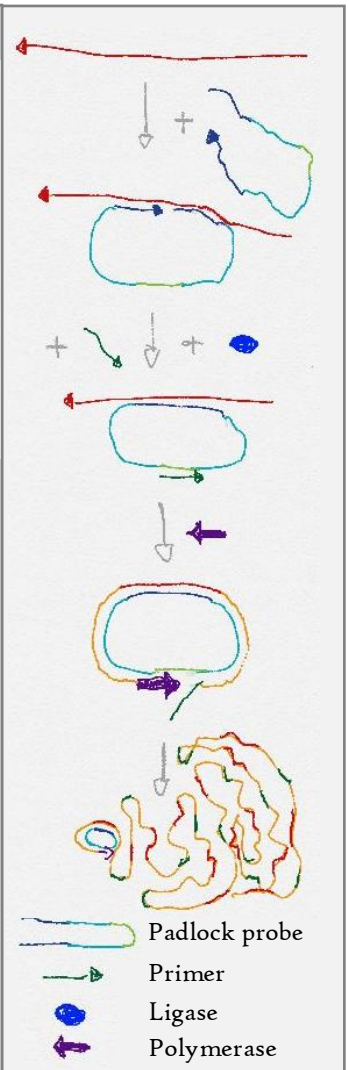

Figure 8. RCA scheme

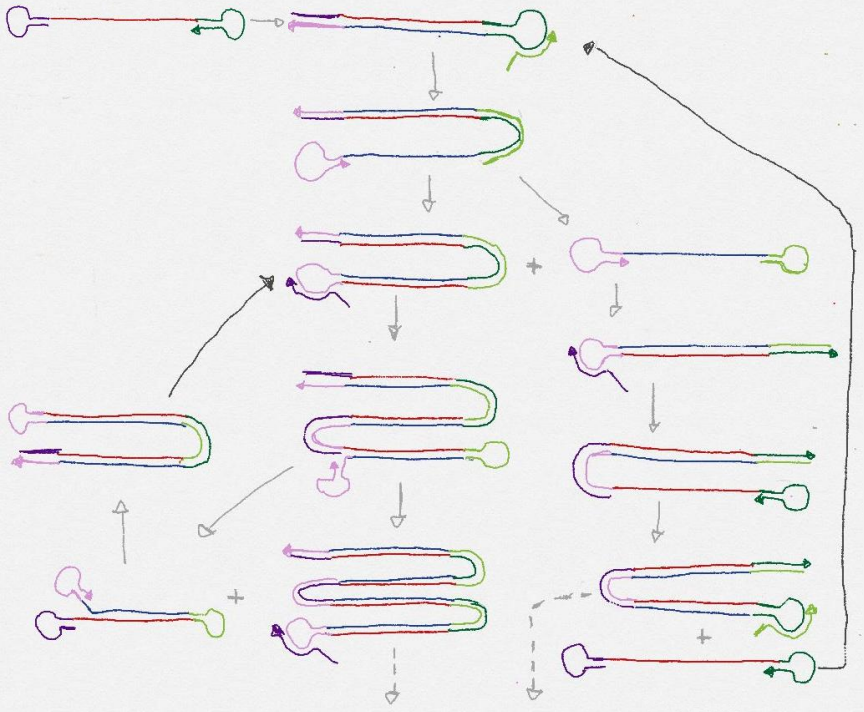

Figure 9. LAMP scheme

- Strand-Displacement Amplification (SDA): specific sequences, recognized by a nicking enzyme, are added at each end of the DNA sequence to be amplified (Figure 6). Nicking enzymes are modified restriction enzymes that cut only one strand of a dsDNA[20]. After nicking, a polymerase with a strand-displacement activity can elongate the cut ssDNA from the 3' extremity, while the other part of the cut strand is removed from the template as the polymerase process. The new dsDNA generates new ssDNAs by the same nicking/polymerizing association, leading to a linear amplification[21]. In addition, new dsDNAs are also created by the elongation of primers hybridized on the ssDNAs, leading to an exponential amplification[22].
- Loop-mediated isothermal amplification (LAMP): this amplification needs 4 primers which recognize 6 different sequences on the target DNA. After primer hybridization, the extremities of the ssDNA form hairpin loops. Through a complex sequence of polymerizing, strand-displacement, generation of new ssDNAs and recycling of dsDNAs (Figure 9), LAMP generates an exponential quantity of complex dsDNA with a large size polydispersity[23].
- Helicase-dependent isothermal Amplification (HDA): HDA is more similar to PCR than the LAMP technique. Instead of a thermal denaturation, a helicase enzyme unwinds the dsDNA, which is then stabilized by single-stranded DNA binding protein (SSB). So, primers have the possibility to bind to the unwind DNA and to be elongated by the polymerase (Figure 7).
- Recombinase Polymerase Amplification (RPA): during RPA, RecA, a recombinase used for homologous recombination[24], binds to a primer, recognizes the same sequence in the target dsDNA and insert the primer between the two strands of the DNA. The free strand is then stabilized by SSBs, recombinase detaches and a polymerase with a strand-displacement activity can elongate the inserted primer.
- Rolling-Circle Amplification (RCA): during RCA, two adjacent sequences in the target DNA are recognized by a padlock probe[25] (Figure 8). The probe is then circularized by a ligase only if the probe is completely complementary to the target. The target or a primer is then elongated by a polymerase with a strand-displacement activity, which rolls around the DNA circle while extending a concatemeric ssDNA that can attain 100kbp[26,27]. This linear amplification has many variants; some of them are exponential (HRCA[28], C2CA[29]...).

These techniques have different advantages and drawbacks. The absence of cycle and the low temperature of some techniques favour the formation of primer-dimer. SDA is especially parasitized by background amplification. LAMP design is not easy as the reaction needs 6 target sequences and a first thermal denaturation step is still necessary. RPA and HDA need two enzymes and SSBs, the optimization is not straightforward. For RCA, the reaction is highly specific, but two steps (ligation and amplification) and magnetic particles are necessary for a clean protocol.

However, instruments for isothermal reaction are easier to create, because the lack of temperature cycles decreases the power consumption and the complexity of the heating and cooling system. Isothermal reactions are also quicker than PCR, with an average duration around 30 minutes. These new methods are more and more used in academic proof of concept for pathogen detection[30–33], but most commercialized systems still rely on PCR.

1.4.2.3 Commercialized DNA detection systems

As discussed previously, DNA amplification allows the use of DNA detection protocols that have, in laboratories, a sufficient sensitivity and specificity for the detection of most pathogen. However, the traditional PCR is also time-consuming, needs sample pre-treatment and can't be directly considered as a POC technique. But companies have succeeded to solve some of these problems to offer fully integrated, automated or portable PCR-based instruments, or even amplification-free DNA detection devices. The following review won't be exhaustive and is condensed on the Table 1, but it will highlight some possible improvements of traditional qPCR and presents innovative DNA detection scheme that are already available on the market.

qPCR devices

Commercialized systems answer two main needs. Increased throughput in laboratories, along with the elimination of contamination problems are possible with a shortening of assay duration and hand-on time thanks to automation and integration of the pre-treatment step into the instrument. In addition, first liners and armies are asking for truly portable and robust systems for a fast detection of pathogenic threats, while centralized laboratories doesn't have the same concerns about footprint and portability.

The GeneXpert system, commercialized by Cepheid, is a lab-based qPCR automated instrument for the detection of pathogenic agents like bacteria or viruses. An integrated cartridge, specific for each pathogen, is used in order to purify the sample and isolate genomic material, using physical and chemical techniques. For example, the Tuberculosis kit concentrates *Mycobacterium tuberculosis bacilli* (MTB) from the patient sample, purifies genomic material after an ultrasonic lysis and amplifies a MTB specific sequence and a drug resistance inducing gene. 9 different kits are available, and all offer an answer in less than 2h, with a minimal hands-on time (less than 2 minutes). Concerning prices, the Xpert system price is $17000, a single cartridge costs approximately $73[6]. It has been shown that in USA, the price of the diagnostic strategy with the incorporation of the Xpert testing doesn't increase the overall cost of the diagnostic (including salaries, confirmatory tests...), and allows a gain of 6.32 QALY for 1000 patients. Finally, the GeneXpert system has been promoted by the WHO in 2010 for Tuberculosis detection in Africa.

The Liat system, commercialized by Cobas, also allows a full testing with minimal hands-on time. The core technology of the pre-treatment system is a consumable containing small bags of reagents. After sample deposition, reagents are selectively released and react successively with the sample to go from raw sample to purified genomic DNA, ready for the qPCR detection. Available kits are restricted to Strept A and Influenza A & B detection. However the system is sensitive (1 to 10 CFU per test for the bacteria detection) and fast. The overall test is only 15 minutes, meaning that the qPCR is ultra-fast, maybe because of a faster cooling and heating system. But these two previous systems remain bench top instruments and don't allow a multiplexed detection of multiple pathogens.

The RAZOR-EX system, commercialized by Biofire Defense, is a portable instrument for multiplex detection of pathogenic threads, specially designed for biodefence applications. The

instrument weights only 4.9kg and is supplied with a rechargeable battery. A kit allows a manual but simple sample treatment. The sample is then divided in 10 different chambers on a cartridge where it rehydrates freeze-dried reagents. 10 different pathogens including Anthrax and Salmonella can be detected by 10 different primer pairs, each of them located in one chamber. The total analysis lasts 30 minutes and has a 100 CFU/ml limit of detection.

Direct DNA detection systems

Some diagnostic tests are sensitive enough and don't need a DNA amplification before the detection. We will focus here on two newly commercialized systems, and we go back later on innovative proof-of-concepts. The first system is commercialized by Nanosphere and is called Verigene. After an integrated sample treatment in a first instrument, the searched DNAs are hybridized on different spots of a micro-array. Depending on the kit, this micro-array spots can be coated with primary oligonucleotide probes for 9 different pathogens simultaneously, mixing bacterial and viral targets. After capture of the sample DNAs, secondary oligonucleotide probes linked with gold nanoparticles recognize the captured DNAs. Nanoparticle size is then increased by a metallization process, in order to enhance the light scattered by the particles. The presence and quantity of searched DNA is then obtained via an optical reading of the micro-array. The test duration is around 2 hours, and the hands-on time lasts less than 5 minutes. It's interesting to note that this instrument can also make a direct detection of protein, using antibodies instead of the oligonucleotide probes. But no information was given about the specificity or sensitivity of the system.

The second system is called Palladium and is commercialized by IntegratedNano. On this system, composed of a cartridge and a small instrument (4.5kg, battery powered), a first sample pre-treatment is made in the cartridge in order to purify DNA from several types of sample. The DNA is then bridged between two electrodes coated with two capture oligonucleotides. Nanoparticles are then unspecifically bounded to the DNA bridges, partially melted and a metallization process allows the creation of a fully metalized bridge. The presence and the concentration of the searched DNA are then easily determined by measuring the conductivity between the electrodes. This technology, portable, can give results in less than one hour, for multiplexed analysis of 5 different pathogens simultaneously (West Nile Virus/Anthrax/Alpha Viruses/Flavi viruses) and with a limit of detection around 1000 copies per sample.

These systems are interesting, as they don't use any enzymes or biological reactions for the whole process, limiting the storage and non-reproducibility problems. The high multiplexing is also a big advantage, especially for applications like biodefence, when a lot of pathogens have to be tested even before the beginning of the symptoms. For example, the Verigene system is sold with multiplexed test for sepsis diagnosis. Prices are also comparable to the GenXpert system: the Verigene system costs $25,000 and individual tests are $50 only. Because these technologies have recently been put on the market, no information is currently available about their effective use in clinics.

Name	Company	Technique	Target	Sample	Time	POC	Other
BinaxNow	Alere	Immunochromatography lateral flow assay	*Legionella*	Urine	15min	Yes	Simple card, no reading system, no fluid control, no electronic. Reagent storage : 2-30°C Minimum hands-on operation LOD : 5×10^4CFU/ml for the Streptococcus assay Classified "Waived" by the FDA
			Staphylococcus Aureus	Positive Blood Culture	30min		
			Streptococcus pneumoniae	Urine CSF	15min		
			Influenza A/B	Nasal swab	15min		
			RSV	Nasal wash	15min		
			Malaria	Blood from fingerstick	15min		
NanoCHIP XL	Savyon Diagnostics	DNA Micro-array	MRSA / VRA / KPC (multiplexed)	Swab	2h 3h	No	Multiplex PCR Micro-array detection
GeneXpert	Cepheid	Integrated sample preparation + qPCR	MTB	Sputum	<2h	No	Hands-on time <1min
			Influenza A/ B / H1N1 (multiplexed)	Nasal wash	75min		Hands-on time : 2min Kit storage : 2-28°C
			MRSA	Nasal swab	<1h		
			C.difficile	Swab	30min		Hands-on time : 2min
			Norovirus	Swab	<1h		Hands-on time <1min

RAZOR-EX	Biofire Defense	qPCR + sample preparation kit	Anthrax, *Brucella melitensis, Botulism A, Coxiella, E. coli 0157*, Tularemia, Ricin, *Salmonella*, Smallpox, and Plague (multiplexed)		30min	Yes	Device weight : 4.9kg Rechargeable battery Freeze-dried reagents Detection of the 10 pathogens with a single assay. LOD : 100cfu/ml
Liat	Cobas	Integrated sample preparation + qPCR	*Strept A* Influenza A/B	Swab	15min	No	LOD : 1 to 10 CFU per test LOD : 0.001 to 0.1 TCID50/ml
Palladium	Integrated Nano	Sample preparation + Electronic detection of DNA hybridization without amplification	West Nile Virus/Anthrax/Alpha Viruses/Flavi viruses (multiplexed)	Multiple	<1h	Yes	LOD : 1000 copies per sample 4.5 kg, battery powered
Verigene	Nanosphere	Sample preparation + detection on micro-array via metallization of nanoparticle probe	*Campylobacter*/*Salmonella*/*Shigella*/*Vibrio*/*Yersinia enterocolitica*/Shiga toxins/Norovirus/Rotavirus (multiplexed)		2h Hands-on time <5min	No	

Table 1: List of commercialized molecular diagnostic tests

As illustrated by these examples, there exists a new class of diagnosis devices based on molecular tests, commercialized and already used on field. Their main advantages are the automation of the sample treatment and the decreasing of the hands-on time. Human errors, need for educated staff and contamination risks are reduced. However, cost reduction, further miniaturization for genomic detection is still needed, while the performance of lateral flow assays could also be improved without any lose in cost or portability. One of the promising tools to continue to improve medical diagnostic test is microfluidics: the science and technologies dealing with micro-scale control of fluids.

2 Microfluidics for molecular diagnostics

2.1 Definition

Microfluidics is the science and technology dealing with fluid at micro-scale, with at least one dimension smaller than 1 millimetre. This field is at the frontiers between physics, chemistry, biology and engineering:

- The fluid mechanics at small scale is different to macroscopic behaviour. Navier and Stokes equation for incompressible fluid, that is the master equation of fluid mechanics, is replaced at small scale by a simplified Stokes equation when gravity and non-linear terms are negligible:

$$\rho \frac{\partial \vec{u}}{\partial t} - \mu \nabla^2 \vec{u} = -\nabla P \quad (1)$$

  where P is the pressure, μ the fluid viscosity, ρ the fluid density and $\vec{u}$ the fluid velocity. This equation is linear and reversible, meaning that turbulences cannot develop at this small scale. For example, streams of two different liquids flowing side by side don't mix together, except by diffusion. At this scale, some forces are enhanced while some others are weakened. Gravity is now less influent than capillarity, electric forces are dominant and inertial effects disappear. This new force equilibrium enables the observation of new physical phenomenon at the microfluidics level. As the flow is laminar, a higher degree of fluid control is also possible.

- Surface chemistry plays a big role at micro-scale. Indeed in a microscopic channel or chamber, the surface-to-volume ratio increases as the inverse of the characteristic distance. In consequence, the effect of the surface chemistry is enhanced. Adsorption and absorption of molecules are favoured, surface charges allow electro-osmosis displacement. This partially explains why analytical chemistry is also one the main application domain of microfluidics. Indeed, the field has been started with the attempt to miniaturize chromatographic technique on a silicon wafer[34].

- Finally, microfluidics has a huge potential for biological or medical application. Diagnostic systems, cell culture and organ-on-chip for drug screening; biological and biophysical studies

represent now a large fraction of the applications. Microfluidics is useful as a tool for a better control of the cell culture conditions, as a way to miniaturize molecular test, as a way to study only a single cell or a single molecule. Moreover, concerning organs-on-chip, hard materials which are traditionally the architecture materials are now more and more replaced by soft biomimetic or natural hydrogel (collagen, Matrigel...): we are assisting to a shift from "biology-on-chip" to "chip-in-biology".

2.2 Microchip and microfabrication

Microfabrication is an important aspect of the development of microfluidics. Innovation was often driven by a new strategy for device fabrication, a new available material, which opens the road for new applications that were not reachable with the previous techniques. Traditionally, microfluidic was considered as an extension of the micro-electromechanical systems (MEMS) with the incorporation of fluidic processing. Microfluidic microfabrication was then inherited from the silicon-based techniques used for MEMS and microelectronics. By analogy, a microfluidic system is also called chip or microchip, and contains microchannels and chambers instead of electronic tracks. The first microchips were created using traditional MEMS materials: silicon and glass, in combination with standard microstructuration methods: photolithography and silicon etching. In consequence, the first microfluidicists were clean-room specialists, and the expansion of the field was limited to laboratories owning this type of expensive equipments. Moreover, prototyping was not easy as the whole fabrication time could span over several days.

The introduction of soft-lithography in 1998 by Georges Whitesides was a real breakthrough[35] (Figure 10). Photolithography was still used to produce a silicon wafer patterned with the structure on SU8, a thick negative resin. But this substrate serves as a mould for an elastomer called polydimethylsiloxane (PDMS). The viscous polymeric base is mixed with a curing agent and poured on the structured wafer. After less than two hours at 70°C, the reticulated, elastomeric polymer is removed from the mould. The structures from the mould are transferred in the PDMS, with a resolution down to 100nm[36]. Then, the channels are closed by bonding the PDMS substrate on a glass slide or a flat PDMS slab after oxidation by oxygen plasma. The treatment creates reactive radicals on the silicon groups which react with each other after contact and forms covalent bonds between the two surfaces.

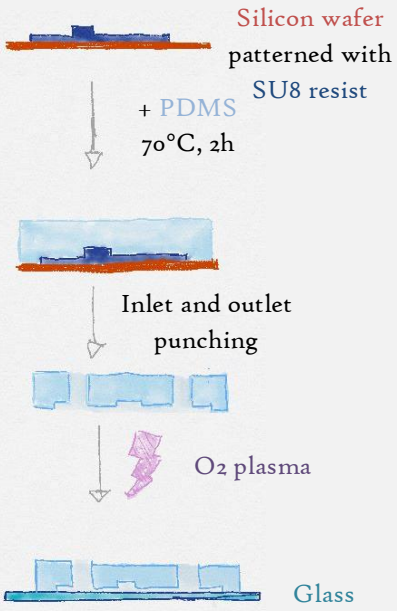

Figure 10. Classical soft-lithography protocol.

Soft-lithography allows fast prototyping of microfluidic chips. After mould fabrication, the same microfabricated wafer can be used for tens of chips, improving the repeatability of the process and decreasing fabrication costs. This new techniques opened the possibility

to export microfluidics outside of clean-rooms. Of course, the mould fabrication still needs clean-room equipments, but lighter than the ones necessary for silicon etching and bonding. And once the mould is finished, microchip fabrication could be done in a normal environment. With this innovation, microfluidics became a new tool for biological labs, and medical diagnostic specialists started to play with this technology.

- The nature and properties of PDMS can be detrimental or a real benefice, depending of the application[37]: PDMS is an elastomer, with a Young modulus going from 0.4MPa to 4MPa depending on the base-to-curing agent ratio. For comparison, glass and silicon Young modulus are around 100GPa. This elasticity is a good point as it allows an easy connection between chip and inlet and outlet tubes, the fabrication of soft membranes for valves[38], the culture of cells that prefer soft substrates[39].
- PDMS is a polymer and can swell in different solvent[40]. Fortunately, for the main diagnostic applications, PDMS is totally impermeable to water[41]. The material is also permeable to gases (oxygen, carbon dioxide and water vapour). This means that dead-end channels could be filled with water, because air bubbles are able to pass into the PDMS bulk; also, water in PDMS channels can evaporate through the walls. Oxygen and carbon dioxide permeability allows long term cell culturing (for miniaturized viral plaguing[42], for example) as the gases necessary for cell respiration are supplied through the channel walls[43].
- PDMS is not an inert material: surface treatment of PDMS is extremely complicated because the modified chains present at the surface of the polymer can move into the PDMS bulk or be covered with native small polydimethylsiloxane chains. Indeed, PDMS polymer is composed of a distribution of large and short chains, the later would be able to move and diffuse freely through the polymer mesh because all the chains are not reticulated, even after several days of curing. As a proof, plasma oxidation of PDMS is permanent if the small, unreacted chains are removed by solvent extraction from the PDMS bulk[44], whereas the hydrophobicity recovery lasts less than 15 minutes for PDMS in usual conditions. Moreover, after 14 days of thermal aging at 100°C, PDMS properties still change[45], proving that complete curing is hard to reach.
- Finally, the porosity and hydrophobicity of PDMS make this material an efficient trap for hydrophobic molecules. Absorption of small molecules like fluorophores has been observed[46]. Adsorption of proteins and nucleic acids, enhanced by hydrophobic-hydrophobic interactions, is a real problem for sensitive molecular application where low-concentrated target could be lost or enzymes could be stuck in the microchip surfaces.

In order to get totally rid of clean rooms, still necessary for photolithography, other techniques can be used. 3D printing of mould or final chips has been developed with fused filament modeling[47], inkjet deposition of photopolymerizable material[48] or micro-stereolithography[49]. In our lab, the alternative technique developed is micro-milling, an improved version of mechanical milling, with a tool diameter going down to 50µm and a lateral and height resolution of 1µm. The 3-axes instrument allows removal of brass or aluminium material, layer by layer. PDMS can be moulded on brass substrate for standard soft-lithography for prototyping. The total duration of the process, with the CAD (Computer Assisted Design) preparation, is less than 8 hours, with a minimal hands-on-time during milling. However, the resolution doesn't compete with clean room techniques and the spacing between structures and the radius of some angles are dictated by the tool size. But contrary to

photolithography, multi-layered structures are easy to fabricate, without any alignment steps. Lastly, new prototypes with new designs could be produced in less than a day.

Other materials are also used for fabrication of microfluidic system. For mass replication, thermoplastics materials offer an interesting alternative to PDMS. These materials (Cyclo-olefin copolymer, PMMA, Polystyrene,...) provide a large range of physical and chemical properties, compensating for PDMS limitations and can also be structured by hot-embossing with the same mould[50]. Moreover, the process is easy to scale up for industrialization which is an important point in the medical diagnosis field, were most of the research projects have the ambition to be transferred into a real technology for commercialization. Along the several other materials encountered in the microfluidics field for molecular diagnosis could be cited: for example paper[51] and plastics capillaries[52,53].

2.3 Microfluidics for molecular diagnosis

Different needs, encountered by molecular diagnostic systems, can be answered by microfluidics: miniaturization of the instrument, integration of multiple steps, automation, discovery of new phenomenon or improvement of known process by the intrinsic qualities of the miniaturization. Reproducibility is also increased by the use of microfluidic systems, because of the removal of contamination or the improved fluid control permitted by the miniaturization. Actually, some of the commercial instruments previously presented already contain microfluidics parts. The GeneXpert cartridge and the core of the Palladium and Verigene systems are microfabricated and work with a really small amount of liquid. Here, a short review of the main advantages of microfluidics for the field of molecular diagnosis will be presented.

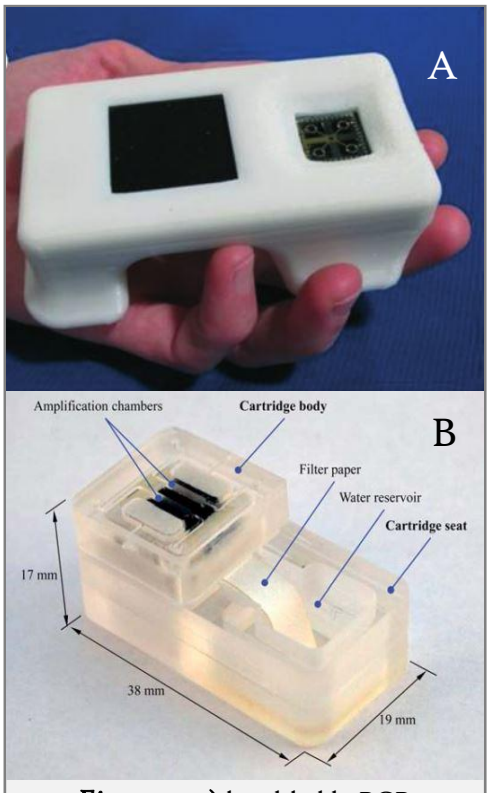

Figure 11. a) hand-held qPCR instrument[56], **b)** self-heating

2.3.1 Improvement of DNA amplification

Miniaturization improves the heating and cooling of a sample, because heat diffusion is an effective heat transfer phenomenon at small scales. Microfluidics could not enhance the enzyme activity of DNA amplification, but it is able to reduce the time needed for one PCR cycle because heating time is the limiting rate of the process. Neuzil *et al.* demonstrated an ultra-fast PCR with 40 cycles in less than 6 minutes, using a miniaturized thin film heater placed on a cantilever supporting 100nL sample[54]. Thermalisation of a flat chamber, containing a regular-size PCR sample, by switching the flowing of hot and cold liquid under the microfluidic chamber succeeded to reach the same performances[55]. Miniaturization also allows the fabrication of portable thermocycler. A hand-held qPCR instrument, weighting 90g with 4 sample slots detected H7N9 avian influenza in less than 35 minutes[56], but power supply was still mandatory (Figure 11). Electricity-free, self-heating block for

LAMP insured a constant temperature for DNA amplification[57]. The heating was brought by an exothermic reaction, fed with a constant flow of water through a paper bridge, and regulated by a phase-change material, allowing the detection of *E.Coli* bacteria without any power supply or battery. Nevertheless, these miniaturized instruments for DNA amplification are only one constituent of a real POC device, when sample treatment and detection have to be integrated with target amplification.

2.3.2 Integrated Point-of-Care system with DNA amplification

Thanks to miniaturization, integration of multiple protocols inside a single chip is now possible. Ferguson *et al*. demonstrated the detection of H1N1 influenza viruses from clinical samples with sensitivity 4 orders of magnitude below the clinical titers[58]. Viral RNA is first captured by antibody-coated magnetic particles in bulk, and then trapped in a microfluidic chamber by permanent magnets while the sample is pushed by a syringe pump. After purification and RT-PCR, the amplification products are detected via a sequence-specific electrochemical AC voltammetry. Even if all the protocol is integrated into a single chip, the system still need a bulky syringe pump to operate. A real challenge is to replace the pumps, syringe-pumps and pressure controllers often used in academic laboratories to flow liquids inside the microfluidic chip for simpler systems or passive actuations in order to miniaturize the chip and all the instrumentation around.

Three different methods for moving samples are used in the POC system presented by Borysiak *et al.* for *E.Coli* detection from whole milk[59]. First, the microfluidic hydrophilic network is filled with LE buffer by capillarity. Sample is added in one end of a long channel with a TE buffer and a constant current is applied across the channel. Bacterial DNA is then separated from the whole milk by isotachophoresis, a mode of electrophoresis where two buffers are used, and the sample is focused in the moving LE/TE interface. After 4 minutes of separation time, the whole chip is warmed to 65°C. This expands air blocked in a perpendicular channel, that expulses the focused DNA into an adjacent chamber containing dried LAMP reagents. After amplification, the resulting fluorescence is recorded via a smartphone camera; the whole method allows the detection of 1000 CFU/ml.

Concerning molecular diagnostics, one efficient platform is the centrifugal microfluidics, or Lab-on-a-Disk. Microfluidic channels are fabricated in a CD-shaped plastic chip which can be mounted into a modified CD reader. The centrifugal force exerted on the fluid during chip rotation moves the sample and reagents from the centre of the chip to the periphery. Valves

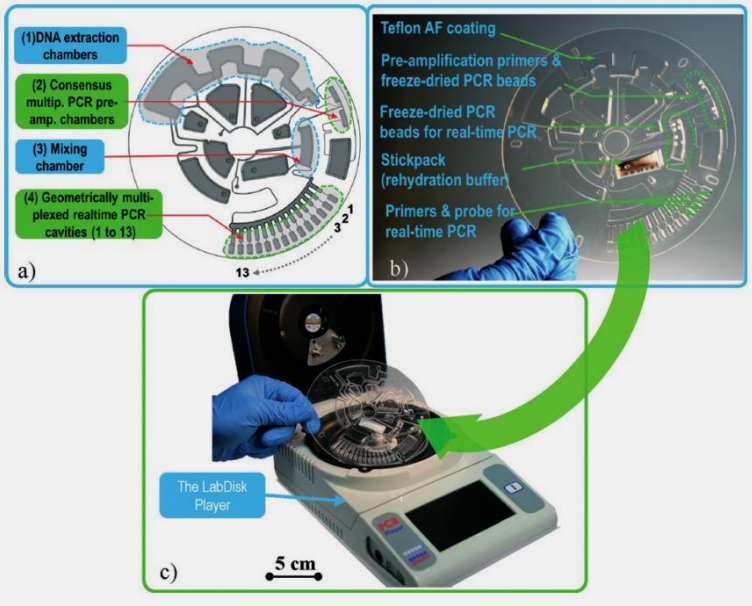

Figure 12. LabDisk platform for the detection of pathogen with qPCR[62].

have been designed in order to retain the liquid until a chosen rotation speed, allowing sequential release of fluids. In addition, fluorescence and colorimetric measurement could be done with a modified laser initially used for CD reading. DNA amplifications are easy to integrate as soon as the instrument around the disc heats or cools. Genomic amplification from 4 different pathogens in milk has been demonstrated in a LabDisk with a real-time RPA and a sensitivity of 4 cells in the 3.2µl sample[60]. Sample treatment can be easily implemented, as shown by Oh *et al.* with a DNA purification on beads followed by a colorimetric detection of LAMP products[61]. Magnetic capture and manipulation have also been shown for sample treatment, with dried reagents and buffer storage into aluminium bags, opened at a certain rotation rate. Bacteria and viruses in serum have been successfully detected by nested-PCR or RT-PCR with a complete automated protocol[62,63] (Figure 12). The instrument around the LabDisk is compact and the protocols easy to follow, allowing the use of these systems as a POC device.

However, microfluidic systems presented on this section don't have the potential to be truly portable, ultra low-cost and electricity-free, as the Alere's lateral flow assays. This is why a new microfluidic platform emerged in 2009, called paper microfluidics. Paper is used to pump liquid, like in the lateral flow assay, but 2D and 3D architectures are built thanks to creation of hydrophobic barriers by wax printing[64], allowing alliquoting, sequential reaction... Molecular diagnostics on paper quickly expanded, with glucose and BSA detection in urine as first proofs of concept[51]. Now, complex protocols have been demonstrated on paper matrix, with nucleic acid isolation from crude cervical sample, papillomavirus detection by LAMP and lateral flow detection in less than one hour[65]. This assay is really portable, electricity-free, easy to destroy after use, easy to use and the material is low-cost. The only critics possible here is the use of enzymes, with the known difficulties concerning storage and the cost of these reagents, and a lower sensitivity compared to others strategies. This is why some systems are trying to eliminate the amplification step and to directly assess the presence of the initial targets.

2.3.3 DNA direct read on microfluidic systems

DNA amplification is used to increase the sensitivity of the detection, by creating a larger number of target copies, and the specificity, because most detection methods only detect DNA and are not sequence specific, which is the case of most of the DNA amplification techniques. Nevertheless, amplification-free, direct read of DNA is possible with sensitive technique and specific probes. Lam *et al.* showed the possibility to electrically lyse bacteria in a microfluidic chamber, followed

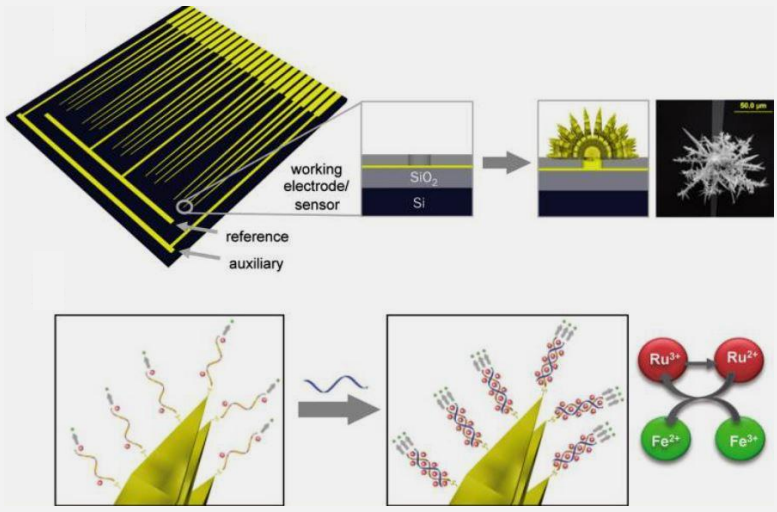

Figure 13. Bacterial detection sensors with nanostructured electrodes[66]. The electrochemical detection scheme for nucleic acids utilizes Ru3+ and Fe3+ electrocatalytic reporter pair.

by the electrochemical detection of RNA after hybridization of the nucleic acids with complementary peptide nucleic acids (PNA)[66] (Figure 13). PNAs are modified nucleic acid, with a neutral backbone and a higher specificity and affinity for DNA and RNA. Because the probes are hybridized on nanostructured surfaces, the high surface over volume ratio of microfluidic chambers increases the capture rate of bacterial DNA, compared to macroscopic wells. Coupled with the electrochemical detection, the method is sensitive enough to detect 1000 CFU/ml in urine.

Fluorescence can also be used for sensitive detection of a single cell. Digital compartmentalization of single *E.Coli* bacterium into water droplets has been performed with a microfluidic flow-focusing droplet generator. The cells are mixed before droplet generation with PNA beacon probes which become fluorescent only when bound to the complementary *E.Coli* RNA. With this technique, a droplet containing a single bacterium becomes fluorescent, allowing the detection of really rare microorganisms[67].

2.3.4 Protein detection

Finally, protein detection has also been adapted in a microfluidic chip. ELISA protocols have been optimized for a large number of pathogen detection, but the manual processing and the cost of reagents don't make it a low-cost and portable technique. This can be solved by miniaturization. Local HIV and syphilis detections, with patient sample collected in Rwanda have been demonstrated with a miniaturized ELISA[68]. The system developed by Chin *et al.* directly processes 1µl of blood without any sample treatment and obtains clinically relevant sensitivity and sensibility. The only negative point is the manual loading of reagents and air spacers in a tube, before the flowing of these plugs into the device thanks to a vacuum produced by a syringe.

Antibodies are difficult to store and preserve. Antimicrobial peptides are a good alternative: they are stable, easier to produce, can target a broad range of microbial pathogens. These peptides target the specific composition of bacterial, viral and fungal lipidic membranes. Mannoor *et al.* demonstrated a microfluidic chamber for the high capture of bacteria strains, with a higher specificity for pathogen *E.Coli*, followed by an electrical detection of the impedance change induced by the bacteria capture[69]. The sensitivity is high even without any amplification or culture step (1000 CFU/ml), but the non-specificity limits the use of the method to a first test for routine screening.

2.4 PhD project: conductometric detection of electro-hydrodynamic aggregates of DNA

As seen previously, microfluidics has several advantages that make its use beneficial for molecular diagnostic devices. Products already on the market, like the GeneXpert instrument, contain microfluidic parts in order to miniaturize the sample and reagent quantities and to automate the whole pre-treatment and detection process. In the academic research, adaptation of reliable protocols into new microfluidic prototypes allows a fully portable or low-cost detection of pathogens. New detection schemes have been demonstrated that use microfluidic confinement and can't be reproduced on a macroscopic protocol. However, along the state of the art presented above, no complete microfluidic solutions combine sample treatment and DNA detection, which is

more universal than protein detection, with a footprint equivalent of the immunochromatography cassette. Most of the commercialized products still have the size of a bench-top system or need a power supply. Lastly, unless for the LabDisk format and the GeneXpert, sample size is closer to the millilitre range and sample pre-treatment always use a large amount of reactant.

Based on previous works realized in the MMBM team, we have developed a new DNA detection module in a microfluidic format. This method, easily miniaturizable, has the potential to be integrated into a portable instrument for on-field detection of pathogen. Moreover, this detection is a direct electrical reading and is label-free because no specific reagent is needed to probe the presence of DNA molecules. This detection scheme is based on a surprising physical phenomenon discovered by Jean-Louis Viovy *et al*. in 1995 that occurred initially during electrophoretic separation of long DNAs. When a capillary or microfluidic channel filled with a solution of long and concentrated DNA is submitted to a high electric field, DNA aggregates and forms 100µm-long DNA rich region. First seen as an artefact, this phenomenon has then been used for DNA detection during the PhD of Mohamed Lemine Youba Diakité, defended in 2012. These electrohydrodynamic aggregates have a different conductivity than the surrounding solution, and a local conductometric measurement is able to detect these DNAs. The second chapter of this manuscript is focused on the underlying physics and the improvements and validation done from the first proof-of-concept in order to increase the sensitivity, the reproducibility and the integration of the system.

However, this system could only detect long DNAs, and most of the known biomarkers are too small to be detected by our device. A large part of my PhD has been dedicated to the development and optimization of a protocol for the elongation and the amplification of small DNA sequence. We focused on isothermal amplification, to limit the cooling and heating of the microsystem. Two strategies will be presented on the third chapter of the thesis: a hyper-branched RCA has first been investigated, and the performance of this elongation and amplification method has then been improved with the addition of a pre-amplification step performed by SDA.

Finally, a new microfluidic technology, called "reconfigurable sliding wall", has been developed as a tool-box for several applications. It was initially based on a neurophysics project of the team which needed a new way to temporally compartmentalize a large microfluidic chamber. With Ayako Yamada, a post-doctoral researcher of the team, we developed a system with a nylon filament as a removable wall to open the chamber when needed. This system has then been applied by Ayako Yamada to 2D cell co-culture, competition assay and integration of biohydrogel slab into a microfluidic chip for 3D cell culture. Personally, I then generalized this first idea in order to use this technology for sample treatment, especially for the development of a microreactor for sequential reactions and for sample preconcentration. Technically, nylon fibre was replaced by solid walls made by 3D printing or with metallic sheet. These sliding walls were used to open and close a chamber or as a sliding valve. The integration of hydrogel membranes into these walls allows the capture, preconcentration and moving of long DNA between different channels prior to the detection.

References

1. Zoetendal, E. G., Vaughan, E. E. & De Vos, W. M. A microbial world within us. *Mol. Microbiol.* **59,** 1639–1650 (2006).

2. Cottinet, D. *et al.* Lineage Tracking for Probing Heritable Phenotypes at Single-Cell Resolution. *PLoS One* **11,** e0152395 (2016).

3. Reller, L. B., Weinstein, M. P., Editors, S. & Storch, G. a. Diagnostic virology. *Clin. Infect. Dis.* **31,** 739–751 (2000).

4. Breitbart, M. & Rohwer, F. Here a virus, there a virus, everywhere the same virus? *Trends Microbiol.* **13,** 278–284 (2005).

5. Wade, W. Unculturable bacteria—the uncharacterized organisms that cause oral infections. *J. R. Soc. Med.* **95,** 81 (2002).

6. H. W. Choi, K. Miele, D. Dowdy, and M. S. Cost-effectiveness of Xpert® MTB/RIF for diagnosing pulmonary tuberculosis in the United States. *Int J Tuberc Lung Dis.* **17,** 1328–1335 (2013).

7. Fang, C., Otero, H. J., Greenberg, D. & Neumann, P. J. Cost-utility analyses of diagnostic laboratory tests: A systematic review. *Value Heal.* **14,** 1010–1018 (2011).

8. Engvall, E. & Perlmann, P. Enzyme-linked immunosorbent assay (ELISA) quantitative assay of immunoglobulin G. *Immunochemistry* **8,** 871–874 (1971).

9. Lazcka, O., Campo, F. J. Del & Munoz, F. X. Pathogen detection: A perspective of traditional methods and biosensors. *Biosens. Bioelectron.* **22,** 1205–1217 (2007).

10. Organization, W. H. Malaria Rapid Diagnostic Test Performance. **4,** (2012).

11. Levy, S. *et al.* The diploid genome sequence of an individual human. *PLoS Biol.* **5,** 2113–2144 (2007).

12. Lukjancenko, O., Wassenaar, T. M. & Ussery, D. W. Comparison of 61 Sequenced Escherichia coli Genomes. *Microb. Ecol.* **60,** 708–720 (2010).

13. Mora, C., Tittensor, D. P., Adl, S., Simpson, A. G. B. & Worm, B. How many species are there on earth and in the ocean? *PLoS Biol.* **9,** 1–8 (2011).

14. Saiki, R. *et al.* Enzymatic amplification of beta-globin genomic sequences and restriction site analysis for diagnosis of sickle cell anemia. *Science* **230,** 1350–1354 (1985).

15. Heid, C., Stevens, J., Livak, K. & Williams, P. Real time quantitative PCR. *Genome Res.* **6,** 986–994 (1996).

16. Holland, P. M., Abramson, R. D., Watson, R. & Gelfand, D. H. Detection of specific polymerase chain reaction product by utilizing the 5'-3' exonuclease activity of Thermus aquaticus DNA polymerase. *Proc Natl Acad Sci U S A* **88,** 7276–7280 (1991).

17. Henegariu, O. & Heerema, N. a. Multiplex PCR: Critical Parameters and Step-by-Step Protocol. *Biotechniques* **23,** 504–511 (1997).

18. McPherson, M. & Møller, S. *PCR: The Basics*. (Taylor & Francis Group, 2006).

19. Jalal, H., Stephen, H., Al-Suwaine, A., Sonnex, C. & Carne, C. The superiority of polymerase chain reaction over an amplified enzyme immunoassay for the detection of genital chlamydial infections. *Sex. Transm. Infect.* **82,** 37–40 (2006).

20. Xu, S. Y. *et al.* Discovery of natural nicking endonucleases Nb.BsrDI and Nb.BtsI and engineering of top-strand nicking variants from BsrDI and BtsI. *Nucleic Acids Res.* **35,** 4608–4618 (2007).

21. Joneja, a. & Huang, X. Linear nicking endonuclease-mediated strand DNA Amplification. *Anal Biochem* **414,** 58–69 (2011).

22. Walker, G. T. *et al.* Strand displacement amplification--an isothermal, in vitro DNA amplification technique. *Nucleic Acids Res.* **20,** 1691–1696 (1992).

23. Notomi, T. *et al.* Loop-mediated isothermal amplification of DNA. *Nucleic Acids Res.* **28,** E63 (2000).

24. Sehorn, M. G. & Sung, P. Meiotic recombination: An affair of two recombinases. *Cell Cycle* **3,** 1375–1377 (2004).

25. Nilsson, M. *et al.* Padlock probes: circularizing oligonucleotides for localized DNA detection. *Science* **265,** 2085–2088 (1994).

26. Banér, J., Nilsson, M., Mendel-Hartvig, M. & Landegren, U. Signal amplification of padlock probes by rolling circle replication. *Nucleic Acids Res.* **26,** 5073–8 (1998).

27. Lizardi, P. M. *et al.* Mutation detection and single-molecule counting using isothermal rolling-circle amplification. *Nat. Genet.* **19,** 225–32 (1998).

28. Yong Zhang, D., Brandwein, M., Chun Hung Hsuih, T. & Li, H. Amplification of target-specific, ligation-dependent circular probe. *Gene* **211,** 277–285 (1998).

29. Dahl, F. *et al.* Circle-to-circle amplification for precise and sensitive DNA analysis. *Proc. Natl. Acad. Sci. U. S. A.* **101,** 4548–53 (2004).

30. Toley, B. J. *et al.* Isothermal strand displacement amplification (iSDA): a rapid and sensitive method of nucleic acid amplification for point-of-care diagnosis. *Analyst* **140,** 7540–7549 (2015).

31. Euler, M. *et al.* Recombinase polymerase amplification assay for rapid detection of Rift Valley fever virus. **54,** 308–312 (2012).

32. Steain, M. C. *et al.* Detection of influenza A H1N1 and H3N2 mutations conferring resistance to oseltamivir using rolling circle amplification. *Antiviral Res.* **84,** 242–248 (2009).

33. Kaocharoen, S. *et al.* Hyperbranched rolling circle amplification as a rapid and sensitive method for species identification within the Cryptococcus species complex. *Electrophoresis* **29,** 3183–3191 (2008).

34. Terry, S. C., Jerman, J. H. & Angell, J. B. A gas chromatographic air analyzer fabricated on a silicon wafer. *IEEE Trans. Electron Devices* **26,** 1880–1886 (1979).

35. Duffy, D. C., Mcdonald, J. C., Schueller, O. J. A. & Whitesides, G. M. Rapid Prototyping of Microfluidic Systems in Poly (dimethylsiloxane). *Anal. Chemiystry* **70,** 4974–4984 (1998).

36. Zhao, X.-M., Xia, Y. & Whitesides, G. M. Soft lithographic methods for nano-fabrication. *J.*

Mater. Chem. **7,** 1069–1074 (1997).

37. Mukhopadhyay, R. When PDMS isn't the best. *Anal. Chem.* 1–5 (2007).

38. Thorsen, T., Maerkl, S. J. & Quake, S. R. Microfluidic Large-Scale Integration. **298,** 580–584 (2002).

39. Engler, A. J., Sen, S., Sweeney, H. L. & Discher, D. E. Matrix Elasticity Directs Stem Cell Lineage Specification. *Cell* **126,** 677–689 (2006).

40. Lee, J. N., Park, C. & Whitesides, G. M. Solvent compatibility of poly(dimethylsiloxane)-based microfluidic devices. *Anal. Chem.* **75,** 6544–54 (2003).

41. Watson, J. M. & Baron, M. G. The behaviour of water in poly(dimethylsiloxane). *J. Memb. Sci.* **110,** 47–57 (1996).

42. Delincé, M. J.-H. *et al.* A microfluidic cell-trapping device for single-cell tracking of host–microbe interactions. *Lab Chip* **16,** 3276–3285 (2016).

43. Halldorsson, S., Lucumi, E., Gómez-Sjöberg, R. & Fleming, R. M. T. Advantages and challenges of microfluidic cell culture in polydimethylsiloxane devices. *Biosens. Bioelectron.* **63,** 218–231 (2015).

44. Vickers, J. A., Caulum, M. M. & Henry, C. S. Generation of Hydrophilic Poly (dimethylsiloxane) for High-Performance Microchip Electrophoresis. *Anal. Chem.* **78,** 7446–7452 (2006).

45. Eddington, D. T., Puccinelli, J. P. & Beebe, D. J. Thermal aging and reduced hydrophobic recovery of polydimethylsiloxane. *Sensors Actuators, B Chem.* **114,** 170–172 (2006).

46. Toepke, M. W. & Beebe, D. J. PDMS absorption of small molecules and consequences in microfluidic applications. *Lab Chip* **6,** 1484–6 (2006).

47. Mcdonald, J. C. *et al.* Prototyping of Microfluidic Devices in Poly (dimethylsiloxane) Using Solid-Object Printing the fabrication of microfluidic devices in poly (dimethyl-. *Anal. Chem.* **74,** 1537–1545 (2002).

48. Anderson, K. B., Lockwood, S. Y., Martin, R. S. & Spence, D. M. A 3D printed fluidic device that enables integrated features. *Anal. Chem.* **85,** 5622–5626 (2013).

49. Comina, G., Suska, A. & Filippini, D. PDMS lab-on-a-chip fabrication using 3D printed templates. *Lab Chip* **14,** 424–30 (2014).

50. Mottet, G. *et al.* A three dimensional thermoplastic microfluidic chip for robust cell capture and high resolution imaging. *Biomicrofluidics* **8,** 1–14 (2014).

51. Martinez, A. W., Phillips, S. T., Whitesides, G. M. & Carrilho, E. Diagnostics for the developing world: microfluidic paper-based analytical devices. *Anal. Chem.* **82,** 3–10 (2010).

52. Ali-Cherif, A., Begolo, S., Descroix, S., Viovy, J. L. & Malaquin, L. Programmable magnetic tweezers and droplet microfluidic device for high-throughput nanoliter multi-step assays. *Angew. Chemie - Int. Ed.* **51,** 10765–10769 (2012).

53. Reis, N. M., Pivetal, J., Loo-Zazueta, A. L., Barros, J. & Edwards, A. D. Lab on a Stick: Multi-Analyte Cellular Assays in a Microfluidic Dipstick. *Lab Chip* **16,** 2891–2899 (2016).

54. Neuzil, P., Zhang, C., Pipper, J., Oh, S. & Zhuo, L. Ultra fast miniaturized real-time PCR: 40

cycles in less than six minutes. *Nucleic Acids Res.* **34,** (2006).

55. Houssin, T. *et al.* Ultra-fast, sensitive and large-volume on-chip real-time PCR for the molecular diagnosis of bacterial and viral infections. *Lab Chip* **16,** 1401–1411 (2016).

56. Ahrberg, C. D., Ilic, B. R., Manz, A. & Neužil, P. Handheld real-time PCR device. *Lab Chip* **16,** 586–592 (2016).

57. Liu, C., Mauk, M. G., Hart, R., Qiu, X. & Bau, H. H. A self-heating cartridge for molecular diagnostics. *Lab Chip* **11,** 2686–92 (2011).

58. Ferguson, B. *et al.* Genetic Analysis of H1N1 Influenza Virus from Throat Swab Samples in a Microfluidic System for Point-of-Care Diagnostics. *J. Am. Chem. Soc.* **4,** 9129–9135 (2011).

59. Borysiak, M. D., Kimura, K. W. & Posner, J. D. NAIL: Nucleic Acid detection using Isotachophoresis and Loop-mediated isothermal amplification. *Lab Chip* **15,** 1697–1707 (2015).

60. Choi, G. *et al.* A centrifugal direct recombinase polymerase amplification (direct-RPA) microdevice for multiplex and real-time identification of food poisoning bacteria. *Lab Chip* **16,** 2309–2316 (2016).

61. Oh, S. J. *et al.* Fully automated and colorimetric foodborne pathogen detection on an integrated centrifugal microfluidic device. *Lab Chip* **16,** 1917–1926 (2016).

62. Czilwik, G. *et al.* Rapid and fully automated bacterial pathogen detection on a centrifugal-microfluidic LabDisk using highly sensitive nested PCR with integrated sample preparation. *Lab Chip* **15,** 3749–3759 (2015).

63. Stumpf, F. *et al.* LabDisk with complete reagent prestorage for sample-to-answer nucleic acid based detection of respiratory pathogens verified with influenza A H3N2 virus. *Lab Chip* **16,** 199–207 (2016).

64. Carrilho, E., Martinez, A. W. & Whitesides, G. M. Understanding wax printing: a simple micropatterning process for paper-based microfluidics. *Anal. Chem.* **81,** 7091–5 (2009).

65. Rodriguez, N. M., Wong, W. S., Liu, L., Dewar, R. & Klapperich, C. M. A fully integrated paperfluidic molecular diagnostic chip for the extraction, amplification, and detection of nucleic acids from clinical samples. *Lab Chip* **16,** 753–763 (2016).

66. Lam, B., Fang, Z., Sargent, E. H. & Kelley, S. O. Polymerase Chain Reaction-Free, Sample-to-Answer Bacterial Detection in 30 Minutes with Integrated Cell Lysis. *Anal. Chem.* **84,** 21–25 (2012).

67. Rane, T. D., Zec, H. C., Puleo, C., Lee, A. P. & Wang, T.-H. Droplet microfluidics for amplification-free genetic detection of single cells. *Lab Chip* **12,** 3341 (2012).

68. Chin, C. D. *et al.* Microfluidics-based diagnostics of infectious diseases in the developing world. *Nat. Med.* **17,** 1015–9 (2011).

69. Mannoor, M. S., Zhang, S., Link, A. J. & McAlpine, M. C. Electrical detection of pathogenic bacteria via immobilized antimicrobial peptides. *Proc. Natl. Acad. Sci.* **107,** 19207–19212 (2010).

CHAPTER 2: Conductometric detection of DNA aggregates triggered by electrohydrodynamic instabilities.

The main objective of this PhD was to build an integrated, portable DNA detection system, based on a first proof-on-concept developed earlier in the MMBM team. This prototype takes profit of a surprising phenomenon called “electrohydrodynamic instabilities”, which allows the aggregation of long DNAs into large objects under the influence of large electric fields. This first chapter will be first dedicated to the description of the electrohydrodynamic instability phenomenon. Then, the prototype will be presented, along with the several improvements made since the beginning of my PhD. This presentation will include an introduction about conductometric measurement in capillary electrophoresis, the description of the microsystem and the electronic systems used for the detection. Finally, a last section will focus on the conductometric signal treatment and a calibration of the system.

Table of contents

1 Electrohydrodynamic instabilities 40
1.1 Capillary electrophoresis 40
1.2 Experimental setup for aggregation visualization 41
1.3 Theory 42
1.3.1 DNA coil shape 43
1.3.2 Salt concentration perturbation 45
1.3.3 Electroneutrality breakdown 49
1.3.4 Electrohydrodynamic aggregation 50
1.3.5 DNA Aggregates shape and dynamic 53
2 Conductometric detection of DNA aggregates 55
2.1 Detection system overview 55
2.2 Principle of the conductometric measurement in capillary electrophoresis 56
2.3 Micro-fabrication and electronics 60
2.3.1 Methods and design for chip microfabrication 60
2.3.2 Excitation and detection electronics 62
2.4 Signal acquisition and treatment 68
2.4.1 Signal acquisition and demodulation 68
2.4.2 Wavelet analysis 69
2.5 Calibration and modelling 77
2.5.1 Exhaustive experimental procedure 77
2.5.2 Optical correlation 78
2.5.3 Conductometric calibration 79
Conclusion of the chapter 83
References 84

1 Electrohydrodynamic instabilities

Take a solution of long DNA at typical biologically relevant concentrations, inject it into a capillary or a microchannel, and apply a strong electric field: DNA aggregates into giant, dynamic patterns. This phenomenon, called electrohydrodynamic instabilities, was originally discovered by Jean-Louis Viovy[1,2], as an artefact in capillary electrophoresis (CE) experiment in 1995.

In this subsection, I will first give a short description of the capillary electrophoresis technique, followed by a description of the experimental conditions required for this DNA aggregation. Most of this chapter will then be dedicated to the explanation of this phenomenon, based on Hervé Isambert *et al.* paper[3] that I will summarize with new quantitative and qualitative descriptions.

1.1 Capillary electrophoresis

Capillary electrophoresis is a separation method for DNA derived from the gel electrophoresis. During a gel electrophoresis experiment, an electric field is applied through a slab of polymer gel, typically agarose or polyacrylamide. DNA samples, loaded in one side of the gel slab, migrate through the polymer matrix. Negative charges of DNA are attracted by the anode located at the other end of the gel. As DNA has a constant charge to size ratio, the size separation is only due to the size-dependant migration through the dense polymer. Capillary electrophoresis with a sieving media uses the same principle and was initially developed to exploit the small lateral dimensions of the capillary, to facilitate heat dissipation and reduce convection, thus overcoming major difficulties plaguing free flow electrophoresis. It has been extensively applied to separate DNA, and was indeed the technique used for the first sequencing of the human genome. A long glass microcapillary is filled with a solution containing mobile entangled hydrophilic polymers, and each ends are immerged into a buffer solution in contact with electrodes (Figure 1).

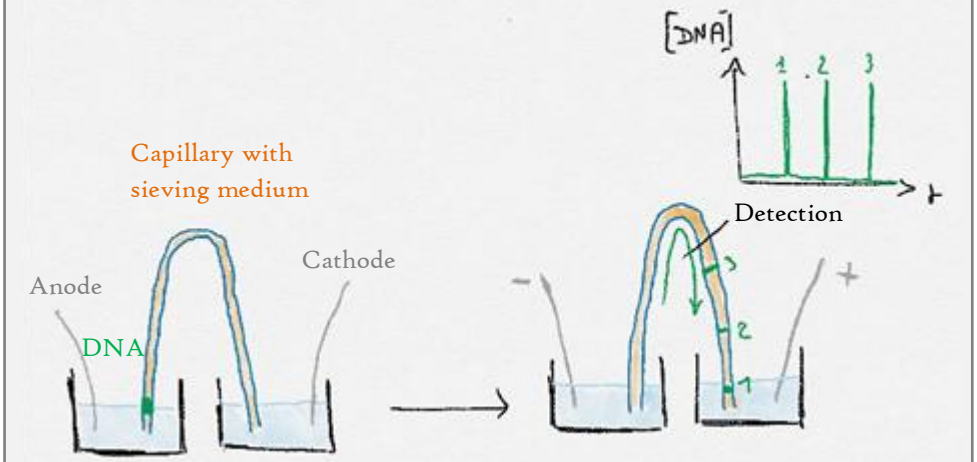

Figure 1. Experimental setup for capillary electrophoresis. A DNA sample with 3 different sizes of DNA is loaded into the capillary. During migration into the capillary filled with sieving medium, 3 DNA bands are separated and visualized through the capillary.

During the nineties, capillary electrophoresis was coupled with Sanger sequencing[4] to enhance separation of products of this sequencing method. However, CE became also one of the bottlenecks of the procedure in the attempts to increase sequencing throughput. This limitation became even harder to resolve for applications requiring to separate long DNA fragments. Moreover, over a certain DNA size, capillaries were blocked by DNA plugs and unexpected and unexplained peaks appeared in the electrophoregrams[2,5].

1.2 Experimental setup for aggregation visualization

L.Mitnik[1] investigated this phenomenon in J.L. Viovy's team with a transparent capillary and a fluorescent videomiscroscope system (Figure 2). A solution of fluorescently labelled 48kbp λ-DNA was homogeneously loaded in a 200µm square capillary filled with 1X Tris-Borate EDTA buffer (TBE) and 0,01% Hydroxypropyl cellulose (HPC) as a sieving medium. A low-frequency (20Hz), high tension was applied between each side of the capillary.

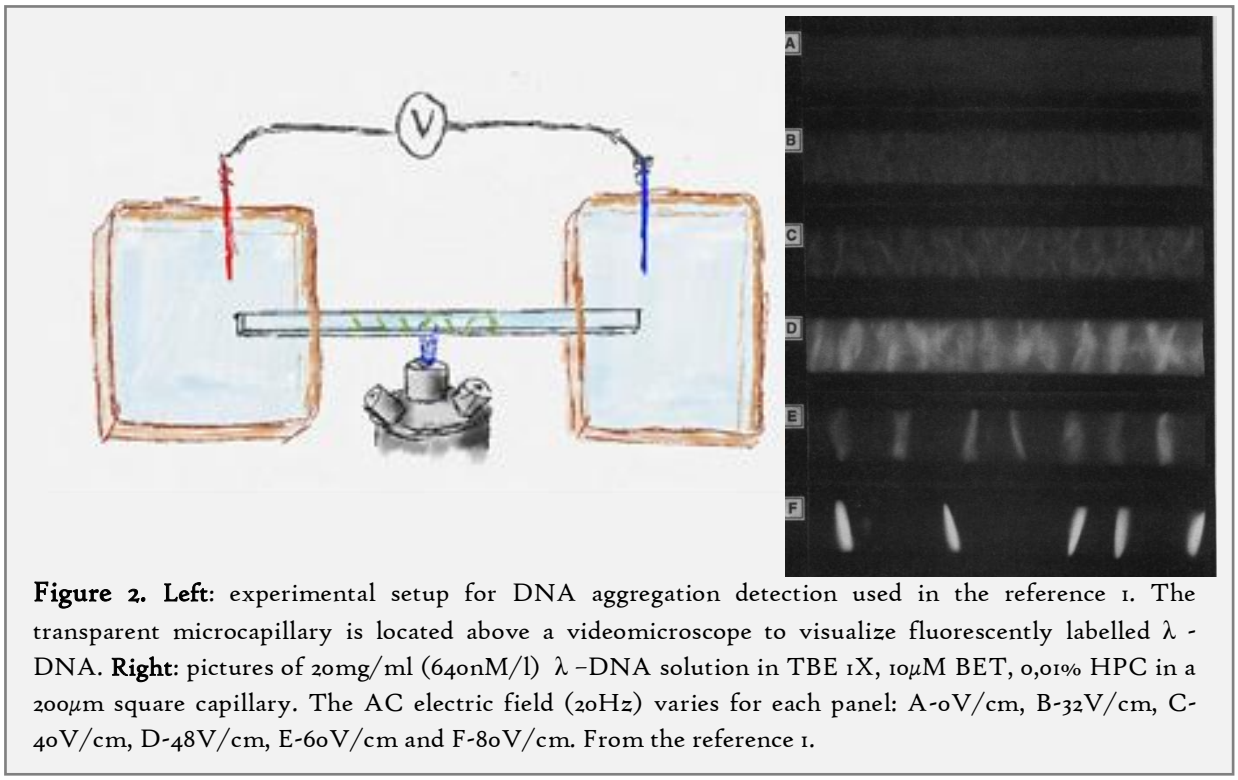

Figure 2. Left: experimental setup for DNA aggregation detection used in the reference 1. The transparent microcapillary is located above a videomicroscope to visualize fluorescently labelled λ -DNA. **Right**: pictures of 20mg/ml (640nM/l) λ –DNA solution in TBE 1X, 10µM BET, 0,01% HPC in a 200µm square capillary. The AC electric field (20Hz) varies for each panel: A-0V/cm, B-32V/cm, C-40V/cm, D-48V/cm, E-60V/cm and F-80V/cm. From the reference 1.

As seen on the Figure 2, the solution of λ-DNA became more and more inhomogeneous as the electric field increased. At low voltage, spinodal decomposition created regions of higher DNA density and these regions fused and densified as the electric field increased. It's interesting to note that a time-lapse of a λ-DNA aggregation under a high electric field presents exactly the same evolution than a sequential increasing in the voltage applied. Aggregation was enhanced when:

- The electric field was increased or the excitation frequency was lowered,
- The concentration of DNA or the DNA length was increased,
- The conductivity of the solution was decreased.

DNA aggregates had three remarkable dynamical features:

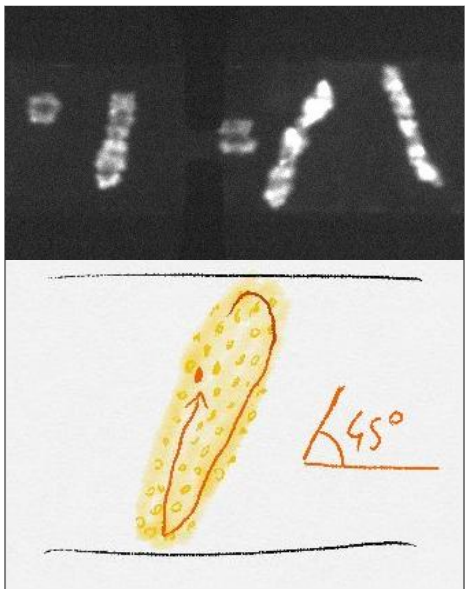

Figure 3. Top: Pictures of Lambda-DNA (50μg/ml, 1.5nM) in TE 1X in a 150x30μm rectangular channel, submitted to 680V/cm at 10Hz. **Bottom**: dynamical features of DNA aggregates.

- First, the angle between the elongated aggregate main axis and the capillary axis was fixed. This angle is equal to ±45° for low-frequency excitation field in a thin capillary with a rectangular section as seen on Figure 3.

- Secondly, the DNA aggregate was highly dynamic, each individual DNA blob recirculated at around 100µm/s in the pattern with an ellipsoid trajectory.

- The final lateral size of the aggregates was roughly the same as the smallest dimension of the confined environment.

From these observations, H. Isambert *et al.* created a theoretical model to explain this electrohydrodynamic DNA aggregation[3]. Colloid aggregation under a high electric field has been explained using different theories, depending on the experimental conditions used. Small DNA aggregates when the electric field is strong enough to dissociate the complex DNA-counterions in presence of a dialysis membrane, which allows the removal of these counterions from the solution[6]. This dissociation also leads to a non-uniform velocity of DNA during capillary electrophoresis[7]. However, neither recirculation nor tilted bands were observed. These features were previously observed in the case of polystyrene beads[8], but the explanation is based on a dielectric constant difference between the colloid and the solution and a spinning of the solid spheres which are meaningless in the case of a DNA suspension.

I will now summarize Isambert's theoretical work and then present how I applied it to λ-DNA with numerical Matlab simulation, in order to give physical insights on this complex phenomenon. To begin, the DNA coil shape without any applied electric field is calculated. The first effect of the strong voltage is a decrease of the concentration of the small ions of the solution around the λ-DNA coil and an electroneutrality breakdown at large scale. This charge creation into the solution is the origin of electrohydrodynamic flows around the DNA. Finally, in presence of a DNA density fluctuation source, like a thermal noise, this electrohydrodynamic coupling creates an instability of the DNA-coil concentration, leading to the apparition of growing regions with a high density of DNA, that we call aggregates.

1.3 Theory

The λ-DNA is first modelled as a macro-poly-ion, with a gyration radius $R_g = 500nm$, carrying around 100 000 negative charges, and a nucleotide distribution c_m. This macro-ion moves by electrophoresis at a velocity $\overrightarrow{v_e}$ with a mobility μ_m, under a high DC external electric field $\overrightarrow{E_0}$, with $E_0 > 100V/cm$, $f < 100Hz$ and aligned with the x-axis (from left to right on the different representations). The solution around the macro-ion contains monovalent cations and anions. Their

concentrations are c_+ and c_-, for simplicity they are assumed to share the same amplitude of electric mobility μ_s and the same diffusion constant D_s.

1.3.1 DNA coil shape

First, the real shape of a λ-DNA coil has to be found. Double-stranded DNA is what we call a worm-like polymer: the flexibility of the dsDNA is weak, compared to usual polymers as polyethylene or polydimethylsiloxane. However, it has been found that dsDNA in a dilute regime in a water solution behaves like an ideal polymer[9]. So, it's possible to model the dsDNA as an ideal random walk having fewer steps (or monomers) than the nucleotide number, with an effective step length l_k, called the Kuhn length (Figure 4). The parameters used for this random coil are the followings:

- The λ-DNA has 48600bp. Each base pair is 3,4Å long. The maximum length of the DNA is $R_{max} = 48600 \times 3{,}4\text{Å} = 16{,}5\mu m$.
- This ideal polymer has N monomers of length $l_k = 100nm$, called the Kuhn length of the polymer[10]. N is calculated with $N = {R_{max}}/{l_k} = 165$.

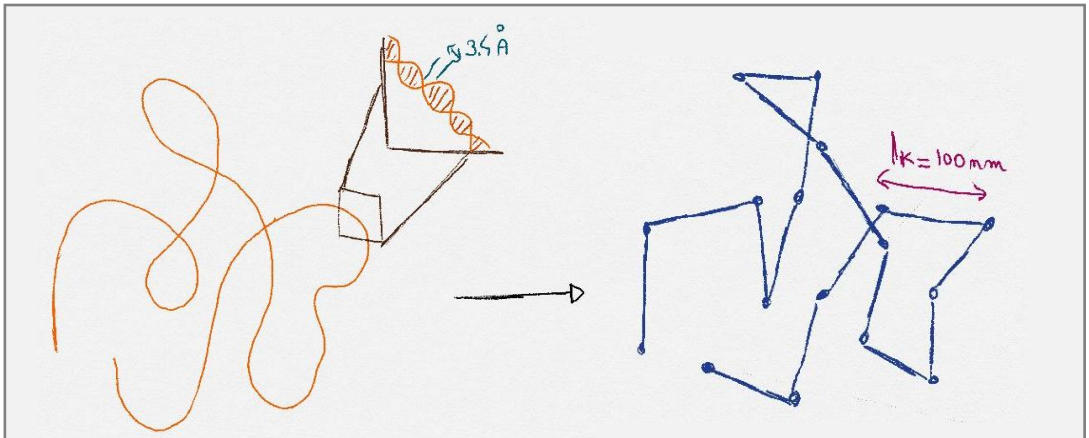

Figure 4. Schematic of a real dsDNA coil, and its ideal polymer equivalent.

This ideal random walk can be easily simulated to find the spatial distribution of the monomers inside the random coil. We are interested by the monomer concentration inside the DNA coil. As the conformation of the coil is highly dynamic, we prefer to work with an averaged profile. The average of the monomer concentration $c_{rw}(r)$ profile in function of the radial distance r for 100000 random walks is presented on the Figure 5. This profile fits well as expected with a simple Gaussian $c_{rw} = A.\exp(-r\text{^}2 / (2\sigma\text{^}2))$, with $A = 4{,}5.10^{20} monomer/m^3$ and $\sigma = 2{,}75.10^{-7}m$.

To go back to the real nucleotide concentration, the previous Gaussian found has to be multiply by $N_{bp} / N = 48600 / 165 = 295$. The nucleotide concentration at a radial distance r from the centre of mass of the coil is finally given by $c_m = B.\exp(-r\text{^}2 / (2\sigma\text{^}2))$, with $B = 1{,}3.10^{23} nucleotide.m^{-3} = 0{,}22 mol/m^3 = 0{,}22 mM$ and $\sigma = 0{,}275nm$ (Figure 6). However, Tang *et al* showed than a single DNA coil collapses under a strong electric field and the gyration radius decreases by a 0,6 factor[11]. This effect is perhaps similar to the electrohydrodynamic instabilities presented here. We won't take this effect into account, as it doesn't significantly change the next results. We won't also take into account the small DNA elongation caused by the presence of

intercalated dyes (SyBr Green or BET), changing the persistence length and contour length of the DNA molecules[12].

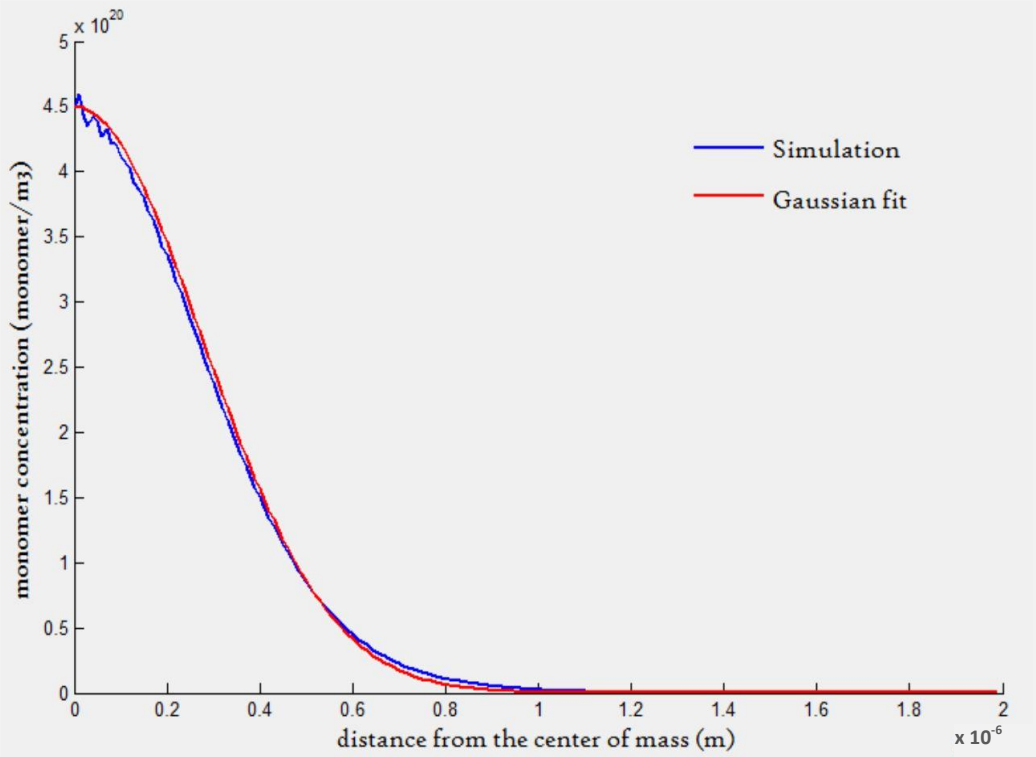

Figure 5. Monomer concentration profile. **Blue:** Matlab simulation, average over 100000 random walks. **Red:** Gaussian fitting, $c_{rw} = 4{,}5.10^{20}.\exp\left(-r^2/2(2{,}75.10^{-7})^2\right)$.

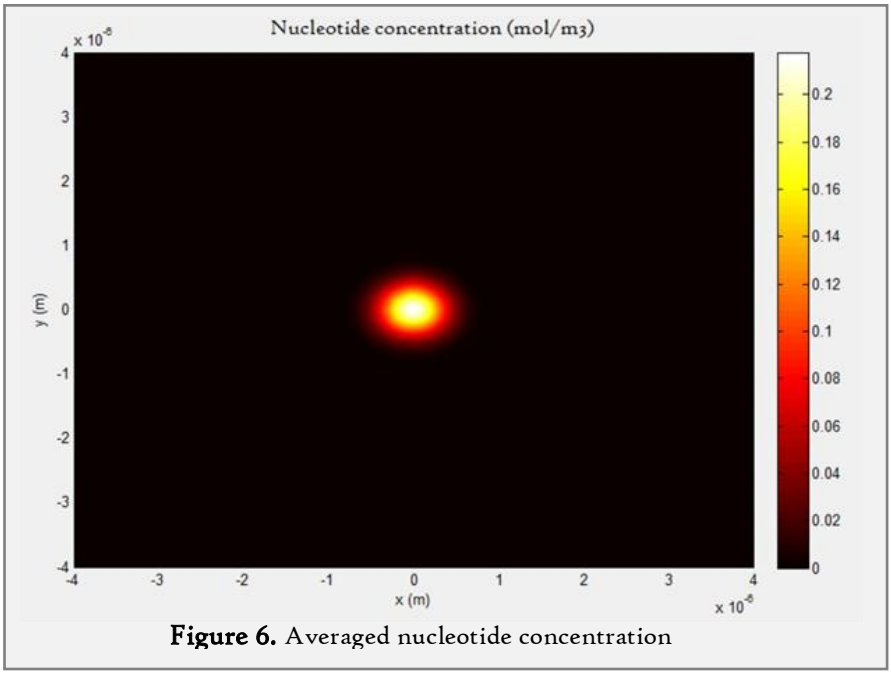

Figure 6. Averaged nucleotide concentration

1.3.2 Salt concentration perturbation

The presence of this macro-ion coupled with the high electric field perturbs the small-ions distribution around the DNA. Using the conservation equations for small ions and the Poisson equation, this salt concentration perturbation is calculated:

$$\partial_t c_+ + \vec{\nabla}.\left(-D_s\vec{\nabla}c_+ + \mu_s c_+\vec{E} + c_+\vec{v}\right) = 0 \quad (2.1)$$

$$\partial_t c_- + \vec{\nabla}.\left(-D_s\vec{\nabla}c_- - \mu_s c_-\vec{E} + c_-\vec{v}\right) = 0 \quad (2.2)$$

$$\vec{\nabla}.\vec{E} = \frac{e}{\varepsilon\varepsilon_0}(c_+ - c_- + z_m c_m) = \frac{\rho_e}{\varepsilon\varepsilon_0} \quad (2.3)$$

Where $\vec{E}$ is the local electric field, $\vec{v}$ is the local velocity, z_m is the number and sign of charge per nucleotide, e is the elementary charge, $\varepsilon\varepsilon_0$ is the dielectric constant of the solution and ρ_e is the local charge density. For all the calculations, the electric field is considered constant. This approximation is good enough for small frequency regime (<50Hz), because the time constant of the reorganization of the small ions is faster than the electric field period.

Usually, in most of the electrokinetic theories, the presence of an external electric field leads to a perturbation of the equilibrium concentration of the small ions around a macro-ion, because the internal electric field in the Debye length's macro-ion is really stronger. Here, the external electric field is so important that we consider the presence of the macro-ion as a perturbation of the "far from equilibrium" regime, which corresponds to the electrophoresis of an electrolyte solution under a strong electric field. The following parameters could then be expanded around an equilibrium value: $\vec{E} = \overrightarrow{E_0} + \partial\vec{E}$, $c_+ = c_s + \partial c_+$, $c_- = c_s + \partial c_-$. Linearization of the equations (2.1), (2.2) and (2.3) also necessitates the assumption $c_{m_{max}} \ll c_s$. Here, the interesting parameter is $S = \partial c_+ + \partial c_-$, which corresponds to the net increase of the salt concentration without any electroneutrality breakdown. The calculation gives this expression of $S_{\vec{k}}$ in the Fourier space:

$$S_{\vec{k}} = -\frac{z_m\mu_s\vec{E}_0.i\vec{k}}{D_s k^2 + z_m\mu_m\vec{E}_0.i\vec{k}}C_{\vec{k}} \quad (2.4)$$

In order to get a physical insight into this result, the 2D projection S_{xy} and the projection S_x along the x-axis have been plotted for three different value of μ_m, the electrophoretic mobility of the macro-ion: $\mu_m = 0$, $\mu_m = \mu_s$ and $\mu_m = \mu_s/3$ (Figure 7, 9 and 10).

The first example corresponds to the limit case $\mu_m \sim 0\ m.s^{-1}.V^{-1}$ and is plotted on the Figure 7. It does not correspond to a DNA blob moving by electrophoresis, but in a fixed and charged membrane. This membrane alters the normal electrophoretic movement of the small ions in the solution under electric field. As seen on the Figure 8, cations are attracted by the anode, and can pass through the negatively charged membrane. However, anions can not cross the membrane, because of electrostatic repulsion. This electronic discrimination creates a region of high concentration of salt at the anode side of the charged membrane, and a region of salt depletion on the cathode side.

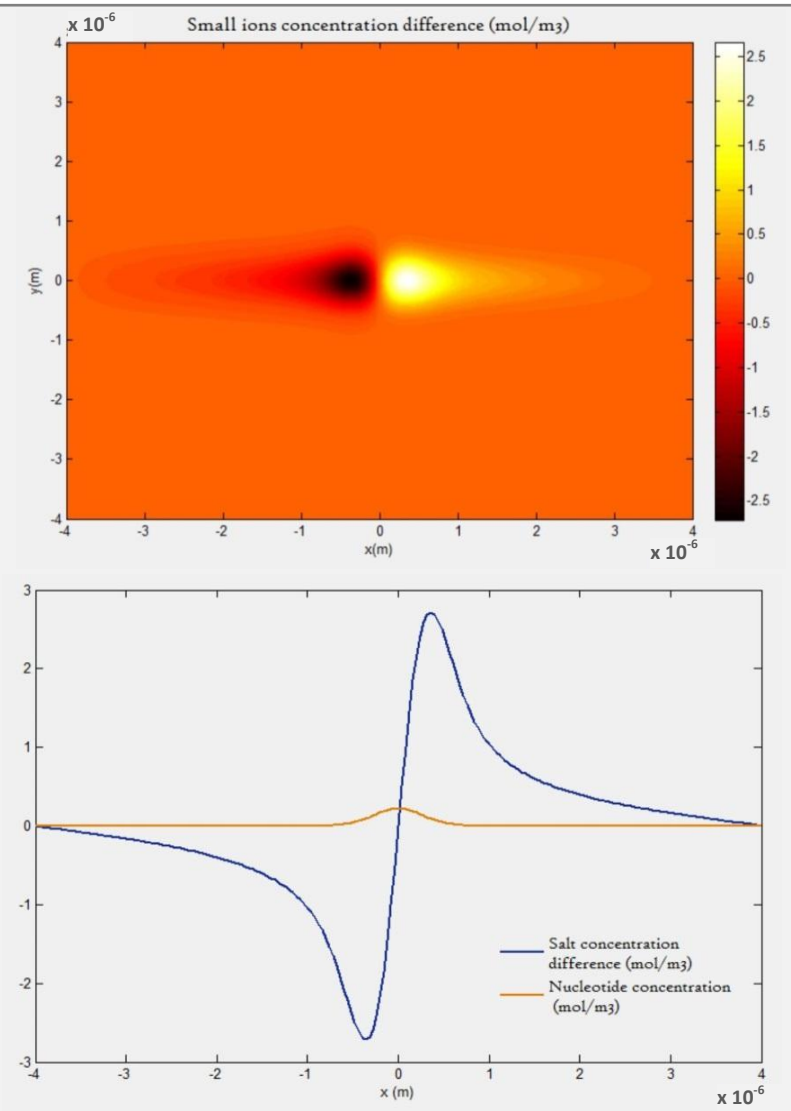

Figure 7. Salt difference S and monomers concentrations around the macro-ion for $\mu_m \sim 0\ m.s^{-1}.V^{-1}$.

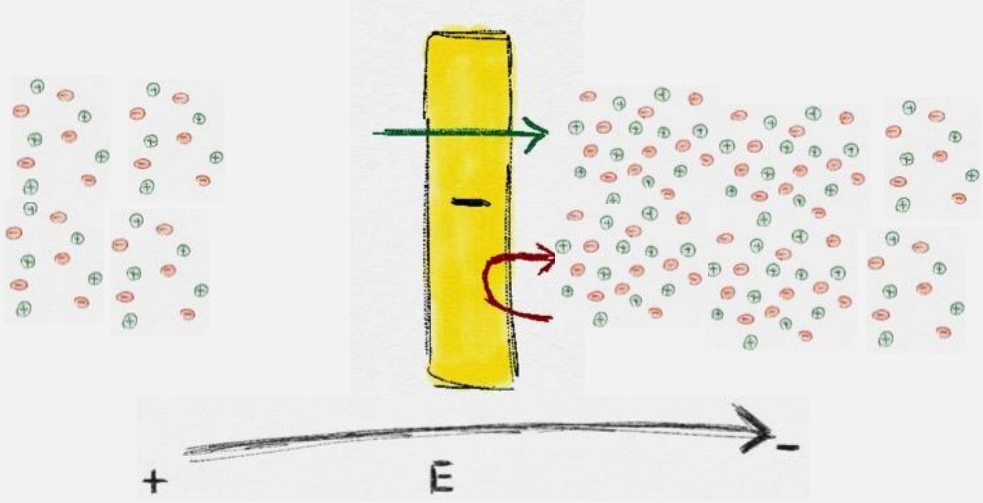

Figure 8. Electrodialysis phenomenon: cations (in green) could pass through the fixed and charged membrane (in yellow) during electrophoresis to the anode. Anions shall not pass through the membrane because of electrostatic repulsion.

The phenomenon reminds the macroscopic one called electrodialysis, which is routinely used to desalt sea water, and to purify tap water in laboratories. Moreover, this qualitative explanation is in adequacy with the result plotted on the Figure 7.

The second example corresponds to the limit case $\mu_m = \mu_s$, plotted in Figure 9. In this example, the macro-ion moves at the same velocity as the small anions during electrophoresis. The previous phenomenon doesn't occur, and $S(x,y) \sim -c_m(x,y)$ to respect the usual electroneutrality condition.

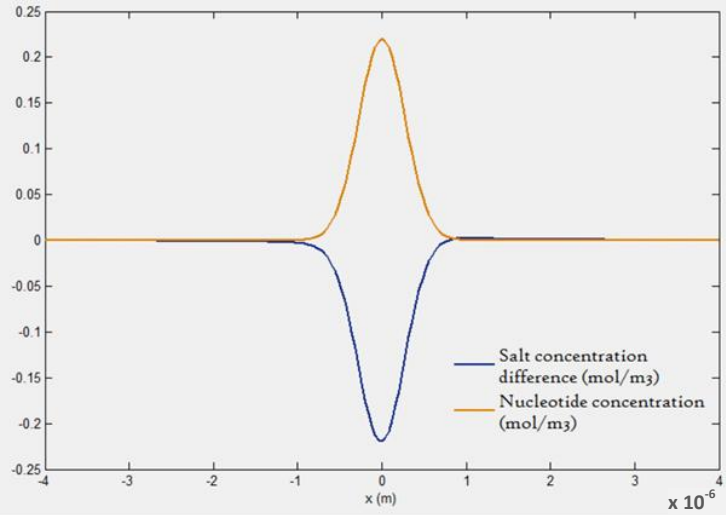

Figure 9. Salt difference S and monomers concentrations around the macro-ion for $\mu_m \sim \mu_s$.

For usual buffer and λ-DNA solution, the mobilities are around $\mu_m \sim 10^{-7} m^2.V^{-1}.s^{-1}$ and $\mu_s \sim 3.10^{-8} m^2.V^{-1}.s^{-1}$ [5], respectively. This situation is represented by Figure 10: $S(x,y)$ is mainly negative, as

$$S_{\vec{0}} = -\frac{\mu_s}{\mu_m} \int c_m d\vec{r} < 0 \tag{2.5}$$

This huge salt depletion with a small increase of the salt concentration at the tail of the macro-ion reminds us both our first and second examples. Qualitatively, as seen on the Figure 11, this also corresponds to the electrodialysis phenomenon, with a moving membrane shifted toward the cathode side of the solution: this moving macro-ion is now mostly surrounded by an ionically depleted zone. It's important to note that this perturbed region is not limited by the physical size of the macro-ion and extends far away from the λ-DNA coil.

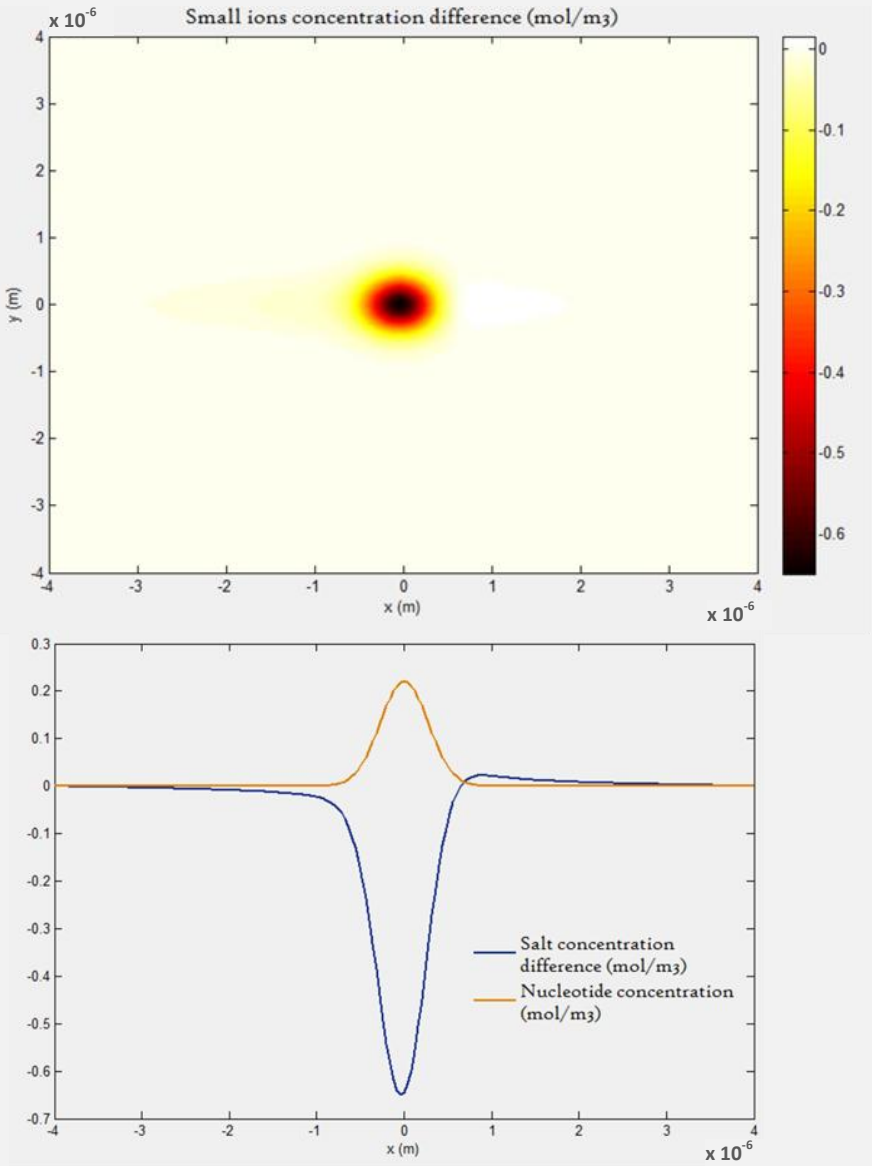

Figure 10. Salt difference S and monomers concentrations around the macro-ion for $\mu_m \sim {}^{\mu_s}/_{3}$.

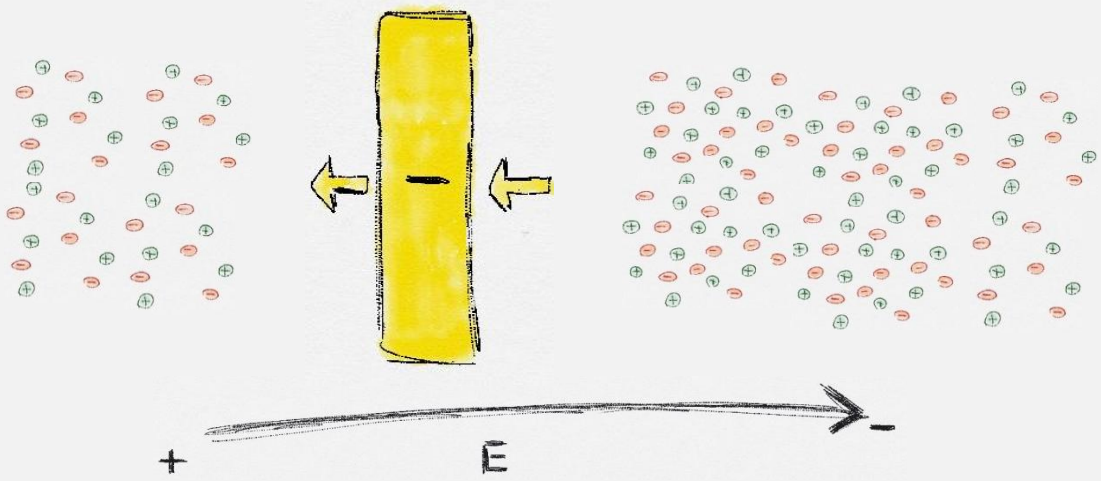

Figure 11. In contrary to the electrodialysis (Cf. in Figure 8), the membrane is not fixed anymore and move toward the anode. Qualitatively, the macro-ion is now surrounded by a depleted solution.

1.3.3 Electroneutrality breakdown

As we know the salt concentration perturbation, it's now possible to solve the Poisson equation present in the initial set of equation, and to obtain ρ_e , the charge density around the λ-DNA coil. After calculation, three different charge sources contribute to the final electroneutrality breakdown:

$$\rho_e = \varepsilon\varepsilon_0 \vec{\nabla}.\vec{E} \approx \varepsilon\varepsilon_0 \left(-\frac{\mu_m}{\mu_s}\frac{\vec{E_0}.\vec{\nabla}c_m}{2c_s} + \frac{z_m kT}{e2c_s}\Delta c_m - \frac{\vec{E_0}.\vec{\nabla}S}{2c_s} \right) \quad (2.6)$$

First term: perturbation due to the moving macro-ion through the electrolyte.

Second term: Equilibrium charge density without any applied electric-field.

Third term: electroneutrality breakdown due to the salt concentration perturbation.

We are mostly interested by the electroneutrality breakdown at large scale, i.e. outside the macro-ion region. For $|\vec{r}| > R_g$, $c_m \sim 0$, $\Delta c_m \sim 0$ and $\vec{\nabla} c_m \sim \vec{0}$. However, as the salt perturbation extends over the DNA coil, as seen on the Figure 10, the third term is dominant at large scale. On Figure 12, the third term and the total charge density around the macro-ion are plotted, for realistic values of mobilities $\mu_m = \frac{\mu_s}{3}$.

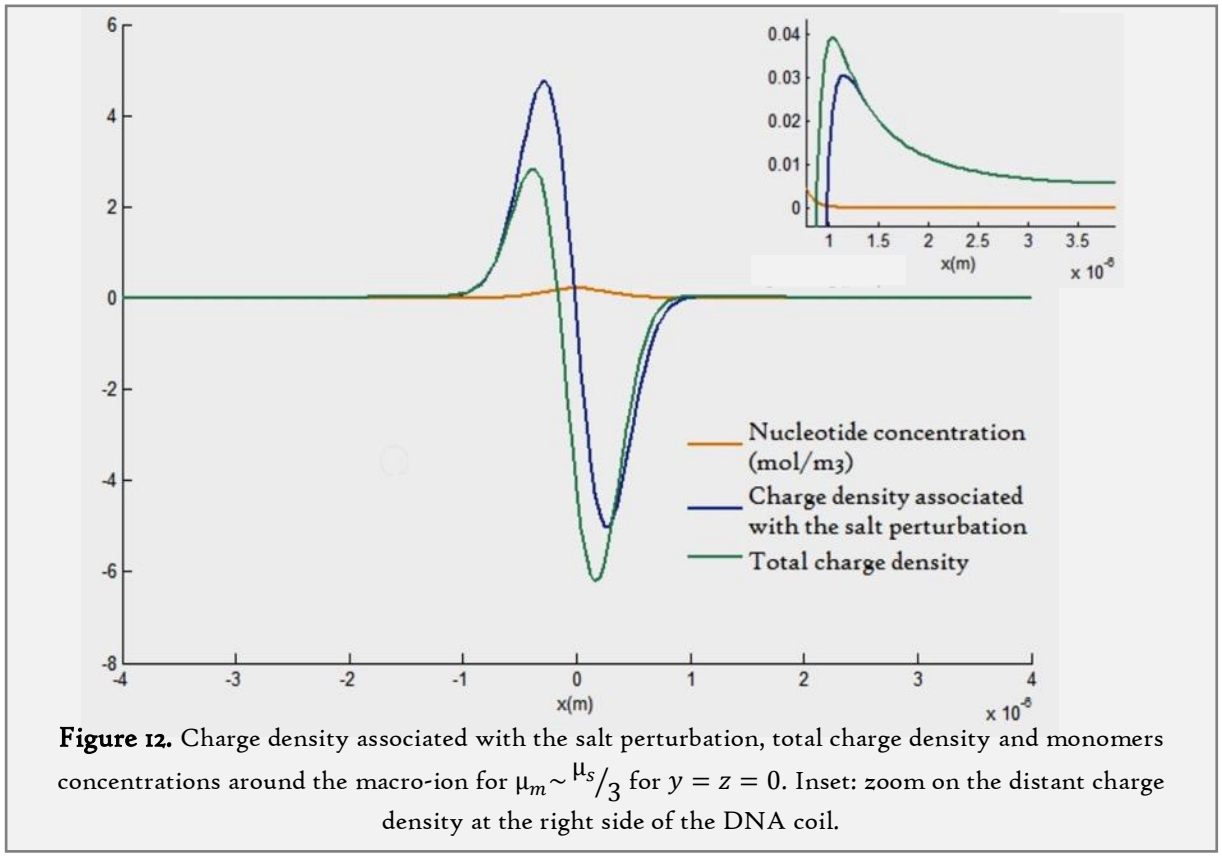

Figure 12. Charge density associated with the salt perturbation, total charge density and monomers concentrations around the macro-ion for $\mu_m \sim {}^{\mu_s}/_3$ for $y = z = 0$. Inset: zoom on the distant charge density at the right side of the DNA coil.

One way to explain physically this charge segregation is to imagine that, because of the strong electric field applied, the two concentration profiles for the anions and cations are not merged anymore. As seen on the Figure 13, the anion profile is shifted toward the cathode and the cation profile is shifted toward the anode. Even if the order of dimension of this shift is several picometres, this is enough to create a net charge creation in each side of the macro-ion, expanding as far as the salt perturbation, as seen in the inset of the Figure 12.

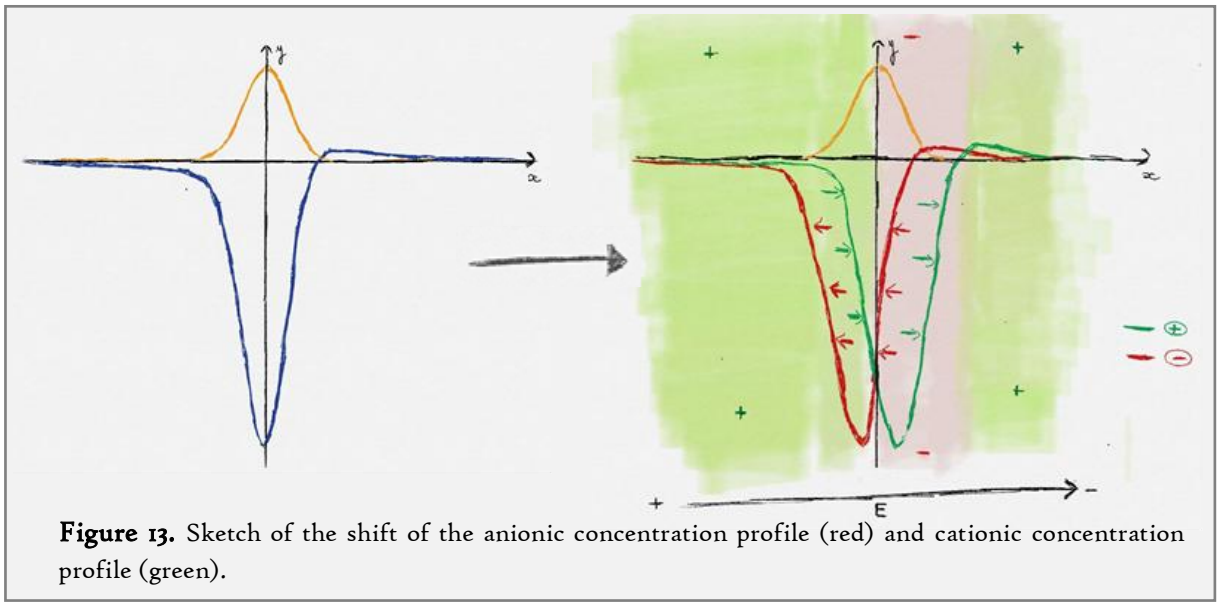

Figure 13. Sketch of the shift of the anionic concentration profile (red) and cationic concentration profile (green).

1.3.4 Electrohydrodynamic aggregation

We have described the physical effect of the strong applied electric field on a single DNA coil, namely a salt concentration perturbation and an electroneutrality breakdown at large scale. We will now focus on the collective behaviour from a homogeneous solution of DNA coils to an aggregated state under this high electric field. The aggregation of the DNA coils into giant aggregates couldn't be explained using only the electrostatic attraction and/or repulsion between the charged regions of the solution around the macro-ion. But this electroneutrality breakdown gives birth to electrohydrodynamic flows around the macro-ions, due to the coupling with the high electric field. Positively (respectively negatively) charged zones are attracted by the anode (respectively cathode). The situation is now a dynamic phenomenon that is taken into account by introducing a new Stokes-like equation in our previous set of equations:

$$\partial_t c_+ + \vec{\nabla}.\left(-D_s\vec{\nabla}c_+ + \mu_s c_+\vec{E} + c_+\vec{v}\right) = 0 \quad (2.7)$$

$$\partial_t c_- + \vec{\nabla}.\left(-D_s\vec{\nabla}c_- - \mu_s c_-\vec{E} + c_-\vec{v}\right) = 0 \quad (2.8)$$

$$\partial_t \nu_m + \vec{\nabla}.\left(-D_m\vec{\nabla}\nu_m - z_m\mu_m\nu_m\vec{E} + \nu_m\vec{v}\right) = 0 \quad (2.9)$$

$$\vec{\nabla}.\vec{E} = \frac{e}{\varepsilon\varepsilon_0}(c_+ - c_- + z_m c_m) = \frac{\rho_e}{\varepsilon\varepsilon_0} \quad (2.10)$$

$$\eta\Delta\vec{v} - \vec{\nabla}P + \rho_e\vec{E} = \vec{0} \quad (2.11)$$

Where ν_m is the DNA coil concentration (and not the previous nucleotide concentration), D_m is the DNA coil diffusion rate, η is the effective viscosity of the solution and P is the pressure in the solution. The idea is then to search for potential causes of instability on this set of equation: if we

modified locally the macro-ion concentration with a small perturbation $\partial\nu_m$, would the system evolve from a quasi-homogeneous state to an aggregated state? As $D_m \sim D_s/1000$, the diffusion is way more stabilizing for small ions. The instability has to be searched in the conservation reaction for the DNA. So, it's possible to linearize the others equations, as we did on the previous section. The resulting nonlinear dynamical equation is:

(2.12)

$$d_t \nu_m - D_m \Delta \nu_m + z_m \mu_m \vec{\nabla}.(\nu_m \partial \vec{E}) + \vec{v}.\vec{\nabla}\nu_m = 0$$

Diffusive term

Non-linear term

Electrohydroconvective term

This non-linear equation is completely stable if the original state is a homogeneous solution of DNA: a short, local concentration modification is quickly dampened to go back to a homogeneous state thanks to a stronger stabilizing diffusive term. But Isambert showed that this expression become instable if a DNA concentration thermal noise is added to the model. Qualitatively, the addition of a thermal noise breaks the balance between the diffusive term and the electrohydroconvective term in favour of the latter. The original concentration inhomogeneity due to the noise is then accentuated by the electrohydrodynamic flow, leading to the creation of giant aggregates (see Figure 14). The non-linear term vanishes at large scale. As this primary aggregate is itself a macro-ion, the surrounding solution undergoes the same phenomenon than the initial DNA coil: salt perturbation at large scale and electroneutrality breakdown. At this new scale, aggregation

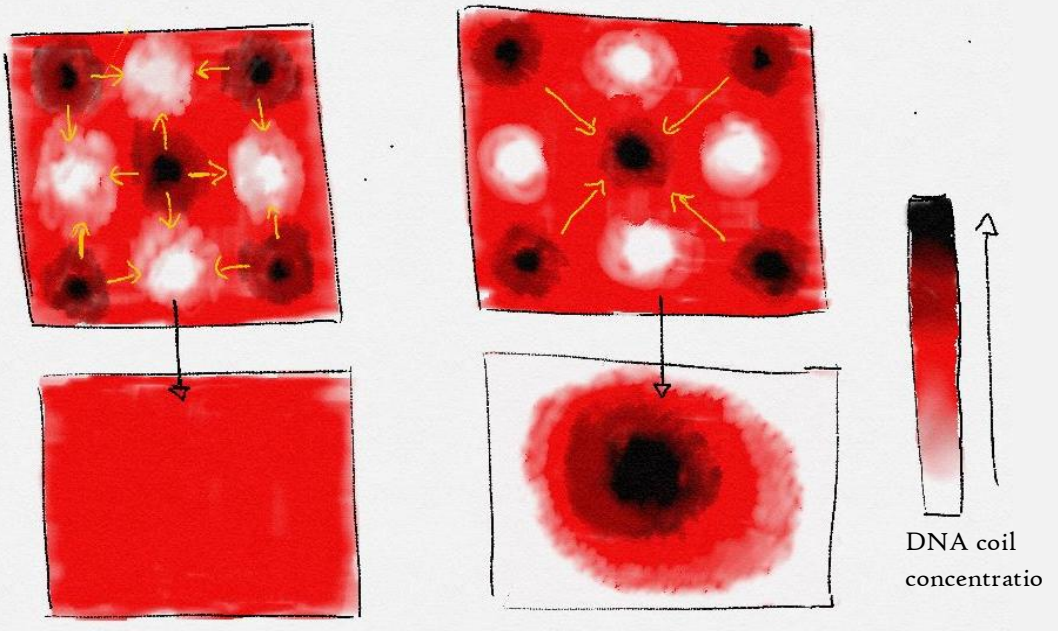

Figure 14. Schematics of the stabilizing and aggregating effect of diffusion, electrohydrodynamic flows and thermal noise.

still occurs, leading to the formation of bigger and bigger aggregates. When the size of the aggregates is close to the capillary or Hele-Shaw cell smallest dimension, the electrohydrodynamic flows (modelled by $\vec{v}$ in the previous equation) are modified by the new boundary conditions, shifting from a 3D infinite space to a quasi-2D confinement. With these new conditions, the model is no longer instable, and the growing of the aggregates stops. This model gives also a condition on the electric field threshold necessary to trigger the instability, i.e. when the electro-hydroconvective term is higher than the diffusive one:

$$D_m \Delta \nu_m < \vec{v}.\vec{\nabla}\nu_m \ \rightarrow E > \sqrt{\frac{kTc_s}{\varepsilon\varepsilon_0 R_g N_n \langle \nu_m \rangle^{1/3}}} \tag{2.13}$$

Where N_n is the number of base pairs per DNA. This condition qualitatively satisfies the experimental observations:

- The aggregation increases when the DNA is longer (R_g and N bigger). The initial electroneutrality breakdown is proportional to the monomer concentration, longer DNAs lead to a charge creation more important and an increased aggregation.

- The aggregation increases when the DNA concentration is higher. The distance between each DNA blobs is important. The attraction is actually triggered by a combination between electrostatic forces and electrohydrodynamic flows, each of them decrease at large distance from the blob. Two blobs have to be close enough to self-attract, and this distance is given by the DNA concentration. We also observed that, with a small concentration of DNA, the aggregation is not limited by the channel dimension. The aggregation stops when two aggregates are too far to be attracted by each other. This threshold dimension is shown on Figure 15 for two different buffers.

- The aggregation decreases when the salt concentration of the solution is higher. On the example, T4 ligase buffer in 10 times more conductive than the Tris-EDTA buffer (10mM of Tris and 1mM of EDTA). The aggregates are bigger and their number is smaller in the TE buffer. This can be explained easily by the fact that electrostatic interactions are screened when the ionic force of the solution increases.

The last point is interesting, because the necessary assumption made in the model in order to linearize the first set of equations (2.1), (2.2) and (2.3), *i.e.* the ionic strength of the buffer is really higher than the DNA one is not valid for experiments with the TE buffer. A highly conductive buffer, useful for the analytical resolution of the model, seems to not be mandatory for the apparition of aggregates.

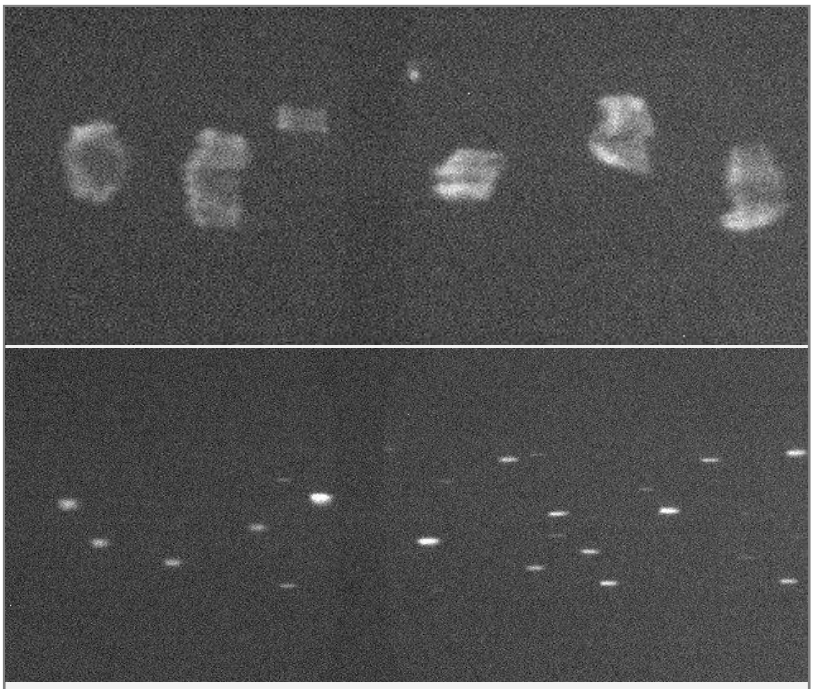

Figure 15. Picture of λ-DNA aggregates on a microfluidic channel. [λ-DNA]=60μg/ml=1.8nM in TE buffer (**up**) and in T4 ligase buffer (**down**). Vex=680V/cm at 10Hz.

1.3.5 DNA Aggregates shape and dynamic

To finish this theoretical presentation, we will now quickly focus on the behaviour of the giant DNA aggregates. As mentioned in the introduction, DNA aggregates have a specific orientation, shifted with a 45° angle from the electric field direction, and a dynamic recirculation is maintained with a specific rotating pattern (see Figure 3).

An aggregate is physically similar to a single DNA of larger molecular mass than individual molecules: it's a localized region with a high concentration of negative, less mobile charges. The aggregate can also be considered as an ionic membrane, except that it has viscoelastic behaviour, *i.e.* it can be irreversibly deformed. All the calculation done in this subsection for the salt perturbation around a single DNA is also valid for a DNA aggregate. At this scale, the charge density is simply

$$\rho_e = -\varepsilon\varepsilon_0 \frac{\mu_s \overrightarrow{E_0}.N_n.\vec{\nabla}v_m}{2c_s\mu_M} \tag{2.14}$$

as

$$S\sim -\frac{\mu_s}{\mu_M} N_n.v_m \tag{2.15}$$

With μ_M the apparent electrophoretic mobility of the aggregate. As a rough approximation, let give to the DNA concentration a Gaussian shape. Then, the side of the aggregate facing the anode is negatively charged, and the one facing the cathode is positively charged. Qualitatively, these charged portions of the solution are attracted by the opposite electrode, but they are blocked by the presence of the aggregate. The easiest way is to bypass the aggregate. As seen on the Figure 16, each

flow shears the aggregates, reshapes it on the typical elongated pattern presented previously. The direction of each flow is given by the original orientation of the aggregate, amplified by the electrohydrodynamic flows. With an AC field, the change in the field direction also changes the charge of the solution: the electrohydrodynamic flow is still toward the same direction. Also, looking at the experiments, the mobility for large aggregates seems to be reduced as compared to the mobility of one DNA coil, because of the presence of large electro-hydrodynamic flows. The decrease of mobility enhances the salt depletion and exacerbates the whole phenomenon. Quantitatively, this flow is easily modelled by the Isambert's theory. Even the preferred angle (45°) is predicted. This result is a strong proof for the validity of this theory. Another feature we consider as a strong asset in favour of the theory is its predictive character:

Isambert also predicted that switching to an isoelectric buffer would reduce the aggregation phenomenon. This suggestion was subsequently tested and separation of DNA from 100bp to 160kbp was indeed performed in capillary electrophoresis without any trouble, at field strengths at which it was impossible with conventional buffers[2].

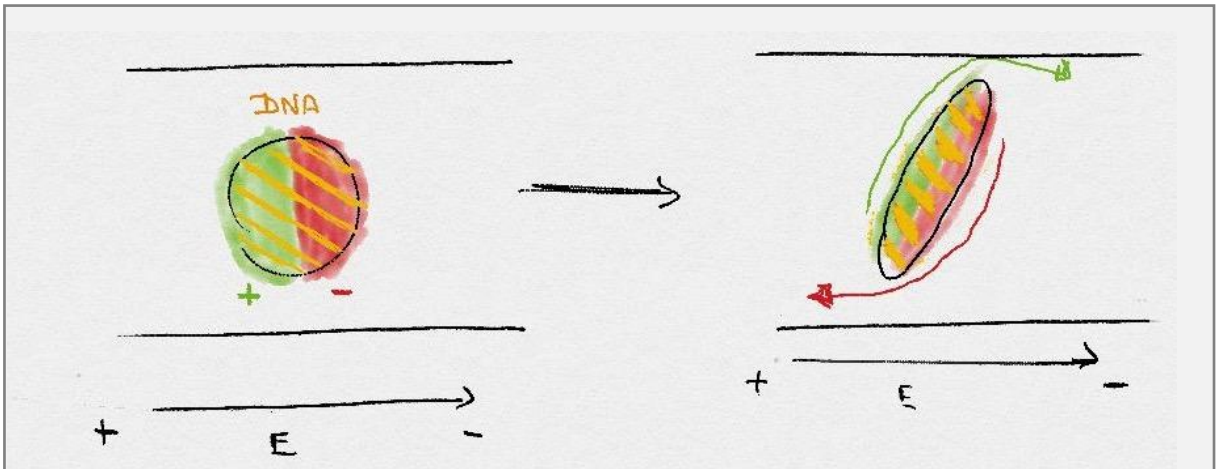

Figure 16. Deformation of a giant aggregate by the electrohydrodynamic flows generated by the positively charged region of the solution (green) and the negatively charged region (red).

2 Conductometric detection of DNA aggregates

After this "golden age" of capillary electrophoresis, however, the emergence of New Generation Sequencing (NGS) methods finally limited the research using Sanger sequencing, and thus capillary methods. In particular, increase of throughput of the electrophoretic separation of long DNAs became less essential, and the DNA electrohydrodynamic instabilities were not studied until 2009, when Jean-Louis Viovy had the idea to use this artefact for DNA detection in a microfluidic format. DNA aggregate should trigger a similar salt perturbation than a single long DNA. So, local conductometric measurement might be able to detect DNA aggregation! Moreover, an electronic detection is label-free and easier to miniaturize than an optical detection, and have the potential to be ultra-portable, because the volume of detection, *i.e.* the volume of a single aggregate, is really small. A first proof-of-concept has been developed by Mohamed Lémine Youba Diakité during his PhD from 2009 to 2012[13]. Then, I improved this system during my own PhD, with an improved design, an upgraded electronic for the control of electric field and signal treatment.

2.1 Detection system overview

The current detection system comprises 4 connected elements: the microfluidic chip, the excitation electronic, the detection electronic and a computer for the control of the electronic systems (Figure 17). We can also add a microscope, because the fluorescence imaging of DNA aggregates is a necessary control during the optimization of the experiment.

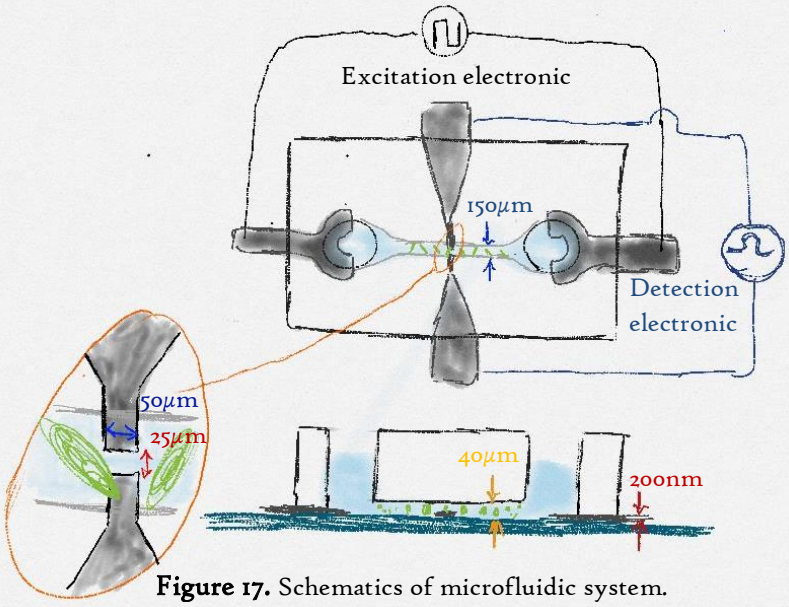

Figure 17. Schematics of microfluidic system.

The microfluidic chip is the core of the system. It contains one channel (5mm x 0.150mm x 0.03mm) and two cylindrical reservoirs in a PDMS substrate, bounded to a glass slide after oxygen-plasma activation. The glass slide is patterned with two pairs of thin gold or platinum electrodes. The first pair is located at the bottom of the 2mm-wide reservoirs and applies the excitation electric field in the microchannel. The second pair of electrodes is located at the middle of the microchannel and is used for conductometric measurement. Because a 25µm gap separates the two electrodes, only a small portion of solution in the channel is measured.

The electrodes for the excitation field are connected to a symmetric, high-voltage (HV) electronic system, controlled by USB. Most of the parameters can be modified, like voltage,

frequency, signal shape... The usual values are an excitation field of $680V_{pp}$/cm, the generated voltage is $340V_{pp}$, with a 10Hz frequency and a quasi-square waveform. In order to make the aggregates pass above the detection electrodes, the duty cycle of the waveform is modified in order to change the average value of the signal. When this mean value is not null, a smaller electric field displaces the aggregates by electrophoresis through the microchannel while the high electric field triggers the aggregation. Lastly, the system is symmetric in order to impose an electric potential of 0V at the location of the detection electrodes. For example, when the potential is at 170V in one reservoir, the other reservoir has a potential of -170V with regards to ground.

The electrodes for the conductometric detection are connected to a detection electronic system. It generates a low sinusoidal current through the electrodes, around 32kHz, in order to pass through the Debye double layer and to avoid electrochemical reaction at the electrode surface. The current amplitude is fixed and the electronic system read the tension between the electrodes, amplifies it and send it to an acquisition card (National Instrument) connected to a computer. The design of detection electronic system was a real difficulty during Youba Diakité's PhD. Interferences from the excitation electric field added a large quantity of noise in the detection signal. Moreover, high current passed from the excitation system to the detection instrument through the detection electrode and the common electrical mass of the devices, creating bubbles by water electrolysis on the electrodes. The final, optimized instrument is balanced, isolated and works on battery, in order to avoid mass loops.

A Labview program on computer is needed to control and synchronize the electronic systems. The excitation electronic is controlled via an USB interface and sends a synchronization signal through the National Instrument acquisition card to the software. The 32 kHz signal from the detection electronic is acquired by the NI card. The amplitude of the 32kHz component is recorded during each positive cycle of excitation square signal, giving a 10Hz demodulation of the detection signal. In order to remove the low and high frequency noises, and because the passage of aggregates above the electrode is not a periodic phenomenon, we use a Matlab-based wavelet decomposition to obtain only the change of conductometry related to the aggregation. Thresholding and denoising treatments are designed to remove supplementary artefacts.

2.2 Principle of the conductometric measurement in capillary electrophoresis

Our DNA detection system is conceptually close to the conductometric detection used in capillary electrophoresis. The principal challenge is to be able to detect a resistance change in an environment submitted to a high DC electric field. We should note that the small frequency of our excitation signal doesn't change most of the encountered issues as it could be considered quasi-DC. Capillary electrophoresis, presented above for DNA separation, is a more general analytical method which can separate all ionic species from mono-ions to large macromolecules. Optical detection is the most widely used technique for DNA separation monitoring thanks to fluorescent dyes like SyBr Green or BET that bind to all nucleic acids. However, for other applications, in which analytes are not naturally fluorescent, optical detection can't be a universal detection method for electrophoresis because fluorescent or coloured probes need to be specifically designed for each target. Methods based on UV absorption are currently used in analytics, but they have a low sensitivity, and require

expensive equipment. In contrary, each ionic species have a specific ionic conductivity: conductometry can potentially be a universal electrophoretic detection.

During conductivity measurement, the conductance G (in Siemens) of the solution is measured through a conductometric cell (see Figure 18). The conductance depends on the dimension of the cell, the electrodes orientation, shape and size. To remove these parameters and to obtain a value that is only dependant on the solution composition, a specific conductivity κ in S/cm is defined as $\kappa = G.k_{cell}$, where k_{cell} is the cell constant in cm^{-1} and is experimentally determined with the measurement of solution with known specific conductivity. Analytical solutions are also available for standard cell configurations.

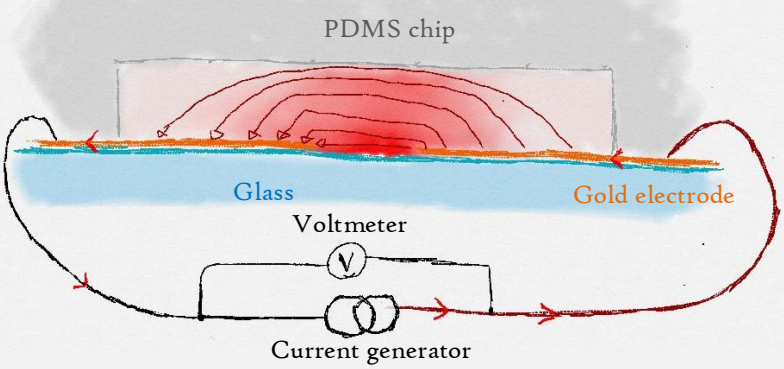

Figure 18. Schematics of detection cell and electronic. Inside the microfluidic channel, the current density flowing from one planar electrode to the second one is ranging from the maximum (red) to the minimum value (white). Current is imposed by the generator and the channel resistance is obtained via the tension measured.

For active cells, a current is imposed and the voltage between the electrodes is measured. Conductance is obtained from the Ohm's law. These relations are valid only for DC current flowing through the electrode, but DC currents create electrochemical reactions at the electrode interfaces. The creation of H^+ and OH^- ions changes the pH of the solution and the conductivity properties and water electrolysis provokes the formation of H_2 and O_2 gas bubbles. To avoid these effects, AC currents are preferred: if the frequency is high enough, electrical conduction would be also support by ionic polarization near the electrode and the produced hydroxide ions and protons would be immediately consumed from one cycle to the other[14]. With AC currents, however, the presence of electrical capacity has to be taken into account. When the electrodes are in contact with the fluid -in the so-called "in-contact measurement"- a Debye ionic double layer appears. The electrode is polarized, and opposite ionic charges are attracted to close to the surface to maintain the global electroneutrality, with a first immobile layer, adsorbed on the electrode, and a second mobile layer. This Debye double layer acts as an electrical capacity. The electrode is polarized, and a double layer of oppositely charged ions stay closed to the metallic surface in order to maintain electroneutrality. So, the impedance of the electrical model of the system is the sum of a real part, containing the resistance of the solution, and an imaginary part containing the capacity of the two double-layers:

$$Z = R_{solution} + \frac{1}{j.\pi.f.C_{Debye}} \tag{2.16}$$

Where C_{Debye} is the double-layer capacity and f the frequency of the current. We can do a quick approximate calculus. $R_{solution} \sim 1M\Omega$ and $C \sim 20\mu F.cm^{-2} \times A$, with A the electrode

surface[15]. Let hypothesizes square electrodes of 50µm for the width. We obtain $Z = 1.10^6 - j \times 6.10^8 \times f^{-1}$, the frequency has to be at least higher than 10 kHz to have an imaginary part ten times smaller than the real part to remove the influence of the capacities.

The major trouble when performing an in-contact conductivity measurement is the interferences provoked by the electrophoretic electric field. They have several sources:

- First, the high electric field for electrophoretic separation imposes an electrical potential along the capillary. Also, the resistance of the electrode is smaller than the solution resistance. So, along the capillary direction, the high electric field lines are deviated from the solution to the electrode (Figure 19). If the electrode was large enough, the difference of potential between each side of the electrode would be higher than the electrolysis potential of water. In consequence, H_2 and O_2 gas bubbles are produced on the electrode surface. Increasing the buffer conductivity or reducing the electrode width is the best solution to avoid this effect.

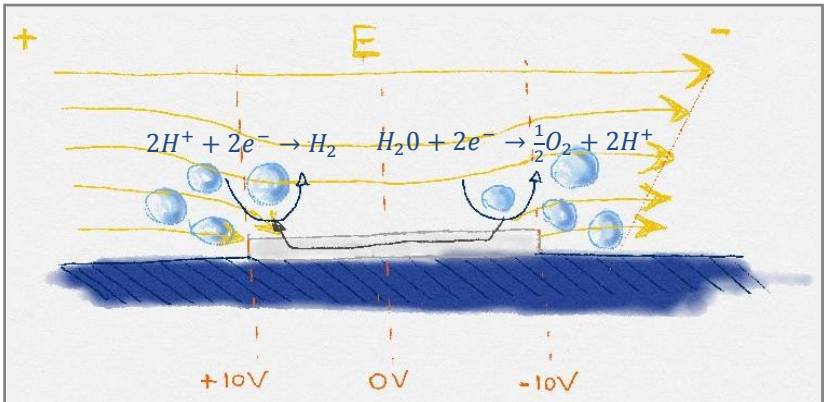

Figure 19. Bubble formation at the electrode edges.

- The second source of interferences is the transfer of current from the excitation system to the detection system. This could be caused by a current loop: the first link between the two systems is the detection electrodes, as current can pass directly from the electrophoretic capillary to the detection electronic through the electrodes. A second link is needed to allow the current to return back into the excitation system (Figure 20). Two main cases are found. The current can transit from the detection electronic to the excitation electronic through the common ground mass. The current can also be transferred via an inductive or capacitive

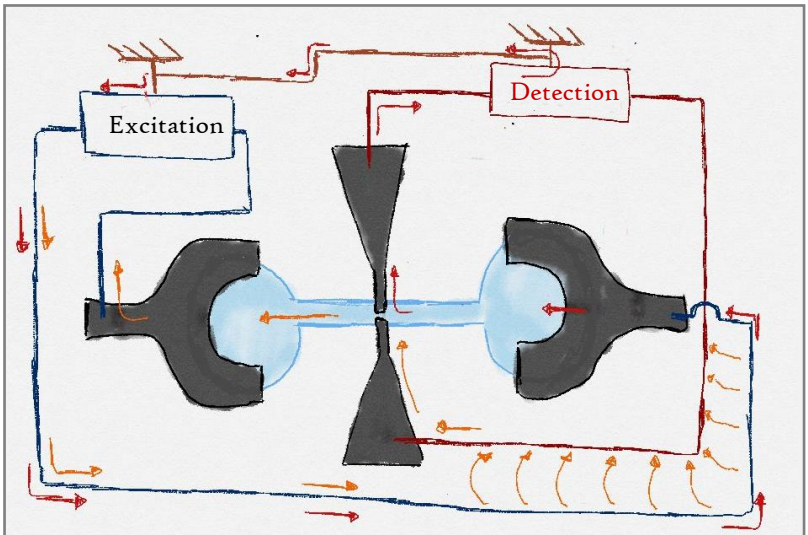

Figure 20. Interferences via a ground loop (red arrows) and via an inductive coupling (orange arrows).

coupling between the two systems as the excitation field radiates from the wires and the channel. These interferences could cause troubles ranging from a loss of sensitivity to bubble formations on the electrodes by water electrolysis.

Different strategies have been tested in order to remove these interferences. First, the position of the conductometric cell according to the point of zero potential is important. In capillary, Huang *et al.* changed the usual location of conductometric cell from the middle to the end of the capillary, close to the grounded reservoir[16]. The potential at the cell location decreased from 1500V to 6V; the electronic was previously isolated by a transformer from the high electrophoretic current[17]. With end-column detector, simple capacitors are sufficient to decouple the detection electronic. The sensitivity was not impaired, with a LOD of 50µM for the detection of Na^+. However, bubbles formation at the electrodes still occurred. The Zare group also presented a floating and isolated electronic in 1998 in order to avoid ground loops[18]. The LOD decreased to 2µM for Na^+. Finally, separation of the detection electronic via optocouplers was also shown with a similar LOD and a smaller footprint for the electronic[19].

The structure of the conductometric cell is also important to reduce the interferences. In the first works on on-column capillary, the electrodes were platinum electrodes inserted and aligned perpendicularly to the capillary[16]. The difficulty on the alignment was a main factor to explain non-reproducibility of these experiments. In the case of microfluidic-based electrophoresis, the lithography technology enables a high control of the positioning of planar electrodes created by lift-off. Different designs for planar electrodes have been tested by Graß *et al.* for conductivity detection[20]. Parallel and aligned electrodes gave similar results in term of sensitivity, but the use of end-column measurement didn't allow checking the interference susceptibility of the different designs. After these results, no particular advances in the field of on-contact measurement have been reported for the last 10 years.

Conductometric measurement can also be done without any direct contact with the solution. In this case, a thin insulated layer of dielectric coats the electrodes. This second option is called contactless and is now more used than the detection with contact for conductometric measurement in capillary and microchip-based electrophoresis. The main advantage is a complete decoupling between the detection electronic and the high electrophoretic field because no DC current could pass from the channel to the detection electrodes. On the other hand, the dielectric layer adds a large resistance and a new capacity between the electrode and the solution. For example, Lichtenberg *et al.* developed a contact-less conductometric measurement in a glass microfluidic chip, with an insulating layer of glass from 10 to 15µm between the electrodes and the solution[21]. The resulting capacity is 1.65pF, to be compared with the 500pF of the Debye's double layer. With the same calculation as previously, the necessary frequency to get rid of the dielectric capacity is around 1MHz. Experimentally, the frequency used on this study is 100kHz and the dielectric impedance is similar to the solution impedance. The electronic needed to work at these higher frequencies is more complex, and the whole detection is really dependant on the thickness of the insulating layer. During his PhD, Youba Diakité chose to develop an on-contact instrument, because this method is reputed to be more sensitive despite the interference complications.

2.3 Micro-fabrication and electronics

The microfluidic chip is composed of a glass slide patterned with gold electrodes for the detection and the excitation, bound to a PDMS chip containing the channel for the DNA aggregation and two reservoirs. The methods for the microfabrication are described below, along with the improvements made from the previous prototype.

2.3.1 Methods and design for chip microfabrication

The microchip design was relatively simple. Two open reservoirs contained 8µl of solution in total. A thin channel, where the DNA aggregation occurred, linked the two reservoirs. Excitation planar electrodes were deposited in the bottom of the reservoirs for the high electric field application. The planar detection electrodes were located perpendicularly in the middle of the microchannel. More precisely, a brass mould was fabricated by micro-milling. A 3D design, shown on Figure 21, was drawn with the CATIA CAD software (Dassault Systemes) and transformed into a file listing the coordinates of the tool, the rotation speed and the milling velocity. A tool with a 1mm diameter created an inverted straight channel with a length of 3mm, a width of 150µm and a depth of 40µm. At each side, the structure is continued by a 2.2mm circle in diameter, with a gentle transition from the channel to the circles during 1mm. In the centre of the circles, 500µm deep, 1.8mm wide holes are drilled. Two alignment structures were added to indicate the middle of the channel.

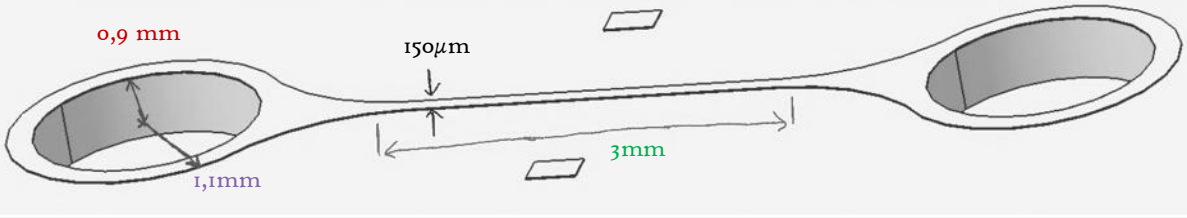

Figure 21. CATIA design for the micro-milled mould.

Sylgard 184 PDMS base was supplemented at a 10:1 ratio with the corresponding curing agent, mixed vigorously and degassed by centrifugation at 4500rpm during 1min. PDMS is then poured in the brass mould, degassed again in a vacuum container to remove the trapped air bubbles and cured at 70°C during 2h at least. After demoulding, individual chips were cut and two reservoirs were punched at each channel extremity with a 2mm surgery puncher. The big PDMS pillars created by the holes on the mould served as a guide for a reproducible punching. The PDMS part is then cleaned with ethanol and scotch tape. No surface treatment was needed because DNA aggregates were not found to be adsorbed and trapped on native PDMS.

Micro-milled mould was preferred over the previous mould produced by photolithography. In fact, the mould has been regularly used since 2013 without any damages. Micro-milling also allows the easy creation of the guiding holes for the reservoir creation. So, the length of the aggregation channel in PDMS is now completely fixed because an imprecise punching does not shorten the channel anymore, and the further alignment to place the electrode at the middle of the channel is facilitated by the alignment structures. Also, the smooth transition between the reservoir and the

straight channel has been found to be important. The electric field increases progressively during the 2D narrowing of the channel and the aggregation begins above an electric field threshold located in the narrowed section. Without this transition, aggregates were created directly at the entrance of the channel and trapped there because of the 3D step, causing a blockage of the channel.

Planar electrodes were patterned on a circular, 2 inches glass slide with a lift-off process. This technique combined photolithography and a deposition of a metallic thin layer. Each slide had two locations for a microchip, each spot containing a pair of detection electrodes and a pair of excitation electrodes. First, a mask was designed with the QCad software and printed on a plastic film by the company Selba with the electrode patterns in transparency (Figure 22). The facing detection electrodes had a width of 50µm, and a gap of 25µm. The excitation electrodes had a crescent shape and were planned to be located at the bottom of the chip reservoir. Then, in clean room, borosilicate glass slides (Neyco) were cleaned with acetone and isopropanol. A thin layer of S1813 positive resin was spin-coated on dehydrated glass slides during 60s at 4000rpm. A 60s softbake was performed at 95°C in order to remove most of the resin solvent. Resin was then illuminated through the photomask in a UV-Kub 2 (Kloé) during 8s, at full power of the LED lamp. The illuminated parts are then more soluble than the unexposed region on the solution called developer. Here, the glass slide was immerged in the AZ726 developer during 10s, and rinsed with pure water. Thin layers of chromium (around 10nm), used as an adhesion layer, and gold (around 100nm) were then deposited on the glass substrate by evaporation (Auto 500 Edwards). The remained resin was then removed with acetone in an ultrasonic bath and only remained the metallic layers located on the glass slide for the electrodes. The PDMS chip and the glass slide were then treated with an oxygen-plasma during 30s, aligned under microscope thanks to the alignment structures and put into contact. The bonded chips were then let at 70°C during at least 24h to recover its initial hydrophobicity[22]. Cables were then soldered to the metallic pad at the tip of the electrodes.

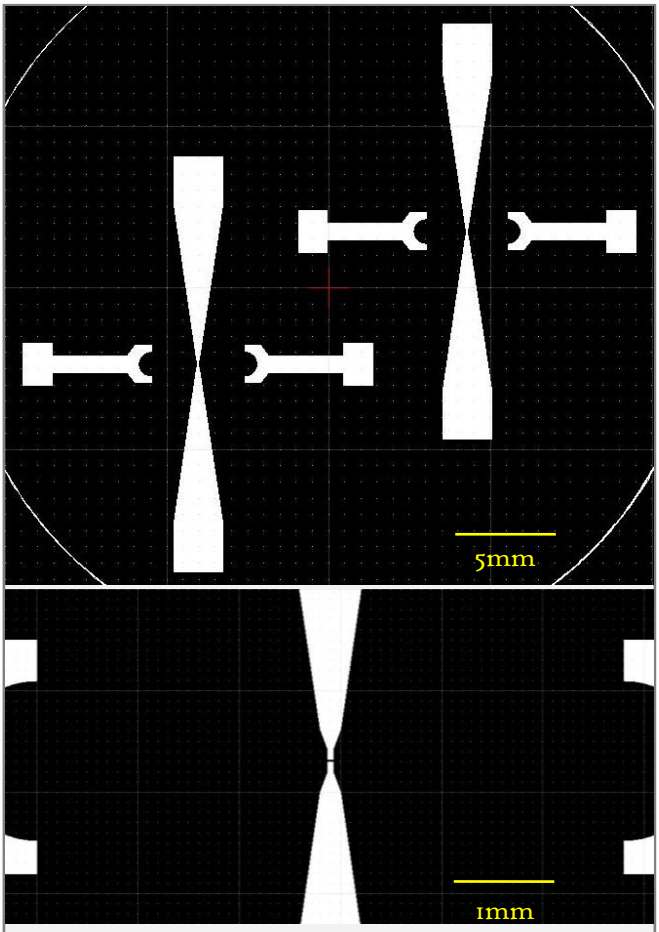

Figure 22. Design of the plastic mask for the planar electrodes (**down** : details of the detection electrode tips).

Gold was deposited by evaporation instead to platinum, which had been previously sputtered. The change of method allows a faster production of the devices no measurable influence on the measured signals. We also decided to integrate planar excitation electrodes in reservoir to facilitate the fluidic control during experiment. Before, wire electrodes were immersed into the

reservoir, which happened to modify the height of liquid in the reservoirs and generated hydrostatic flow inside the channel. With integrated electrodes, equilibrium is easier to reach by moving liquid from one reservoir to the second with a syringe and experiments without any parasitic flow are possible. The crescent shape of the integrated electrodes has been designed to minimize the concentration of the electric field in one point because all the points of the electrode frontier were at the same distance from the channel entrance. Moreover, the planar electrode had the same area than the wire electrode. In consequence, excitation electrodes were not damaged during the course of an experiment in spite of the high potential applied, up to +170V.

2.3.2 Excitation and detection electronics

Two different electronic systems were dedicated to the generation of the high electric field for the aggregate generation on one side, and for the conductometric measurement on the other side. The excitation electronic had been improved during my PhD with the help of Robert Breton, from the Kenium company, and the detection electronic is currently under re-development. All the results presented on this manuscript were realized with the original detection module developed during Youba Diakité's PhD.

Excitation electronic

DNA aggregation only occurs under high electric fields. A special high-voltage (HV) generator was needed for this experiment. The specifications for this system were:

- The electric field could vary between 0 and 450V_{pp}.
- The frequency of the field could vary between 5 and 1000Hz
- The signal shape was a square signal in order to maximize the power of the electric field. However, if the transition between the high and the low levels was too abrupt, the electromagnetic interferences experienced by the detection electronic would be detrimental to the experiment performance. Smoother transitions imply a decreased amount of high frequencies in the spectrum of the signal, which radiate more than lower frequencies. To do so, a ramp was added between the low and high levels. The duration of the ramp r, given as a percentage of the cycle time, could vary between 0 and 20% (Figure 23).
- The applied voltage had to be symmetric. The detection electrodes were located at the middle of the microchannel: this implies to be at the zero potential at this point to avoid interferences between the high electric field and the detection system. The easiest way was to build a symmetric generator: when one electrode was at the potential U, the other electrode

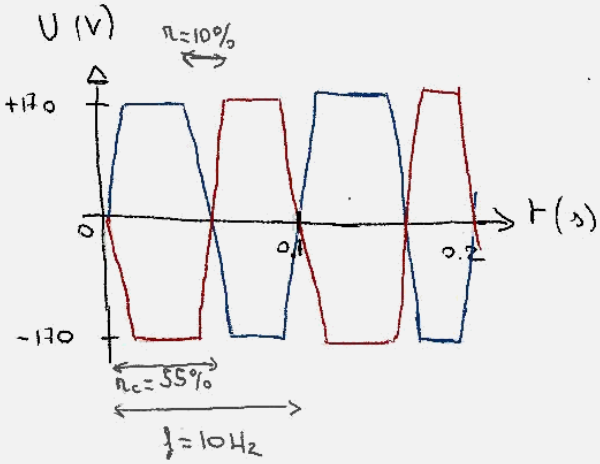

Figure 23. Schematic of the excitation signal on the first electrode (blue) and on the second electrode (red).

was at the potential -U. The possibility to displace the zero potential point by reducing the absolute potential in only one of the two electrodes was also implemented. This option could be useful is the position of the detection electrode has to be changed in future design.

- The duty cycle r_c (the percentage of time when the voltage is at the high level) could vary between 25 and 75%. Changing the duty cycle modifies the average of the AC electrophoretic signal, which is useful in order to move DNA aggregates via electrophoresis in one direction or the other.
- In the preparation of a portable system, the electronic was able to work with two 12V-lithium battery, and to memorize the parameters of the field in order to be independent from the computer, which is only necessary in order to change these parameters with a USB connection.

A wire-wrapped prototype has been produced and used for most of the experiments (see Figure 24). In practical, a PIC microcontroller communicated with the computer via USB, send instruction to a slave PIC microcontroller and digital potentiometers, control the LEDs and a screen display. The slave processor produced the shape of the signal according to the instruction of the master processor. The digital signal was then converted to an analogue, attenuated and positive signal. The offset was removed to centre the signal on 0V, and a special amplifier (PA343 amplifier) increased the tension until +/- 225V for the first HV output. The amplifier was supplied by high tension produced by a DC-DC converter (FS05CT) from a 24V battery or a standard transformer supplied by the domestic voltage. For the second HV output, the signal produced by the digital-to-analogue converter could be attenuated by a digital potentiometer and was inverted by an inverting operational amplifier, the offset was removed and the signal was amplified up to +/- 225V for the second HV output. Without any attenuation, this signal is the opposite of the first HV output.

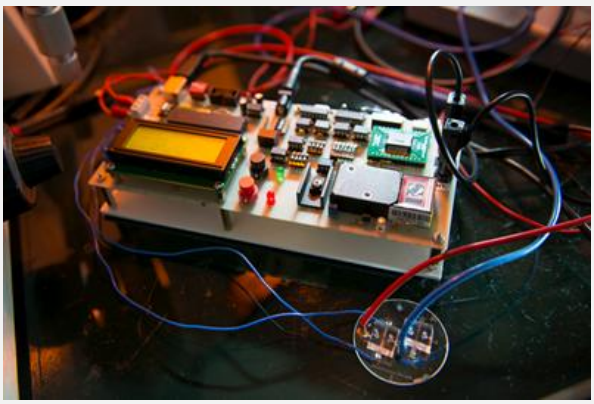

Figure 24. Picture of the excitation electronic, connected to the microchip.

The system also measured the intensity delivered by the two outputs in order to have a supplementary monitoring of the conductivity of the buffer, or detect accidental bubble formations. Intensity was recorded after the end of a ramp and averages were displayed every 10 cycles at a 5µA approximation. The HV generator was controlled by USB by Labview, via the use of dynamic link libraries (DLLs). The recording of the measured intensity was also possible. The parameters for the field could be stored inside the memory of the PIC controller in order to unplug the generator from a computer. In fact, the high-voltage could also be switch on and off with two push buttons on the prototype. Most of the time, the parameters used for the excitation were the following:

- Amplitude: $340V_{pp}$
- Frequency: 10Hz
- Ramp duration: 10% of the period
- Duty cycle: between 52% and 55%

Detection electronic

A large part of Youba Diakité's PhD was dedicated to the development of the detection electronic. The basic principle of the conductometric measurement is the following. A stable current at 32kHz was sent to the detection electrodes, and the tension between the two electrodes was amplified and sent back to the acquisition card. As said previously, one of the major drawbacks of contact-conductometry is the interferences between the excitation field and the detection electronic. Special precautions had to be taken to remove these interactions that could cause bubble formation in the electrodes and an important noise on the measured conductometric signal. To do so, the electronic system was designed with a balanced architecture and isolation from the excitation electronic, and the device is supplied by 9V batteries.

Electronic isolation

Isolation is frequently needed in usual electronic. The first aim is to eliminate DC tensions before a sensitive component that couldn't hold more than a specific input voltage. If two parts of the electronic device didn't share the same mass and one is floating according to the second one, the baseline potential would be different. Isolation is then needed when transmitting a signal between the two parts, in order to remove this constant potential difference, called common mode voltage. Common mode voltage is present in all the conductor of the measured circuit. In our case, the common mode voltage is mainly due to the high excitation electric field that is present in the two detection electrodes. Isolation could also be used to decouple two systems and to avoid ground loops by eliminating the direct transfer of charges between the two parts. Finally, the elimination of common mode voltage caused by magnetic and inductive interferences is necessary to increase the signal to noise ratio of the system. Isolation could be performed with different components:

- A simple capacitor is efficient to block DC components and low frequencies. It's also easy to integrate, doesn't have any limitation in the high frequencies and is insensitive to magnetic perturbation. However, a capacitor couldn't avoid a ground loop in the case of AC signals or the AC components associated with the steps in square excitations.
- Isolation transformers allow current transfer from one circuit to a second one thanks to a magnetic flux between two coupled electrical windings. Transformers could decrease the common mode voltage transfer by 100 to 140dB. Moreover, a transformer eliminates any direct transfer of electrons and efficiently breaks ground loops. But this component is difficult to miniaturize and is sensitive to magnetic interferences.
- Opto-isolators transfer a signal from a first circuit with a LED and to second circuit containing a phototransistor. Opto-isolators are efficient to suppress ground loops and are insensitive to interferences, but their non-linearity and loss of power during the transfer limit their use to digital communication.
- A simple operational amplifier could remove most of the common mode voltage and noises when mounted as a differential amplifier. The output of the component is the subtraction of the signal coming in the two inputs. If the useful signal is present in the V_- input, and the ground is linked to the V_+ input, the common mode potential and the noises present

simultaneously in the signal and the ground are removed in the $V_{out} = Gain\,.\,(V_- - V_+)$ output.

- More complex components, called isolation amplifiers, are sold in order to solve most of the isolation problem. The output of the component is floating according to the inputs. The isolation barrier removes the common mode voltage and eliminates ground loops, in contrary to a simple differential amplifier. The common mode voltage rejection ratio is 160dB for low frequencies, meaning that the necessary common mode voltage $V_{cm}$to obtain the same output than the differential mode voltage $V_{dm}$is $V_{cm} = 10^8 \times V_{dm}$, which is higher than the maximum potential of the excitation field. The component is also less sensitive to interferences. But its main disadvantage is its limited bandwidth at 50kHz.

Fortunately, 50kHz is still high enough to overcome the capacity of the Debye layers of the active, on-contact conductometric cell. So, the final solution chosen for a correct isolation of the electronic detection was the isolation amplifier. Moreover, in order to definitely remove ground loops, the electrical supply of the detection electronic was insured by six 9V-batteries.

Balanced electronic

The isolation systems proposed above are efficient to decouple the detection electronic and the high electric field used to generate the aggregation, in term of suppression of the ground loops and the current coming from the high electric field. The system, however, is not protected against electromagnetic interferences. These interferences could be due to low-radiofrequency radiation or to magnetic coupling, coming from the HV generator or the environment around the detection system. To eliminate these artefacts, a balanced circuit has been designed. The basic idea is to divide the input treatment into two branches, with the same signal in each branch, but in phase opposition. If the electronic system or the cable coming from the electrodes were submitted to a magnetic or electromagnetic interference, this interference would create similar artefacts in phase in the two branches or two cables. So, the perturbation would be part of the common mode voltage and could be easily removed by the previous isolation technique while the useful signal, in phase opposition, could be obtained by subtracting the signals of the two branches.

To build a perfect balanced circuit, some characteristics have to be respected:

- The two branches have to be identical. The same components, if possible from the same supplier, with the same impedance have to be used in each branch in order to keep the two artefacts identical.
- The two branches have to be physically close to each other. If the perturbation was really localized and the two branches far from each other, the created perturbation would be different in the two branches, leading to difficulties in noise removal. For cables, this requirement is achieved by twisting together the two wires.
- Finally, the signal produced in each part of the balanced circuit has to be perfectly symmetrical and in phase opposition.

In addition to this, standard precautions are still useful to limit the interferences. For example, the electronic has to be placed in a metallic case to remove the perturbations with a Faraday shield. The use of shielded cables is also necessary, for example BNC cables.

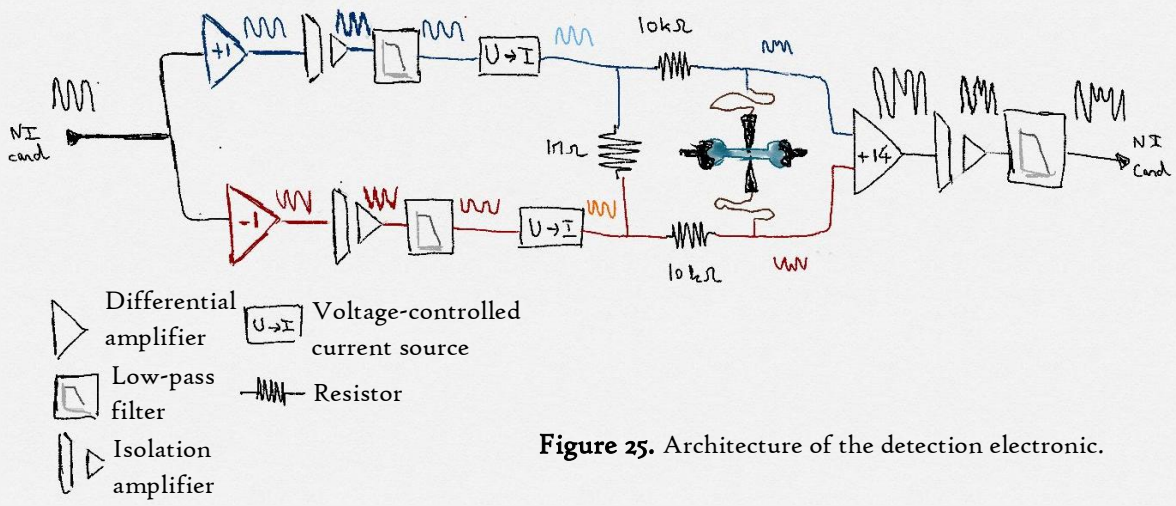

Figure 25. Architecture of the detection electronic.

Architecture of the detection electronic

The whole detection system is represented on Figure 25. First, a control signal is sent from the National Instrument acquisition card to the input of the detection electronic. A first stage divides the signal into two balanced branches, with an inverting operational amplifier on one side and a non-inverting amplifier on the other side. The acquisition card is then isolated from the rest of the detection instrument by two isolation amplifier (ISO124). Low-pass filters (cut-off frequency at 50kHz) and offset tuning stages are necessary to remove the noise and the DC offset produced by the ISO124. AC currents are then created by two current sources controlled by the isolated input signal. The frequency and shape are identical to the input ones, and the current amplitude is fixed by the tension amplitude. The current is then transferred to the detection electrodes via BNC cables through a resistor bridge (see Figure 26). The tension between the electrodes is amplified by a differential amplifier with a 14X gain. A last isolation stage with one ISO124 and one low-pass filter treats the measured signal, which is recorded by the acquisition card.

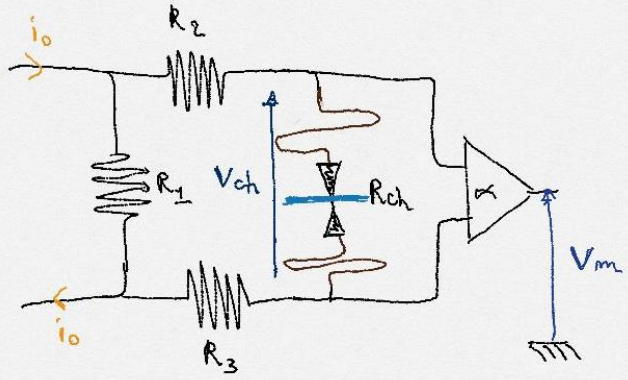

Figure 26. Detail of the resistor bridge.

Because of the resistor bridge, the tension measured is not proportional to the resistance in the channel. In fact, the theoretical relationships are:

$$V_m = \alpha V_{ch} = \alpha i_0 \frac{R_{ch} R_1}{R_{ch} + R_1 + R_2 + R_3} \quad , \quad R_{ch} = \frac{K}{\sigma} \tag{2.17}$$

$$V_m = \alpha i_0 \frac{K R_1}{K + \sigma . (R_1 + R_2 + R_3)} \tag{2.18}$$

With K the cell constant of the detection electrodes. αi_0 could be determined without the electrodes plugged into the detection electronic ($R_{ch} = +\infty$). We measured 2.2V, leading to $\alpha i_0 = 220nA$. Experimentally, we also compare the voltage measured after demodulation to the conductivity of the solution in the channel. This conductivity is calculated using the intensity measured by the excitation electronic and the channel dimensions:

$$\sigma = \frac{i_{ex}.L}{U_{ex}.h.l} \tag{2.19}$$

With $L = 5mm, h = 40\mu m, l = 150\mu m, U_{ex} = 340V$. The fit of the theoretical curve (Figure 27) with the experiment gives a value for the cell constant for the detection electrodes: $K = 2{,}3.10^6 m^{-1}$. Theoretical determination of the cell constant for a planar configuration is possible with the conformation theory[14]. This theory uses large approximation on the electrode shape and the presence of non-ideal resistor and capacitance in the schematic model of the electrode, and underestimates fringing effect. So, in the literature, the theoretical calculation of cell constants are often different from experiments by a factor that can go up to 30 times[20]. In our case, the calculus gives a value too small to be explained only by the imprecision of the theory: $K = 2.10^4 m^{-1}$. The presence of a closed channel above the electrode could be one contribution of this difference. However, since the fitting is good, we didn't search the reason for this difference. Three observations could be made from Figure 27. First, the measured signal decreases when the conductivity increases. The points above the red line (less than 10% of the total number of measurements; point density is higher close to the red line) are experiments where the apparent conductivity for the detection system is smaller than the one measured by the excitation one: it could be due to a bad soldering, a

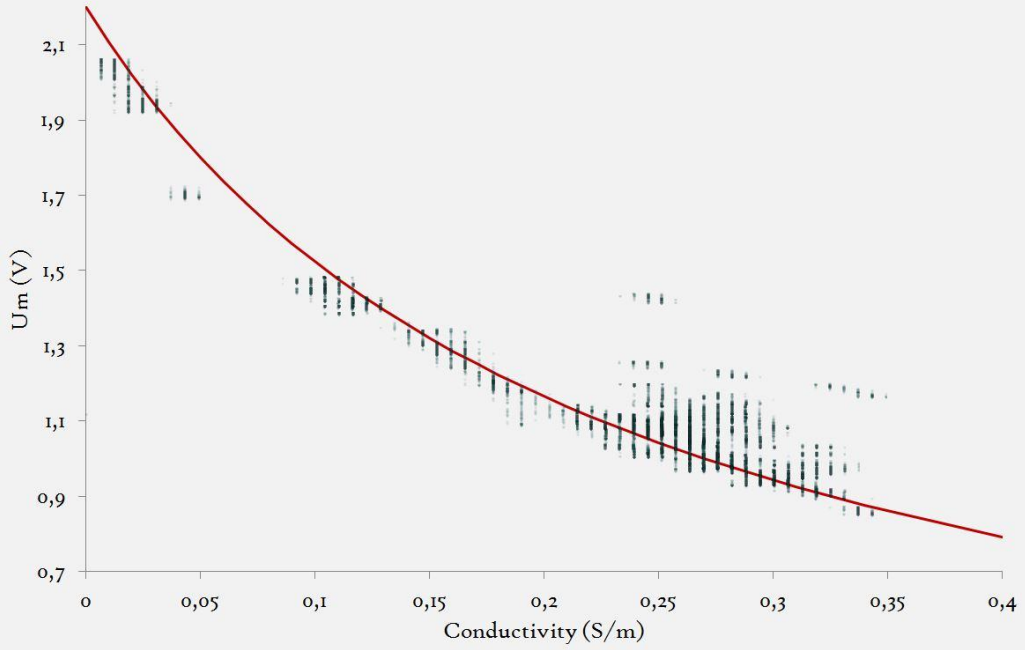

Figure 27. Relationship between the tension measured after demodulation and the conductivity of the solution in the channel, calculated from the intensity measured by the excitation electronic (transparent blue points). The red line is the theoretical relationship between the tension after demodulation and the conductivity of the solution.

default on the planar electrodes or a bad electrical connection which increase the electrical resistance between the channel and the detection electronic. Finally, the main teaching of these experiments is that the sensitivity of the detection electronic depends on the conductivity of the buffer used. If the conductivity is weak, the slope of the green curve is large and the electronics can discriminate easily a small change of conductivity, because it would create a large change in the measured voltage. In contrary, in a highly conductive buffer, a small change of conductivity creates a smaller change in voltage. Working with a low-conductivity buffer is favourable, both for the conductivity measurement and for the DNA aggregation.

With all these precautions, the simultaneous use of the excitation and detection electrodes didn't provoke any bubble formation on the detection electrodes, which had been the case without isolation. The balanced electronics removed most of the interferences.

2.4 Signal acquisition and treatment

2.4.1 Signal acquisition and demodulation

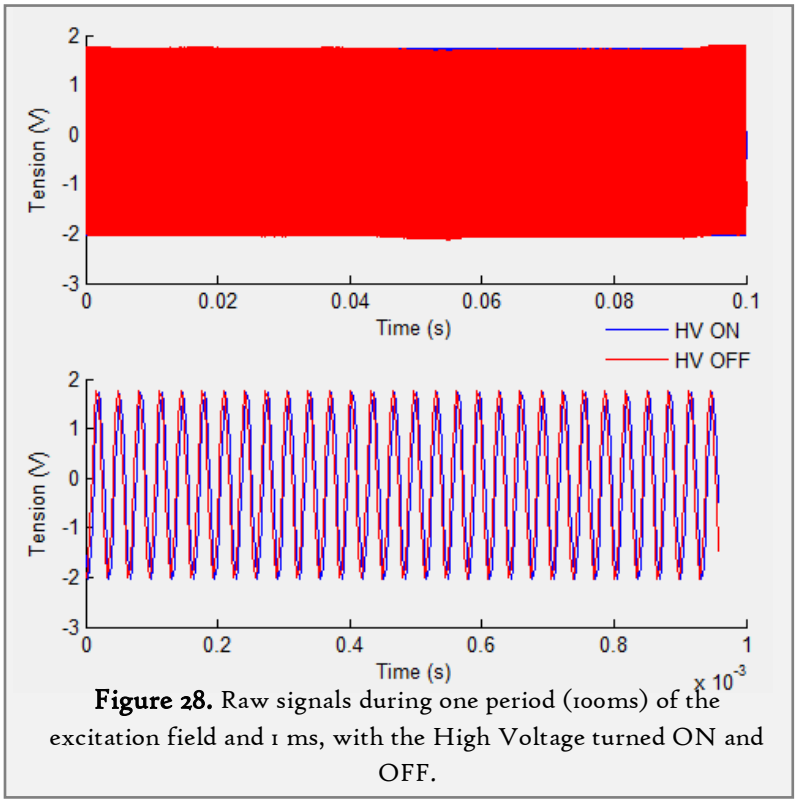

Figure 28. Raw signals during one period (100ms) of the excitation field and 1 ms, with the High Voltage turned ON and OFF.

Processing of the final signal was still necessary because the raw signal was not directly useful, as shown in Figure 28. First, the signal has to be demodulated. The carrier frequency is finally 31250Hz, because we chose an acquisition frequency of 312,5kHz in order to have a period ($T = 3.2ms$) compatible with the period of the internal clock of the acquisition card that is $T_{clock} = 10ns$, which wasn't the case for a 320kHz acquisition. The conductivity measurement is hidden into the amplitude of the carrier wave. As seen on Figure 29, despite the electronic isolation, there is still noise injected into the amplitude of the signal (average calculated over 10 periods). When the high voltage is OFF, the perturbation is mainly a 50Hz noise, due to the electrical environment. With the excitation electronic turned ON, a supplementary noise appear. Two perturbations (at 0.05s and 0.095s on Figure 29) correspond to the transitions between the high and low state of the quasi-square excitation field. They could be due to a capacitive coupling and inductive coupling between the detection circuit and the excitation field, because these interactions favour higher frequency.

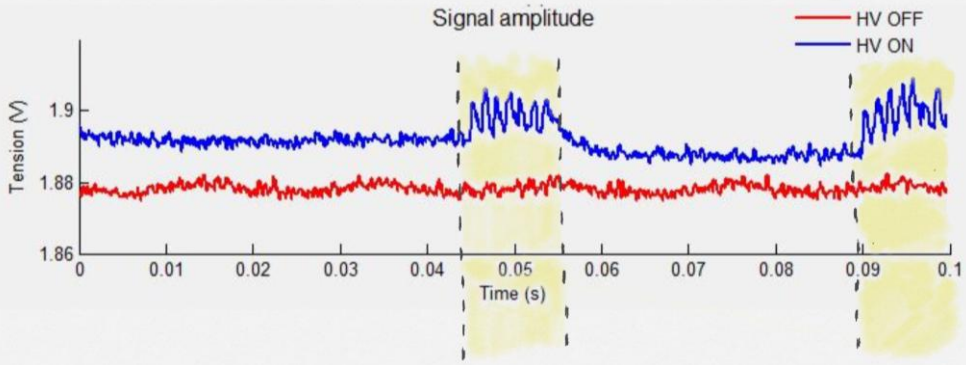

Figure 29. Amplitude of raw signals during one period of the excitation field, with the High Voltage turned ON and OFF. High voltage ramps are located in the periods highlight in yellow.

To remove this noise, the improved signal treatment developed during my PhD selects only the first part of the signal before the first perturbation at 0,045s. To do so, a digital synchronization signal following the excitation field shape, without the ramps, coming from the excitation system is also acquired by the acquisition card. The transition between the low and high level of the synchronization signal triggers the beginning of the acquisition, which last less than a half-period of the excitation field: only the plateau after the ramp is acquired. The demodulation is then performed by a Fourier transform of the truncated signal and the measurement of the amplitude of the 32125Hz component. The final signal has a 10Hz frequency, which was the frequency of the excitation signal during all the experiments. Fortunately, this sampling rate is fast enough: a DNA aggregate doesn't pass above the electrode in less than a half-second.

2.4.2 Wavelet analysis

Spectral characteristic of aggregation

The signal after demodulation has to be treated in order to obtain a quantitative value of the presence, quantity and intensity of aggregates. Qualitatively, the presence of aggregates is visible as tension peaks in the signal shape of Figure 30. A slow shift of the baseline always occurs. No obvious trends were seen. This shifting could be attributed to the evaporation of buffer on the reservoirs, to the slow change of pH or to the growing of bubble gas above the excitation electrodes. High frequency noise (close to 10Hz) is visible on the blank control, mainly due to the noise of the detection electronic. It's interesting to note than blank controls with and without the high voltage present comparable noises: the previous precautions were efficient to remove the perturbations produced by the excitation electric field. Some short peaks and fast changes of the baseline are also visible on the blank control: these events could be produced by the moving or the merging of bubbles above the excitation electrodes, which change abruptly the electric field distribution or provoke a short liquid flow in the channel.

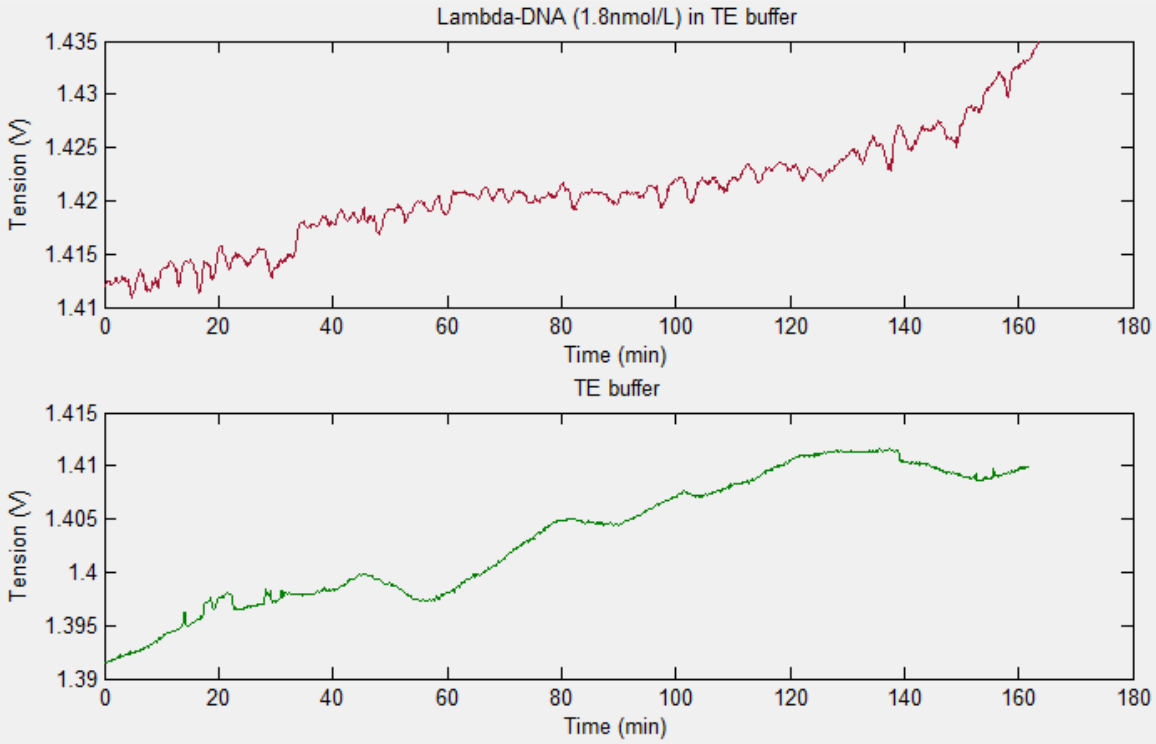

Figure 30. Demodulated signal of the conductometric detection of Lamda-DNA (1.8nmol/L) in Tris-EDTA 1X buffer (**up panel**), and a blank control (**down panel**).

The passage of aggregates above the detection electrodes is not really periodic, even if a typical characteristic distance between two aggregates could be observed. Sometimes, the duration of the electrophoretic movement between the reservoir and the detection electrodes is not long enough for the aggregation to be at equilibrium. The aggregate sizes are not monodisperse, leading to different peak sizes and intensity in the conductometric measurement. All these reasons make a characterization with a Fourier transformation complicated. With the advices of François Amblard, a wavelet analysis of the signal was chosen.

Principle of the wavelet analysis

Wavelet analysis is a powerful tool to obtain information about the presence of transitory peaks in a signal[23]. The principle is the following: the temporal signal $x(t)$is scanned with a pattern called wavelet $\varphi(u)$, which has a temporal extension and a shape similar to the shape of the peaks analyzed, and a zero average value (Figure 31). In order to scan the complete temporal signal, a collection of wavelets generated from the mother-wavelet are needed. Two parameters could be modified from the mother wavelet:

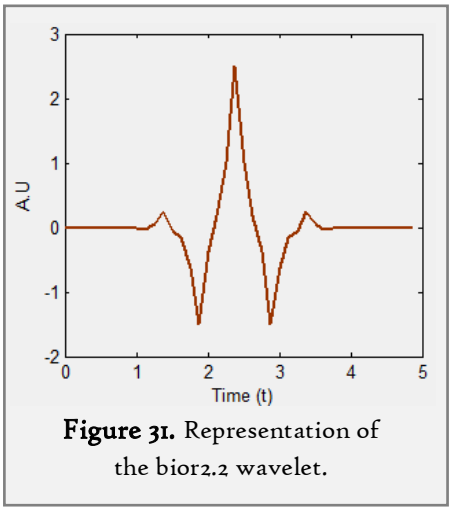

Figure 31. Representation of the bior2.2 wavelet.

- The position of the centre of the wavelet called t, along the time-axis. This translation on time of the wavelet allows a scanning of the entire temporal signal.
- The scale factor of the wavelet called a. The

dilatation of the wavelet allows a scanning of peaks of different width and size. In order to keep the same energy in the wavelet for the different width, the intensity of the wavelet decreases when the width increases.

$$\varphi_{a,t}(u) = \frac{1}{\sqrt{a}}\varphi(\frac{u}{a}) \tag{2.19}$$

A coefficient (called CWT) is calculated for each position along the time-axis of the wavelet and each scale factor:

$$x(t) \to CWT(a,t) = \int x(u)\varphi^*_{a,t}(u)du = \langle x, \varphi_a \rangle \varphi_{a,t}(u) = \frac{1}{\sqrt{a}}\varphi(\frac{u}{a}) \tag{2.20}$$

The information contained into the $CWT(a,t)$ is complete: the reverse transformation, from the coefficient to the initial temporal signal is possible. In fact, this continuous wavelet transform is even a redundant transformation of the initial signal, as coefficients with close scale factors or close positions share together a fraction of the signal information. Reducing the number of sampling points is possible without any information loss. Moreover, it's a necessity to move to a discrete wavelet transform since the transformation is digitally computed. For Fourier transform, the sampling limit is twice the maximum frequency. For wavelet transform, a critical sampling is obtained for $(a,t) \to (a_j, t_{j,k}) = (2^j, k.2^j)$.

The corresponding wavelet transform, discrete and non-redundant is:

$$x(t) \to d_x(j,k) = \int x(u)\varphi^*_{j,k}(u)du = \langle x, \varphi_{j,k} \rangle \tag{2.21}$$

$$\varphi_{j,k}(t) = 2^{-j/2}\varphi(2^{-j}t - k) \tag{2.22}$$

For our application, we use the wavelet transform for a multi-resolution analysis. The idea is to project the initial temporal signal into a subspace V_j in order to obtain a first approximation of this signal. The difference between the approximation and the previous signal in the V_{j-1} subspace is called detail signal $S_j\,(t)$ and obtained with the inverted wavelet transform, which use a dual wavelet $\dot{\varphi}_{j,k}(t)$ for the reconstruction:

$$S_j\,(t) = approx_{j-1}(t) - approx_j(t) = \sum_k d_x(j,k)\dot{\varphi}_{j,k}(t) = \sum_k \langle x, \varphi_{j,k} \rangle \dot{\varphi}_{j,k}(t) \tag{2.23}$$

This iteration could be performed several times, to obtain a decomposition of the initial signal in a sum of detail signals and a final approximation:

$$x(t) = approx_J(t) + \sum_{j=1}^{j=J} S_j\,(t) \tag{2.24}$$

The mean of the absolute value of the detail signals $Q_j = \langle |S_j(t)| \rangle$ describes at the same time the quantity of peaks in the detail signal and their intensity. This descriptor has been used for the quantification of our results during the whole project. Its reliability as a quantitative descriptor is discussed on a future section.

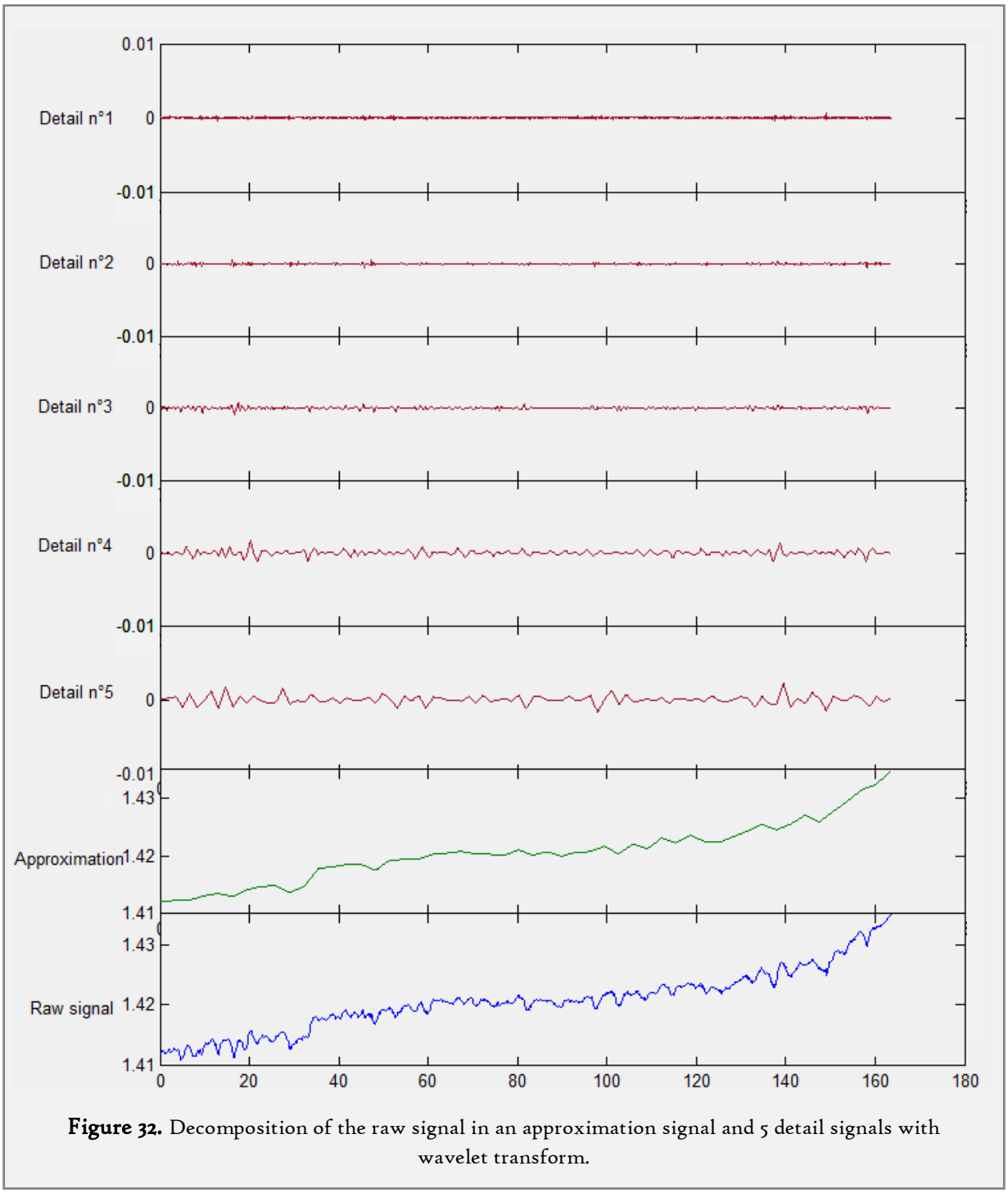

Figure 32. Decomposition of the raw signal in an approximation signal and 5 detail signals with wavelet transform.

An illustration is still the best explanation. On Figure 32, the positive signal of Figure 30 is decomposed into an approximation and 5 detail signals. The detail with index 1 corresponds to the wavelet transform with the smallest wavelet in width, close to the sampling rate (10Hz) of the signal. The resolution, or the minimum feature size measured, decreases by a factor 2 between each detail

signal. The approximation signal only contains the slow variation of the baseline. The peaks associated with the passage of aggregates seem to be distributed between the details n°5 and n°4. Noise around 10Hz is removed on the details n°1 and 2. As a consequence, decomposition on a unique detail signal would not be sufficient to obtain only the peaks associated with the aggregate passages.

Denoising algorithm

Further treatments are needed to remove the artefacts present, for example, on the blank control of Figure 30. The aggregation increases at the beginning of the measure and the baseline is less stable. The first 40 seconds are removed from the calculus of Q_j. The duration of the measure is fixed at 100 seconds. Increasing this duration doesn't change the result by more than 5%. To remove the artefacts present in the middle of the signal, a threshold strategy has been chosen. The detail signal is temporally cut into 10 segments of the same size. The $q_{j,i}$ parameters are calculated for each of these segments. A threshold t_j is fixed for each detail signal. This algorithm is then followed for decomposition into 5 detail signals:

$$For\ j\ going\ from\ 1\ to\ 5:$$
$$S_j^i(t)\ is\ the\ detail\ signal\ S_j(t)\ without\ the\ segment\ i\ having\ the\ highest\ q_{j,i}$$
$$Q_j = \langle|S_j(t)|\rangle\ and\ Q_j^i = \langle|S_j^i(t)|\rangle$$
$$If\ Q_j - Q_j^i > t_j.Q_j$$
$$The\ segment\ i\ is\ removed\ from\ S_j(t)\ and\ the\ algorithm\ makes\ a\ new\ iteration\ from\ the\ line\ 2$$
$$If\ not, the\ signal\ S_j(t)\ is\ clean\ and\ the\ algorithm\ goes\ to\ j+1$$
$$A\ final\ Qdenoised_j = \langle|S_j(t)|\rangle\ is\ calculated.$$

The algorithm remove the segment were the artefacts are present. The thresholds t_j were determined after several experiments in order to remove obvious artefacts. The final values are:

Detail n°	1	2	3	4	5
Threshold t_j	0.05	0.05	0.05	0.09	0.12

Figure 32 shows one example of a successful denoising treatment, on an extremely noisy blank control. The red portions of the detail signal n°4 correspond to the removed segments of the signal. 40 seconds at the beginning and 20 seconds at the end are automatically suppressed. Also, 4 segments over the 10 segments of the signal between 40 and 140s are removed because of the presence of brutal shifts of the baseline. On this example, without denoising, $Q_4 = 57\mu V$, and with the denoising treatment, $Q_4 = 16\mu V$.

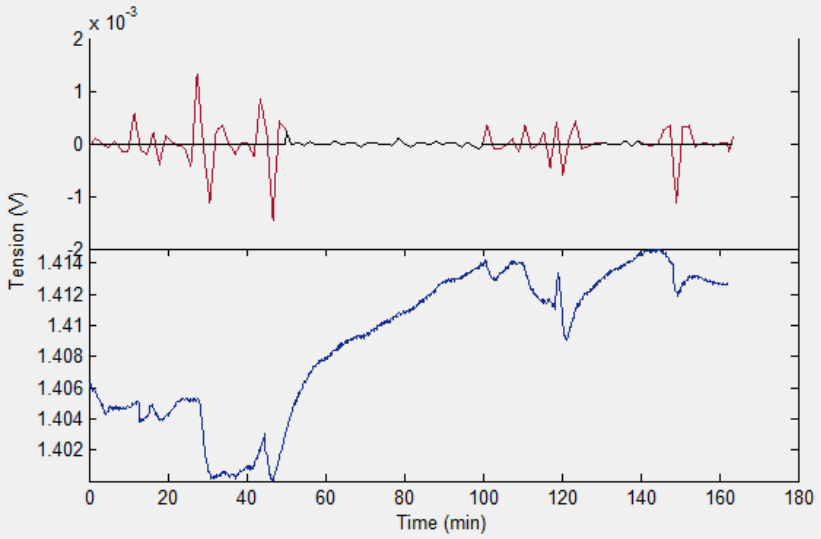

Figure 32. Raw signal of a blank control (**down**), detail signal n°4 after denoising (**up**). The red portions are the removed segments for the quantification.

Wavelet decomposition of synthetic signal

Before treating real signals, a short Matlab simulation was performed in order to assess and understand the wavelet decomposition process, and to validate the choice of $Q_j = \langle |S_j(t)| \rangle$ as an efficient descriptor. Synthetic signals containing peaks similar to those observed during aggregation were created and treated with the wavelet analysis algorithm described previously. Several parameters of the signal, like the intensities of peaks, their durations between two peaks, their widths, and shapes were modified (Figure 33) and the consequences on the quantification descriptors for several detail reconstruction were stored and plotted.

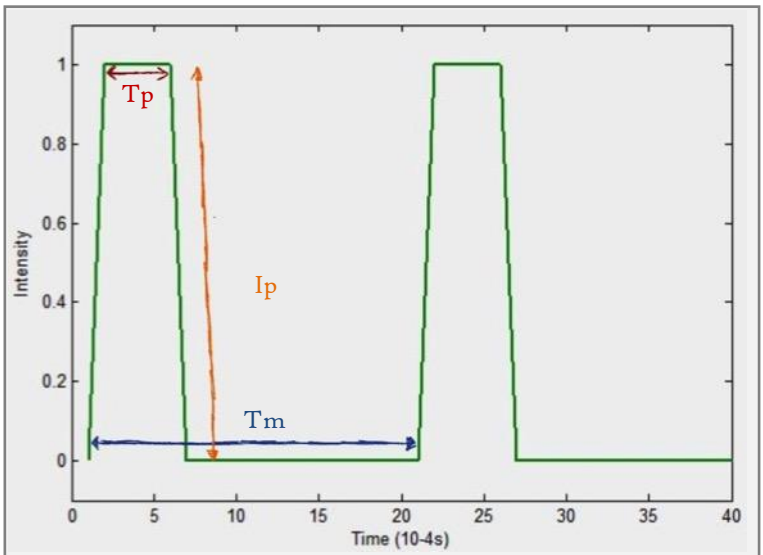

Figure 33. Representation of the synthetic signal for the wavelet simulation.

As seen before, it's too optimistic to believe that the peaks would appear in only one detail signal. On Figure 34, descriptor values associated with the details 1 to 10 are shown, along with the mean of the absolute value of the synthetic signal (Q_b), and the means of the absolute values of two combinations of detail signal: $Qsum_{2-5} = \langle |\sum_{i=2}^{5} S_i| \rangle$ and $Qsum_{1-10} = \langle |\sum_{i=1}^{10} S_i| \rangle$. The different parameters associated with the tests of Figure 34 are listed below:

	Ip	Tm (s)	Tp (s)
Figure 34, top	From 0.1 to 10	1	0.1
Figure 34, middle	1	From 0.5 to 10	0.1
Figure 34, bottom	1	From 1 to 100	From 0.1 to 10 with Tp=Tm/10

The influence of the peak intensity on the Q values is the easier to decipher. As seen on the top of the Figure 34, all the Q values for the detail signals are obviously proportional to the peak intensity. This result is simply due to the linearity property of the wavelet decomposition. The proportionality coefficient is different between each detail signals and should be linked to the similarity between the wavelet width and the peak width, which is chosen small on this test. In consequence, the details Q_2 and Q_3 associated with a short wavelet are closed to the reference value Q_b.

Interpretation is more complicated for the influence of the interval time (Figure 34, middle panel). The reference Q_b decreases when the interval increases because the number of peaks is smaller. For small intervals, the detail signals from 1 to 4 have the highest Q. The contribution of the higher detail signal is low because the peak width is small ($T_p = 0.1s$). When T_p is higher, the contribution of higher detail signals increases and the contribution of the detail signals from 1 to 3 decreases (data not shown). However, in all cases, the combination value $Q_{sum\,2-5}$, and in a lower extend $Q_{sum\,1-10}$, are roughly proportional to the reference Q_b, showing that this descriptor correctly take into account the number of peaks in the raw signal.

On the bottom panel of the Figure 34, the sensitivity to the peak width is tested. The width of peaks changes with the spacing between peaks, in order to keep a constant Q_b. As we will see in the next section, this situation reflects well the real behaviour of the DNA aggregation. On this test, we can observe that the signal detail contribution is related to the peak width according to the wavelet decomposition principle. The signal details associated with short wavelets respond to the presence of short peaks, and larger peaks excite detail signals associated with larger wavelets. The plot of Q versus the peak width is noisy. Nevertheless, each Q-value presents a broad maximum covering several seconds of peak width. Concerning the combination values, $Q_{sum\,1-10}$ is way more efficient to follow Q_b than a combination of a smaller number of detail signals ($Q_{sum\,2-5}$) which decays quickly as the peak widths increase and doesn't take into account the larger peaks.

However, we shouldn't forget that the main objective of the wavelet treatment is to remove the peaks from a noisy environment. Sinusoidal signal with a frequency ranging from 0.01 to 10Hz were submitted to the wavelet treatment (Figure 35). We observe that each detail signal was excited by a broad range of frequencies, around half a decade. The combination descriptor $Q_{sum\,1-10}$ responds to all the frequencies, which means that this descriptor doesn't remove any noise from a raw signal. A descriptor which is a combination of a fewer quantity of detail signal, as $Q_{sum\,2-5}$, is efficient to remove the high frequency and low frequency noise.

The choice of the right descriptor will depend mainly on the noise present in the raw signal. A combination of a small number of detail signals allows an efficient removal of most of the noise, but is not able to recognize all the peak widths. In the other hand, a combination of a larger number of detail signal detects correctly all the peaks, but is also highly sensitive to noise.

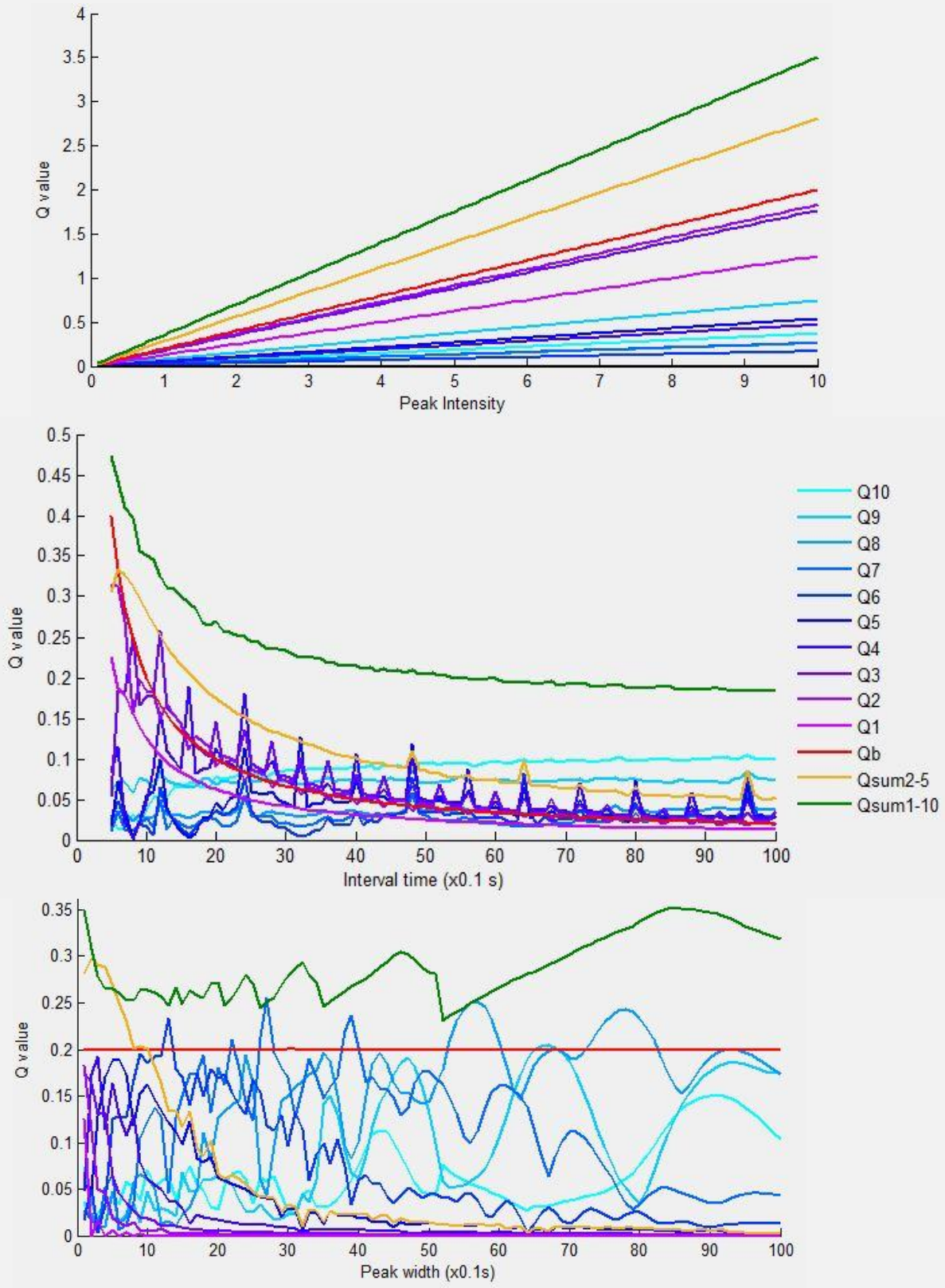

Figure 34. Top: influence of the peak intensity Ip on the Q-values. Other parameters are Tm=1s, Tp=0.1s. **Middle**: influence of the interval time Tm on the Q-values. Other parameters are Ip=1, Tp=0.1s. **Bottom**: influence of the peak width Tp on the Q-values. Other parameters are Ip=1 and Tm=10xTp.

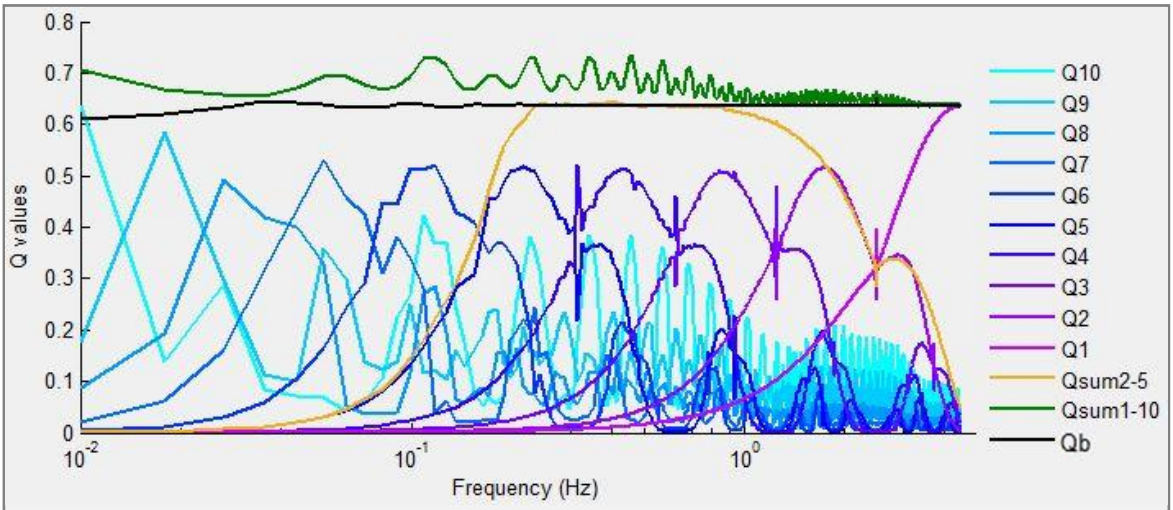

Figure 35. Influence of the noise frequency on the Q values.

2.5 Calibration and modelling

The first task that should be done concerning a new detection method is to assess the different parameters of the system. Is the detection qualitative or quantitatively significant? What is the LOD? What is the dynamic range of detection? Is the detection linear? But, even before answering to these questions, a first test with a correlation optic/conductometric has been made in order to prove that we were really detecting DNA aggregates. The system has then been modelled, and calibration experiments with a model DNA have been performed.

2.5.1 Exhaustive experimental procedure

At this point of the manuscript, an exhaustive description of the experimental protocol after the microfabrication of the chip is necessary.

- DNA solution was mixed with SyBr Green I (Molecular Probes) previously diluted at 10X in pure water in order to reach a final concentration of 1X. For calibration, the DNA stock solution was a 48kbp λ-DNA stock at 500µg/ml (15nM) from New England Biolabs. This stock solution was diluted into Tris-EDTA 1X buffer.
- 8µl of solution was injected into the microfluidic chip with a P20 micropipette. The good sealing between the pipette cone and the elastic PDMS reservoir allowed the entrance of the solution in the channel.
- The level of solution in each reservoir was equilibrated by pushing or pulling the liquid from one reservoir with a plastic syringe until any flows were suppressed. Air bubbles could also be removed from the channel with this operation. Monitoring was performed with a Zeiss Axiovert 135 TV microscope and a Nikon DS-Q1Mc camera, with white light or the FITC channel of the epifluorescent microscope.
- Detection and excitation systems and the National Instrument Card (USB X series) were turned on in this order.
- The controlling program was started with Labview. The excitation high voltage was applied, the input signal for the detection system was generated by the NI card and the output signal of the detection system was acquired. A first measurement of the exact frequency of the

excitation signal was done during 20s. The output signal and the intensity of the excitation current were then recorded and stored in a .txt file during 180s and the calculus of Q_j started 40s after the beginning of the recording to take into account the low aggregation kinetics.

- A movie of the fluorescence channel was recorded from the beginning the application of the high electric field to the end of the conductometric recording. The parameters used were a 22.5X gain, 100ms of exposure time and 5 frames per second.
- Measurements were always triplicated with the same solution.
- The same chip was used for several solutions. Removal of the DNA solution was performed with a P10 micropipette. The reservoirs and channel were washed with 20µl of pure water pushed with a P20 micropipette, and the washing solution was then removed with a P10 micropipette.

2.5.2 Optical correlation

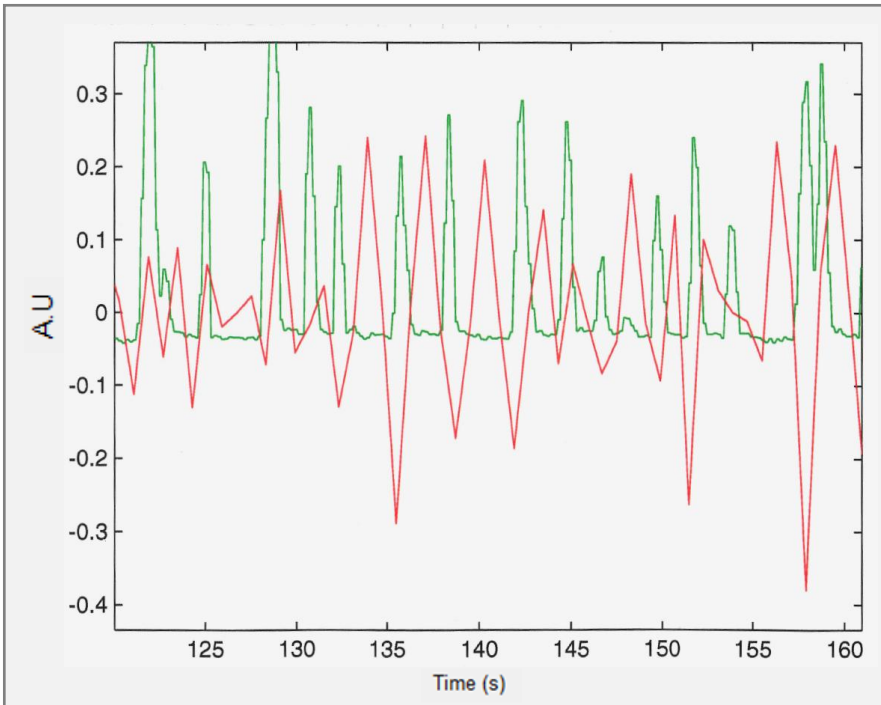

Figure 36. Correlation between an optical reading and a conductometric measurement of a DNA aggregates tainted with SyBr Green 1X. **Red**: renormalized detail signal n°4 after treatment. **Green**: Normalized fluorescent intensity between the detection electrodes.

First, in order to understand the relation between the passage of an aggregate above the electrodes and the associated conductivity change, a simultaneous recording of both the conductometric signal and the fluorescence of SyBr-Green labelled DNA between the electrodes was performed. The obtained graphics after treatment is presented in the Figure 36. Several observations could be made:

- At each passage of an aggregate above the electrodes, controlled with the fluorescence intensity, an event appears on the conductometric signal simultaneously.

- These events are constituted by a negative peak during the fluorescent detection of the aggregates. Surprisingly, this means that the aggregate conductivity is higher than the buffer conductivity. This conductivity increasing is not in agreement with a generalization of the Isambert's theory for large aggregates. As stated previously, buffer is necessarily highly conductive in the model in order to facilitate analytical resolution. However, in this case, the ionic strength of the buffer is so small that salt depletion is not seen anymore. The conductivity increase should be trigger by an increased concentration of co-ions in the vicinity of the highly concentrated DNA aggregates.
- However, we also observe an increasing of the signal before and after each aggregate passage. Two hypotheses could be made. First, the wavelet used present a positive peak surrounded by two negative peaks. Perhaps the presence of these positive peaks on the signal is the signature of the wavelet shape used.
- The intensities of the fluorescence and conductometry are not necessary correlated. The fluorescence detection is a locally, precise measurement, while the conductometry scans a larger volume of solution, because of the spreading of electric field line.

Finally, this first proof-of-concept experiment, compared with negative controls, is a good proof that we are effectively able to detect the passage of DNA aggregates above the detection electrodes. The underlying phenomenon, *i.e.* overconcentration of co-ions or salt depletion, depends on the buffer ionic strength.

2.5.3 Conductometric calibration

To advance in the characterization of DNA aggregates, a calibration was performed. The first objective is to obtain a calibration curve of the conductometric detection by varying the initial DNA concentration in the solution. Pictures of the fluorescent DNA aggregate were also taken, in order to obtain qualitative measurement of the aggregate size and fluorescence in function of the initial concentration.

Aggregates characteristics

DNA concentration was increased from 0 to 90µg/ml, with 3 measurements for each concentration. First, example pictures are shown in Figure 37. Qualitatively, the shape of aggregates changes drastically when the initial DNA concentration increases. The aggregate shape is also strongly influenced by the electrophoretic velocity of DNA. Indeed, the formation kinetics is slow (around 10s before complete aggregation). The electrophoretic drift has to be slow enough to obtain quasi-static aggregate sizes at the middle of the channel. At 1µg/ml, only DNA blobs are visible. These objects reach a snowball shape as the concentration is multiplied by a factor 10. At 50µg/ml, the aggregates reach the specific tilted shape, and flow recirculation around the aggregate is visible. The volume of aggregates continued to increase with the concentration, along with the recirculation speed. The number of object decreased also when concentration increased. Also, it seems that the DNA concentration in the aggregate is roughly constant and doesn't depend on the initial concentration. All these observations have been quantified, using the previous pictures and the ImageJ software.

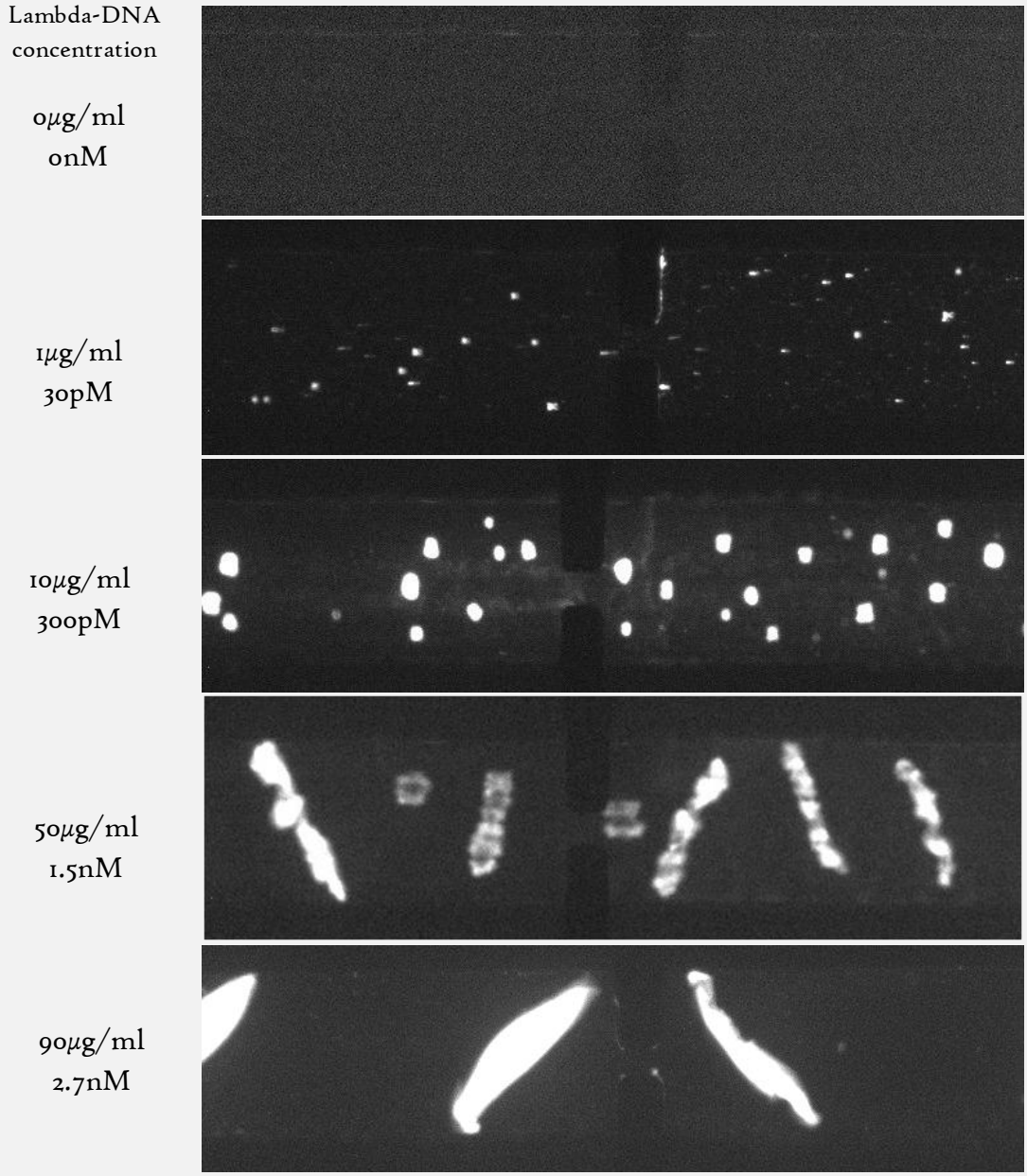

Figure 37. Picture taken during fluorescent microscopic observation of lambda-DNA aggregation, for different initial concentration.

The different graphics of Figure 38 show the results of this quantification. The most impressive change is the increase of the mean volume of the aggregates when the DNA concentration increases. The decrease of the number of aggregate is less violent. The combination of these two factor explains the fact that the volume per aggregate, which is the volume initially occupied by all the DNA molecules which are finally attracted into a single aggregate, increases quickly with the DNA initial concentration. With these result, it's possible to obtain the average concentration of DNA in an aggregate. Because of the conservation of the DNA quantity, the DNA concentration inside an aggregate is equal to the initial concentration, multiplied by the volume per aggregate and divided by the mean volume of one aggregate, with the assumption that all DNAs are

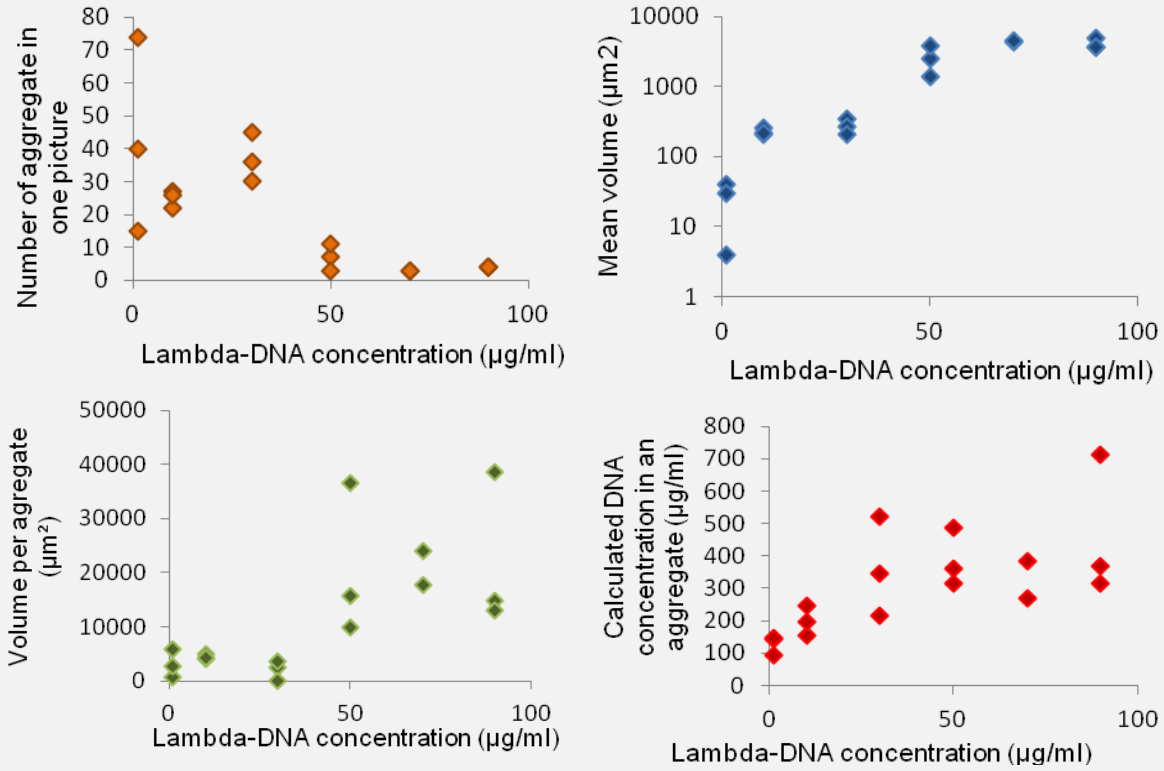

Figure 38. Evolution of the number of aggregate, the mean aggregate volume, the volume per aggregate and the calculated DNA concentration in an aggregate in function of the initial DNA.

aggregated. This hypothesis seems valid as the remaining fluorescence in bulk during aggregation is really low. Compared to the large range of initial concentration, the variation of the obtained concentration in aggregates is not significant. This concentration increases by a factor 3 when the initial concentration increases by a factor 50. More important, this information give us the concentration factor of the aggregation phenomenon: from 5X for 90µ/ml of initial DNA concentration to x100 for 0.1µg/µl.

Conductometric results

The results of the calibration are plotted on the Figure 39. From the conductometric curves, several characteristics of the detection method could be extracted.

The Limit of detection of the method, using the descriptor $Qsum_{2-5}$, is 50µg/ml (=15nM). Compared to the fluorescent observation, the conductometry is less sensitive, as the small aggregates already visible at 1µg/ml are not detected by the conductometry measurement. Although the DNA concentration in this small aggregate is constant, the volume occupied by the aggregate is too small. If the apparent increase of conductivity is due to a real, unexplained conductivity increasing in the aggregate, it's possible to demonstrate with quick approximations that the conductance between the electrodes is proportional to the volume of the aggregate. However, the apparent conductivity change could also be due to the high convection around the aggregate for an initial DNA concentration above or equal to 50µg/ml. A complete modelling of the chain of measure is useless without a good comprehension of the phenomenon.

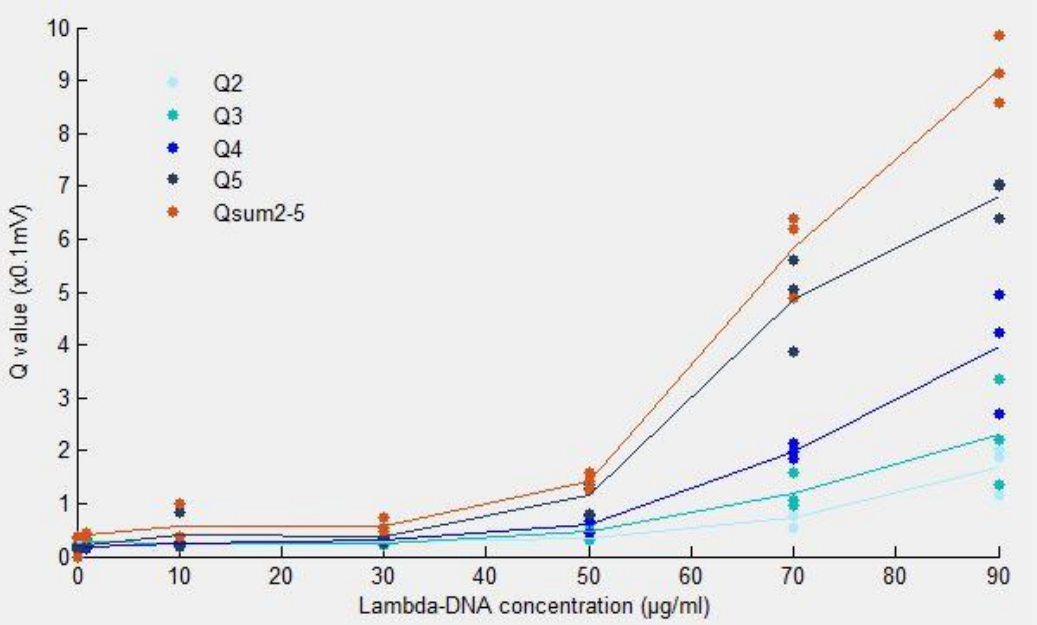

Figure 39. Q value versus the lambda-DNA concentration. The lines indicate the mean of the triplicates.

Fortunately, after 50µg/ml, the descriptor value increased linearly when the initial concentration increased. But despite this characteristic, electrohydrodynamic instabilities are not the best technique for an absolute determination of an initial DNA concentration. The repeatability of the measure is not excellent: the coefficient of variation is at 22% for the worst measurement (10µg/ml). In addition, the dynamic range of the method is small. Two phenomenon, which limit the detection efficiency, appear for the highest concentration of DNA.

- First, when an aggregate completely fills the cross-section of the channel, the velocity of the aggregate decreases strongly, maybe because of the shear induced by the electrohydrodynamic flows against the channel walls. This object, quasi-immobile, captures the next aggregates. Sometimes, the following aggregates don't coalesce with the big ones because the electrohydrodynamic flows repulse the two objects. Such a repulsion block the channel and the DNA patterns never reach the detection cell.
- The second phenomenon is a trapping of large aggregates at the detection electrode surface. Next aggregates coalesce with the trapped one, until the quantity of DNA is large enough to detach from the electrode because of the electrophoretic force of the high electric field. Fortunately, this capture doesn't modify substantially the detection, as the coalescence of new aggregates create the same signal as a passing above the detection cell. However, this trapping could also enhance the previous phenomenon and completely block the channel. This trapping is not dependant of a surface treatment, of the hydrophobicity of the channel, and occurs even when the detection electrode are detached from the detection system. One possible explanation is an attraction of the DNA aggregates by dielectrophoresis. DNA molecule is highly polarisable, and the presence of planar electrodes modifies the electric field lines in the channel. A gradient of electric field could attract long DNA by dielectrophoresis, and this effect has already been demonstrated with planar electrodes and lambda-DNA by Asbury *et al*[24,25]. The only way to diminish this effect would be to increase the buffer conductivity, in order to reduce the electric field deviation. So, a compromise has

to been done between a good aggregation, facilitated by a buffer with a small conductivity, and the elimination of the effect by a solution with a higher ionic force.

Conclusion of the chapter

In this chapter, we first introduced the electrohydrodynamic instabilities with the H. Isambert *et al.* theory. Qualitative explanations and simulation were added to obtain a physical insight of the phenomenon, which was initially a deleterious artefact during capillary electrophoresis. Then, the previous prototype of a conductometric DNA detection using this phenomenon, created by Y. Diakité, has been described with all the improvement added during my own PhD. Microfabrication, design, electronic and signal treatment have been revisited and completed. Finally, a calibration of the conductometric system gave us the main characteristic of the detection system. The detection is able to detect a minimum of 50µg/ml (15nM) of initial lambda-DNA, which is the first conductometric detection of DNA in an electrophoretic device. The whole system is also more robust and more sensitive than the previous detection device in electrode-solution direct contact mode described in the literature.

However, the system is not able to quantify the initial DNA quantity on a large range of concentrations and the limit of detection of 15nM is high compared to some amplification-free detection. To bypass this disadvantage, we decided to apply this method to the end-point detection of DNA amplification products. As only long DNAs could be detected, and because most of the known and useful biomarkers are shorter than several hundreds of base pairs, we developed a new reaction which amplify and elongate a short DNA into a large quantity of detectable long DNAs. This elongation-amplification method is the subject of the next chapter.

References

1. Mitnik, L., Heller, C., Prost, J. & Viovy, J. L. Segregation in DNA solutions induced by electric fields. *Science* **267,** 219–22 (1995).

2. Magnúsdóttir, S., Isambert, H., Heller, C. & Viovy, J. Electrohydrodynamically induced aggregation during constant and pulsed field capillary electrophoresis of DNA. *Biopolymers* **49,** 385–401 (1999).

3. Isambert, H., Ajdari, A., Viovy, J.-L. & Prost, J. Electrohydrodynamic patterns in macroion dispersions under a strong electric field. *Phys. Rev. E* **56,** 5688–5704 (1997).

4. Sanger, F. & Coulson, A. R. A rapid method for determining sequences in DNA by primed synthesis with DNA polymerase. *J. Mol. Biol.* **94,** 441–448 (1975).

5. Guszczynski, T., Pulyaeva, H., Tietz, D., Garner, M. M. & Chrambach, A. Capillary zone electrophoresis of large DNA. *Electrophoresis* **14,** 523–530 (1993).

6. Musheev, M. U., Kanoatov, M., Retif, C. & Krylov, S. N. Stable DNA Aggregation by Removal of Counterions. *Anal. Chem.* **85,** 10004–10007 (2013).

7. Musheev, M. U., Kanoatov, M. & Krylov, S. N. Non-uniform velocity of homogeneous DNA in a uniform electric field: consequence of electric-field-induced slow dissociation of highly stable DNA-counterion complexes. *J. Am. Chem. Soc.* **135,** 8041–6 (2013).

8. Hu, Y., Glass, J., Griffith, A. & Fraden, S. Observation and Simulation of Electrohydrodynamic Instabilities in Aqueous Colloidal Suspensions. *J. Chem. Phys.* **100,** 4674–4682 (1994).

9. Shafran, E., Yaniv, A. & Krichevsky, O. Marginal Nature of DNA Solutions. *Phys. Rev. Lett.* **104,** 128101 (2010).

10. Rubinstein, M. & Colby, R. Polymer physics. 442 (2003).

11. Tang, J., Du, N. & Doyle, P. S. Compression and self-entanglement of single DNA molecules under uniform electric field. *Proc. Natl. Acad. Sci. U. S. A.* **108,** 16153–8 (2011).

12. Rocha, M. S., Ferreira, M. C. & Mesquita, O. N. Transition on the entropic elasticity of DNA induced by intercalating molecules. *J. Chem. Phys.* **127,** 1–15 (2007).

13. Diakité, M. L. Y. *et al.* A low-cost, label-free DNA detection method in lab-on-chip format based on electrohydrodynamic instabilities, with application to long-range PCR. *Lab Chip* **12,** 4738 (2012).

14. Jacobs, P., Varlan, A. & Sansen, W. Design optimisation of planar electrolytic conductivity sensors. *Med. Biol. Eng. Comput.* **33,** 802–10 (1995).

15. Guijt, R. M., Evenhuis, C. J., Macka, M. & Haddad, P. R. Conductivity detection for conventional and miniaturised capillary electrophoresis systems. *Electrophoresis* **25,** 4032–4057 (2004).

16. Huang, X. & Zare, R. N. Improved end-column conductivity detector for capillary zone electrophoresis. *Anal. Chem.* **63,** 2193–2196 (1991).

17. Huang, X., Pang, T. J., Gordon, M. J. & Zare, R. N. On-Column Conductivity Detector for

Capillary Zone Electrophoresis. *Anal. Chem.* **59,** 2747–2749 (1987).

18. Zhao, H., Dadoo, R., Reay, R. J., Kovacs, G. T. A. & Zare, R. N. Electrically floating conductivity detection system for capillary electrophoresis. **813,** 205–208 (1998).

19. Mo, J., Liu, W. & Mo, S. An on-column miniature conductivity cell and a photocouple separator for conductivity detection by capillary electrophoresis. *Anal Commun* **35,** 365–367 (1998).

20. Graß, B., Siepe, D., Neyer, A. & Hergenröder, R. Comparison of different conductivity detector geometries on an isotachophoresis PMMA-microchip. *Anal. Bioanal. Chem.* **371,** 228–233 (2001).

21. Lichtenberg, J., de Rooij, N. F. & Verpoorte, E. A microchip electrophoresis system with integrated in-plane electrodes for contactless conductivity detection. *Electrophoresis* **23,** 3769–3780 (2002).

22. Eddington, D. T., Puccinelli, J. P. & Beebe, D. J. Thermal aging and reduced hydrophobic recovery of polydimethylsiloxane. *Sensors Actuators, B Chem.* **114,** 170–172 (2006).

23. Abry, P. *Ondelettes et turbulences*. (1997).

24. Asbury, C. L. & van den Engh, G. Trapping of DNA in nonuniform oscillating electric fields. *Biophys. J.* **74,** 1024–30 (1998).

25. Asbury, C. L., Diercks, A. H. & van den Engh, G. Trapping of DNA by dielectrophoresis. *Electrophoresis* **23,** 2658–66 (2002).

CHAPTER 3: Amplification-elongation reaction for the detection of small DNA biomarkers

During the previous chapter, proof-of-concept detection of long DNAs has been demonstrated. The system only detected concentrated DNAs: DNA amplification is necessary to obtain the desired final quantity of molecules in the case of detection of few pathogens. This amplification is also useful to make the whole method specific to a unique biomarker or sequence. Youba Diakité chose the Long-Range PCR for amplifying long DNAs and successfully obtained a signal with these PCR products. Nevertheless, because long sequences are prone to be damaged before the amplification and most of the known sequences are short, the final biochemical reaction would have to produce long products from initial small sequences.

Our first idea was to use the Rolling-Circle Amplification (RCA) as an elongation method, and to take profit of an exponential refinement called Hyperbranched Rolling-Circle Amplification (HRCA) to produce highly concentrated and long products. The mechanism and the kinetic of the reaction have been explored using real-time fluorescence monitoring, modelling and simulation. However, because of the limitation of the HRCA, a second two-step reaction has been developed. A first isothermal, Strand-Displacement Amplification (SDA) preceded an elongation step using RCA. The whole development of these amplifications was subjected to specific constraints. In fact, the reaction has to be integrated into the final microsystem. Isothermal one-step reaction, without any reactant addition, running into a low-conductivity buffer would be the perfect achievement.

Table of contents

1 Searching for a compatible DNA amplification 90
1.1 Specifications and constraints for an amplification reaction 90
1.1.1 Long-Range PCR 90
1.1.2 Specification and constraints 91
1.2 Rolling-Circle Amplification and refinements 92
1.2.1 Development of the Rolling-Circle Amplification technique 92
1.2.2 RCA detection and applications 95
1.2.3 Exponential refinements 96
2 Hyperbranched Rolling-Circle Amplification 101
2.1 First elongation experiments 101
2.1.1 HRCA protocols 101
2.1.2 Buffer conductivity and compatibility 103
2.1.3 HRCA aggregation 105
2.3 Real-time HRCA 107
2.4 Simulation 110
2.4.1 Algorithm description 110
2.4.2 Results 114
2.5 HRCA topology 118
3 Amplification-elongation scheme 121
3.1 Strand-Displacement Amplification 121
3.2 Coupling with RCA 125
3.3 Reaction limitations and perspectives 128
References 130

1 Searching for a compatible DNA amplification

1.1 Specifications and constraints for an amplification reaction

The limit of detection of our detection system was too high to use our device directly with a raw sample containing pathogens. DNA amplification was necessary to increase the final quantity of DNA to a detectable concentration. As the main amplification reaction used in laboratories and in diagnostic equipments is the Polymerase Chain Reaction (PCR), and the strength of the electrohydrodynamic instabilities used for detection increases strongly with the size of DNA chains, the first application of the prototype developed by Youba Diakité was the amplification of long DNA with a Long-Range PCR.

1.1.1 Long-Range PCR

The electrohydrodynamic aggregation occurs only for long fragments, above 5kbp. Detection of PCR products is possible only if this amplification technique can be applied to long DNA sequences. Unfortunately, PCR has been originally designed for the amplification of short sequences and the PCR efficiency decreases quickly for fragment longer than 5kbp[1]. The main explanation is the error rate of the *Taq* polymerase: 2.10^{-4} to 2.10^{-5} mutation per nucleotide per cycle[2]. The longer the sequence is, the larger the number of mismatches. When a mismatch is inserted, the *Taq* polymerase, which has a low rate of mismatch extension, couldn't extent the strand anymore. This partially replicated strand could not be used during the next cycles and the macroscopic PCR efficiency decreases[3].

To allow the amplification of longer sequences, Long-Range PCR[4] has been developed by W.Barnes in 1994. Two optimizations were performed to ensure amplification until 35kbp. First, a polymerase with a 3' exonuclease activity, enabling a proof-reading polymerization, was added in a small quantity in order to remove the mismatch created by the main enzyme. Secondly, it has been observed that the denaturation step at 95°C could depurinate the DNA fragments (a guanine or an adenine detaches from the deoxyribose skeleton). As the fragment length increases, a depurination has a greater probability to happen. Shortening denaturation steps or working on a specific buffer reduces this reaction and allows a complete polymerization.

In his proof-of-concept paper, Youba Diakité detected a 10kbp product from a Long-Range PCR of Lambda-DNA[5]. A kit commercialized by Qiagen, comprising an optimized enzyme mix and buffer, was used for the experiments. The thermal cycles were 93°C for 15s (denaturation step), 62°C for 30s (annealing step) and 68°C during 10min for the 10 first cycles, then 20 additional seconds were added at each supplementary cycles (extension step). For 40-cycles experiments, the cycling lasted nine hours and half. This is explained by the long duration of the extension step, necessary for the DNA duplication by a single polymerase from the 3' extremity of the primer to the end of the long ssDNA template. Detection of products from an initial concentration of 60aM (100fg of initial DNA, 1800 copies) was achieved after 32 cycles. However, the duration of the amplification is a real drawback. Moreover, in the case of a real sample, genomic material could be damaged by the pre-treatment and the micro-organism lysis. As the sequence of interest is long, the probability to cut the

DNA between the two primers increases. Lastly, most of the known biomarkers are short, below 1kbp, and cannot be targeted by this strategy.

Despite all this disadvantages, this experiment was enlightening. First, DNA amplification created a quantity of products large enough to be detected via an electrohydrodynamic aggregation. Secondly, the Long-Range PCR buffer was not too conductive for aggregate formation and successful conductometric detection. Finally, in term of limit of detection, this result is close to the standard method and the conductometric detection has even proved to be more sensitive than gel electrophoresis, in spite of the absence of fluorescent labelling for detection.

1.1.2 Specification and constraints

A new DNA amplification method needs to be set up, if we wish to apply this device to the detection of small biomarkers. This new method must comprise both amplification and elongation of the initial target. Moreover, we aim at the design of a truly portable and integrated system, so supplementary constraints are imposed.

- Based on the previous calibration with Lambda-DNA, the final DNA quantity after amplification would have to be around 1.5nM, working in the best conditions. Also, the final size of the products has to be higher than 5kbp. The longer the DNA, the smaller the limit of detection should be.

- Buffer conductivity is one of the critical parameter of the method. Increasing the concentration of small ions increases the electric field threshold for aggregation formation because $E_t \propto \sqrt{c_s}$. In addition, as seen on the calibration curve of the detection electronic, when the buffer conductivity increases, the ability to detect small change of conductivity between the detection electrodes diminishes. Keeping the buffer conductivity low is thus important for the limit of detection of the device. In addition, with highly conductive buffers, the intensity of the current flowing through the microchannel is more important, and enhances the perturbations on the detection electronic and the formation of gas bubbles on the excitation electrodes, leading to their destruction. Gas bubbles appeared for conductivities higher than 750mS/m. For comparison, Tris-EDTA buffer is 3.5mS/m and the Long-Range PCR buffer has a conductivity of 350mS/m. Unfortunately, buffer composition is not a very flexible parameter, as several ions are essential co-factor of enzymes, as magnesium ions, and the solution needs to keep a well-adjusted pH. A slight change in buffer composition could have dramatic effects on the amplification efficiency. For example, the Phi29 polymerase efficiency varies to 1.4%, 69% and 229% of the normal efficiency in the absence of Mg^{2+}, addition of NaCl (100mM) and ammonium sulphate, respectively[6].

- To ensure the reliability of the whole measurement, the DNA amplification method has to be specific and reproducible. Because the electrohydrodynamic-based detection is not specific at all - the only criteria for a positive test is the presence of long DNAs -, the specificity of the DNA amplification is primordial. For bacteria detection, the targeted sequence should be the only one to be amplified. Also, the resistance to contamination and the reproducibility of the system are important factors.

- The previous points are direct biological constraints for the DNA amplification development. Other specifications could be added, in order to simplify the integration of the amplification inside a microsystem. First, to avoid complex monitoring and control of the microchip temperature, isothermal amplifications were preferred over reaction using thermal cycling. If possible, the absence of high temperature initiation for the denaturation of dsDNA targets would be better, to avoid excessive water evaporation and vapour bubble formation.

- The number of steps in the reaction scheme is also important. Adding a reactant is not straightforward in a portable microreactor. Valves and sequential reactions have already been implemented in microfluidics[7,8], but most of the methods used for that are not compatible with a portable system. In order to avoid the need to implement such technological complication, the development of a single-step DNA amplification and elongation reaction would be greatly appreciated.

- Then, if a single step reaction cannot be achieved, the successive reactions would preferably be performed in the same buffer, or at least in a mix between the original buffer and a new component, in order to avoid the need for buffer exchange. Indeed, changing completely the buffer between different steps is complicated because a solid support, like magnetic particles, has to be used. Compatibility between the different enzymes would be a key of the biochemistry development, along with the fact that products and reactant in excess from one step should not interfere with the next steps.

Apart PCR, several amplifications have been developed during the last 20 years. SDA, LAMP, RPA, HDA and RCA were quickly described in the chapter 1. All these techniques are isothermal and most of them could compete with PCR regarding sensitivity, while creating the same final DNA quantity. Lastly, some of them are easy to implement and are single step. But only the LAMP and the RCA produce products longer than the initial target. We chose to explore the Rolling-Circle amplification because the products are really longer than the LAMP products, and exponential amplification is available with some improvements of the original technique. The strategy chosen could be qualified as a "elongate first, and amplify" scheme. Before presenting the results obtained with this strategy, we propose below a detailed review of the RCA and its alternative version.

1.2 Rolling-Circle Amplification and refinements

1.2.1 Development of the Rolling-Circle Amplification technique

Rolling Circle Amplification was developed by combining two previously known techniques: the Rolling Circle Replication (RCR), similar to the *in-vivo* bacterial plasmid replication, and the padlock probe technology.

Beside their large, circular genomes, bacteria also possess small dsDNA circles, called plasmids, with a size ranging from 1kbp to several Mbp. Their replication is insured by a specific mechanism, called rolling-circle replication[9]. First, an initiator protein (Rep) nicks one of the two strands of the plasmid at an initiator sequence (see Figure 1). The Rep protein attaches to the 5' end of the cut strand and recruits single-stranded binding protein (SSB) and helicase. The latter enzyme

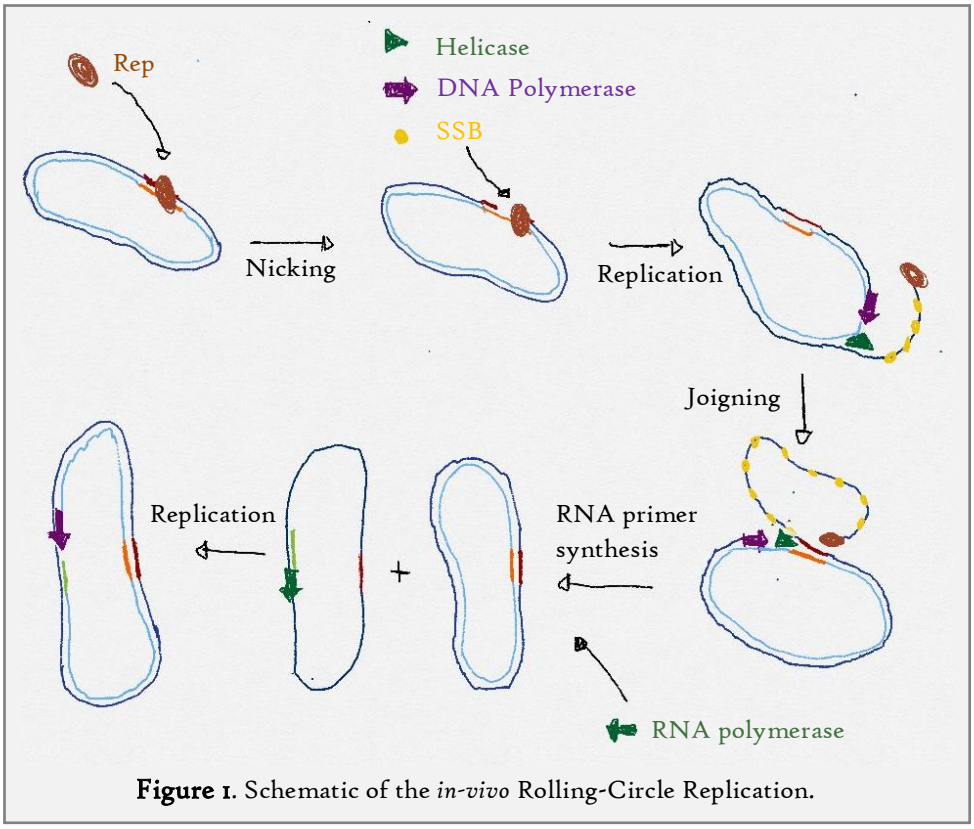

Figure 1. Schematic of the *in-vivo* Rolling-Circle Replication.

can unwind and separate the two complementary strands from the 5' end, and SSB protein stabilizes the resulting ssDNA strand. At the same time, the 3' end of the cut strand is elongated by a standard polymerase. Once one turn of the template strand is done by the enzymes, the Rep protein cuts again the displaced strand and joins the two extremities to create a new ssDNA plasmid. Creation of a primer and elongation to a dsDNA plasmid are performed in the model of the Okazaki fragments, and sealing of the final nick is done by a DNA ligase.

Helicase and SSB proteins are necessary for the replication of these long circles. However, in 1995 and 1996, two teams led by Eric Kool and Si-Qun Xu observed the *in-vitro* replication of short ssDNA circles, down to 26nt, without the help of these auxiliary proteins[10,11]. The result was really surprising, firstly because of the absence of auxiliary proteins, and secondly because these small circles cannot be transformed into dsDNA circles: dsDNA is too rigid to be circularized for a size smaller than 150bp. Indeed, this result was finally understood by studying in detail the mode of action of the used polymerases, and the topological behaviour of DNA. Several polymerases have been tested: *E.Coli* DNA Polymerase I, Klenow Fragment, T4 and T7 polymerase. After priming of the small circle by a short oligonucleotide, polymerases initiate the elongation from the 3' end of the primer. But torsion is exerted by the addition of new base pairs: the strand under elongation self-unwinds after the polymerase and detaches from the circle (See Figure 2). The polymerase doesn't stop after one turn of the circle, and the produced ssDNA is a concatemer of the complementary sequence of the circle sequence, that can be longer than 12kbp. It's interesting to note that some of these polymerases don't have a strand-displacement activity, which is not necessary for the replication of small circles. In addition, because the circles are smaller than the polymerase size, the DNA substrate rolls under the polymerase, whereas the polymerase moves along longer plasmids.

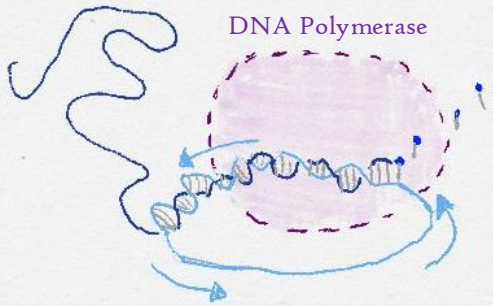

Figure 2. Schematic of the self-unwinding of ssDNA during RCR of small circles. Arrow indicates the circle DNA movement under the polymerase.

For larger circles which could be fully transformed in a dsDNA circles (>150bp), the helicase could be replaced by polymerases with a strand-displacement activity. The SSB is not essential, but its presence avoids the termination of the replication by a strand-switching mechanism, in which the polymerase moves from the template circle to the created ssDNA and transforms it into a dsDNA[12].

Padlock probes were invented in Ulf Landegren's team in 1994. They consist in short phosphorylated oligonucleotides containing two probing sequences in the 3' and the phosphorylated 5' extremities, attached together with a linking sequence[13]. Padlock probes could recognize a target ssDNA by hybridizing each probing sequence with half of the targeted sequence (see Figure 3). A heat denaturation step is necessary when working with dsDNA. Then, the nick between the 2 arms of the padlock probe is closed by the action of a ligase enzyme. The main advantage of this technique is the high specificity of the ligation. A mismatch due to a single point mutation located at the 3' end of the padlock probe is enough to block the ligation and the circularization of the probe[14]. Initially, padlock probes closing was detected by electrophoresis, as the linear oligonucleotide didn't move at the same velocity that the corresponding ssDNA circle. The combination by Landegren's team[15] and David C. Ward's team[16] of a highly sequence specific, padlock probe discrimination and a further signal detection by amplification of the ligated circle with a RCR greatly increased the sensitivity of the first technique. This combination was called "Rolling-circle amplification" (or RCA).

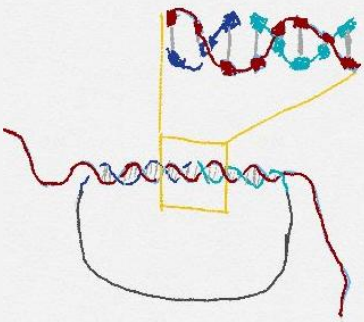

Figure 3. Schematic of the hybridization of a padlock probe (blue) on a target ssDNA (red).

To start the amplification, the circularized padlock probe could be primed by a short oligonucleotide. The second solution consists in probing the searched sequence near to its 3' end: the polymerization can thus begin from the end of the sequence. If a few numbers of nucleotides are left hanging after the probing sequence, a polymerase with 5' to 3' exonuclease activity could remove these extra nucleotides to begin the reaction (See Figure 4). This amplification reaction has a linear kinetic: the DNA quantity increases linearly over time until 500kbp per initial molecules after 12h of reaction[15]. The final quantity of DNA is proportional to the circularized padlock probe quantity and depends also on the processivity and strand-displacement activity of the polymerase used. Either the padlock probes are large enough to need a polymerase with

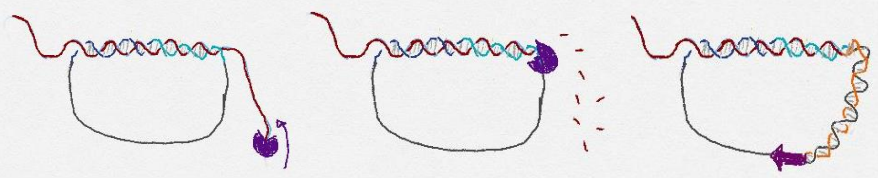

Figure 4. Schematic of the removal of nucleotides from the 5' end of the target by a polymerase with exonuclease activity ( ), followed by RCA catalysed by the same enzyme ( ).

strand-displacement activity, or this activity is necessary when the circle is primed by a short oligonucleotide, in order to remove the target ssDNA while elongating the primer. The position of the probing sequence in the target DNA might also be important. When the circularized probe is amplified via an additional primer, the chemical link between the probe and the targeted sequence (by base-pairing) is removed by the strand-displacement activity of the polymerase. However, the targeted strand is still physically entangled in the padlock probe. The probe could now diffuse along the strand, preferably to the 3' end, because of torsion exerted by the elongation of the probe[15]. RCA might be inhibited as long as the target sequence is still entangled: shorter distances between the probing sequence and the 3' end of the target DNA are thus favourable. This effect seems to be polymerase-dependant, as the Bst polymerase has been shown to be able to amplify padlock probes localised very far from target ends[17].

1.2.2 RCA detection and applications

The first applications of RCA were motivated by the really high specificity of the method, since the sensitivity of the technique did not reach the performance of exponential PCR in terms of sensitivity. The best example of such applications is the detection of single nucleotide polymorphisms (SNP) in cell genome, as a single mismatch between the padlock probe and the target DNA could block the ligation.

As well as for qPCR, fluorescence detection could be used for a real-time monitoring of the product accumulation. Intercalating dyes (SyBr Gold), fluorescently-labelled oligonucleotides coupled with magnetic particles have been used by Qi *et al.* for the detection of SNPs[18]. Labelled oligonucleotides, complementary to the ssDNA RCA product, allowed a dual-colour assay for the simultaneous detection of heterozygous state. However, a pre-amplification of the genomic target was necessary to reduce the target length and to increase the initial quantity of targets.

Intercalating dyes reacts with the PCR products and padlock probes, not only with the RCA products, and washing step are necessary for labelled oligonucleotides. To obtain a better signal to noise ratio and a real-time monitoring, molecular beacons were designed in order to recognize the long RCA product[19]. Molecular beacons are composed of a fluorophore and a quencher, brought to close proximity by a DNA stem loop. Once the sensing region of the molecular beacon hybridizes onto each repetition of the concatemer DNA, fluorophore and quencher are separated and the probe could fluoresce. Detection of an initial target quantity of 1fmol (50pM) was reached, but the linear amplification of the RCA didn't allow to improve the sensitivity further.

RCA product from a single target is a long DNA, which is most of the time physically condensed into a DNA coil. With fluorescent probes (intercalating dye or labelled-oligonucleotides), a single coil (around 1µm in size) could be easily seen with a microscope. Whereas bulk detection of RCA products is not sensitive enough, this technique allows a digital count of target copies. This digital amplification was first described with RCA products immobilized on a glass surface[16,20]. Immobilized oligonucleotides trapped padlock probes or targets, which captured afterward targets or padlock probes, respectively. RCA elongates the capture oligonucleotide, as seen on the Figure 5, and two specific labelled-oligonucleotides allowed the detection of mutated and wild DNA[16] with a ratio of mutated over wild DNA of 1:100. Without immobilization, the counting of DNA coils after a bulk RCA has been performed with confocal imagery of a flowing solution in a microfluidic channel[21].

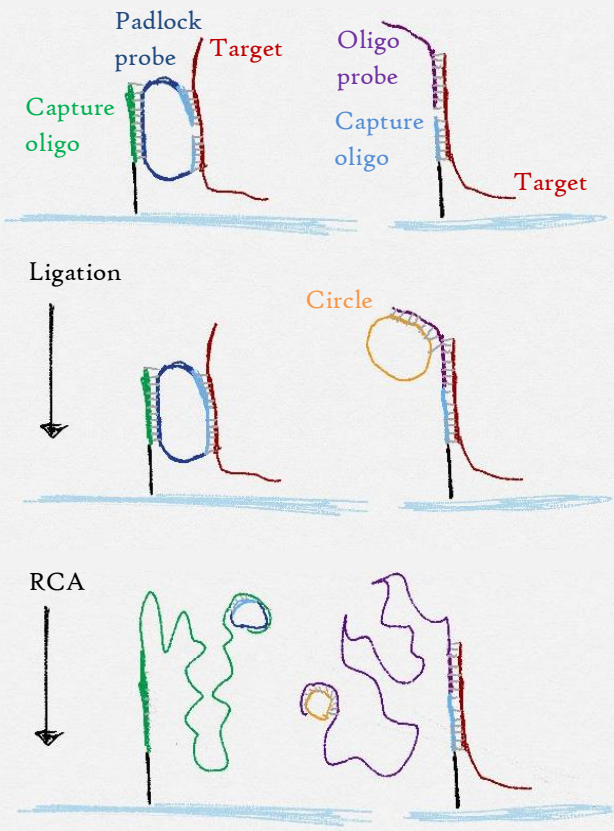

Figure 5. Schematic of two strategies of capture, ligation and RCA in the case of immobilized RCA[16,20]. Washing steps were not represented.

DNA microarray has also been improved with RCA, in order to detect DNA[22], mRNA[23], or proteins converted to DNA signal via a DNA-linked antibody[24]. Other detection means have been explored for immobilized RCA products like electro-chemiluminescence[25], electrochemical detection[26], phase contrast of vapour condensation[27] or electrical detection via a RCA metalized bridge[28]. Lastly, the support for immobilization could be changed to enhance target capture, using *e.g.* micro-beads for microfluidic trapping[29] or hydrogel-based particles[30].

With the possibility to obtain single-molecule detection, RCA has been implemented in *in-vivo* experiments for direct observation of nucleic acids in fixed cells. Because of the large molecular mass of the product coil, diffusion of the amplification product is slowed down and nucleic sequences could be precisely localised. SNPs could be localised directly on genomic DNA thank to the addition of an anchor primer, which allows RCA to occur even in the middle of long DNA[31]. mRNA[32,33] localisation or mutation discrimination in mitochondrial DNA[34] have also been performed.

1.2.3 Exponential refinements

Concerning our main topic, *i.e.* pathogen detection, RCA kinetics is too slow to be used in bulk detection as easily as PCR or LAMP, without using a microscope. To increase the kinetics of the reaction, exponential refinements have been developed from the initial RCA.

Hyperbranched RCA

Also simply called Exponential RCA (ERCA), this technique has been described for the first time simultaneously in the Ward's first paper about RCA[16] and a Hongbo Li's paper[35] (where it's called RAM, as Ramification-extension Amplification Method). The only difference with a classic RCA is the addition of two primers. The first primer is identical to a part of the padlock probe, and can thus hybridize with multiple sequences present in the long single-stranded product of the RCA (see Figure 6). Primers are elongated by the polymerase, and as the polymerase processes, the strand-displacement activity of the enzyme displaces the other encountered primers under elongation. ssDNA branches are eventually completely detached from the RCA products. The second primer is complementary to another part of the padlock probe and can hybridize with multiple sequences

present in the ssDNA branches. For short branches, the primer elongation creates a short dsDNA. For longer branches, the same branching phenomenon occurs. This reaction creates an exponential accumulation of DNA. However, the products have a large range of size, going from the padlock probe length to several kilobase pairs, always by a multiple of the probe length.

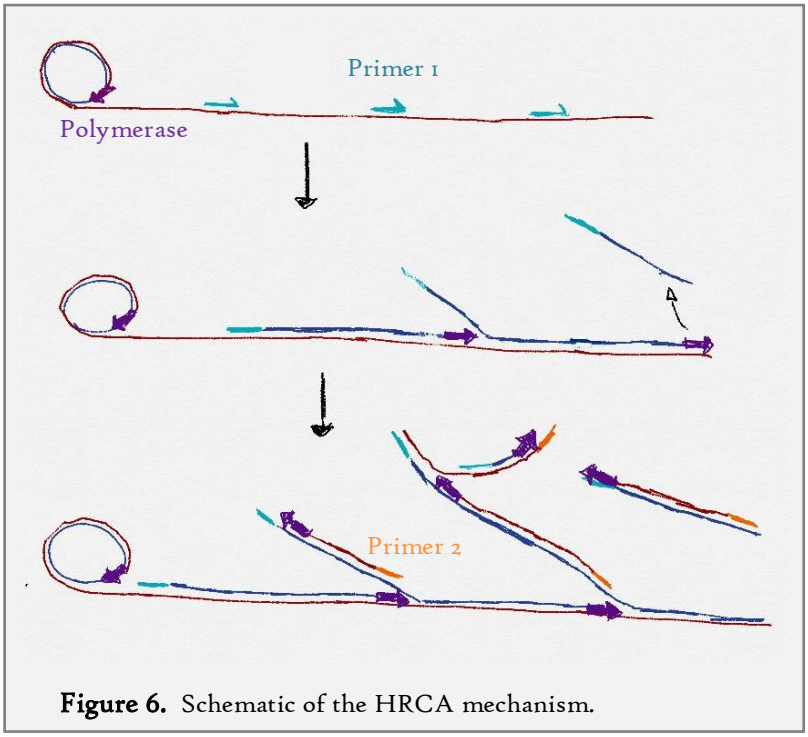

Figure 6. Schematic of the HRCA mechanism.

HRCA has been rapidly used for bulk detection of DNA in solution. However, optimization of HRCA is more complicated than for a classical RCA:

- The choice of the polymerase is more critical. Bst polymerase is often preferred over the Phi29 polymerase, the main enzyme for classic RCA, this latter showing sometimes a small efficiency for HRCA[16]. It has been hypothesised that, despite its higher processivity, the initiation of the elongation by the Phi29 is not optimal because an oligonucleotide primer is not the *in-vivo* initiator for Phi29 polymerase. In contrary, Bst polymerase should be more robust as it needs *in-vivo* a fewer number of accessory proteins than Phi29 for initiation[17].

- Phi29 and wild Bst polymerases have a 5' to 3' exonuclease activity which digest primers before their incorporation, unless they are protected by two phosphorothioate bonds in the 5' end[36]. Another current solution is to use modified enzymes without the exonuclease activity (indicated as exo-Bst polymerase, for example).

- The primers design is important and delicate, because primer-dimer complications came back as a main source of non-specific noise.

- For bulk reaction, the presence of uncircularized padlock probes could be problematic during the polymerization step. Second primers can hybridize to the probes, which will be partially transformed into double stranded DNAs after elongation. The probe could also play the same role as the first primer and initiate a branching of the RCA product. One solution is to treat the ligation product with exonuclease I and III, which destroy ssDNA and dsDNA, but can't digest circular DNA. Using magnetic beads to capture ligated products allows the washing and replacing of the solution in order to remove unreacted padlock probes.

When the above difficulties are mastered, HRCA can be a really sensitive detection method. The sensitivities claimed by the papers listed in Table 1 are often under 100 copies of initial DNA, mainly with classical fluorescence detection or gel electrophoresis. With intensive optimization, specificity could be keep as high as in the case of RCA, with examples of successful detection of SNPs

Reference	authors	Year	Ligation	Polymerase	detection	Sensitivity	Other
Mutation detection and single-molecule counting using isothermal rolling-circle amplification[16]	Paul M. Lizardi *et al.*	1998	*T.Thermophilus* DNA ligase	Vent (exo-) DNA or Bst + Phage T4 gene-32 protein	Exonucleolysis and gel electrophoresis	20 molecules of circularized circles	-
Amplification of target-specific, ligation-dependent circular probe[35]	David Yong Zhang *et al.*	1998	T4 DNA ligase + exonucleolysis	Phi29 polymerase	Exonucleolysis and gel electrophoresis	-	bead-based protocol
High-throughput genotyping of single nucleotide polymorphisms with rolling circle amplification[14]	Fawad A Faruqi *et al.*	2001	Ampligase	Bst DNA polymerase	Amplifluor Fluorescence	50ng of AluI digested genome. Single molecule from purified circle	-
Detection of rare DNA targets by isothermal ramification amplification[17]	David Y. Zhang *et al.*	2001	Taq DNA ligase	exo- Bst DNA polymerase	Exonucleolysis and gel electrophoresis	100 Raji cells / 10 circularized molecules	bead-based protocol
High accuracy genotyping directly from genomic DNA using a rolling circle amplification based assay[37]	Osama A Alsmadi *et al.*	2003	Ampligase	U DNA Polymerase	Amplifuor Fluorescence	Genomic or WGA samples	Hairpin probes
Hyperbranched rolling circle amplification as a rapid and sensitive method for species identification within the Cryptococcus species complex[38]	Sirada Kaocharoen *et al.*	2008	PFU DNA ligase, then exonucleolysis	Bst DNA polymerase	SyBr Green	PCR amplified genomic DNA from bacteria culture.	-
Detection of influenza A H1N1 and H3N2 mutations conferring resistance to oseltamivir using rolling circle amplification[39]	Megan C. Steain *et al.*	2009	PFU DNA ligase, then exonucleolysis	Bst DNA polymerase	SyBr Green	10^8 initial mutated target in 10^{11} wild molecules	-
A mechanism for ramified rolling circle amplification[40]	Thomas P Beals *et al.*	2010	Circularized template	Bst DNA polymerase	SyBr Green	50 molecules per reaction	-
Sensitive and isothermal electrochemiluminescence gene-sensing of Listeria monocytogenes with hyperbranched rolling circle amplification technology[41]	Yi Long *et al.*	2011	Taq DNA ligase + inactivation + exonucleolysis	Bst DNA polymerase	ECL detection	1fM of gene concentration	-
Establishment of a sensitive and specific Hyperbranched rolling circle amplification assay and test strip for TSV[42]	Yuran Zhaoa *et al.*	2014	T4 DNA ligase + inactivation	Bst DNA polymerase	Test strip	10 copies of reference material	-

Table 1. Summary of the HRCA papers, with the experimental conditions, enzymes, and sensitivity.

in patient sample[14]. HRCA has also been detected via various means, included fluorescence for precise identification of bacteria from the *Cryptococcus* species[38], electro-chemiluminescence for *Listeria* detection[41], test strip for portable monitoring of the Taura syndrome virus[42], and integrated into a droplet microfluidic platform for digital, single molecule analysis[43].

C2CA

Another refinement of RCA is called C2CA, for Circle-To-Circle Amplification. Developed by Matt Nilsson's team, the principle of this exponential amplification is the following[44]:

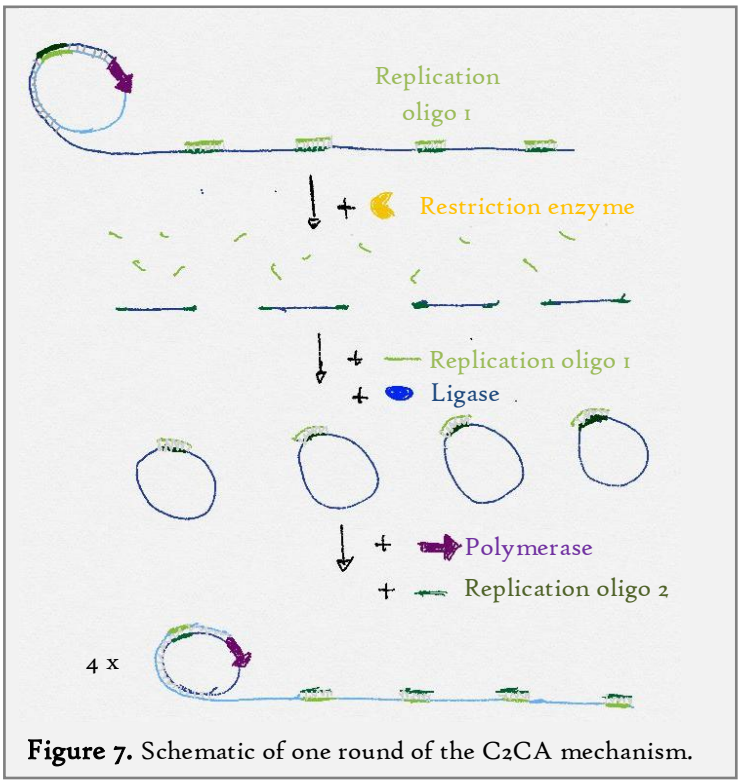

Figure 7. Schematic of one round of the C2CA mechanism.

- A first RCA is performed with padlock probes which contain one site for enzymatic restriction. After elongation, short oligonucleotides called replication oligo, complementary to the restriction sequences in the long ssDNAs are added. These short dsDNAs are then cut by restriction enzymes and cut replication oligos detach (see Figure 7).
- Resulting monomers are circularized by a ligase, with unreacted replication oligos as templates.
- A new round of RCA begins with the addition of polymerases.
- This sequence of monomerization/ligation/RCA could be repeated several times, as the reaction is not product inhibited.

C2CA presents many advantages. The limit of detection is around 200 molecules for bulk fluorescence detection, and decreases to 10 molecules in 5µl for 3 rounds of reaction with a discrete DNA coil counting, which also have a dynamic range going up to 10^8 molecules[45]. The linear amplification of each individual generation allows a better control than an exponential amplification. Contrary to HRCA, multiplexing is possible because the robust conditions don't favour one target and the initial proportion of different targets is conserved at the end of the amplification. In spite of the high number of steps, the C2CA has been successfully integrated in a droplet microfluidic platform, using electrowetting and magnetic purification with beads to perform all the sequential reactions[46].

PG-RCA

A last refinement of RCA presented here is the PG-RCA, or Primer generation-RCA, developed by T.Murakami, J. Sumaoka and M. Komiyama[47]. In this alternative method, circular probes are used directly without any ligation step. Hybridization of the target sequences with the circular probes starts the RCA (see Figure 8). Supplementary circles are also complementary with the ssDNA RCA products. One restriction sequence is located at the duplex DNA formed, allowing a nicking enzyme to cut the long ssDNA products. These segments could initiate new RCAs with the circular probes. These cascade reactions create an exponential accumulation of monomer-circle duplexes. End-point products analysis on a gel electrophoresis gives a ladder pattern. Each product has a size which is a multiple of the circle size, with a maximum around 4 times the circle size. The reaction is one-step and the sensitivity is close to 50 molecules in the best conditions and with genomic samples. Surprisingly, the lack of a ligation step doesn't affect strongly the specificity of the method. Detection of mRNA was performed with a 3 way junction initiation, in order to increase the specificity of the system[48]. Ligation initiation has also been used for SNP discrimination, followed by a detection of the PG-RCA products by a quantum dot-based FRET strategy[49].

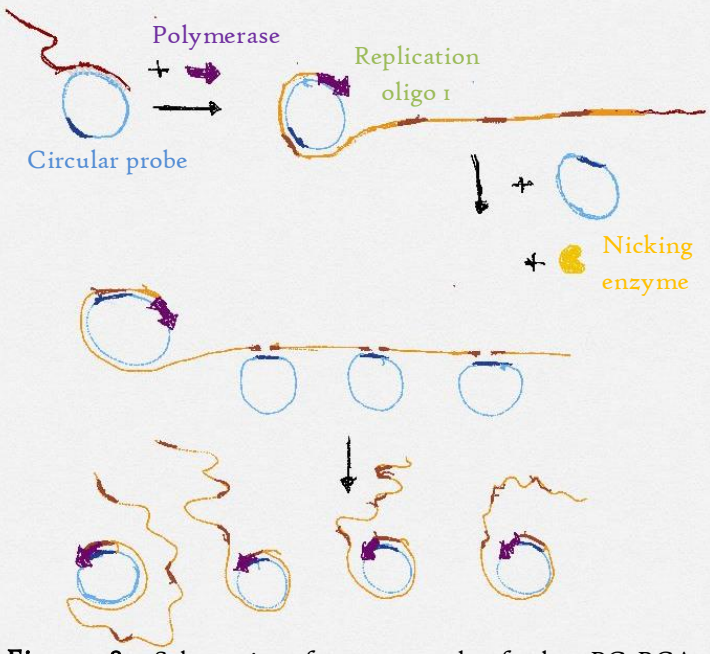

Figure 8. Schematic of one round of the PG-RCA mechanism.

For more information about RCA, and the possible detection strategy built on this technique, a good review of advanced techniques has been published in 2014[50].

2 Hyperbranched Rolling-Circle Amplification

Our first strategy used the RCA for an elongation of the DNA target, followed by an amplification of this elongated products via the Hyperbranched ramification. Our first protocol was based on a short collaboration with Ismail Cissé and Ulrich Bockelmann from the Nanobiophysics Lab of the ESPCI Paris, that we extensively optimized by ourselves during this PhD. Why did we choose HRCA over C2CA or PG-RCA? First, C2CA protocol is too complex regarding our constraints. The multiple ligation, amplification and restriction steps can't be process without adding new reagents in the solution. The use of magnetic purification is also too complicated to be integrated easily without building a dedicated microfluidic system[51]. Concerning PG-RCA, the technique seems to produce mainly products around 500bp: new ssDNA products are immediately cut into smaller fragments.

2.1 First elongation experiments

For our first experiments, we focused on the feasibility of a biomarker elongation via RCA and HRCA, starting with a high concentration of DNA target, coupled with the conductometric detection via electrohydrodynamic aggregation of the elongated products. Would the elongated product of RCA be long enough to be aggregated? Are the RCA buffers too conductive for our applications? Would it be possible to merge the ligation and amplification steps into one, or to perform these two reactions in the same buffer?

2.1.1 HRCA protocols

Different protocols have been used during my PhD project, with several optimizations and evolutions. The original protocol came from Ismail Cissé, and several improvements have been made during a one-week visiting with David Herthnek in the SciLifeLab (Uppsala/Stockholm University). A general protocol was established, from which actual protocols are derived with difference in the buffer composition, target, padlock probe and primer concentrations, duration of the different steps and introduction time of reagents.

- <u>One step-protocol:</u>

  The HRCA mix is composed of:

  - A commercial buffer, chosen among Long-Range buffer 10X (Qiagen), T4 ligase buffer 5X (Thermofisher), Phi29 polymerase buffer 10X (NEB) or Cutsmart buffer 10X (NEB), diluted at a final concentration of 0.75X or 1X.
  - dNTP mix containing dATP, dGTP, dCTP and dTTP, diluted at a final concentration of 1mM each.
  - Bovine Serum Albumin (BSA) diluted at a final concentration between 0.1 and 1.5mg/ml. BSA concentration change didn't affect the reaction.
  - rATP at a final concentration of 1mM, except for the T4 ligase buffer.
  - Padlock probes. Synthetic oligonucleotides (IDT) are listed on the Table 2. Final concentration varied along experiments. Three different target/padlock probe combinations (called "system") were used during this PhD.

- Targets. Synthetic oligonucleotides (IDT) are listed on the Table 2. Final concentration varied along experiments.
- Primers. Two types of primers were used. Exoresistant random hexamers were purchased from Thermoscientific and diluted at a final concentration of 10µM or 2.5µM. Specific primers (IDT) are listed on the Table 2 and were used diluted at 5µM or 1µM each.
- Phi29 polymerase (NEB), at final concentration of 500U/ml.
- T4 ligase (NEB), at 25U/ml.
- Pure water, sterilized to complete the solution.

Different temperatures and durations of the single-step reaction were used. One-step protocols are not common in the literature. Indeed, the presence of the polymerase and primers could strongly inhibit the ligation, as the padlock probes could be transformed into dsDNA by elongation of a primer hybridized with the probe, impeding its circularization by the ligase.

- Two step protocol:

The previous protocol was transformed into a two-step protocol with the following modifications:

- Primers and polymerase were added after a first incubation called "ligation step". The ligation step was 30min long at 37°C.
- Heating step at 65°C during 10min was sometimes added after the ligation step in order to inactivate the T4 ligase.
- The "amplification" step duration varied along the experiments, for a temperature between 30°C and 37°C.
- Final heating step at 65°C during 2min was sometimes added at the end in order to inactivate the polymerase.

dNTPs are the nucleotide bricks for the DNA polymerization. BSA has two different uses: this molecule, inert, could stabilize enzymes as restriction enzymes or ligase. It also avoids the adsorption of molecules in the tube or microsystem walls by saturating the surfaces. 3 different systems have been designed. The first one, called "tWt" system, came from two Nilsson's paper[19,34]. The corresponding probe is directed against mitochondrial genes, but the biological target didn't really matter, as this system was involved mainly in optimization experiments. The "qHRCA" system is a completely synthetic system, designed to avoid dimerization and non-specific interactions. The "S.A." probe is directed against a *Staphylococcus aureus* gene coding for the NO.-inducible L-lactate dehydrogenase (ldh1). The corresponding target came from a study for the development of a strand-displacement amplification-based assay for the detection of MRSA[52]. For most of the experiments, SyBr Green I was added before introduction into the microfluidic system at a final concentration of 0.5X, in order to be able to visualize aggregates by fluorescence microscopy.

Name	Function	Size	Sequence
System "tWt"			
tWt	Target	30nt	5'-GTTTGTTAAGATGGCAGAGCCCGGTAATCG
ppWt	Padlock probe	90nt	5'-Phos-CTGCCATCTTAACAAACCCTTTCCTCTATGATTACTGACCTACG ACCTCAATGCTGCTGCTGTACTACTCTTCTATGCGATTACCGGGCT
Primer 1	Primer	20nt	5'-CCTCTATGATTACTGACC*T*A
Primer 2	Primer	17nt	5'-AGAGTAGTACAGCAG*C*A
System "qHRCA"			
HRCA target	Target	30nt	5'-TTTGGGAAACGCTTAGGAACCGGAATTAAG
HRCA circle	Padlock probe	90nt	5'-Phos-TAAGCGTTTCCCAAANNNNNNNNNNNNNNNNNNNNATCGA CTGAGTGCTANNNNNNNNNNNNNNNNNNNNNNNNCTTAATTCCGG TTCC
HRCA Primer 1	Primer	15nt	5'-ATCGACTGAGTGC*T*A
HRCA Primer 2	Primer	15nt	5'-TTTGGGAAACGCT*T*A
System "S.A."			
ldh1+N 2	Target	115 nt	5'-TACTTCCTCAGCCATAACATCTCCTCGAACTTTTTCAGTGTCTAAATC AATGATGACTAATTCATCAACAATGCTTTGGTTCACTAATGAAAATGCGT AGCTTGCTGAGGAGACT
Circle S.A	Padlock probe	90nt	5'-Phos-AGTCATCATTGATTTTTTTTTTTTTTTTTTTTTTTTTTTTTT TTTTTTTTTTTTTTTTTTTTTTTTTTTTTTTTTTGTTGATGAATT
RCA S.A	Primer	12nt	5'-AAAAAAAAAA*A*A
Circle Random	Padlock probe	90nt	5'-Phos-AGTCATCATTGATTTNNNNNNNNNNNNATCGACTGAGTG CTANNNNNNNNNTAAGCGTTTCCCAAANNNNNNNNNTTGTTGATG AATT
HRCA Primer 1	Primer	15nt	5'-ATCGACTGAGTGC*T*A
HRCA Primer 2	Primer	15nt	5'-TTTGGGAAACGCT*T*A

Table 2. List of the 3 different target-probe systems used. Sequences with the same colour inside a system are complementary. Underlined sequences are identical. Phos- indicates a 5' phosphorylation. * indicates a phosphorothioate bond.

2.1.2 Buffer conductivity and compatibility

We focused first on buffers compatible with the T4 DNA ligase and the Phi29 DNA polymerase enzymes. Several tested buffers are listed on the Table 3, with their composition and conductivity. TE buffer is added as a reference for conductivity.

- Commercially provided by New England Biolabs as the optimized buffer for the Phi29 polymerase, the Phi29 buffer is too conductive for our application, with conductivity around 1120mS/m.

- Composition of the commercial buffer for T4 ligase is similar to the Phi29 buffer: Tris-HCl and $MgCl_2$ are present with the same concentration. They both share DTT that is a redox molecule which avoids the protein oxidation. ATP is an essential cofactor of the ligase, while Mg^{2+} is necessary for both Phi29 polymerase and T4 ligase. The absence of $(NH_4)_2SO_4$ should decrease only by a factor 2 the Phi29 polymerase efficiency when used on the T4 ligase buffer[6]. Nevertheless, T4 ligase buffer is less conductive than Phi29 polymerase buffer.

- The solution proposed by I.Cissé was to use directly the Long-Range PCR buffer for the RCA, because this buffer had already a low conductivity. PCR polymerases need magnesium ions, and the only cofactor which has to be supplemented is ATP.

- Cutsmart buffer is a product developed by New England Biolabs as a universal buffer for more than 200 restriction enzymes. This buffer has also the advantage to be compatible with a wide range of enzymes, including Phi29 polymerase and T4 ligase, if ATP was added to the solution. The conductivity of this buffer is also in the same range of conductivity as the Long-Range buffer, around 400mS/m, because of the substitution of small and mobile ions by the less conductive acetate molecules.

Buffer name	Supplier	Composition	Conductivity	pH
TE buffer	Home-made	10mM Tris-HCl 1mM EDTA	3.5mS/m	8
Long-Range PCR buffer	Qiagen	unknown	350mS/m	-
T4 ligase buffer	Thermofisher	50 mM Tris-HCl 10 mM $MgCl_2$ 1 mM ATP 1 mM DTT 5% (w/v) PEG-8000	500mS/m	7.6
Phi29 polymerase buffer	New England Biolabs	50mM Tris-HCl 10mM $MgCl_2$ 10mM $(NH_4)_2SO_4$ 4mM DTT	1120mS/m	7.5
Cutsmart buffer	New England Biolabs	50mM Potassium Acetate 20mM Tris-acetate 10mM Magnesium Acetate 100µg/ml BSA	400mS/m	7.9

Table 3. TE buffer and the main buffers used into this manuscript for RCA, with their composition and properties.

The different buffers were used in experiments using a large quantity of targets, in order to check their compatibility with the T4 ligase and Phi29 polymerase. For the T4 ligase buffer, Phi29 polymerase buffer and Long-Range PCR buffer, three one-step experiments in a tube were performed with these parameters: tWt system, $[target]_f$=130nM, $[probe]_f$=675nM, [exo-resistant primer]$_f$=6.25µM, 37°C during 1h. At the end of the incubation, the solutions had viscoelastic behaviours: during pipetting, a liquid bridge formed between the pipette tip and the rest of the solution (see Figure 9). This effect has already be described[53] and corresponds to the formation of a

physical DNA hydrogel, because of the entanglement of the high quantity of long RCA products. Later, the same result has been obtained multiple times for the Cutsmart buffer with two-steps RCA experiments using the S.A. system with $[target]_f$=100nM, $[probe]_f$=100nM and 1h of polymerization at 35°C.

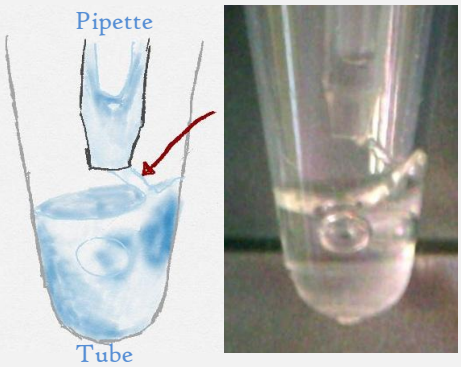

Figure 9. Picture (right) and drawing (left) of the viscoelastic bridge (red arrow) between the HRCA solution and the pipette.

As a conclusion, we can say that these four buffers are compatible with the T4 ligase and Phi29 polymerase. Long-Range PCR buffer, used at the beginning of my PhD, has been finally eliminated because its composition is a commercial secret, which limited the optimization of the buffer. Phi29 polymerase buffer is too conductive for our detection method. Fortunately, the T4 ligase buffer is similar and less conductive than the Phi29 polymerase buffer, and has proven to be a perfect candidate for an assay with a single solution for ligation, polymerization and conductometric detection. Also, T4 ligase buffer has sometimes been replaced by the Cutsmart buffer without any detrimental effect on the amplification efficiency. However, as specificity has never been precisely quantified, for example with targets presenting SNPs, T4 ligase buffer was preferred in order to keep the ligation step in the best possible conditions.

2.1.3 HRCA aggregation

The previous results, based on rheological observations, proved that elongation of small biomarkers into really long DNAs was possible in several conditions. Now, I'll present a first proof-of-concept experiment performed early during my project. The aim was to demonstrate that elongation by HRCA of a large quantity of target allowed the detection of small biomarkers with our method.

The one-step protocol used during this experiment included the Long-Range PCR buffer, exo-resistant random hexamers at a concentration of 2.5µM, the tWt system with [probe]=660nM and [target]=133nM. Incubation times at 37°C were 15, 30 and 45min. A control at 0min (no incubation) and a negative control (without target) incubated during 45min were also performed. Conductometric measurement was conducted with the protocol presented in the previous chapter and pictures of the fluorescently-labelled aggregates were taken, as shown on Figure 10.

Aggregations of HRCA products were optically visible on the pictures for incubation time of 15 and 30 minutes. For 45 minutes, amplification was so strong that a viscoelastic DNA hydrogel was created, which blocked the microchannel after injection. Aggregation was not possible with such an entangled solution. The two control experiments were negative, demonstrating that it was effectively the HRCA products that were aggregated, and that the ligation step was specific and didn't circularize padlock probes in absence of target. Concerning the conductometric detection, compared to the two controls, the measurement at 30minutes clearly proved the presence of DNA aggregates. A slight increasing of the Q-value of $Q_{sum2\text{-}5}$ was seen at 15 minutes, but repetition of the experiment would have been necessary to confirm this weak increasing. With these results, we can assess that HRCA elongation is fast (less than 30minutes) and detectable both optically and by conductometry. Nevertheless, only elongation has been tested, because of the high concentration of

initial targets. We should now reduce this target concentration in order to check the amplification efficiency of the HRCA regarding low initial concentrations of target. Unfortunately, simply dividing by 100 the target concentration completely removed DNA aggregation in our microfluidic system. To understand the cause of this failure, systematic experiments were planned and a simulation of the branching phenomenon was created.

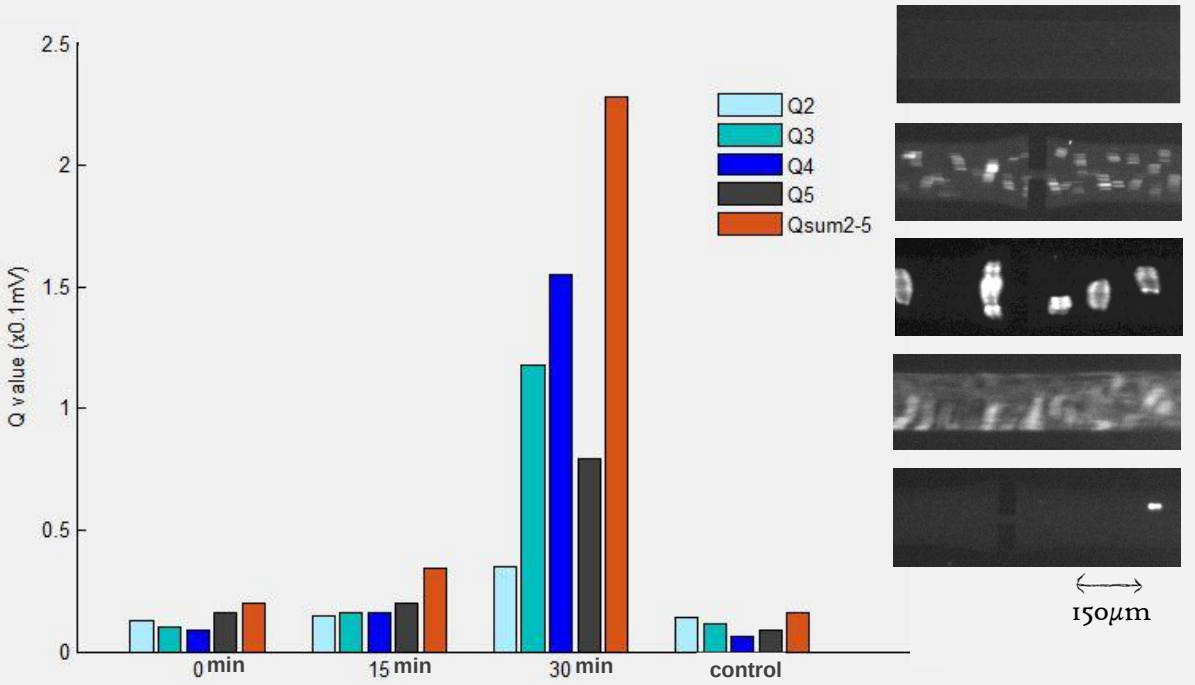

Figure 10. Left: conductometric measurement of HRCA products, versus the incubation time (0, 15, 30min). Negative control (without target) was incubated during 45min. **Right:** the images are representative pictures for 0min, 15min, 30min, 45min of incubation and the negative control (from top to bottom).

The HRCA mechanism is rather complicated and still not completely understood. In the literature, most studies were only interested in the total DNA quantity and did not care about the length distribution of the products, their state (ssDNA or dsDNA) or the physical behaviour of the produced DNA. In order to get an insight inside these characteristics, two complementary experiments were designed:

- First, real-time HRCA experiments were performed with SyBr Green I as a fluorescent reporter in a commercial qPCR device. This study brought information about the amplification kinetics and the dependency on the different components of the mix.

- A Matlab simulation of the ramification experiment was created in order to obtain data concerning the size distribution of the HRCA products.

Capillary and gel electrophoresis experiments were performed to obtain a size separation of the products, without success for products longer than 1kbp. Microscopic observations have also been performed with fluorescent oligonucleotide in order to stain specifically RCA products or HRCA branches.

2.3 Real-time HRCA

Real-time monitoring of HRCA by fluorescence has already been described in several studies[14,37–40]. Specific molecular beacons or simple DNA intercalating dyes were used, depending on the targeted specificity and multiplexing of the assay. In our case, we choose to work with a model system described in the Table 2 as the "qHRCA" system. The padlock probe, target and primer sequences were designed to minimize undesirable interactions without any biological constraints like specific recognition sequences. Only the amplification was monitored, the ligation step was performed in tube; the ligase was inactivated and uncircularized padlock probes and unreacted targets were destroyed with exonuclease I and III (final concentration 10U and 100U, respectively) during 45min at 37°C. Circles were titrated with a fluorescent Qubit analyzer (Invitrogen), and then diluted. Final mix was prepared with Sybr Green I and the Phi29 polymerase was added right before the introduction of the solution in a qPCR device (SmartCycler from Cepheid). This apparatus was previously calibrated to remove the bias between each site and a supplementary tube containing solution with SyBr Green I and Lambda-DNA was monitored during each assay to quantify the photo-bleaching contribution and to normalized all the curves, to get rid of the fluorescence variability due to the aging of the dye.

The concentrations of the mix component were varied to find the optimum HRCA mix. For other components, the normal concentrations were [SyBr Green]=0.2X, [dNTP]=1mM, [primers]=15nM, [Circle]=10pM, [Phi29 polymerase]=50mU/µl, and the incubation was at 35°C. Results are presented on the 4 panels of the Figure 11.

SyBr Green I:

SyBr green I is an intercalating dye which fluoresces preferentially when associated with dsDNA; fluorescence in presence of ssDNA decreases to 4% of the previous efficiency[54]. Sybr Green I has also been shown to inhibit amplification reaction at high concentration during PCR[55]. Optimal concentration of the dye was first searched before any other optimization. As seen on the panel a) of Figure 11, the plateau obtained at the end of the HRCA had a higher intensity when the SyBr Green concentration increased. The total fluorescence seemed to be roughly proportional to the dye concentration for the same quantity of product. The curve shape also changed depending on the SyBr Green concentration, however: for example, at 0.4X, the presence of the dye delayed the beginning of the exponential growth. The 0.1X curve reached 100 U.A. at 7min while the 0.4X curve reached this threshold around 13min. The plateau was also reached later. This delay was the proof of an inhibition of the amplification by the dye. For further experiment, a concentration of 0.2X was chosen, as the delay was negligible as compared to 0.1X while the total fluorescence was doubled.

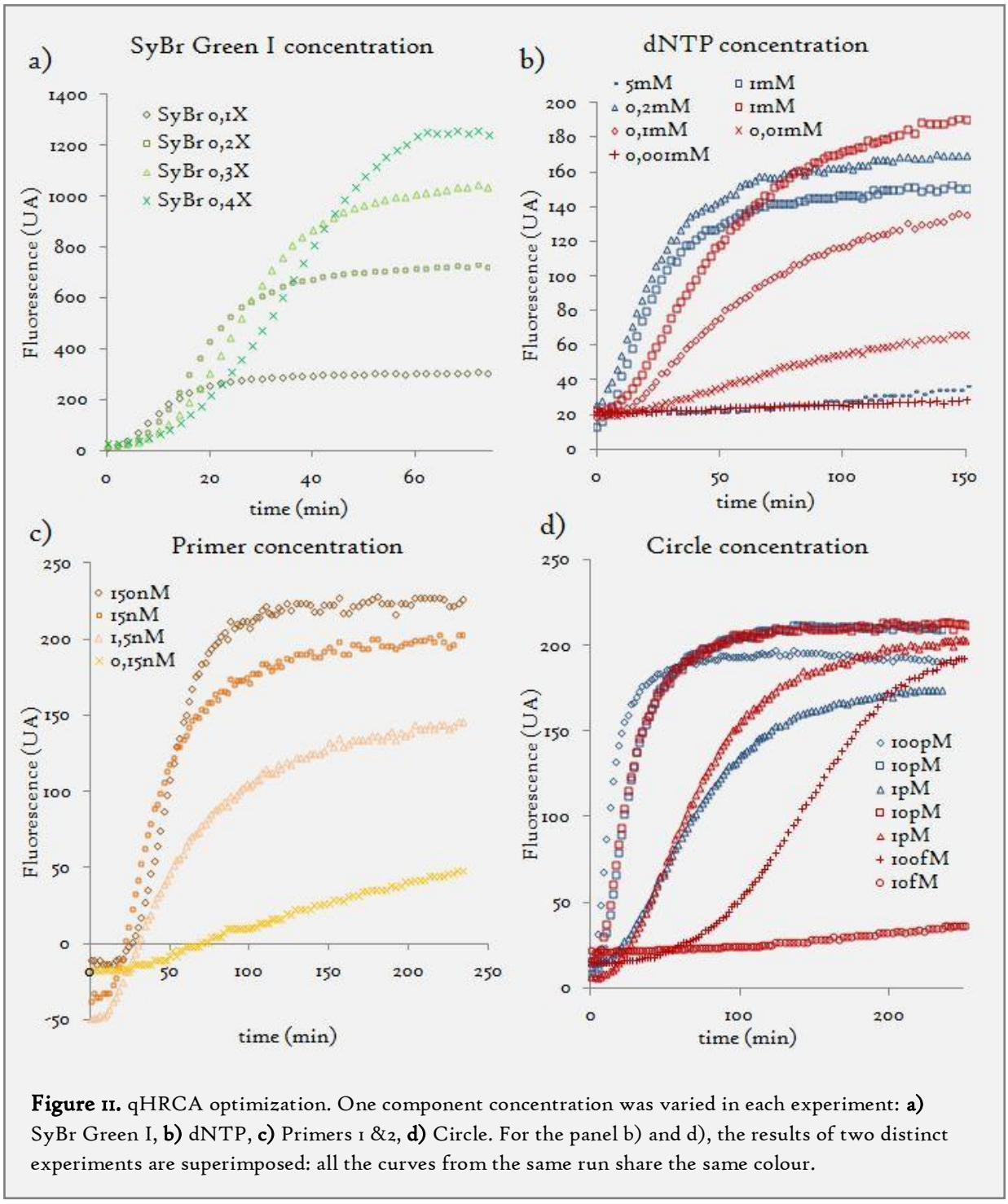

Figure 11. qHRCA optimization. One component concentration was varied in each experiment: **a)** SyBr Green I, **b)** dNTP, **c)** Primers 1 &2, **d)** Circle. For the panel b) and d), the results of two distinct experiments are superimposed: all the curves from the same run share the same colour.

dNTP concentration:

In panel b), the dNTP concentration has been decreased from 5mM to 0.01mM within two distinct experiments. The plateau intensity was minimal for 5mM, indicating that this concentration strongly inhibited the reaction, whereas the maximum was reached for 1mM and 200nM. For concentration ranging between 200nM and 1nM, the final intensity decreased as the dNTP concentration decreased. The slope of the exponential growth also decreased when the concentration decreased. Such a phenomenon could be explained by the fact that the Phi29 polymerase stops during the polymerization when the arrival of dNTP is limiting: the kinetics of the

reaction diminished. For the plateau intensity, qualitatively, the fewer the dNTPs, the fewer the products. Quantitatively, the plateau intensity is not proportional to the dNTP concentration, suggesting that dNTPs are not the limiting factor of the reaction for concentration above 0.1mM. Typical concentrations of 1mM were used for other experiments.

Primer concentration:

Primer concentrations used for normal HRCA experiments (1 or 5µM) could not be used here: because of the small fluorescence induced by ssDNA, a high primer concentration hided a large part of the exponential amplification. Here, range was set between 150pM and 150nM, to be compared with a Circle concentration of 10pM. The plateau intensity and the growth slope always decreased when the concentration decreased. For the plateau, the final quantity of products should relate to the quantity of primers. But the proportionality between the two quantities was not respected, indicating that primers are not the only limiting factor for [primer]>1.5nM, or the HRCA products quantity is not proportional to the primer quantity.

Circle concentration:

Two distinct experiments have been performed to investigate the influence of the Circle concentration, blue curves and red curves in panel d of the Figure 11, respectively. The curves for 10pM and 1pM almost overlapped, indicating that the experiments were reproducible enough to interpret the results as a single assay. Decreasing the circle concentration mostly affected the growth slope, whereas the final plateau stayed identical for all the tests. The dependence of the slope with the Circle concentration limits strongly the detection of smaller quantity of initial targets. This HRCA protocol has thus a limit of detection of 100fM (or 1 million of molecules), which is far from some literature example, going down to the single circle[14].

The kinetic behaviour is different from qPCR curves, where decreasing the target number doesn't modify the amplification kinetic, but only change the cycle threshold, *i.e.* the time at which the amplification curve crosses a threshold located at 3 times the noise level. In the literature, two behaviours were observed for qHRCA: PCR-like amplification[14,37,40] or template-number sensitive reaction[38,39]. However, in all the studies, the polymerases used were the Bst polymerase, or the Vent polymerase. Phi29 polymerase has been reported as a bad option for HRCA, on the basis that the initiation rate is too slow without the presence of the associated initiation proteins or that the Phi29 processivity is too high and could inhibit the ramification by replicating available priming sites too quickly.

However, this argument should not be sufficient to explain the disappearance of DNA aggregation for an initial concentration smaller than 100nM, whereas DNA production was observable down to 100fM. With qHRCA, no information was obtained concerning the size distribution of the HRCA products. Another explanation could be associated with the size of the produced DNAs, being too small to be subjected to the electrohydrodynamic aggregation.

2.4 Simulation

In order to better decipher the HRCA mechanism and to obtain an insight into the size distribution of the amplification products, a Matlab simulation was set up. In contrast to PCR, which has been widely studied, with a large contribution of theoreticians, a detailed theoretical model of HRCA is still lacking.

For PCR, the mechanism of the reaction has been known and the exponential growth explained since the early development of the technique, but the exact source of the plateau phase was still controversial. Deterministic models with mass law and kinetic calculation[56,57] were first set up, followed by more complex stochastic explanations[58]. HRCA has been modelled only once by Thomas Beals *et al.*[40] In this paper, a qualitative explanation of the HRCA was produced without taking into account hybridization and enzymatic kinetics. A good prediction of the distribution of the product sizes was obtained only for short incubation times before the reaction went into completion and for the eight shortest products. Because we are, in our case, interested in the product distribution at the end of the reaction, and especially in the quantity of long products, we developed a new model by incorporating enzyme and DNA kinetics. Because the new model is no longer analytically tractable, Matlab simulations have been developed.

2.4.1 Algorithm description

Only one circle was simulated during each run. Thus, all the concentrations had to be understood as concentrations per circle. The results had to be multiplied by the circle concentration, and because the model was stochastic, several simulations had to be averaged to obtain a macroscopic result. The simulation was also divided in iterations. One iteration corresponds to the time needed for the polymerization of a new padlock probe-sized monomer. During one iteration, the RCA ssDNA product was elongated, and strand-displacement separated dsDNAs. In consequence, new targets for primers were exposed. The binding probability of primers was calculated with DNA hybridization kinetics, and then the binding probability of polymerases on the new DNA-primer hybrids was also computed. Polymerase velocity was affected by the dNTP concentration. Thus, the duration of one iteration was not fixed and varied during the course of the reaction. The principle of the algorithm is detailed below, with a qualitative explanation and a technical description:

1. Initiation:

   At the beginning, initial concentration of the reactants, kinetic constants and reaction parameters like incubation time are entered (see Table 4 for usual values). For the polymerase, the conversion from Units/ml to molar concentration was obtained using the specific activity of the enzyme.

   From the incubation time, the padlock probe length and the polymerase initial velocity ($v_0 = k_{cat}$ in nucleotide per second), a number N of iterations was obtained: $N = t_{incubation} * v_0 / l_{monomer}$. A matrix with element from 1 to N in the first line was constructed and contained the future ssDNA monomers. HRCA branches partly detached by strand displacement were contained in the other lines of the matrix. Each strand was

recorded as being in the forward or reverse direction. A graphical explanation is visible on Figure 12. The state "k" of the monomer corresponded to a physical configuration:

- For "k">1, the monomer was not already produced but will be created at the iteration number "k".
- For "k"=1, the monomer was a target ssDNA and could be hybridized with a primer of the opposite strand direction.
- For "k"=-1, the monomer was a primer/target hybrid.
- For "k"=-2, a polymerase bound to the primer/target hybrid and started the polymerization from this monomer.
- For "k"=-3, the monomer has been replicated by a polymerase which initiated the reaction from another primer/target hybrid.

Parameters	Usual values	Source
[dNTP]	4mM	
[Primers]	15nM	
[Circles]	10pM	
[Phi29 polymerase]	8nM	Specific activity : 1.10^6Units/mg
Primer : k_{on}	10^5-10^7 $mol^{-1}.s^{-1}$	[59]
Primer : k_{off}	10^{-8} s^{-1}	[59]
Phi29 polymerase : k_{on2}	10^7 $mol^{-1}.s^{-1}$	Based on Klenow fragment constant[60]
Phi29 polymerase : k_{off2}	0 s^{-1}	High processivity
Phi29 polymerase : K_m	20. 10^{-6} mol	Based on Klenow fragment constant[60]
Phi29 polymerase : k_{cat}	2 - 100 s^{-1}	[6,16,60,61]

Table 4. Concentrations and kinetic constants

2. Elongation

In our model, the polymerization of the DNA is not a continuous process. Instead, at the beginning of each iteration "i", the ssDNA RCA product increases directly of one monomer length. In practice, the elements with the state "i" in the first line of the matrix are transformed in "1" to take into account the RCA product elongation.

3. Branching

If an elongated primer "-2", with a final length n, is located after a dsDNA ("-2" or "-3") under elongation, a new branch is created in the matrix, with one target ssDNA "1" (the new ssDNA displaced by the polymerase) and n-1 future monomer numbered from "i+1" to "n+i". The displaced dsDNA "-2" is transformed into a ssDNA "1".

4. Replication

dsDNA strands are elongated, so that a length of one monomer of ssDNA "1" directly located after a dsDNA ("-2" or "-3") is transformed into dsDNA "-3".

5. DNA hybridization

Hybridization of one target strand "1" with the primer of the opposite direction was governed by a kinetically limited reaction:

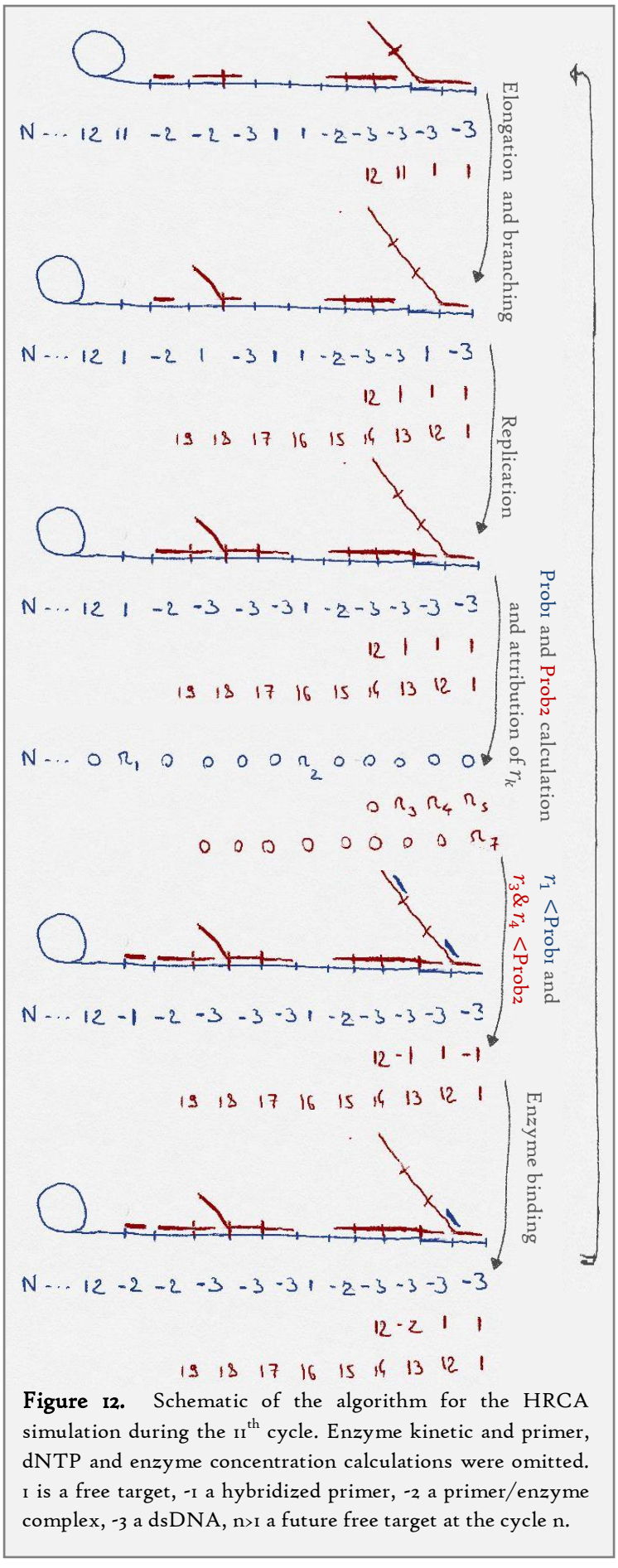

Figure 12. Schematic of the algorithm for the HRCA simulation during the 11th cycle. Enzyme kinetic and primer, dNTP and enzyme concentration calculations were omitted. 1 is a free target, -1 a hybridized primer, -2 a primer/enzyme complex, -3 a dsDNA, n>1 a future free target at the cycle n.

$$T_j + P_j \underset{k_{off}}{\overset{k_{on}}{\rightleftarrows}} H_j$$

Where T is the target ssDNA with the direction "j", P the primer of the opposite direction, H the target/hybrid and k_{on}, k_{off} the binding and the dissociation constants. Law of mass action gave the evolution of the target/primer hybrid in function of time and target and primer concentrations:

$$\frac{\partial[H_j]}{\partial t} = k_{on}[P_j][T_j] - k_{off}[H_j]$$

This equation was numerically solved, and the value of $[H_j]$ was recovered at the time t_{cycle} calculated as the time needed for the polymerase to replicate one monomer. k_{on} and k_{off} were obtained from the literature[59]. Because the obtained concentration was most of the time smaller than the number of free target, a probability of binding was calculated as $Prob_j = [H_j]/[T_j]$. Then, random numbers r were allocated to each targets and a primer would effectively bind the target if $r < Prob_j$, and the state of the monomer was changed from "1" to "-1".

6. Polymerase binding

After primer hybridization, the probability of a polymerase association with the target/primer hybrid was calculated:

$$H + E \underset{k_{off2}}{\overset{k_{on2}}{\rightleftarrows}} EH$$

Where H is the target/hybrid for the forward and reverse direction, E the polymerase, EH the enzyme/DNA

complex and k_{on2}, k_{off2} the binding and the dissociation constants. The same numerical calculation was performed. However, no exact value for k_{on2} and k_{off2} were found in the literature. The only values available were those for the Klenow Fragment Polymerase, determined from a kinetic study using quartz microbalance[60]. The obtained values were $k_{on2} = 10^5 mol^{-1}.s^{-1}$ and $k_{off2} = 10^{-3}s^{-1}$. However, the Klenow Fragment and the Phi29 polymerase don't share the same mechanism for polymerization. The Phi29 polymerase is highly processive and is able to produce >4kbp fragments without detaching[61], whereas the Klenow fragment polymerase has a jump-like processivity, with frequent detachment and rebinding of the same enzyme. To take into account the Phi29 processivity, we made the assumptions that $k_{off2} = 0s^{-1}$ and k_{on2} could be higher than the Klenow's value. After getting $[EH]$, the probability of binding was calculated as $Prob2 = [EH]/[H]$. Then, random numbers r were allocated to each target/primer hybrid and an enzyme would effectively bind the DNA complex if $r < Prob2$, and the state of the monomer was changed from "-1" to "-2".

7. dNTP, primers and enzymes consumption

Only primers complexed with an enzyme were counted as used, and subtracted from the total number of primers. dNTPs used during the elongation step were also subtracted from the total number of dNTPs. For the polymerase, the counting of the number of active enzymes was more complicated, because a polymerase can stay attached to a substrate for the polymerization of one to several tens of monomers. We made the assumptions that an enzyme was, in average, used for the creation of short fragments smaller than 4 monomers. In consequence, the total number of free enzymes in solution is the total number of molecules minus the bound enzymes during the 4 last iterations.

8. Polymerase velocity calculation

The Phi29 polymerase velocity is a function of the dNTP concentration. Indeed, when dNTPs are the limiting reactant, incorporation of the nucleotides during polymerization is slowed down. The enzyme doesn't detach from the substrate but its velocity decreases[61]. The enzyme behaviour is often modelled with a Michaelis-Menten kinetics:

$$EH + dNTP \underset{\leftarrow}{\overset{K_m}{\rightarrow}} EH/dNTP \xrightarrow{k_{cat}} dsDNA/E$$

$$v = \frac{k_{cat}.[E].[dNTP]}{K_m + [dNTP]}$$

Where K_m is the dissociation constant of the nucleotide/enzyme-ssDNA complex, k_{cat} is the catalytic elongation rate constant, $EH/dNTP$ the nucleotide/enzyme-ssDNA complex and $dsDNA/E$ the dsDNA-enzyme complex. k_{cat} value varied from 2 nucleotides per second to 100 nucleotides per second in the literature[6,16,60,61]. $K_m = 20.10^{-6} mol$ came from the Klenow Fragment constant. Depending on the enzyme and dNTP concentration, the next iteration could have a different duration $t_{cycle} = l_{monomer}/v$.

The algorithm then loops back to step 2, until the completion of the Nth iteration or decrease of the concentration of dNTP to 0.

2.4.2 Results

Most of the kinetic constants were found in the literature or extrapolated from data concerning other polymerase, but some of them could vary from several order of magnitude, as k_{on}, k_{on2} and k_{cat} (or v_0). As a consequence, it was necessary to compare the results obtained with the simulation with the previous qHRCA curves in order to obtain realistic values for the unknown parameters. However, because the experimental data presented template-number sensitive kinetics, which was the symptom of an imperfect amplification, perhaps because of the use of the Phi29 polymerase, a perfect fit between the simulation and this data set can't be obtained. The Figure 13 presents the main outputs of the simulation. On panel a), qHRCA curves were compared with the simulated fluorescence signal from 5 repetitions of the simulation, for the best fitting parameters $k_{on} = 10^5 mol^{-1}.s^{-1}$, $k_{on2} = 10^7 mol^{-1}.s^{-1}$ and $k_{cat} = 30 s^{-1}$. This fluorescence signal corresponded to the amount of dsDNA plus 4% of the amount of ssDNA, to take into account the low fluorescence of SyBr Green hybridized with dsDNA, and normalized with the experiment data. On panel b), evolutions of various variables were plotted, like the normalized dNTP, primers and enzyme concentrations and the binding probabilities for primers or enzymes. The fluorescent signals for different circle concentrations were plotted on panel c). Panel d) show the distribution of size for the HRCA products (dsDNA, ssDNA and partly dsDNA), averaged over 5 simulations.

During the search for optimal parameters, we observed that the simulation was robust when subjected to small changes in circle, primer, enzyme and dNTP concentrations. However, binding probabilities and reaction kinetics changed drastically with a slight modification of k_{on} and k_{cat} and larger variation of k_{on2}. As seen on the panel a), the best trial still did not overlap with experimental data. Slope of the exponential growth increased when the probability of primer binding and the velocity of the polymerase increased and could be finely tuned while staying in experimental values for these two parameters. The temporal offset of the curve was directed by the polymerase binding constant; however, the obtained constant for a complete fitting was over the range of realistic values (more than 1000x the experimental Klenow value). In the literature, Phi29 was reported as a non-optimal polymerase for HRCA, we thus decided to avoid a time-intensive comprehension of Phi29 polymerase limitations and to delay this final optimization to a future work with the usually used Bst polymerase. Nevertheless, the obtained kinetics was qualitatively in agreement with the kinetics observed in the literature, and we could thus exploit the simulation results, keeping in mind that our main focus is to have access to a reasonable understanding of the size distribution of the produced fragments, and not a full understanding of the underlying biochemical kinetics.

Panel b) presents the evolution of primers, enzyme and dNTP concentrations. dNTP was not the limiting factor of the reaction, in contrast to primers 1 and 2, which were simultaneously consumed after 1 hour of reaction. Enzyme concentration decreased first, but since the enzyme was continuously released and reused, its quantity stabilized around 25% of the initial value. Hybridization probabilities were low for the primer binding (under 1%), indicating that priming could be the limiting step, to be compared with the enzyme binding probability which decreased from 20 to 5% as the simulation run. Because dNTP concentration stayed high, the polymerase velocity didn't change during the reaction. Despite the stochastic model, the reproducibility of the simulation was good, because the curves overlapped for 5 repetitions of the simulation.

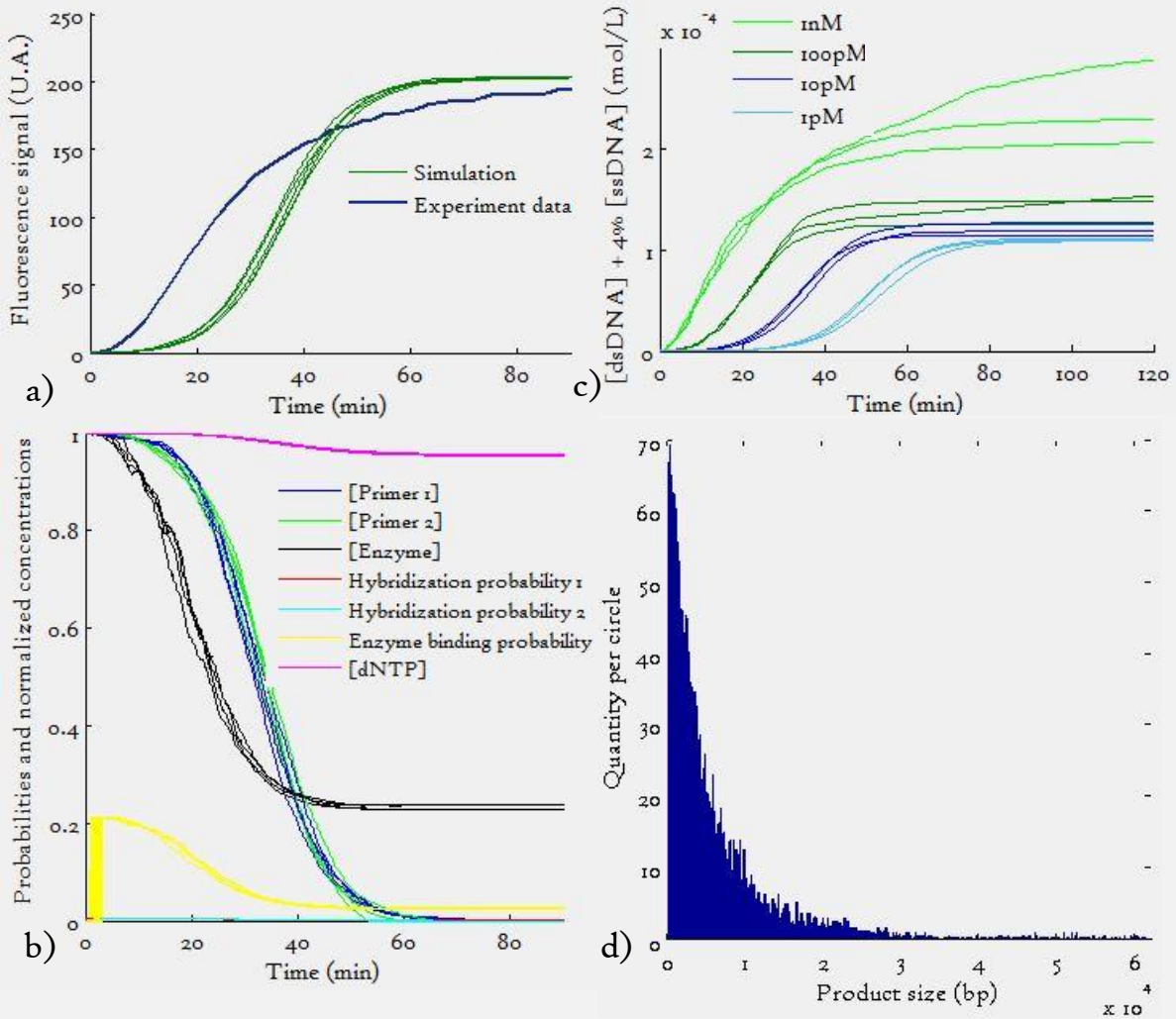

Figure 13. Results from the simulation. **a)** Comparison of the experimental data from the qHRCA experiments and 5 repetition of the simulation with the best parameters to fit the data for [Circle]=10pM. **b)** Evolution of the normalized concentrations of primers, dNTP and enzyme, and binding probabilities during simulation for [Circle]=10pM. **c)** Simulated fluorescent curves for different circle concentrations. **d)** Size distribution of the HRCA products, averaged on 5 simulations.

Varying the circle concentration changed the response time of the curve (panel c), which could be defined as the real-time equivalent of the PCR cycle threshold, *i.e.* the time when the curve reached three times the background level. The dependence of this response time against the circle concentration is given on Figure 14. The simulation suggested that the response time could be used for quantification of the initial circle concentration. This result was contradicted by our experimental results (strong non-linear dependence) but in agreement with some previous publications[14,40]. The growth slope also changed with the circle concentration in our simulations, and this variation was compared to the experimental one in Figure 15. Indeed, the slope variation was weaker for the simulation and non-monotonic, with no more than 20% of decrease. For the experimental data, a monotonic decreasing of the growth slope is observed.

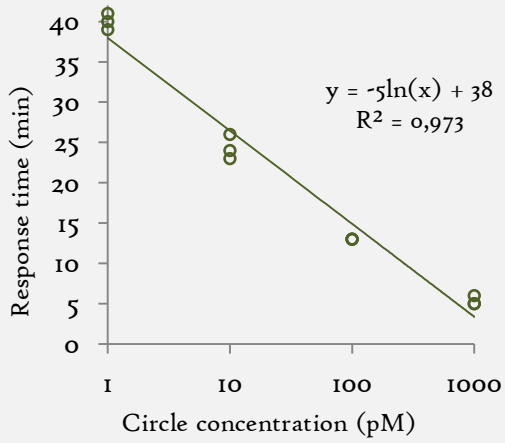

Figure 14. Response time versus circle concentration for simulated HRCA curves.

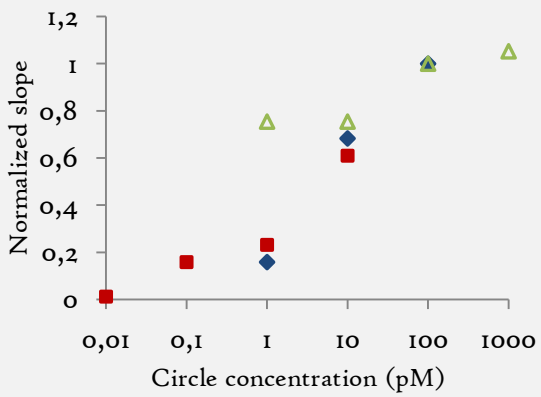

Figure 15. Growth slope dependance on circle concentration, for the two qHRCA experiments of panel d) of Figure 13 (red and blue) and the corresponding simulation (green).

Finally, the main information given by this simulation was the distribution of the product size at the end of the reaction. On panel d) of Figure 13, the average size distribution for [Circle]=10pM over 5 repetitions is represented. A large distribution was obtained, with a maximum for the smaller products (90bp) around 70 short DNA per circle, and a small quantity of long products, until 60kbp. Because the electrohydrodynamic aggregation occurs for products roughly longer than 5kbp, we counted only the products longer than this threshold for future quantification. The dependences of the number of long products with the different kinetic constants are plotted in Figure 16. The primer hybridization constant k_{on} had a big influence on these number (panel a). When the constant is decreased, the priming probability decreases strongly too: a larger number of primer targets are not primed. The distance between two primed sites increases: branches are consequently longer. The enzyme binding constant k_{on2} has a smaller influence on the number of large products, mainly because enzyme binding is not the limiting step of the reaction (panel b). However, the number of large product is proportional to polymerase velocity: when the polymerase works faster, a primer target is available for priming during a smaller duration, because it can be replicated by an incoming polymerase quicker. As these targets are less primed, the size of large product increases. This information could be interesting in the case of the development of an optimal HRCA protocol for our application: the choice of the polymerase is important, and the processivity of the enzyme has a big influence on the final size of products.

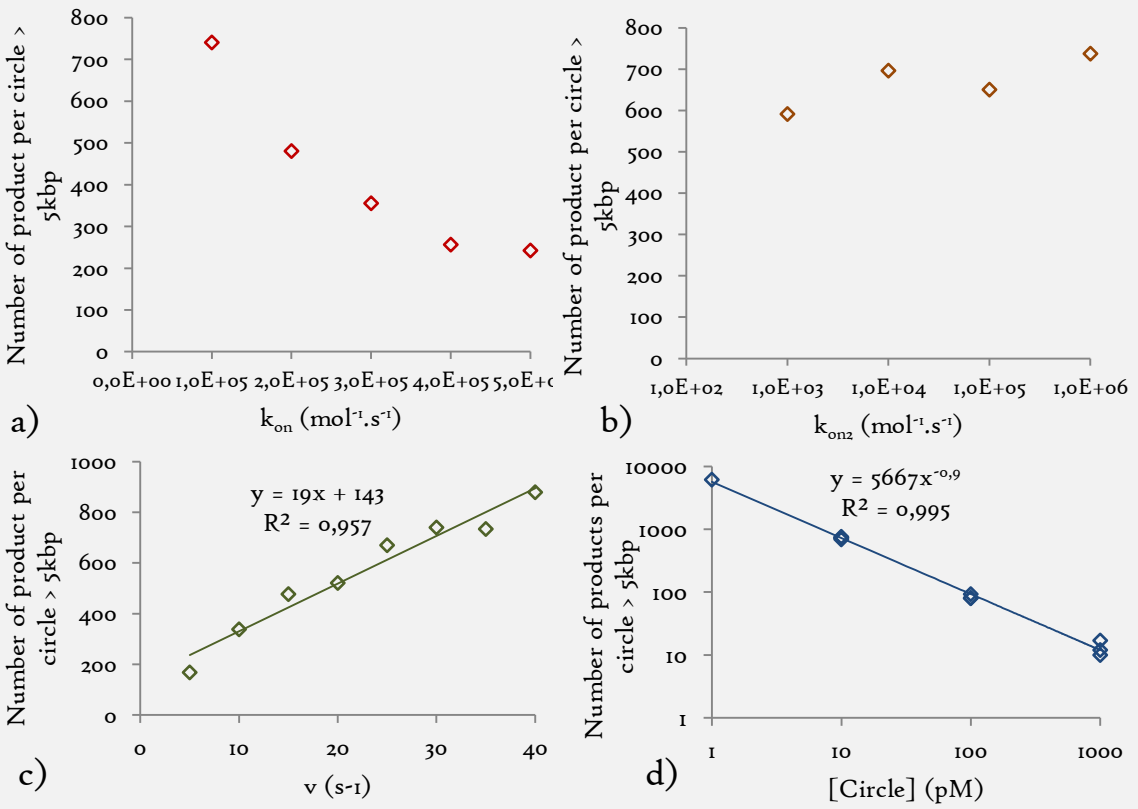

Figure 16. Number of product longer than 5kbp, in function of: **a)** k_{on}, **b)** k_{on2}, **c)** v, **d)** the Circle concentration.

Finally, the dependence of size distribution on the circle concentration is presented on panel d). The number of long product was inversely proportional to the circle quantity: when the circle concentration was divided by a factor 10, the number of product longer than 5kbp per circle increased by a factor 10. This result indicates that, independently of the initial concentration of target, the final concentration of long products would stay the same for all reactions. With the parameters of this simulation, the final concentration of long products was around 10nM, which was close to the 15nM limit of detection of our DNA detection device. This quantity was limited by the primer quantity, which was low during the qHRCA experiments and this simulation. Increasing the primer quantity could increase the final quantity of long products, improving the device LOD. Nevertheless, primer concentration was already high during the HRCA performed for aggregation detection. Concerning the simulation, increasing the quantity of primer (or decreasing the circle quantity) increased strongly the quantity of branches per circle, leading to longer and longer simulation time.

The addition of priming and enzymatic kinetics allowed a better fitting of real-time curves, compared to the previous published model. The simulation was able to handle an exponential amplification, which means that the matrix size and data quantity increased exponentially during the simulation. An adaption of the model to Bst polymerase should enable a real comparison with experimental data sets. Finally, a last improvement has to be implemented into the algorithm: for now, we made the assumptions that the polymerase was used during 5 cycles in average, because most of the products produced were expected to be short. Instead, each polymerase has to be

followed and put back into the pool of free enzymes only at the end of its actual replication process, which should be longer than 5 cycles. In consequence, our simulation over-evaluated the quantity of free enzymes, leading to a quicker reaction and a smaller quantity of long products. Nevertheless, independently of the first PhD objectives, this HRCA simulation gave interesting qualitative results and insights on the HRCA mechanism.

2.5 HRCA topology

HRCA products were not detected via our microfluidic device when the concentration of targets was reduced.

- A first explanation, revealed by real-time HRCA experiments, was the bad amplification efficiency of the reaction when the number of circles was decreased. The lower limit for a complete reaction was 100fM (1.8 million of DNA copies). This template-number sensitive reaction has been attributed in the literature to the use of the Phi29 polymerase, even if the same behaviour has been observed for the Bst polymerase in apparently non-optimized protocols.

- In addition, the size distribution of the HRCA products was obtained by an HRCA simulation, which gave qualitative results on the reaction performance. Production of long-products was possible and seemed to be enhanced at low circle concentration, which leaded to a constant final concentration of long DNA at the end of the reaction, independently of the initial target concentration. Quantitative results gave a final concentration close to the LOD of the microfluidic detector.

- However, this optimistic result was contradicted by the aggregation experiments. If HRCA was still efficient for concentration higher than 100fM, and the final quantity of long products constant, why didn't we detect something for [Target]=100pM? Either the long DNA quantity was finally smaller than the LOD, or a supplementary explanation was needed.

In contrast to PCR, in which the produced dsDNA are short and linear, the HRCA products are long (for the main RCA concatemer), condensed and branched. Topology has to be taken into account, especially in our case, where our objective is to obtain a uniform concentration of long DNAs. Could the long products of HRCA escape the RCA coil and go into the free solution?

During my PhD, different trials have been made in order to observe the topology of HRCA products. Direct observation by microscopy of fluorescently-labelled products has been tried, but the resolution was not good enough to obtain the topology of a single HRCA product. Observation of my HRCA products aligned on a surface by capillary assembly was performed by Aline Cerf (LAAS, Toulouse) by Atomic Force Microscopy (AFM). One example of the resulted picture is presented on Figure 17. Long bundle of fibres (more than 10µm) were visible, with bigger DNA coils located at the middle of the fibres. HRCA products seemed to aggregate into long and complicated structures. However, it was impossible to determine if these structures would be constituted by a single Hyperbranched molecule, or if several long DNA products were entangled by physical or chemical interactions via base pairing.

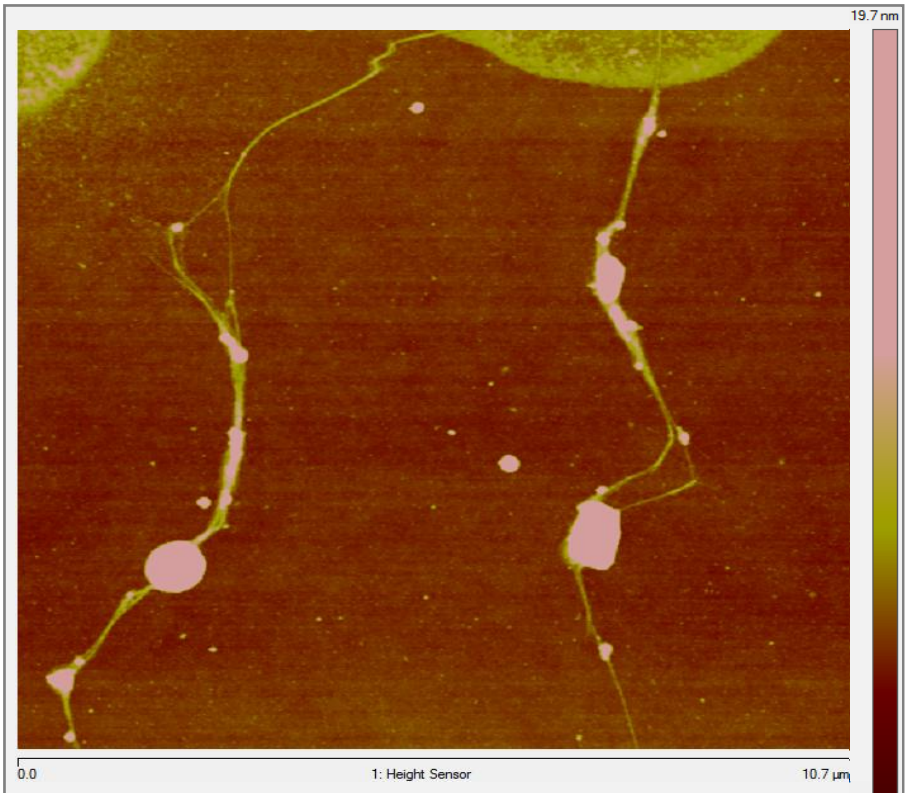

Figure 17. AFM pictures from HRCA products, aligned by capillary assembly, from Aline Cerf.

Without an efficient way to visualize the HRCA product topology, the previous question about HRCA products escaping the DNA blob could only be answered with additional physical considerations.

Let consider a long HRCA product. The longer DNA is the RCA product, mainly in the form of a dsDNA. As this product is easily longer than 10kbp, we could make the assumption that this DNA coil is similar to the DNA coil presented on the section 1.3.1 of Chapter 2, with a radius around 250nm. How long would it take for a dsDNA, longer than 5kbp, to diffuse from the core of this coil to the free solution? Diffusion of individual polymer, entangled in a polymer solution has been studied extensively, with microscopic experiments and theory like the reptation model of de Gennes[62]. This model states that a linear molecule entangled in a dense solution of polymer could only diffuse along its axis in a worm-like behaviour. On this case, the diffusion coefficient is a function of the polymer length and the polymer concentration: $D \sim L^{-2}.C^{-1.75}$. Fortunately, self-diffusion of dsDNA has been studied by fluorescence microscopy[63]. Figure 18, extracted from this paper, presents the

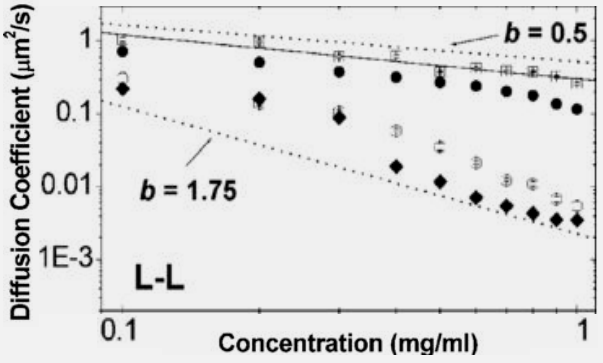

Figure 18. Diffusion coefficient for linear dsDNA against polymer concentration for four different dsDNA length: 5.9 kbp (open squares), 11.1 kbp (filled circles), 25 kbp (open hexagons), and 45 kbp (filled diamonds). From [63]

dependence of the diffusion coefficient for different length and different concentration of nucleic acids. The diffusion coefficient varies between 0.01 and 1µm²/s. We are interested in the flux J of molecules outside the DNA coil:

$J = -D\frac{\partial C}{\partial r}$. Let's take $D = 0.1\mu m^2/s$, a polymer concentration of $0.5mg/ml = 10nM$ for a 30kbp molecule and a radius $r = 250nm$.

$$J = 4.10^{-12} mol.m^{-2}.s^{-1}$$

The number of molecules going outside the coil is: $N = J.A = J.4.\pi.r^2 \sim 2\ molecules/s$.

Depending on the diffusion constant, this product escape could go from 720 to 72000 molecules per hour. But, for our system, we target a minimal concentration of 1000 DNA copies and need around 6.10^{11} final products. Even with the maximum escape rate, a successful detection couldn't be performed in less than 8000 hours of diffusion.

Only physical entanglement between linear DNA was taken into account in the previous short calculation. HRCA products are branched, leading to a decreasing of the diffusion coefficient. Freedman *et al.* studied the diffusion of star-liked DNA dendrimer of only 2kbp, which showed the same order of magnitude for the diffusion coefficient in Lambda-DNA solution[64]. In addition, chemical interactions between HRCA products could also take place into the DNA coil. Indeed, our HRCA simulation gave us another interesting result: because DNA continued to be displaced even after the consumption of all the primers, a large portion of the HRCA products are partially single-stranded at the end of the reaction. The ratio dsDNA to ssDNA was 50% in average. This partial replication exposed complementary ssDNA which could interact strongly by base pairing, limiting or inhibiting the escape of products by diffusion. This result could also explain the behaviour difference between Lambda-DNA and HRCA aggregation in our microsystem. While Lambda-DNA aggregates diffused quickly after the end of the electrical excitation, HRCA aggregates kept their shape and didn't seem to diffuse after aggregation. This stability could be explained by chemical interactions between the multiple DNA coils constituting the aggregates.

As a partial conclusion, the use of HRCA as an elongation-amplification reaction was proved to be a bad option. Even if we optimize the HRCA protocol, using Bst polymerase instead of Phi29 polymerase, the long DNAs produced by the reaction wouldn't be homogenously distributed in solution, but would preferentially stay compacted into giant DNA coils. This configuration is not favourable for our detection strategy. In order to avoid this entanglement trapping of long product, we switched to another strategy: we first amplified the short target with a first isothermal amplification, and then we elongated the highly concentrated products by a simple RCA reaction.

3 Amplification-elongation scheme

In order to amplify short DNA target into a high quantity of short ssDNA, several amplification methods exist. We immediately eliminated PCR, because we stayed focused on isothermal strategy. LAMP products were too complex for this application. Between HDA, RPA and SDA, we decided to develop a SDA protocol. The choice was mainly motivated by the higher number of protocol found in the literature and the apparent simplicity of the technique.

3.1 Strand-Displacement Amplification

Strand-Displacement Amplification has been quickly introduced in Chapter 1. During PCR, the created dsDNA are separated with a heat denaturation step. During isothermal amplification, this dsDNA denaturation has to be performed by a combination of several enzymes. In the case of the SDA, the removal of the synthesized DNA strand is due to the strand-displacement activity of the polymerase used, but the creation of a priming zone for the polymerase is necessary. This action is performed by a nicking enzyme, *i.e.* a restriction enzyme which cut only one of the two strands of its specific template. The polymerase could thus elongate the cut strand from the 3' side of the nick, and remove the ssDNA located between the nick and the 5' end of the template. This nicking/polymerizing cycle could be easily repeated and leads to linear accumulation of ssDNA (see Figure 19). To obtain an exponential amplification, primers are added into the solution. These oligonucleotides hybridize with the created ssDNA, and are elongated to create new dsDNA templates for the nicking/polymerizing cycle.

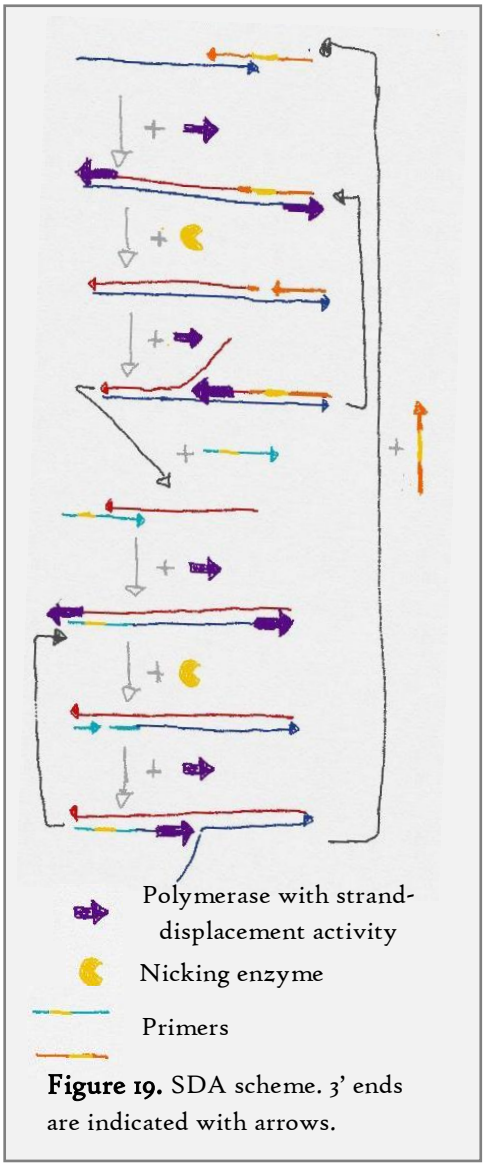

Figure 19. SDA scheme. 3' ends are indicated with arrows.

SDA was invented by G.Walker *et al.* in 1992, and was quickly used for the detection of the *M. Tuberculosis* bacteria[65,66]. Nicking was first performed with regular restriction enzymes and a template protected with hemiphosphothioated recognition site. Natural nicking enzymes were then discovered or engineered[67] and used with SDA[68]. The last innovation concerning SDA concerned the initiation step of the reaction. Most of the targets were long, genomic dsDNA. The original protocol needed a denaturation step around 95°C, plus 4 primers (the two usual plus two additional oligonucleotides called "bump primers"). The initiation step is illustrated in the Figure 20. Regular primers containing the specific sequence for the nicking enzyme in their non-template specific part were elongated after hybridization with the separated template. The bumper oligonucleotide bound the template behind the primer, and the polymerase removed the elongated primer

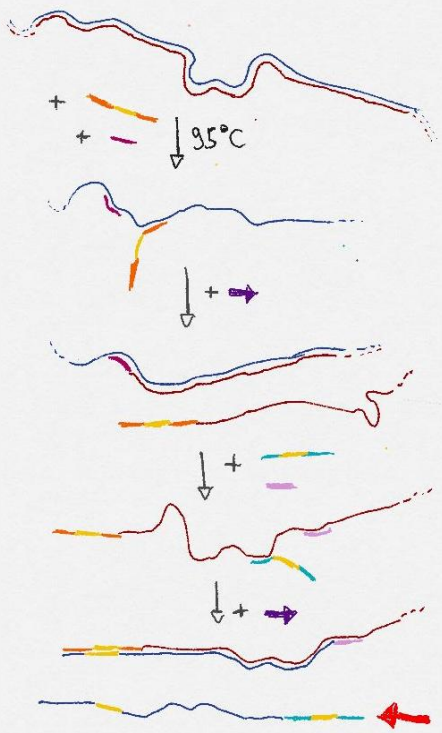

Figure 20. Initiation of the SDA. Final product is indicated by the red arrow. Bumper oligos are in purple and pink, while the primers are in orange and blue, with the restriction site in yellow.

while replicating the substrate from the bumper. The same process occurred again with this removed ssDNA as template, leading to a dsDNA flanked with nicking-specific sequences at both ends, ready for the amplification. A truly isothermal amplification has been developed, taking into profit the natural opening of genomic DNA for primer and bumper hybridization[52], without stating if this DNA breathing was enhanced by the buffer formulation or not. MicroRNA detection also allowed to remove the whole initiation step, as mRNA are well delimited, single-stranded nucleic acid[69,70].

After trying to reproduce two SDA protocols, without good results, we decided to copy the protocol and DNA template and primers proposed by B. Toley *et al*[52]. The final protocol and mix used were the following:

- The buffer was the Cutsmart buffer (NEB) at a final concentration of 1X, instead of the original buffer made with 50mM of potassium phosphate and 3.8mM of magnesium sulfate.
- dNTP mix containing dATP, dGTP, dCTP and dTTP, diluted at a final concentration of 1mM each.
- The target was a synthetic oligonucleotide (IDT) similar to one strand of the *Staphylococcus aureus*-specific gene coding for the NO.-inducible L-lactate dehydrogenase (ldh1) present in Table 5. Final concentration varied along experiments.
- Two types of primers were used. Two extension primers, for the forward and the reverse direction, were synthetized (IDT). These primers contained a complementary (respectively identical) part to the ldh1 gene, and a second part containing the nicking-specific sequence. Two bump primers, for the forward and reverse direction, were also synthesized. The final concentrations were 250nM for the extension primer 1, 500nM for the extension primer 2 and 50nM for the two bump primers. Because of the higher concentration of extension primer 2, the reaction was asymmetric and created an excess of ssDNA as compared to a symmetric reaction.
- The polymerase used was the Bst 2.0 WarmStart polymerase (NEB), at final concentration of 800U/ml. This polymerase is an engineered variant of thermostable *Bacillus stearothermophilus* polymerase, and has a strong strand-displacement activity, no exonuclease activity and is inhibited by an aptamer which is released at temperatures higher than 45°C.
- The Nt.BbvCl nicking enzyme was the altered form of the BbvCl restriction enzyme, from NEB. The final concentration was 200U/ml.
- Pure water, sterilized to complete the solution.

Temperature has been increased from 49°C to 56°C to improve the reaction yield, and reaction duration was fixed at 30 minutes in a thermocycler.

System "S.A."		
ldh1	165 nt	5'- AAAGGGAACAAAGTTGTATTAATAGGTAATGGTGCAGTAGGTTCAAGCTA CGCATTTTCATTAGTGAACCAAAGCATTGTTGATGAATTAGTCATCATTGAT TTAGACACTGAAAAAGTTCGAGGAGATGTTATGGATTTAAAACATGCCACA CCATATTCTCCAACAACAGTTCGTGTGAAAGCTGGCGAATACAGTGATTGT CATGATGCGGATCTAGTTGTCATCTGTGCTGGTGCTGCACAAAAACCTGG AGAAACACGTTTAGATTTAGTATCTAAAAACTTGAAAATATTCAAATCAATT GTTGGTGAAG
Extension Primer 1	45nt	5'-GCATAATACTACCAGTCT**CCT**CAGCAAGCTACGCATTTTCATTAG
Extension Primer 2	44nt	5'-TAGAATAGTCGCATACTT**CCT**CAGCCATAACATCTCCTCGAACT
Bump Primer 1	19nt	5'-AGGTAATGGTGCAGTAGGT
Bump Primer 2	17nt	5'- CCAGCTTTCACACGAAC

Table 5. List of the oligonucleotides used for SDA. Sequences with the same colour inside a system are complementary. Underlined sequences are identical. Nicking sequences are in purple, and the nicked bond is bolded.

The amplification products were analyzed by denaturing polyacrylamide gel electrophoresis (PAGE). This electrophoresis method allows the precise separation of nucleic acids in denaturing condition, thanks to a urea-based buffer. Because all DNAs are denatured, precise quantification of DNA size is possible, and aggregates due to hybridization are avoided. The gel electrophoresis system was from Invitrogen (Novex system) with pre-casted TBE-Urea 15% Polyacrylamide gels. 2.2µl of sample were mixed with 3.3µl of gel loading buffer II and 1.1µl of TBE. After mixing, heat denaturation during 5min at 95°C separated the dsDNA, and the hybridization was inhibited by the urea buffer. Electrophoresis was performed during 40min at 160V. Fluorescent staining of the gel was made with a 20min immersion of the gel in TBE buffer stained with 2X SyBr Gold. Imaging of the gel was done in an Amersham 600 Imager. Two pictures from gel electrophoresis were presented in Figures 21 and 22. The first figure showed the gel electrophoresis of SDA products incubated at different reaction temperature, from 40 to 60°C. Positive controls where performed with $[ldh1]_f$=1pM and the negative controls were target-free. The first well was filled with 10bp DNA ladder from Invitrogen.

The first thing visible on this gel electrophoresis picture was the presence of a huge quantity of parasite reactions. Negative and positive controls presented a large number of bands between 30nt and 200nt, whereas SDA products should be only 101nt for the ssDNA and 121nt for the denatured dsDNA. This phenomenon is a well-known drawback of SDA. Primer-dimers are responsible for part of this background, especially the bands around 47 and 57nt[52]. But the mechanism for the formation of the other bands has not been investigated, even if non-templated nucleotide addition[71] or *ex-nihilo* synthesis of nucleic acids by thermostable polymerase[72], enhanced by the presence of a nicking enzyme[73,74] were suspected. However, information could be obtained from this picture. Below 45°C, the reaction seemed to be partly inhibited because of the Warmstart characteristic of the polymerase, whose aptamer fully detaches above 45°C. As the temperature increased, a difference appeared between the positive and negative controls. SDA products bands were brighter in the positive control, along with new bands at large size (around 200nt). Background noise decreased for 60°C. With this picture, one can assess that SDA amplified the targets preferentially for high temperature. We fixed the incubation temperature at 56°C for the rest of the experiments.

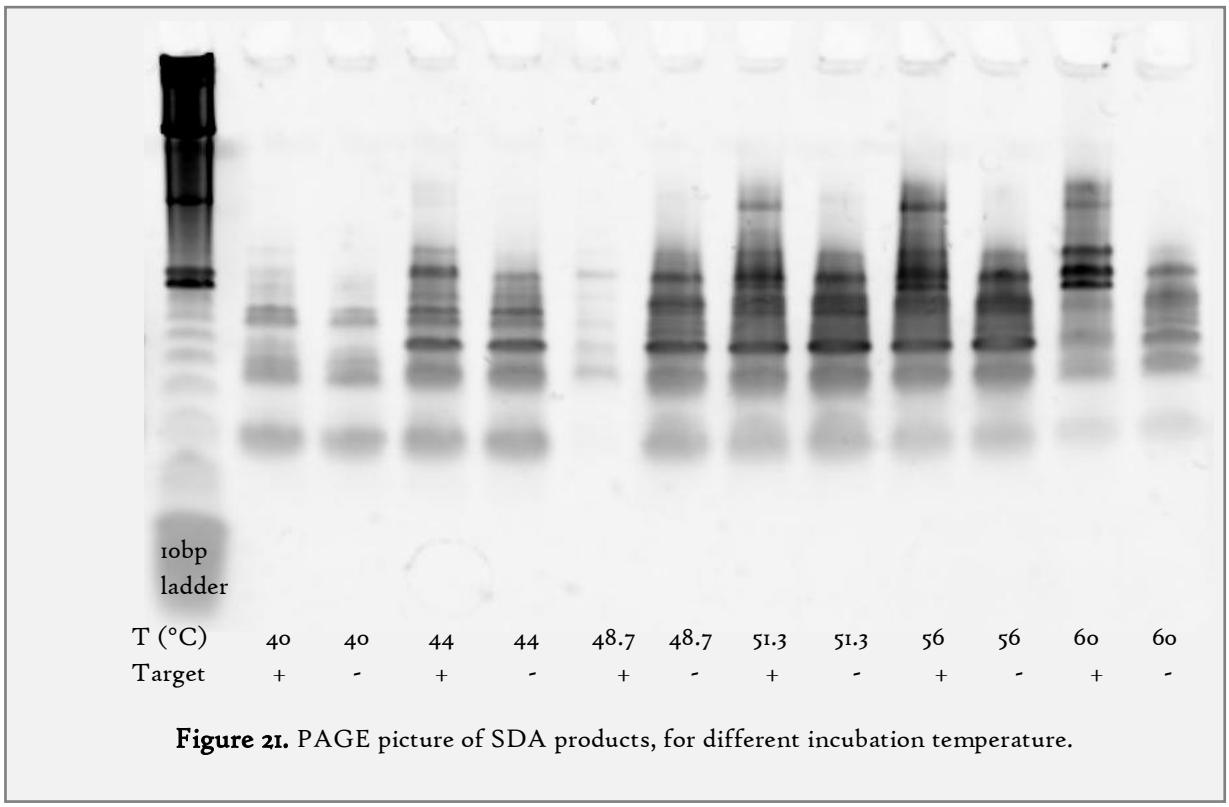

Figure 21. PAGE picture of SDA products, for different incubation temperature.

On Figure 22, different target concentrations were subjected to SDA, and imaged in a PAGE. The same background was observed, but the bands for the SDA products were well visible for [ldh1]=1pM. For the smaller concentrations, these bands disappeared in the background. PAGE was not the best way to conclude about the SDA efficiency, specificity and sensitivity, because this technique did not detect specifically the ldh1 amplicons. However, when compared to the original paper, our results are poor[52]. Indeed, PAGE was also used to detect the SDA result and an initial concentration of 10 targets could be seen. A second round of Rolling-Circle Amplification was performed on these SDA products to obtain a specific detection of the amplified target.

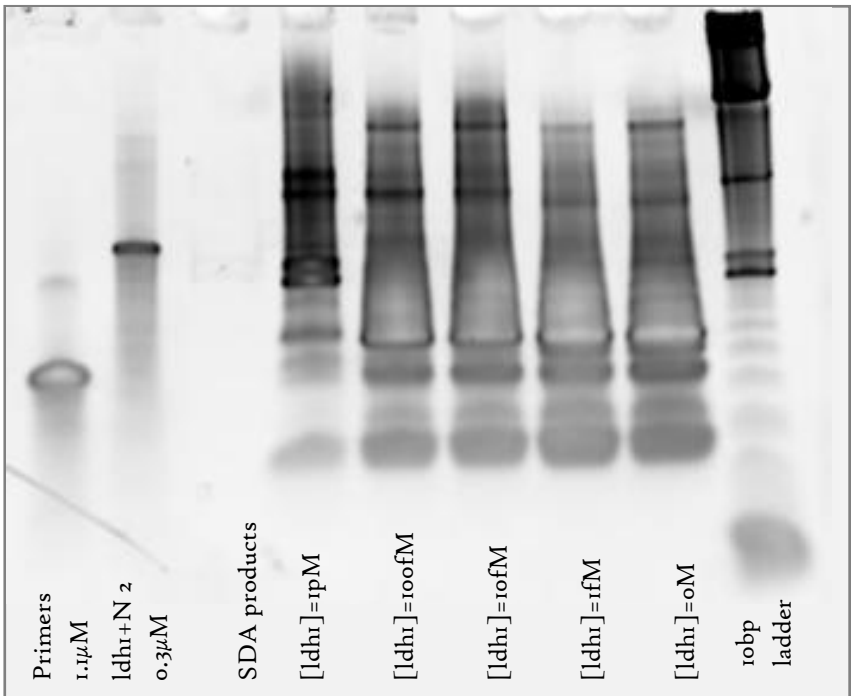

Figure 22. PAGE picture of SDA products, for different target concentration. Primers and synthetic oligo with the size of expected products were also added.

3.2 Coupling with RCA

After the expected amplification of short targets by SDA, the SDA products, mainly ssDNA, had to be elongated above 5kbp to be easily detected by our aggregation-based detection device. To do so, the easiest way was to perform a second round of Rolling-Circle Amplification. The protocol was similar to the two-step protocol for the HRCA, without primers, and with the S.A. system presented on the Table 2. "ldh1+N 2" was used as a positive control, as this synthetic oligonucleotide possessed the same sequence as the SDA products, with a central part recognized by the "Circle S.A." padlock probe. SDA samples were added at a final quantity of 25% of the mix volume. T4 ligase buffer was used for its low conductivity at a final concentration of 0,75X instead of 1X, because the SDA sample was already buffered. Finally, incubation time was arbitrary fixed at 3h.

Amplification yield were assessed at the end of the incubation directly in the microfluidic detector. In case of strong positive result, the solution presented high visco-elastic behaviour due to the entanglement of the long RCA products, and pipetting was sufficient to determine the fate of the reaction. Microscopic observations of fluorescently-stained product of the SDA-RCA reaction, for different initial target concentration, are presented on the Figure 23.

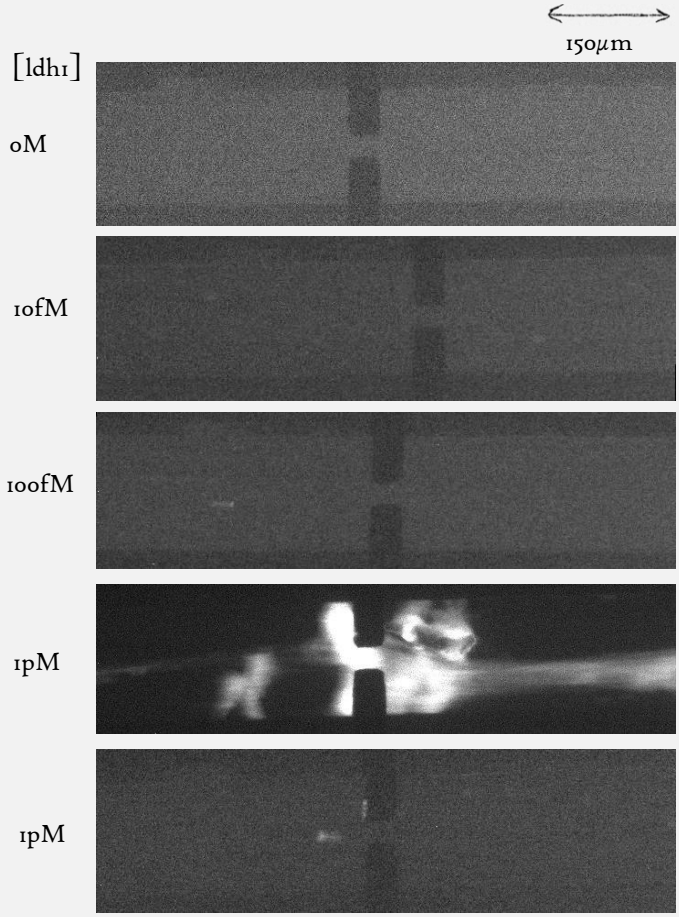

Figure 23. Pictures taken during fluorescent microscopic observation of SDA-RCA product aggregation, for different initial concentration. The two pictures at 1pM were from the same solution.

The negative control was perfect, as no aggregation or even big DNA blobs were visible. Trials with an initial concentration of 10fM and 100fM were also blank, with rare and small aggregates, undetectable by conductometry. The solution with [ldh1]=1pM was visco-elastic during pipetting. Two pictures of the same solution inside the microchannel were presented. On the top one, a visco-elastic DNA hydrogel was blocked in the channel. Aggregation occurred, but the entangled DNA could not be displaced by electrophoresis. In consequence, conductometric measurement was negative. On the bottom pictures, no DNA hydrogel was present on the channel. No aggregates appeared during excitation. Decreasing the padlock probe concentration did not solve the problem, because the DNA products, even created in a smaller quantity, were still entangled into visco-elastic hydrogel.

On one side, the SDA-RCA scheme allowed a "yes or no" detection of a successful amplification via a simple, easy and rapid pipetting for an initial target concentration of 1pM. However, conductometric detection was not possible because of the high entanglement of the RCA products. The segregation of dense DNA hydrogel on one side, and DNA free solution of the other part was surprising and a real drawback. RCA experiments with positive controls were performed with a decreased quantity of padlock probe or smaller incubation times, without leading to the apparition of detectable aggregates. Segregation was maintained, and the only apparent modification of the results was a decrease in the quantity of dense DNA hydrogel when incubation time of padlock probe concentration was decreased. This behaviour was really different from what we observed with HRCA products (see Figure 10). Perhaps the RCA products, more flexible and chemically sticky, are more efficient to produce highly entangled DNA-hydrogel than dsDNA products of HRCA. In addition, thymine skeleton of the padlock probe was first designed to eliminate the branching of the RCA product by the unreacted probes. The presence of a poly-thymine sequence was chosen to avoid the hybridization of the 3' end of the probe and the elongation of the probe. However, the presence of an excess of uncircularized padlock probes could explained the quick formation of dense DNA hydrogel by reticulating RCA products which had mainly poly-A sequences (see Figure 24).

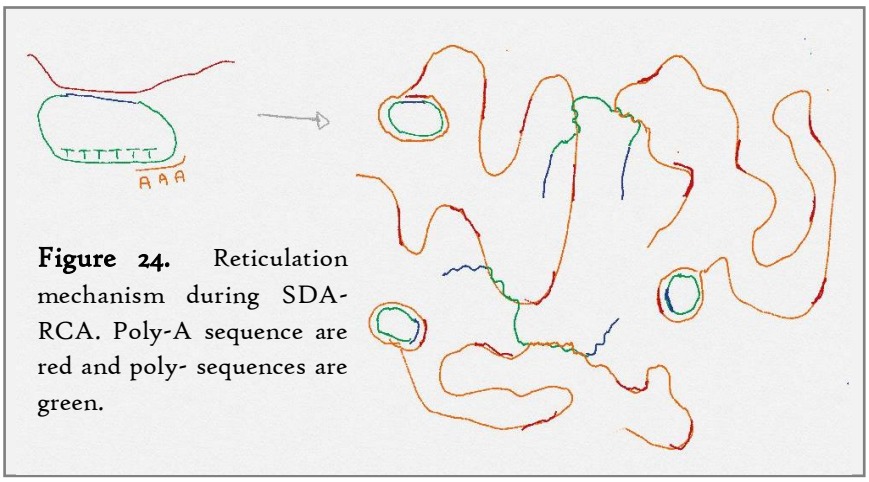

Figure 24. Reticulation mechanism during SDA-RCA. Poly-A sequence are red and poly- sequences are green.

In order to obtain detectable aggregate with the conductometric detection, a new padlock probe called "Circle Random" was redesigned with a random skeleton in order to limit interactions between products from two different circularized padlock probes. Primers from the "qHRCA" system were used to perform an HRCA instead the simple RCA step. These two modifications eliminated the formation of visco-elastic hydrogel and allowed the aggregation of the SDA-HRCA products into detectable objects (see Figure 25). Detailed protocol with final concentration of the different reactants is shown on the Appendix.

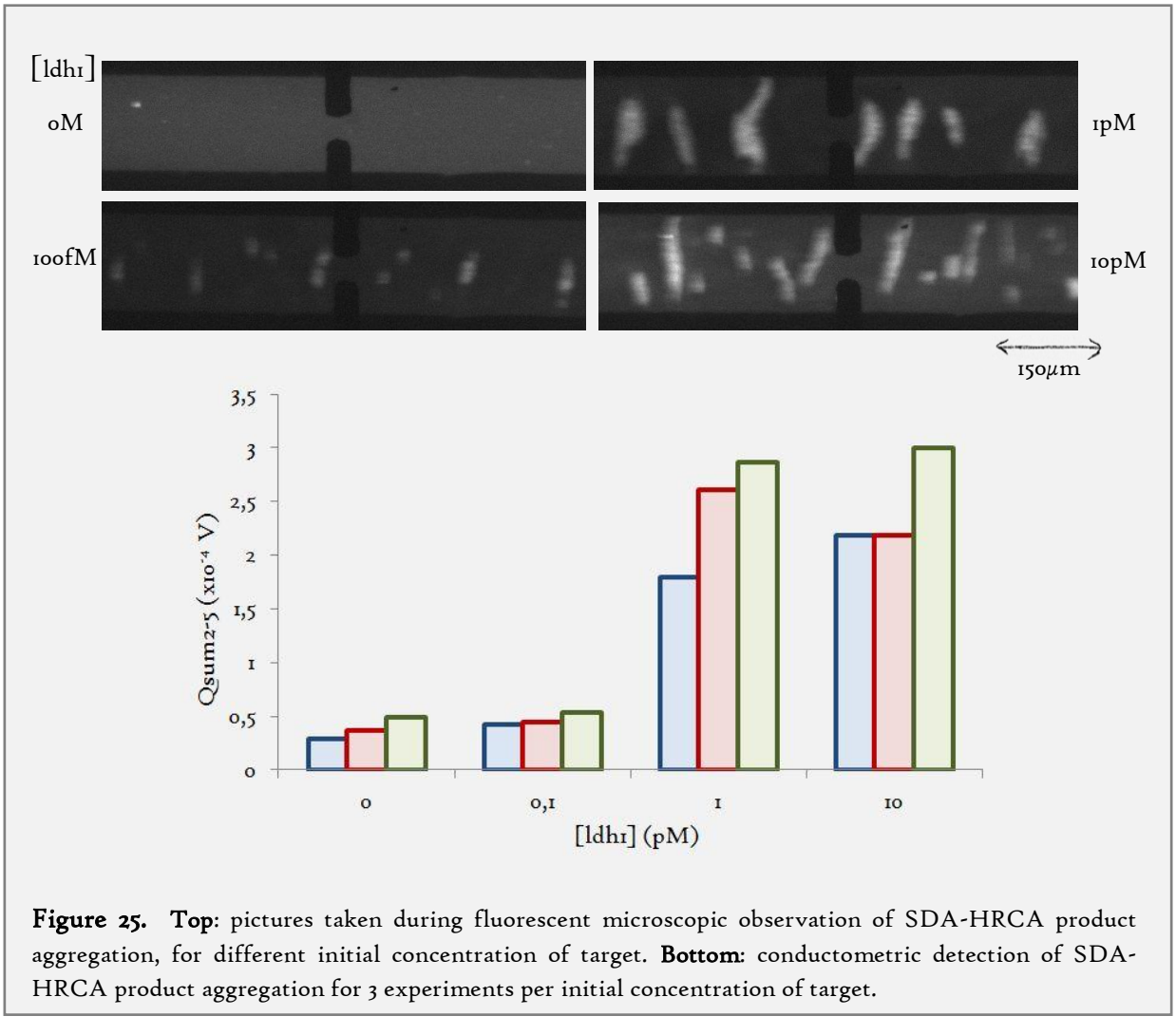

Figure 25. **Top**: pictures taken during fluorescent microscopic observation of SDA-HRCA product aggregation, for different initial concentration of target. **Bottom**: conductometric detection of SDA-HRCA product aggregation for 3 experiments per initial concentration of target.

Contrary to SDA-RCA, DNA aggregations of the SDA-HRCA products via electrohydrodynamic instabilities were observed in the microfluidic system for an initial concentration of target of 100fM, 1 and 10pM. These aggregates were easily detectable for 1 and 10pM. Previous calibration showed that the aggregate quantity and size would not increase with further increased in the target concentration, because the limiting reactant was the padlock probe, set at 50nM. HRCA produces less flexible dsDNA, whose chemical interactions with other DNA are more limited than in the case of RCA products. This could explain the huge behaviour difference between SDA-RCA and SDA-HRCA products.

3.3 Reaction limitations and perspectives

We succeeded to obtain a conductometric detection of small targets thanks to the SDA-HRCA strategy. The detection could also be done simply by pipetting the amplified solution directly in tubes after SDA-RCA reaction, opening the route to another detection device, were amplification could be monitored not by conductometry, but also by viscosimetry. However, before moving to such new developments, it is time to come back to our initial list of constraints to be fulfilled by an amplification method, and check what specifications have been fulfilled with our SDA-HRCA strategy and what the perspectives are in order to solve these last problems.

- Sensitivity, size and quantity of final products

The developed method successfully amplified short targets into a large quantity of long DNA. Because the elongation step was a RCA, the final length of products could go up to 70kbp and depends mainly on the incubation time. The final quantity of products was large enough to be detected with our aggregation-based conductometric measurement, for an initial concentration of target of 1pmol. The limitation seemed to come from the SDA step, which was less efficient than in the original study when monitored with a gel electrophoresis. In addition, in the original paper, a maximum yield of 50nM was obtained for initial concentrations above 20 copies (>3aM), which was theoretically sufficient for our detection. Optimization of the SDA protocol until state-of-the-art level is thus the last step to work on to obtain a really sensitive strategy.

- Buffer

Buffer conductivity was kept at a low level thanks to commercial buffers with conductivity small enough for our application. No specific work has been done to reduce the conductivity while keeping the buffering efficiency. One possible option could be to dilute commercial buffer (Cutsmart or T4 ligase buffer) and supplement them with magnesium ions and rATP. Buffers were also chosen for their enzyme compatibility. Bst polymerase, T4 ligase and Phi29 polymerase could all work in the dual buffer (Cutsmart supplemented with T4 ligase buffer during RCA).

- Specificity and reproducibility

Specificity of the method was insured by the specificity of the two steps. SDA is a specific method, even if it is plagued with a high background noise. In fact, addition of high quantity of genomic material was not detrimental to the reaction performance[52]. RCA step was highly specific and did not amplify the background products of SDA. In theory, RCA should be specific enough to

recognize single-point mutation. This specificity has not been checked here. As a perspective, the two reactions in series could be practical for the development of a nested strategy. Highly conserved gene region over multiple bacteria strains could be targeted by the SDA step (for example, gyrB gene[75]), whereas several padlock probes designed to target strain specific, minor changes into this conserved sequence could then recognize several pathogen.

Reproducibility was not optimized for the SDA step and minor changes in the protocol seemed sometimes to have a big impact on the reaction efficiency. Concerning RCA, large numbers of experiments have been performed, and product yields and specificities were robust.

- Isothermal amplification

Even if we succeeded to avoid PCR and thermal cycling, our strategy was still not fully isothermal. First, SDA and RCA incubation temperatures were different: 56°C for the Bst polymerase, between 30°C and 35°C for the ligase and Phi29 polymerase. Isothermal incubations could be reached with a thermostable ligase like the Ampligase, which is widely used for RCA, hoping that this enzyme also work in our buffers. Bst polymerase was also tested as a good substitute to Phi29 polymerase for the elongation step without any changes in the buffer composition or protocol.

The SDA protocol was supposed to work without the initial heat denaturation of the genomic target. This claim has not been verified during our study. Heat inactivation of the Bst polymerase, used during the SDA, was unfortunately necessary. Simultaneous presence of T4 ligase and Bst polymerase from the SDA during the ligation step led to the apparition of false positive results, with a large quantity of DNA aggregates without any targets in the RCA mix. If this phenomenon only occurred with T4 ligase, fully isothermal protocol could be achieve with the replacement of T4 ligase by Ampligase and a one-step RCA protocol.

- Number of steps

A single step reaction, combining amplification and elongation was not reached. HRCA study showed that an elongation-then-amplification strategy could not create the needed product quantity. Hybrid strategy as PG-RCA could not create long products. SDA and HRCA have been merged in a single step scheme by L.-R. Zhang *et al,* but this strategy only worked with microRNA targets[69]. In our case, addition of padlock probe and ligase was necessary to perform the RCA step.

- Integration

Finally, the reaction integration into a microfluidic chip was only the subject of quick trials. The amplification step of HRCA has been performed directly on chip and monitored by conductometry without any problems, with a large initial target concentration mimicking the quantity of SDA products. No surface treatment was necessary. Heating of the microfluidic chip has been developed in collaboration with Laurent Malaquin and Ezgi Tulukcuoglu with ITO coated glass slides and a PID controller. However, because of the several steps of the reaction, compartmentalization and addition of reagents have to be performed on-chip.

Due to time reasons, we had to stop DNA amplification optimization at this point. The last improvements to obtain a fully isothermal, sensitive and quick elongation and amplification of short biomarkers seem to be within reach. The last chapter of this manuscript will now focus on a new microfluidic technology developed during my PhD, which found application for sequential reaction on-chip, or DNA preconcentration.

References

1. Saiki, R. K. *et al.* Primer-directed enzymatic amplification of DNA with a thermostable DNA polymerase. *Science* **239,** 487–491 (1988).

2. Lundberg, K. S. *et al.* High-fidelity amplification using a thermostable DNA polymerase isolated from Pyrococcus furiosus. *Gene* **108,** 1–6 (1991).

3. Cline, J., Braman, J. & Hogrefe, H. PCR fidelity of pfu DNA polymerase and other thermostable DNA polymerases. *Nucl. acids res.* **24,** 3546–51 (1996).

4. Barnes, W. M. PCR amplification of up to 35-kb DNA with high fidelity and high yield from lambda bacteriophage templates. *Proc. Natl. Acad. Sci. U. S. A.* **91,** 2216–2220 (1994).

5. Diakité, M. L. Y. *et al.* A low-cost, label-free DNA detection method in lab-on-chip format based on electrohydrodynamic instabilities, with application to long-range PCR. *Lab Chip* **12,** 4738 (2012).

6. Blanco, L. *et al.* Highly Efficient DNA Synthesis by the Phage Phi29 DNA Polymerase. *J. Biol. Chem.* **264,** 8935–8940 (1989).

7. Du, W., Li, L., Nichols, K. P. & Ismagilov, R. F. SlipChip. *Lab Chip* **9,** 2286–2292 (2009).

8. Lee, C.-C. *et al.* Multistep synthesis of a radiolabeled imaging probe using integrated microfluidics. *Science* **310,** 1793–6 (2005).

9. Khan, S. A. Rolling-circle replication of bacterial plasmids. *Microbiol. Mol. Biol. Rev.* **61,** 442–55 (1997).

10. Liu, D., Daubendiek, S. L., Zillman, M. A., Ryan, K. & Kool, E. T. Rolling circle DNA synthesis: Small circular oligonucleotides as efficient templates for DNA polymerases. *J. Am. Chem. Soc.* **118,** 1587–1594 (1996).

11. Fire, A. & Xu, S. Q. Rolling replication of short DNA circles. *Proc. Natl. Acad. Sci. U. S. A.* **92,** 4641–4645 (1995).

12. Ducani, C., Bernardinelli, G. & Hogberg, B. Rolling circle replication requires single-stranded DNA binding protein to avoid termination and production of double-stranded DNA. *Nucleic Acids Res.* **42,** 10596–10604 (2014).

13. Nilsson, M. *et al.* Padlock probes: circularizing oligonucleotides for localized DNA detection. *Science* **265,** 2085–2088 (1994).

14. Faruqi, A. F. *et al.* High-throughput genotyping of single nucleotide polymorphisms with

rolling circle amplification. *BMC Genomics* **2,** 4 (2001).

15. Banér, J., Nilsson, M., Mendel-Hartvig, M. & Landegren, U. Signal amplification of padlock probes by rolling circle replication. *Nucleic Acids Res.* **26,** 5073–8 (1998).

16. Lizardi, P. M. *et al.* Mutation detection and single-molecule counting using isothermal rolling-circle amplification. *Nat. Genet.* **19,** 225–32 (1998).

17. Zhang, D. Y., Zhang, W., Li, X. & Konomi, Y. Detection of rare DNA targets by isothermal ramification amplification. *Gene* **274,** 209–16 (2001).

18. Qi, X., Bakht, S., Devos, K. M., Gale, M. D. & Osbourn, a. L-RCA (ligation-rolling circle amplification): a general method for genotyping of single nucleotide polymorphisms (SNPs). *Nucleic Acids Res.* **29,** E116 (2001).

19. Nilsson, M., Gullberg, M., Dahl, F., Szuhai, K. & Raap, A. K. Real-time monitoring of rolling-circle amplification using a modified molecular beacon design. *Nucleic Acids Res.* **30,** 1–7 (2002).

20. Hatch, A., Sano, T., Misasi, J. & Smith, C. L. Rolling circle amplification of DNA immobilized on solid surfaces and its application to multiplex mutation detection. *Genet. Anal.* **15,** 35–40 (1999).

21. Melin, J., Jarvius, J., Göransson, J. & Nilsson, M. Homogeneous amplified single-molecule detection: Characterization of key parameters. *Anal. Biochem.* **368,** 230–238 (2007).

22. Nallur, G. *et al.* Signal amplification by rolling circle amplification on DNA microarrays. *Nucleic Acids Res.* **29,** E118 (2001).

23. Ericsson, O. *et al.* A dual-tag microarray platform for high-performance nucleic acid and protein analyses. *Nucleic Acids Res.* **36,** e45–e45 (2008).

24. Schweitzer, B. *et al.* Multiplexed protein profiling on microarrays by rolling-circle amplification. *Nat. Biotechnol.* **20,** 359–365 (2002).

25. Su, Q., Xing, D. & Zhou, X. Magnetic beads based rolling circle amplification–electrochemiluminescence assay for highly sensitive detection of point mutation. *Biosens. Bioelectron.* **25,** 1615–1621 (2010).

26. Zhang, S., Wu, Z., Shen, G. & Yu, R. A label-free strategy for SNP detection with high fidelity and sensitivity based on ligation-rolling circle amplification and intercalating of methylene blue. *Biosens. Bioelectron.* **24,** 3201–3207 (2009).

27. Zhang, J. *et al.* A smart device for label-free and real-time detection of gene point mutations based on the high dark phase contrast of vapor condensation. *Lab Chip* **15,** 3891–3896 (2015).

28. Russell, C. *et al.* Gold Nanowire Based Electrical DNA Detection Using Rolling Circle Amplification. *ACS Nano* **8,** 1147–1153 (2014).

29. Sato, K. *et al.* Microbead-based rolling circle amplification in a microchip for sensitive DNA detection. *Lab Chip* **10,** 1262–6 (2010).

30. Chapin, S. C. & Doyle, P. S. Ultrasensitive Multiplexed MicroRNA Quantification on Encoded Gel Microparticles Using Rolling Circle Amplification. *Anal. Chem.* **83,** 7179–7185 (2011).

31. Zhong, X. B., Lizardi, P. M., Huang, X. H., Bray-Ward, P. L. & Ward, D. C. Visualization of

oligonucleotide probes and point mutations in interphase nuclei and DNA fibers using rolling circle DNA amplification. *Proc. Natl. Acad. Sci. U. S. A.* **98,** 3940–5 (2001).

32. Christian, A. T. *et al.* Detection of DNA point mutations and mRNA expression levels by rolling circle amplification in individual cells. *Proc. Natl. Acad. Sci. U. S. A.* **98,** 14238–14243 (2001).

33. Zhou, Y. *et al.* In situ detection of messenger RNA using digoxigenin-labeled oligonucleotides and rolling circle amplification. *Exp. Mol. Pathol.* **70,** 281–288 (2001).

34. Larsson, C. *et al.* In situ genotyping individual DNA molecules by target-primed rolling-circle amplification of padlock probes. *Nat. Methods* **1,** 1–6 (2004).

35. Yong Zhang, D., Brandwein, M., Chun Hung Hsuih, T. & Li, H. Amplification of target-specific, ligation-dependent circular probe. *Gene* **211,** 277–285 (1998).

36. Dean, F. B., Nelson, J. R., Giesler, T. L. & Lasken, R. S. Rapid amplification of plasmid and phage DNA using Phi 29 DNA polymerase and multiply-primed rolling circle amplification. *Genome Res.* **11,** 1095–9 (2001).

37. Alsmadi, O. A. *et al.* High accuracy genotyping directly from genomic DNA using a rolling circle amplification based assay. *BMC Genomics* **4,** 21 (2003).

38. Kaocharoen, S. *et al.* Hyperbranched rolling circle amplification as a rapid and sensitive method for species identification within the Cryptococcus species complex. *Electrophoresis* **29,** 3183–3191 (2008).

39. Steain, M. C. *et al.* Detection of influenza A H1N1 and H3N2 mutations conferring resistance to oseltamivir using rolling circle amplification. *Antiviral Res.* **84,** 242–248 (2009).

40. Beals, T. P., Smith, J. H., Nietupski, R. M. & Lane, D. J. A mechanism for ramified rolling circle amplification. *BMC Mol. Biol.* **11,** 94 (2010).

41. Long, Y., Zhou, X. & Xing, D. Sensitive and isothermal electrochemiluminescence gene-sensing of Listeria monocytogenes with hyperbranching rolling circle amplification technology. *Biosens. Bioelectron.* **26,** 2897–2904 (2011).

42. Zhao, Y., Yin, W., Wang, Y., Wang, G. & Li, B. Establishment of a sensitive and specific hyper-branched rolling circle amplification assay and test strip for TSV. *J. Virol. Methods* **209C,** 41–46 (2014).

43. Mazutis, L. *et al.* Droplet-based microfluidic systems for high-throughput single DNA molecule isothermal amplification and analysis. *Analytical chemistry* **81,** 4813–21 (2009).

44. Dahl, F. *et al.* Circle-to-circle amplification for precise and sensitive DNA analysis. *Proc. Natl. Acad. Sci. U. S. A.* **101,** 4548–53 (2004).

45. Jarvius, J. *et al.* Digital quantification using amplified single-molecule detection. *Nat. Methods* **3,** 725–727 (2006).

46. Kühnemund, M., Witters, D., Nilsson, M. & Lammertyn, J. Circle-to-circle amplification on a digital microfluidic chip for amplified single molecule detection. *Lab Chip* **14,** 2983–92 (2014).

47. Murakami, T., Sumaoka, J. & Komiyama, M. Sensitive isothermal detection of nucleic-acid sequence by primer generation-rolling circle amplification. *Nucleic Acids Res.* **37,** e19–e19 (2009).

48. Murakami, T., Sumaoka, J. & Komiyama, M. Sensitive RNA detection by combining three-way junction formation and primer generation-rolling circle amplification. *Nucleic Acids Res.* **40,** e22–e22 (2012).

49. Zeng, Y. *et al.* A quantum dot-based microRNA nanosensor for point mutation assays. *Chem. Commun. (Camb).* **50,** 7160–2 (2014).

50. Ali, M. M. *et al.* Rolling circle amplification: a versatile tool for chemical biology, materials science and medicine. *Chem. Soc. Rev.* **43,** 3324 (2014).

51. Ali-Cherif, A., Begolo, S., Descroix, S., Viovy, J. L. & Malaquin, L. Programmable magnetic tweezers and droplet microfluidic device for high-throughput nanoliter multi-step assays. *Angew. Chemie - Int. Ed.* **51,** 10765–10769 (2012).

52. Toley, B. J. *et al.* Isothermal strand displacement amplification (iSDA): a rapid and sensitive method of nucleic acid amplification for point-of-care diagnosis. *Analyst* **140,** 7540–7549 (2015).

53. Lee, H. Y. *et al.* DhITACT: DNA Hydrogel Formation by Isothermal Amplification of Complementary Target in Fluidic Channels. *Adv. Mater.* **27,** 3513–3517 (2015).

54. Zipper, H., Brunner, H., Bernhagen, J. & Vitzthum, F. Investigations on DNA intercalation and surface binding by SYBR Green I, its structure determination and methodological implications. *Nucleic Acids Res.* **32,** e103–e103 (2004).

55. Rutledge, R. G. & Stewart, D. A kinetic-based sigmoidal model for the polymerase chain reaction and its application to high-capacity absolute quantitative real-time PCR. *BMC Biotechnol.* **8,** 47 (2008).

56. Schnell, S. & Mendoza, C. Enzymological Considerations for the Theoretical Description of the Quantitative Competitive Polymerase Chain Reaction (QC-PCR). *J. Theor. Biol.* **184,** 433–440 (1997).

57. Gevertz, J. L., Dunn, S. M. & Roth, C. M. Mathematical model of real-time PCR kinetics. *Biotechnol. Bioeng.* **92,** 346–355 (2005).

58. Velikanov, M. V & Kapral, R. Polymerase chain reaction: a Markov process approach. *J. Theor. Biol.* **201,** 239–249 (1999).

59. Plum, G. E., Breslauer, K. J. & Roberts, R. W. in *Comprehensive natural products chemistry* 7, 15–53 (1999).

60. Matsuno, H., Niikura, K. & Okahata, Y. Direct monitoring kinetic studies of DNA polymerase reactions on a DNA-immobilized quartz-crystal microbalance. *Chem. - A Eur. J.* **7,** 3305–3312 (2001).

61. Eid, J. *et al.* Real-time DNA sequencing from single polymerase molecules. *Science* **323,** 133–8 (2009).

62. de Gennes, P. G. *Scaling Concepts in Polymer Physics*. (1979).

63. Robertson, R. M. & Smith, D. E. Self-diffusion of entangled linear and circular DNA molecules: Dependence on length and concentration. *Macromolecules* **40,** 3373–3377 (2007).

64. Freedman, K. O. *et al.* Diffusion of Single Star-Branched Dendrimer-like DNA. *J. Phys. Chem. B* **109,** 9839–9842 (2005).

65. Walker, G. T. *et al.* Strand displacement amplification--an isothermal, in vitro DNA amplification technique. *Nucleic Acids Res.* **20,** 1691–1696 (1992).

66. Spargo, C. a *et al.* Detection of M. tuberculosis DNA using thermophilic strand displacement amplification. *Mol. Cell. Probes* **10,** 247–256 (1996).

67. Xu, S. Y. *et al.* Discovery of natural nicking endonucleases Nb.BsrDI and Nb.BtsI and engineering of top-strand nicking variants from BsrDI and BtsI. *Nucleic Acids Res.* **35,** 4608–4618 (2007).

68. Joneja, a. & Huang, X. Linear nicking endonuclease-mediated strand DNA Amplification. *Anal Biochem* **414,** 58–69 (2011).

69. Zhang, L. R., Zhu, G. & Zhang, C. Y. Homogeneous and label-free detection of micrornas using bifunctional strand displacement amplification-mediated hyperbranched rolling circle amplification. *Anal. Chem.* **86,** 6703–6709 (2014).

70. Shi, C., Liu, Q., Ma, C. & Zhong, W. Exponential Strand-Displacement Amplification for Detection of MicroRNAs. *Anal. Chem.* **86,** 336–339 (2014).

71. García, P. B., Robledo, N. L. & Islas, Á.́ L. Analysis of non-template-directed nucleotide addition and template switching by DNA polymerase. *Biochemistry* **43,** 16515–16524 (2004).

72. Ogata, N. & Miura, T. Creation of genetic information by DNA polymerase of the archaeon. *Nucleic Acids Res* **26,** 4652 (1998).

73. Zyrina, N. V. *et al.* N.BspD6I DNA nickase strongly stimulates template-independent synthesis of non-palindromic repetitive DNA by Bst DNA polymerase. *Biol. Chem.* **388,** 367–372 (2007).

74. Liang, X., Jensen, K. & Frank-Kamenetskii, M. D. Very efficient template/primer-independent DNA synthesis by thermophilic DNA polymerase in the presence of a thermophilic restriction endonuclease. *Biochemistry* **43,** 13459–13466 (2004).

75. Czilwik, G. *et al.* Rapid and fully automated bacterial pathogen detection on a centrifugal-microfluidic LabDisk using highly sensitive nested PCR with integrated sample preparation. *Lab Chip* **15,** 3749–3759 (2015).

CHAPTER 4: The sliding wall technology - and its applications for sequential reaction and sample preconcentration

"La curiosité est un vilain défaut", or as our English friends say, "curiosity killed the cat". Fortunately, this expression is (most of the time) false in the scientific field. Curious, I developed in parallel of my main project a new technological toolbox for microfluidics, that we called "sliding walls". This project started at the origin as an extension of a technological idea from Ayako Yamada, post-doc in the team, that I help to initiate. For a neurobiological study, compartmentalization between neuronal axons and neuronal bodies was necessary. A transient partition of a microfluidic chamber was realized with a nylon fibre, which could be easily removed at any time. This tool has then been successfully applied by Ayako to 3D and 2D cell co-culture. Despite my smaller contribution to these applications, a short presentation of this work will be included in the first section of this chapter, to explain the origin of the following developments. Regarding my own contribution, I have been working on extending the versatility of nylon fibre replacing it by rigid elongated microfabricated structures, the "sliding walls". These walls have been made in resin or metal and shaped by 3D-printing, micro-milling or soft lithography. Contrary to fibres, these sliding walls could open and close chamber or channels, serve as valves or could contain hydrogel membranes for further functionalities. This toolbox has then been used to propose a new, simple way to perform sequential reaction into a microchip, for a future integration into the conductometric DNA detection project. A second proof-of-concept for preconcentration of genomic DNA has also been realized.

Table of contents

1 Fibre-based transient compartmentalization 138
2 Sliding wall toolbox 139
2.1 3D-printed walls 139
2.1.1 Reversible compartmentalization 139
2.1.2 Valve 140
2.2 NOA walls for valves 141
2.3 Metallic walls for reconfigurable microfluidic 143
3 Microreactor for sequential reactions 145
4 Sample preconcentration 148
4.1 Agarose membrane 148
4.2 Preconcentration for the DNA detection system 149
4.3 Membrane fabrication 150
4.4 Glass-PDMS hybrid surface 152
4.5 DNA preconcentration 153
5 Perspectives for the sliding wall toolbox 156
References 157

1 Fibre-based transient compartmentalization

As previously explained the starting point of this project was the need to compartmentalize neurons in microfluidic devices. Indeed, Ayako was investigating different approaches to guide axons of neurons on physical, chemical or hybrid patterns on the surface of a microfluidic device, in the context of *in-vitro*, artificial brain-on-chip. However, only axons should be present on the patterns, and the cell bodies had to adhere in a seeding region outside the structures, as seen on Figure 1. Compartmentalization of large microfluidic chambers was hardly achieved in the literature. Only one technology was found, where a wall fixed on the chamber roof was moved up and down thanks to an inflated control channel located above the wall[1,2]. Ayako has proposed an alternative approach: a nylon fishing line (diameter of 75µm) was inserted into the PDMS microchamber before the chip bonding in order to separate physically the patterned and the seeding areas (see Figure 2). The nylon fibre could then be easily removed after cell adhesion by pulling it out of the chamber by a free extremity. A first paper was published with the study results and this first proof-of-concept of microchamber compartmentalization[3].

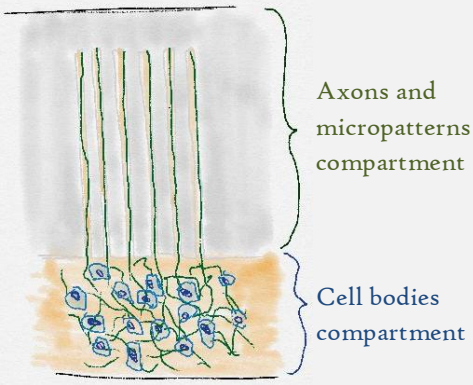

Figure 1. Neurons on a compartmentalized experiment

However, we were rapidly convinced that besides this first proof of concept, it could be useful for a wider range of applications. Indeed microdevices with 4 fibres were fabricated forming a five compartments chip. This device was used to inject different cell types and hydrogel (mimicking the extra cellular matrix) in the different compartments. After gelling, fibres were removed and collagen slabs were formed. With different cell types in the different compartments, 3D co-culture could be easily performed and one example of culture side-by-side of neurons and glial cells was demonstrated in a second paper[4].

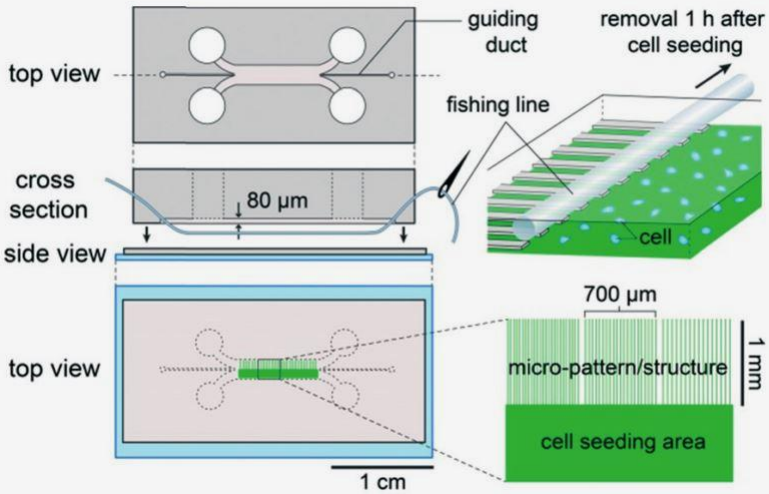

Figure 2. Schematic of the realization of a fibre-based transient compartmentalization in the context of axon array. Neurons were seeded in the cell seeding area. After cell adhesion, the nylon fibre was removed, allowing the axons to grow in the micro-pattern/structure area. From [3].

2 Sliding wall toolbox

2.1 3D-printed walls

Based on these promising results with the cylindrical fibre, I thus investigated how microfabricated structures can advantageously replace them for microfluidic applications. Once we considered the use of solid walls with rectangular sections, 3D-printing was an evidence for a fast prototyping and realization of these complex structures. Our team has a high-resolution stereolithographic 3D-printing system (DigitalWax 0.28J+ from DWS). The printer principle is depicted on Figure 3. A transparent tank was filled with a photosensitive resin. A movable head could move vertically into the tank with a precision of 10µm. A 405nM laser, with a 50µm spot, was then directed through the bottom of the tank with mirrors mounted on galvanometers in order to scan the X and Y directions. Laser photopolymerized a layer of resin located between the head and the tank bottom. The head then move upward and a new layer could be created. Lateral resolution was close to 50µm, except for the first layers which were over-exposed in order to enhance the resin bonding to the head. Vertical resolution was the head displacement resolution for normal structure. However, for suspended structures (*i.e.* with void above the part to create), the laser could polymerize a larger height of resin than the height of one layer. This length, dependent on the absorption of the laser by the liquid resin, has been estimated around 200µm. Two different commercial resins were used with similar mechanical properties. One was optically transparent and the second one was grey and opaque. The different possibilities offered by 3D-printing will be presented in the next sections. In particular, we focused first on the demonstration of different functionalities offered by the sliding walls technology: reversible compartmentalization and valves.

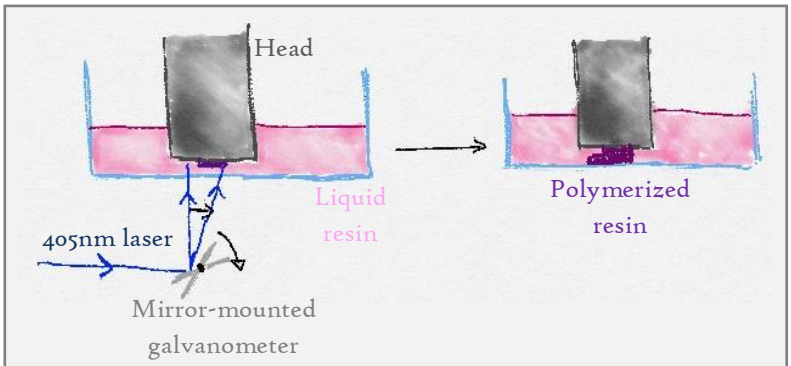

Figure 3. Stereolithography principle.

2.1.1 Reversible compartmentalization

We first investigate how sliding walls behave compared with nylon fibre regarding compartmentalization experiment. A mould was microfabricated, containing a rectangular chamber (10mm x 2.6mm x 460µm) crossed by a long channel (33mm x 500µm x 800µm) which served as a guiding duct for the wall. 4 inlets were punched in the PDMS replica, two in each side of the channel. One extremity was opened on the side of the PDMS replica when bounded on a flat PDMS slab. A 3D-printed wall with a rectangular section was introduced into the channel from the open side, as seen on Figure 4. To achieve complete sealing the wall dimensions were larger than the channel ones (wall height was 970µm and wall width was 680µm). However, thanks to the PDMS elasticity, wall insertion didn't damage the channel during insertion. One side of the compartment was filled with water stained with orange dye whereas the second half of the chamber was filled with unstained

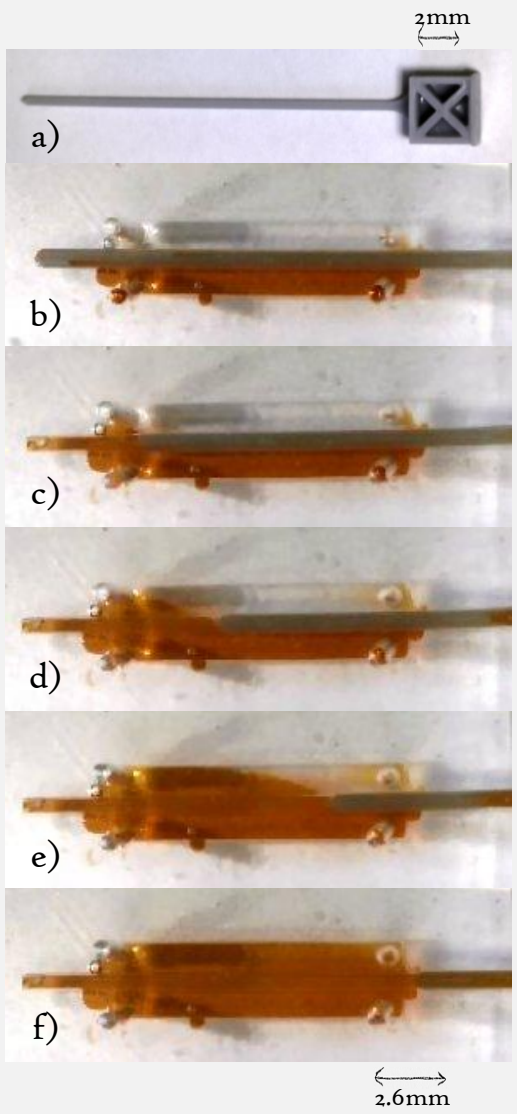

Figure 4. Compartmentalization with a 3D-printed wall. **a)** 3D printed wall with a width of 680μm and a height of 970μm. **b)** to **f)** Time-lapse of the manual removal of the wall from the PDMS chamber and orange ink displacement from the bottom compartment to the top compartment. Total duration: 30 seconds.

water. No leakage on the other compartment was observed. The wall was then moved manually outside of the chamber. During wall removal, a fast mixing of the two compartments occurred because of convection.

Compared to the fibre-based compartmentalization, this alternative had the possibility to easily seal again the two compartments by simply pushing back the solid wall into the channel.

2.1.2 Valve

Valves are essential components for fluid control in complex microfluidic platfors and have been the subject of numerous technological developments. Integrated valve conceptions started at the beginning of microfluidics with complex MEMS valves made by silicon technologies[5]. In 2000, in the S.R. Quake's team, Unger *et al.* developed a monolithic pneumatic valve made on PDMS with an inflatable control channel located above a flow channel for the fluid of interest which immediately became the most used valve in microfluidic[6]. Their small size allowed the integration of millions of valves per cm-square[7,8] and the principle was then diversified to allow different actuation means[9] or geometries[10–12]. Other interesting valves were produced, with mobile element[13,14], bubble gate[15], integrated pinched-valves[16,17] or Braille display[18]. All these different valves have different performances, complexities in term of microfabrication or control. However, we found a few number of simple valves with manual actuations for portable and equipment-free systems. One example was a torque-actuated valve by D. Weibel *et al*[19] which allowed the opening and closing of channel by turning screws located above the microchip.

Fabrication of complex structures was made possible thanks to 3D-printing. In particular, we aim at demonstrating how this sliding wall technology could be used as a valve. In order to obtain valves, walls could be microfabricated so that they present apertures (windows). As shown on Figure 5, panel a, the transparent 3D-printed wall had to be printed from the side; overexposure of the first layers was visible at the bottom of the left part of the structure. Stability of the suspended wall was difficult to insure. To do so, the structure was printed as a bridge and cut after fabrication into two sliding walls, as seen on Figure 5. Two 350µm wide windows were created in the middle of a wall with a height of 940µm (±10µm) and a width of 740µm (±70µm).

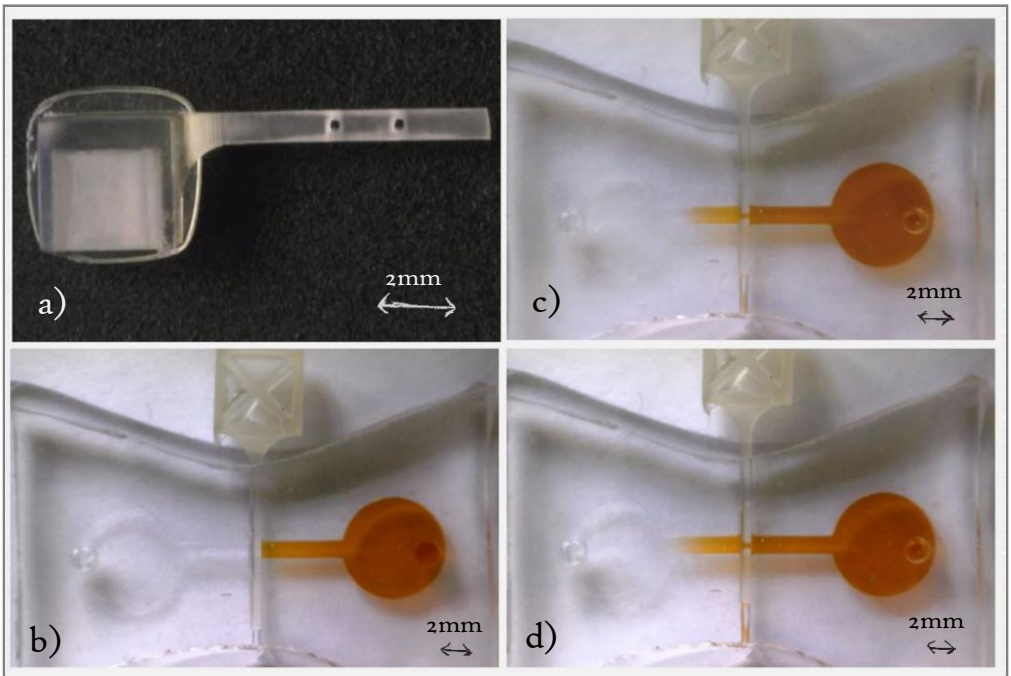

Figure 5. 3D printed valve. **a)** 3D-printed wall with a 950μm x 650μm section and two 350μm windows, seen from the side. **b)** Closed-valve with the windows outside the channel. **c)** and **d)** Diffusion of the orange ink after the sliding of one window into the channel.

A new microdevice was produced to characterize this approach with two large reservoirs linked by a channel with a rectangular section (1mm x 630µm). This channel was crossed by a guiding duct with a smaller section than the sliding wall: 520µm x 780µm, opened in each sides of the microfluidic chip. The replica was then plasma-bonded on a flat PDMS slab and the sliding wall was inserted inside the guiding duct, with one of the window in the channel (valve ON). The reservoirs and the channel were filled with water, the wall was moved to put the window outside of the channel (valve OFF) and a drop of orange ink was deposited on the right reservoir, as seen on the panel b of Figure 6. The stained-water only crossed the wall after moving of the sliding wall into the ON position and diffused toward the left reservoir (panel c and d). These experiments demonstrate that using walls with holes allows opening and closing channels at will without requiring any double layer soft lithography or additional instrumentation. However, some leakage was visible at the tip of the wall on the panel d: some improvement had to be done on the wall roughness to obtain a really leakage-free valve.

2.2 NOA walls for valves

The main cause for the leakage between the wall and the microchip was the roughness of the 3D-printed walls on the z-axis (≈10µm). Considering the fast development of 3D-printing, this limitation should be quickly overcome and 3D-printed wall with a flat surface would be soon easy to produce. However, in the meantime, we searched for another microfabrication method, which could allow the creation of really flat sliding wall. We finally opted for the use of photosensitive glue, called NOA 81 that presents interesting properties regarding our applications. NOA 81 is biocompatible, slightly elastic with a Young modulus of 325MPa and has a good optical transparency[20]. 3D structures

could be easily transferred from a PDMS mould to the photopolymerized NOA[21] with the following protocol. PDMS mould was sealed with a flat slab of PDMS by natural adhesion between the two surfaces (see Figure 6 for the mould design and the protocol scheme). A NOA 81 drop was then deposit at an open side of the mould, and filled the PDMS mould by capillarity. As PDMS is permeable to oxygen, and NOA polymerization is inhibited by the presence of this gas, a thin layer of uncured NOA stayed after UV illumination (90s at 30mW/cm², 365nm). The NOA structure could thus be unmoulded from the PDMS and fully cured by a second illumination. An optional heating at 150°C during 1h30 could harden the structure. The final roughness of the produced sliding wall was dependent of the roughness of the PDMS mould. In our case, micro-milling was used to produce the first structures, transferred in the PDMS by soft-lithography. The flatness of our new NOA walls was around 200nm, which corresponded to the mean roughness of the micro-milled mould.

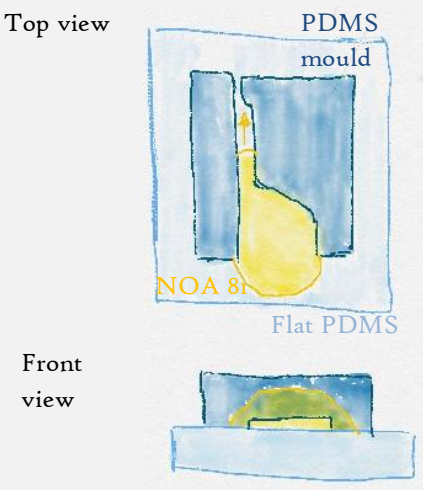

Figure 6. Schematic of the NOA structuration between two PDMS moulds.

To assess the performance of this new sliding wall, a sealing assay was performed with a sliding wall without window to test the resistance of the valve in an OFF position. The sliding wall was inserted into the guiding duct of the PDMS microdevice and blocked the channel. The section of the wall was 500µm x 500µm; the dimensions of the guiding duct varied from 70% to 95% of the dimensions of the wall. The channel was filled from one side with fluorescein solution and a pressure was applied (step of 10mbars), with a pressure controller (MFCS, Fluigent) to determine the leakage pressure or threshold pressure. The fluoresecein leakage was monitored by fluorescence microscopy. Figure 7 shows that, as expected, a low-pressure threshold (40mbar) was achieved for large guiding ducts (90 and 95%). For smaller guiding ducts, perfect sealing until the maximum pressure delivered by the MFCS could be observed, but this result was not reproducible. We make the assumption that the sealing improved with smaller guiding duct because of a stronger compression produced by the PDMS surface on the sliding wall. Besides the failures were probably due to the difficult insertion of the wall into the tight guiding ducts, leading to damage along the surfaces which favoured leakages. At medium contraction ratio (85%), the threshold pressure was more reproducible and was around 300mbars. This threshold pressure was high enough to allow the use of the NOA sliding wall as a valve in most of the experiments run in our

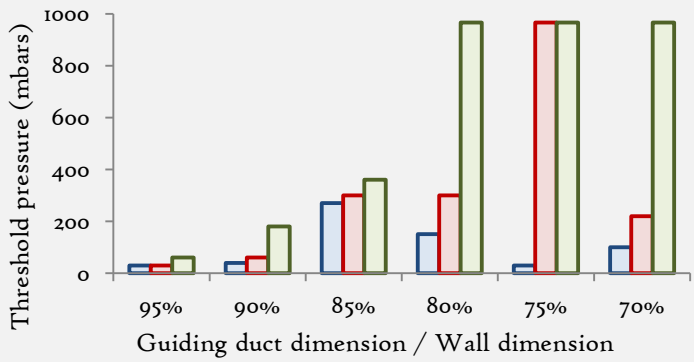

Figure 7. Threshold pressures for NOA sliding wall before leakage, for different dimension of the guiding duct. Results for 3 experiments were plotted.

team. Thanks to this new fabrication method of the sliding walls, we greatly improved their performance compared to 3D-printed walls, which experienced leakages even without overpressure.

2.3 Metallic walls for reconfigurable microfluidic

The main drawback of NOA material regarding sliding walls fabrication was its elasticity. Walls were more and more flexible as their dimensions decreased and this lack of rigidity was problematic during wall insertion and pushing of the sliding wall inside the guiding duct. We searched for another materials and microfabrication methods in order to decrease the sliding wall dimensions while keeping a structure rigid enough for insertion. With the help of Ivan Ferrante, we milled 100µm-thin sheets of stainless steel in order to produce planar sliding walls. Fabrication of these sliding walls was more direct than for NOA walls: the stainless steel sheet was taped to a brass block and directly milled by micromilling in order to cut the wall shape out of the metal sheet. Additional channels could then be milled on the wall (see Figure 8). Channel depths were close to 50µm and the minimum width of these structures was 50µm, which was the smallest available tool diameter. After polishing of the milled channel, the wall surfaces had the roughness of the commercialized steel sheet, around 2µm.

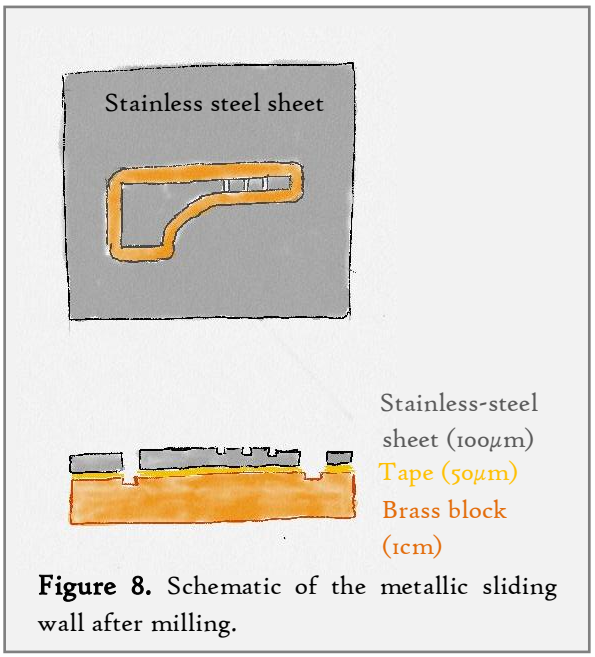

Figure 8. Schematic of the metallic sliding wall after milling.

We first assess the threshold pressure for metallic wall, to check if this material was flat enough to be used in leakage-free configuration. The wall used was 24mm long and 950µm large. The PDMS microdevice contained a long channel (14mm x 350µm x 50mm), crossed by a guiding duct with variable dimensions. An experiment similar to the one conducted for NOA wall was performed, and the results are shown in Figure 9. We observed similar results than for the NOA walls. The threshold pressure did not increase as much as in the NOA case. The elongated shape of the sliding wall could explain this tendency, as the compression exerted by the PDMS roof and ceiling on the sliding wall should decrease with the larger planar wall, compared to the NOA wall

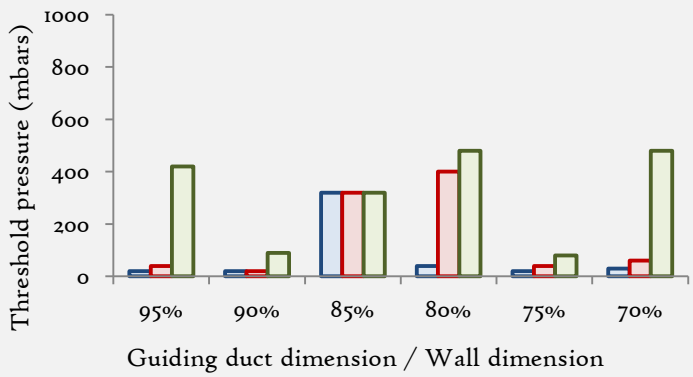

Figure 9. Threshold pressures for stainless steel sliding wall before leakage, for different dimension of the guiding duct. Results for 3 experiments were plotted.

with a 500µmx500µm section. Otherwise, the best results were still obtained with a contraction ratio of 85%. Guiding duct scratching was more visible for the guiding ducts with a small section.

New applications appeared with the development of these thin, channel-engraved sliding walls. Indeed, by engraving different channel geometries on a single wall, moving the wall could be equivalent to reconfigure the channel network of the microfluidic chip. Reconfigurable microfluidics has already been the subject of several technological developments. Some of the called "reconfigurable microfluidics" concerned more systems which could be assembled in different configuration before using the microdevice[22–24]. Systems with a large number of valves could be named reconfigurable, because the fluidic path could be modified during operation[7,25]. Other system used elastic chips and a change in pressure applied in the whole chip to open or close communication between parallel channels[26]. Finally, the closest example to our proposition of reconfigurable microfluidic network is the SlipChip, where a microdevice constituted of 2 planar, patterned substrates (glass or plastic) could be reconfigured simply by making one of the 2 substrates moving alongside the other[27].

We thus developed a first proof-of-concept of reconfigurable network with a switch valve. Two engraved channels with a height of 50µm and a width of 100µm were milled at the top of the stainless steel wall. Depending on the position of the sliding wall, the liquid from an input channel could flow to one of two different output channels (see Figure 10). We have demonstrated that this switch valve is able to operate without any leakage for an applied pressure of 900mbar at the inlet. This applied pressure corresponded to a 550mbars difference between the engraved channel and the atmospheric pressure due to the input channel resistance, which was slightly better than the tolerance of the previous experiment. To give another order of magnitude, the associated flow rate was 13µl/s, which is higher than the typical flow rates used in many microfluidic applications. This first proof-of-concept demonstrated the use of sliding wall for reconfigurable microfluidics with a high pressure tolerance, sufficient for most of the usual microfluidic applications. Moreover, the simple manual actuation of the wall movement is a real advantage for portable application and microdevices with minimal equipment. Further improvements have still to be done in order to block the sliding wall in the interesting positions or for the automation of the wall movement with motors.

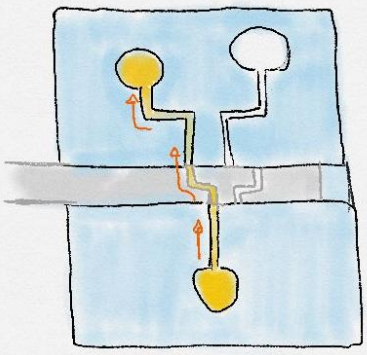

Figure 10. Schematic of the switching valve. Pulling the sliding wall to the left change the fluidic path to the right outlet

Even if these experiments and proof-of-concepts were initially disconnected from the DNA detection project, the sliding walls were quickly exploited for the integration of the conductometric measurement inside a larger device which should also contain a microreactor for sequential reactions.

3 Microreactor for sequential reactions

One of the objectives of the DNA detection project was to integrate the different analytical steps (sample treatment, DNA amplification and DNA detection) into a single portable microdevice. Sliding walls, with their easy and manual control were considered as good candidate for this integration. We first focused on the development of a microchamber for sequential reactions. Indeed, our DNA amplification method requires several steps and reagent addition. In the literature, several technologies were used to perform sequential reactions in microfluidics format, but there are all linked to a specific platform: droplets with EWOD[28], LabDisk[29], pneumatic valve-based system[30] or integration of magnetic particles supports[31]. Droplets and LabDisk are not compatible with our DNA detection system, and pneumatic systems need a precise control of flow or pressure, difficult to implement in portable systems.

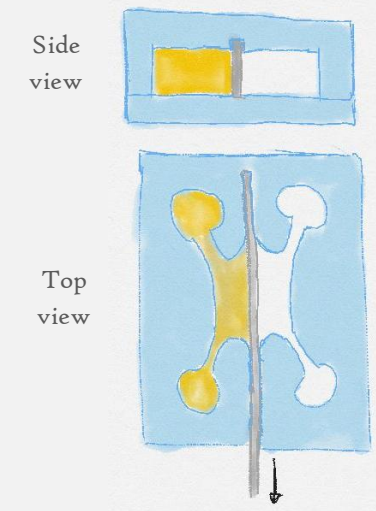

Figure 11. Schematic of vertical wall compartmentalization.

Ayako's approach with nylon fibre is ideal for compartmentalization. Reactions could be realized with several compartments sequentially opened. However, after opening, no fast mixing was observed on the chamber because the components only diffused from one compartment to the other. In order to accelerate the mixing, the surface between two compartments has to be increased. We proposed to replace nylon fibre by vertical metallic walls in order to increase the height of the microreactor (see Figure 11).

A first series of experiments was performed to check the sealing efficiency of this compartmentalization method. A metallic wall was milled on a 200µm thick copper sheet, with a length of 10mm and a width of 950µm. A brass mould was also created, with a 5.5mm x 2mm x

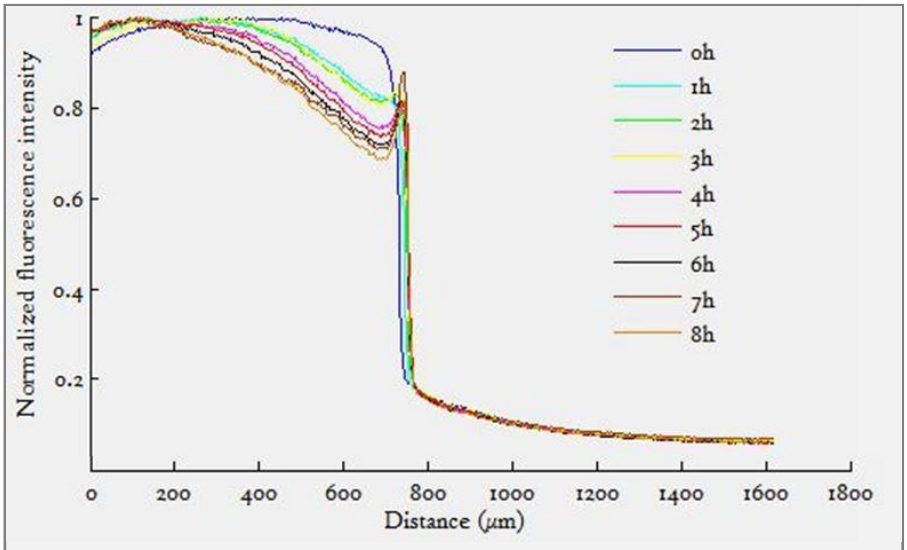

Figure 12. Sealing assay with vertical metallic wall and evolution of fluorescence over time. Wall is located between 750 and 950µm.

0.7µm chamber crossed by a guiding duct with a 150µm x 800µm section. PDMS replica of the brass mould was plasma-bounded with a flat PDMS slab. One compartment was filled with pure water and the other contained a fluorescein solution. Fluorescence monitoring was performed (one measurement per hour during 8h). As shown on Figure 12, no fluorescence increase was observed in the water compartment, proving a perfect sealing between the two halves of the chamber.

After these preliminary experiments, we designed a microreactor on the same principle for sequential reactions, with the project to apply it to the SDA-RCA reaction on-chip. 4 compartments are needed with different relative volume:

- A sample compartment containing target DNA.
- A SDA compartment containing the SDA buffer, enzymes, dNTPs and primers, with a volume five times larger than the sample volume.
- A ligation compartment containing the RCA buffer, ligase, dNTPs and padlock probe, with the same volume as the SDA compartment.
- A RCA compartment containing the Phi29 polymerase and a priming oligonucleotide with a similar volume than the sample chamber.

The mould design is represented on Figure 13. The chamber, in light blue, has the following dimensions: 3mm x 1.5mm x 0.7mm. Three vertical guiding ducts (in green) are 10mm long, 100µm large and 850µm high. The distance between the guiding ducts is 0.5mm. The ratio between the guiding duct height and the guiding duct interval is fixed at 2 because of the milling tool aspect ratio. 4 inlets are driving the 4 different mixes in the 4 compartments. Outlets are located at the end of the guiding ducts. Three corresponding sliding walls were micro-milled in a 100µm high stainless-steel sheet with the following dimensions: 24mm x 100µm x 950µm.

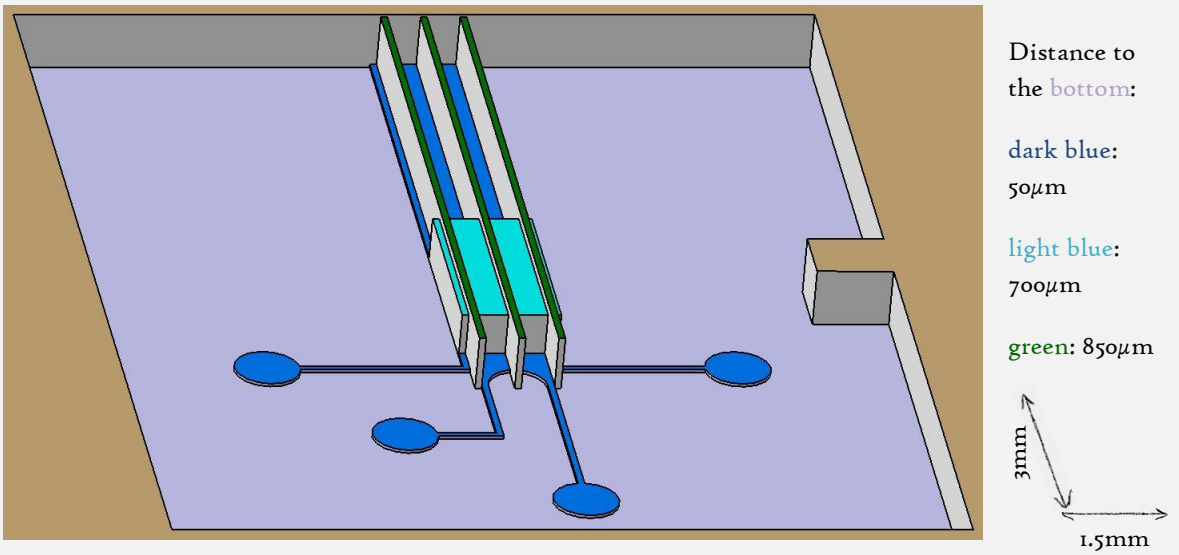

Figure 13. 3D design of the brass mould for the sequential

The total volume of the microreactor is necessarily a compromise. In one hand, for most of the pathogen detection applications, the initial sample volume is large, around 1ml. The need for small initial volume of sample is not current, except for cerebrospinal fluid. Knowing that 1000

CFU/ml is a standard threshold for bacteria detection, decreasing the sample volume down to 1µl could lead to false negative result. On the other hand, a large sample volume needs a higher quantity of expensive enzymes and reagents. Because most detection systems are designed for a final volume close to 30µl (less than 5µl in our case), high quantities of amplification products are useless. In practice, a preconcentration step is often used to trap microorganisms or genomic material from the initial sample volume and allows a decreasing of the sample volume to several microlitres. Finally, because it's easier to dilate the dimensions of the microreactor for further experiment than to shrink them, we decided to make our first trial with a miniaturized system, close to the smaller reachable size with our microfabrication method. Indeed, the sample and RCA compartments contained 0.21µl, the SDA and ligation volumes were 1.05µl.

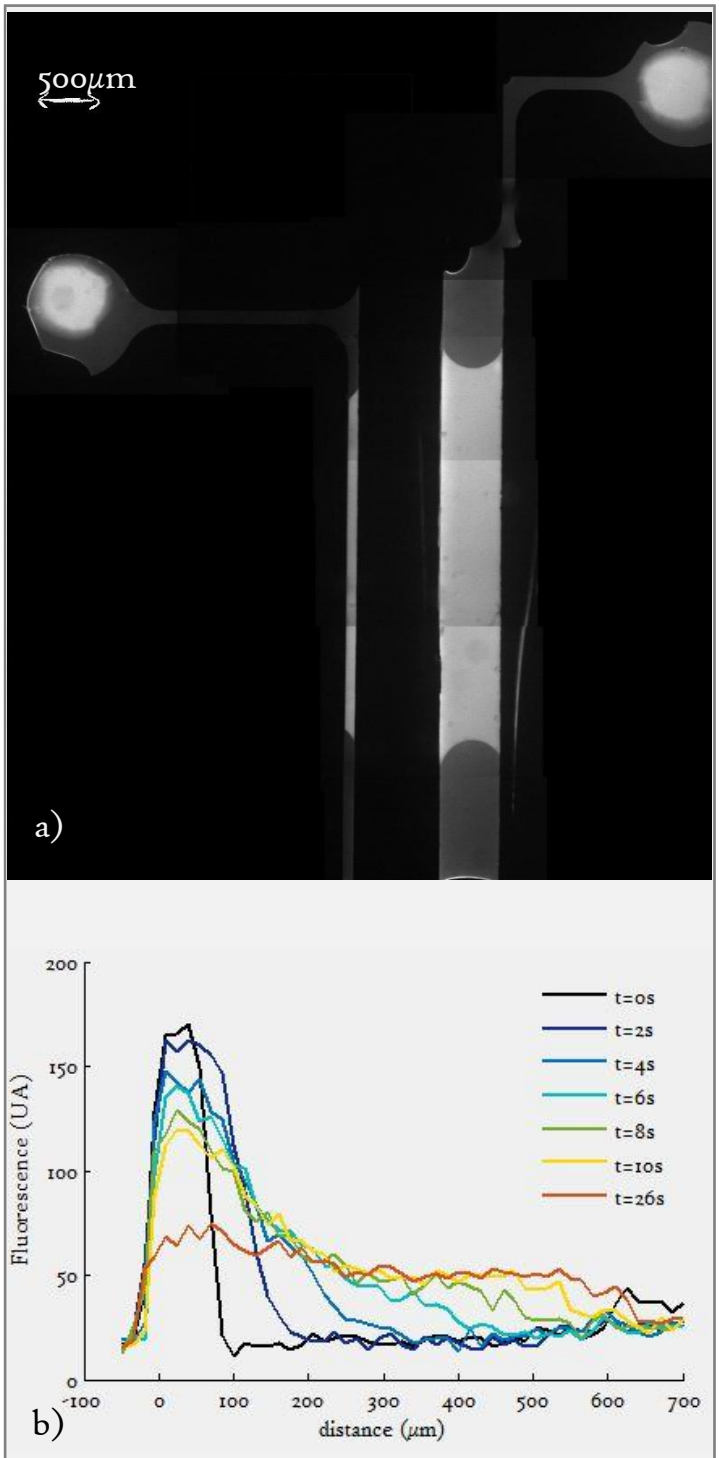

Figure 14. a) Fluorescence picture of the sequential microreactor with the sample (left) and ligation (right) compartments filled with fluorescein, and the SDA and RCA compartments filed with tap water. **b)** Fluorescence from the sample compartment spreading over time after removal of the sliding wall between the sample and the SDA compartments.

Unfortunately, the parallel development of the SDA-RCA did not go until the completion of a purely isothermal configuration. With the current state of the amplification method, a heating step up to 80°C is necessary to inactivate the Bst polymerase. The simultaneous loading of all the reaction components is impossible without inactivating the T4 ligase and Phi29 polymerase during this heating step. Waiting for a true isothermal reaction, the microreactor has been tested only with fluorescein solutions. The sample and ligation compartments have been filled with fluorescein solution, while tap water was introduced in the SDA and RCA compartments. No leakage was observed, as shown on Figure 14, panel a). Removal of the sliding walls

allowed a quick homogenization of the fluorescence, in less than 26s (see panel b). The fluorescence spreading was not only due to diffusion, contrary to the fibre-based microsystem. The higher dimensions of the chamber here might add turbulence in the flow produced by the wall removal.

The principle of the sequential reactions has been demonstrated with this design. SDA-RCA reaction could now be integrated into a simple, portable and manually-actuated microsystem - as soon as a purely isothermal scheme would be developed. Independently of the DNA detection study, the use of sliding wall for the integration of membrane into window of walls has also been explored. But this new functionality quickly gave birth to a new sample preconcentration system, whose final aim will be to be integrated with the DNA detection system.

4 Sample preconcentration

4.1 Agarose membrane

Another useful functionality that we demonstrated with sliding walls was the easy integration of membranes within the microfluidic chips. Membranes were widely used to trap or filter molecules or particles, to preconcentrate analytical targets, to allow the diffusion of small molecules without convection. However, membrane integration is not an easy task and often requires complex microfabrication. Membrane could be created during fabrication for a silicon-based chip[32,33] or commercial plastic or PDMS membranes could be sandwiched during chip bonding between layers of glass or PDMS[34]. Hydrogel membranes were also directly polymerized inside the chip channels after bonding, thanks to photopolymerization of PEGDA[35,36] or the formation of membrane between alginate and chitosan compartments[37,38].

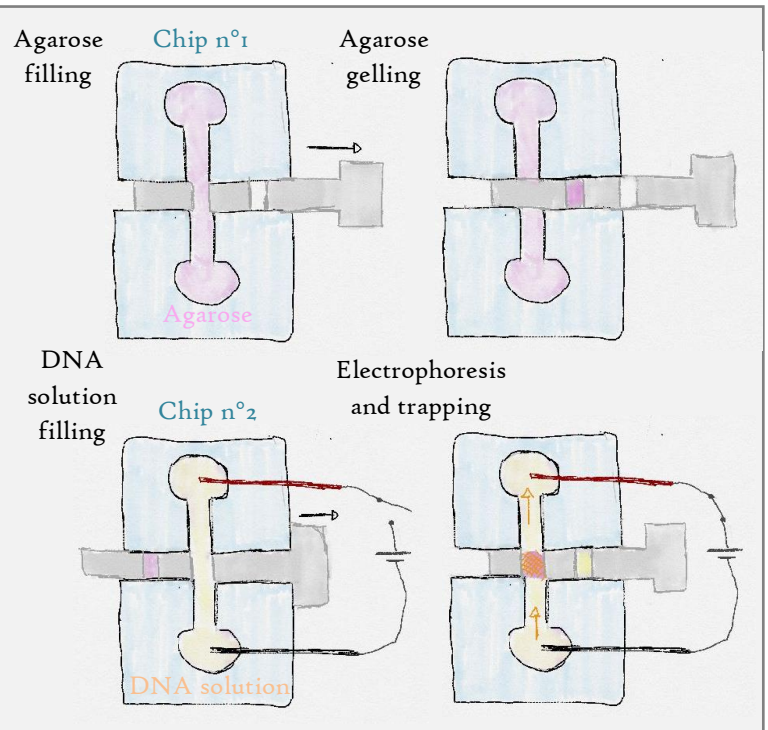

Figure 15. Schematic of the protocol for agarose membrane formation and electrophoretic trapping of Lambda-DNA.

All these methods are specific for a single membrane material. We demonstrated the integration of a membrane into a sliding wall which could allow the use of several hydrogels as membrane. The first proof of concept was realized with an agarose membrane integrated inside a window of the previous 3D-printed chip, and DNA trapping inside the membrane was performed as a first demonstration.

First, the sliding wall was inserted into the PDMS microchip described on the valving section, with one window being directly in the channel (see Figure 15). Then, the channel was filled with an agarose solution at 2.5% (w/w) in water just after boiling. To allow for membrane formation, the wall was moved to remove the agarose-filled hole from the main channel, and the whole microchip was set at room temperature during 1h for agarose gelling. The sliding wall was then removed from the microchip, and inserted in a similar PDMS chip (called Chip n°2 on the Figure), for DNA preconcentration. Channel and reservoirs were filled with TE buffer containing 500ng of Lambda-DNA stained with SyBr Green I. Agarose membrane was then moved into the channel, and a 100V tension (supplied by a HVS448 system from LabSmith) was applied between two platinum electrodes immerged in the reservoirs. The DNA molecules thus migrate and were preconcentrated at the agarose membrane. As shown on Figure 16, the membrane was quickly saturated with fluorescent DNA molecules entangled in the hydrogel mesh in less than 5 minutes. But, because of the roughness of the 3D-printed wall and the large pores of the hydrogel membranes, DNA succeeded to pass through the wall.

4.2 Preconcentration for the DNA detection system

This first proof-of-concept successfully demonstrated the possibility to easily integrate a hydrogel membrane within the sliding walls, without any complicated microfabrication or instrumentation, and to perform elementary trapping of biomolecules. The application of this DNA capture could be useful for the bacterial detection project. Preconcentration or filtering of bacteria or bacterial genomic DNA from a large sample could be necessary in order to reduce the sample volume before lysis or DNA amplification. Several microfluidic systems have already been published for sample treatment, but most of them rely on syringe pumps or pressure control. Because our system already integrates electrodes and manual loading of fluids by pipetting, electrokinetic techniques quickly became an evidence for sample treatment. Electrophoretic bacteria preconcentration against a hydrogel membrane has already been demonstrated[39]. Electrophoretic preconcentration of DNA[36] and protein[35] have also been described against a Polyethylene Glycol Diacrylate (PEGDA) membrane. In our case, DNA preconcentration could be useful for two different reasons:

- First, DNA or bacteria trapping would be necessary if a large sample has to be treated. Captured DNA could then be amplified in a smaller volume compatible with on-chip sequential reactions.
- Secondly, post-amplification concentration of reaction products could improve the LOD of the aggregation-based detection. Indeed, our system detects the presence of DNA aggregates in a microfluidic channel. During the 3 minutes-long experiments, several tens of aggregates were detected and the final quantity of DNA located inside the reservoirs would be high enough to create thousands of aggregates. With the measure of the aggregate size and internal DNA concentration made in Chapter 2, we can state that a large DNA aggregate is composed of approximately 300 000 Lambda-DNA molecules. The system is sensitive enough to detect the passage of a single aggregate above the electrodes: if DNA molecules were preconcentrated until reaching this quantity in a small volume, and a high electric field was applied, it would be possible to create one single aggregate and to detect it. This

strategy could reduce the necessary post-amplification DNA quantity to a really small number, easily produced by the SDA-RCA processing of several initial target copies.

For this project, I was assisted by Yang Liu who did a 6-months internship in the team. His project was to develop a DNA preconcentration system, which could be integrated to the aggregation-based detection system. NOA walls were preferred to 3D-printed structure to avoid leakae. His first task was to characterize the sealing properties of sliding walls. The finalized sealing assays presented previously for NOA and metallic walls are part of his experimental work. Three main difficulties had to be overcome at the beginning of his project: the realization of a perfect sealing between the wall and the PDMS chip, the creation of a controlled membrane in a wall window and the integration of the system on the PDMS-on-glass detection chip.

4.3 Membrane fabrication

The previously used agarose membrane was not considered as a good candidate. Even if trapping of Lambda-DNA was demonstrated, a large quantity of molecules succeeded to migrate through the hydrogel due to the large pore size. Moreover, the release of the preconcentrated DNA was not immediate and reversal of the electric field did not caused the migration of a concentrated DNA plug upstream. We consider the use of PEGDA hydrogel which was already used in the team for the fabrication of particles by stop-flow lithography[40] and membrane for preconcentration of proteins[35]. PEGDA hydrogel is created via photopolymerization of PEGDA molecules in a buffer in presence of an UV-sensitive photoinitiator. Hydrogel properties depend on the size the PEG group and the concentration of PEGDA molecules. For example, for a size of 2000Da and a concentration of 30% in weight of PEGDA, the mesh size of the hydrogel is expected to be around 20Å[41]. PEGDA polymerization only necessitates UV light. Hydrogel shaping could be performed via a patterned light or with a PDMS mould; PEGDA does not stick to PDMS surface because of the presence of an unpolymerized layer of hydrogel in contact with the oxygen-rich PDMS surface.

The previous example with the agarose membrane was a quick trial, without any optimization. Leakage was observed between the sliding wall and the PDMS surface of the chip, mainly caused by the high roughness of the 3D printed wall. Besides, fabrication of NOA walls with windows was not as easy as it was with 3D-printing. We first tried to use NOA walls with two indentations (design 1-Figure 16). The PDMS microchip was the same as the one used in the leakage assay, with a 10mm x 250µm x 300µm channel crossed by a 425µm x 425µm guiding duct (85% of contraction ratio). The hydrogel formation and DNA electrophoresis protocol was identical to the one presented for agarose membrane in Figure 15. After insertion of the sliding wall in the guiding duct, with the first indentation in contact with the bottom of the channel, PEGDA solution (45% of PEGDA 700, 3.75% of Darocur® (2-Hydroxy-2-methyl-1-phenyl-propan-1-one), 51.25% of Tris-EDTA 1X) was introduced in the channel. Sliding wall was moved and 30 seconds of UV-illumination at 358nm with an epifluorescence microscope allowed the photopolymerization of the PEGDA present in the

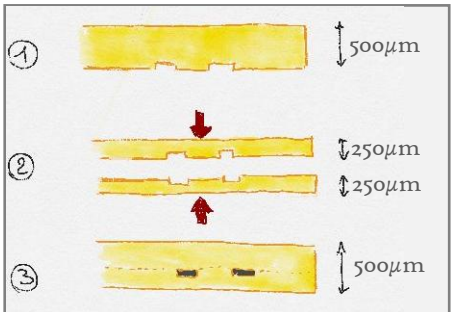

Figure 16. Schematic of the side view of the 3 designs for NOA walls with a window for a PEGDA membrane.

indentation. The sliding wall was then introduced in a second microchip with the second indentation (membrane-free) in the crossing between the guiding duct and the channel. Tris-EDTA buffer supplemented with SyBr Green I (10X) was introduced in the channel. The membrane-filled indentation was displaced inside the channel and 1ng of Lambda-DNA (10^{10} molecules) was introduced into one of the reservoir. 80V/cm was generated between two platinum wires located on the two reservoirs. Fluorescent imaging revealed a large leakage of fluorescent molecules through the wall. Two reasons could explain this failure: because of the uncured layer of PEGDA, there was no tight contact between the hydrogel and the PDMS surface. In addition, PEGDA scratching was observed during wall movement.

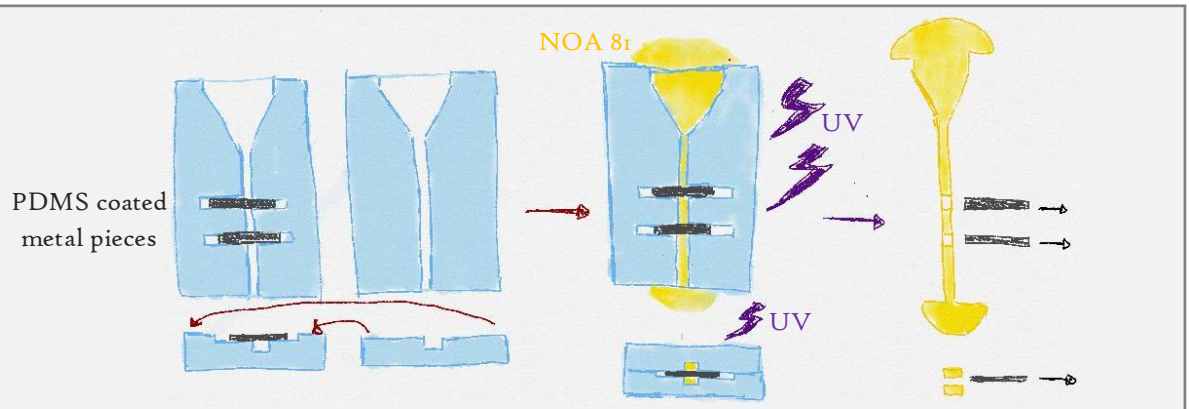

Figure 17. Schematic of protocol for the fabrication of NOA walls with windows. **Top:** top view. **Bottom:** side view.

To overcome these limitations regarding PEGDA membrane, a second protocol for wall fabrication was developed. NOA walls were composed of two indented parts (see design 2 on Figure 16) which were partially polymerized under the UV lamp. The 2 halves were then aligned and a second curing was performed to stick them together. However, as each half of the wall was too flexible, aligning was a difficult task and a bad positioning of the two parts would lead to a bad sealing of the sliding wall.

A third design presented on Figure 16 has finally been developed, with a window produced with a rectangular metal piece. The protocol is shown on Figure 17. Two PDMS moulds with 500µm x 250µm channels were produced from a micro-milled brass mould. On one of them, two additional channels (section 250µm x 100µm) crossed the main channel. Rectangular pieces of stainless steel, milled on a 100µm-thin sheet were placed on the two additional channels after being coated with a thin layer of liquid PDMS. The two PDMS parts were then aligned and filled with NOA 81 by capillarity. A first exposure at 30% of the maximum power of the UV lamp during 40s was performed. PDMS coating of the

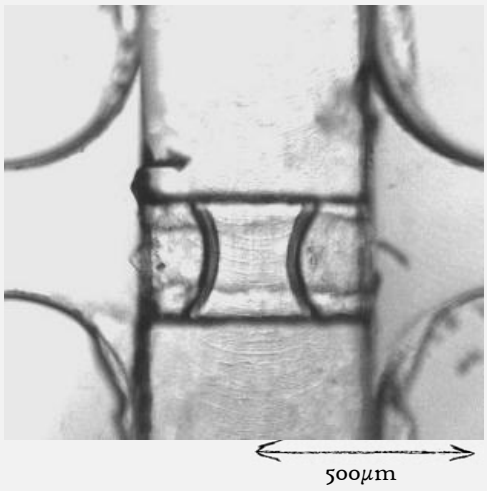

Figure 18. Microscopic picture of a sliding wall (vertical) inserted at the cross between guiding duct and channel, with a PEGDA membrane located in the horizontal window.

rectangular pieces of steel allowed an easy removal from the polymerized wall and a second polymerization at 100% during 1min was made to completely cure the NOA 81, followed by heating at 150°C during 1h30. A drop a PEGDA solution (45% of PEGDA 700, 3.75% of Darocur®, 51.25% of Tris-EDTA 1X) was then deposed in one of the window by pipetting and photopolymerization was performed in an ozone cleaner during 2 minutes. One example of classical microscopic picture is depicted on Figure 18. Before polymerization, the liquid PEGDA filled the whole window. After polymerization, the hydrogel shrinked by more than 50% along the window axis, as seen on the picture. However, the adhesion between the hydrogel and NOA seems good, because no shrinkage was seen on the other directions on this particular example.

4.4 Glass-PDMS hybrid surface

As previously mentioned, our sliding wall-based components need a microchip with a PDMS bottom in order to avoid leakage between the wall and the bottom of the channel, thanks to the PDMS elasticity which efficiently seals the wall. Unfortunately, the DNA detection system requires a glass bottom to integrate the planar electrodes for aggregation formation and aggregation detection (metallic electrodes having a poor adhesion on PDMS). Other methods are available for electrode fabrication (solidified liquid metal[42], conductive inkjet[43], conductive PDMS[44],...), but the minimal dimensions of the electrodes created with these methods are too large for our application, where the electrode size has to be close to the DNA aggregate width.

Yang proposed to etch a rectangular space on the glass slide and to fill it with PDMS. First, gold/chromium planar electrodes were deposited by lift-off on round glass slides. Electrode design was similar to the excitation electrodes of the DNA detection microchip. At the centre of the electrodes interval, an 8mm x 8mm square was completely etched with a laser cutter (GCC LaserPro) as seen on Figure 19. A PDMS slab with a flat surface was silanized under vacuum with trichloro(1H,1H,2H,2H-perfluorooctyl)-silane and put on the top of the etched part of the glass slide. Uncured PDMS was poured from the underside of the glass slide in the etched space. After degassing and curing at 70°C during 2h, silanized PDMS was removed. The new PDMS surface in the etched part was not completely flat: a meniscus of 20µm in height appeared where the new PDMS was previously in contact with the silanized PDMS. The same phenomenon occurred

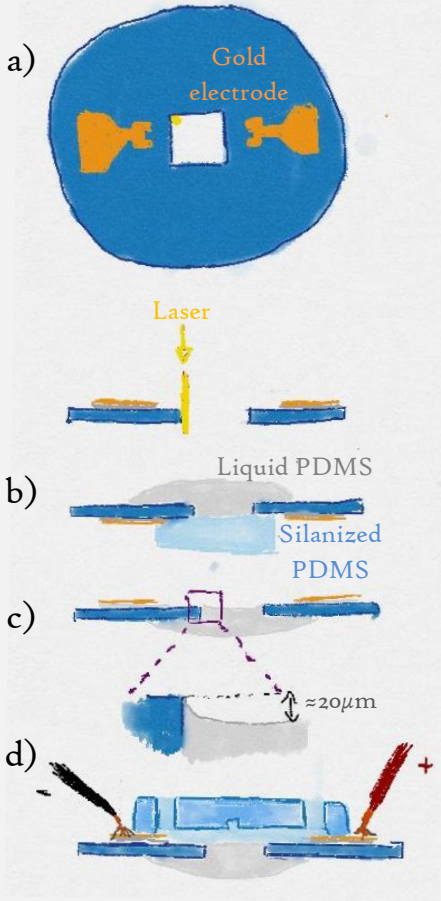

Figure 19. Schematic of protocol for the fabrication of the glass-PDMS surface. **a)** Top and side view of the laser etching of patterned glass slide. **b)** Pouring of liquid PDMS over silanized PDMS. **c)** Zoom of the meniscus over the cured PDMS after removal of the silanized PDMS. **d)** Plasma-bonding of the PDMS microchip and soldering of electrical contacts.

also when silanized PDMS was replaced by a silicon wafer, proving that this deformation was not due to the silanized PDMS elasticity but was more related to a stress relaxation after removal of the flat surface. It has been found that PDMS shrinks of 1% during curing and this deformation is temperature-dependant[45]. However, curing at room temperature did not make the meniscus disappear. Perhaps this stress is also partially present without any temperature change and is due to a volume change during curing. Because of the anchorage of the PDMS to the glass surfaces, the horizontal stress is transferred to the vertical direction (PDMS Poisson coefficient is 0.5), leading to this meniscus creation. Fortunately, using a softer PDMS (20:1 ratio between Sylgard base and curing agent) to fill the etched part allows to bond efficiently the PDMS chip with the glass/PDMS surface while applying pressure between the two parts.

4.5 DNA preconcentration

DNA preconcentration experiments were performed with the final sliding wall design. PEGDA membrane in a sliding wall was prepared shortly before the experiment and immerged in TE 1X. Sliding wall was inserted inside the guiding duct, with the free window in the channel. TE 1X supplemented with SyBr Green I (10X) was loaded into the channel. PEGDA membrane was then moved into the channel by sliding the NOA wall. Lambda-DNA (1ng or 0.1ng) were loaded into one of the two reservoirs and a negative potential (-40V or -120V) was applied in the DNA reservoir, while an opposite potential was applied in the other reservoir. Fluorescent pictures were taken; voltage and current intensity were monitored throughout the experiment course.

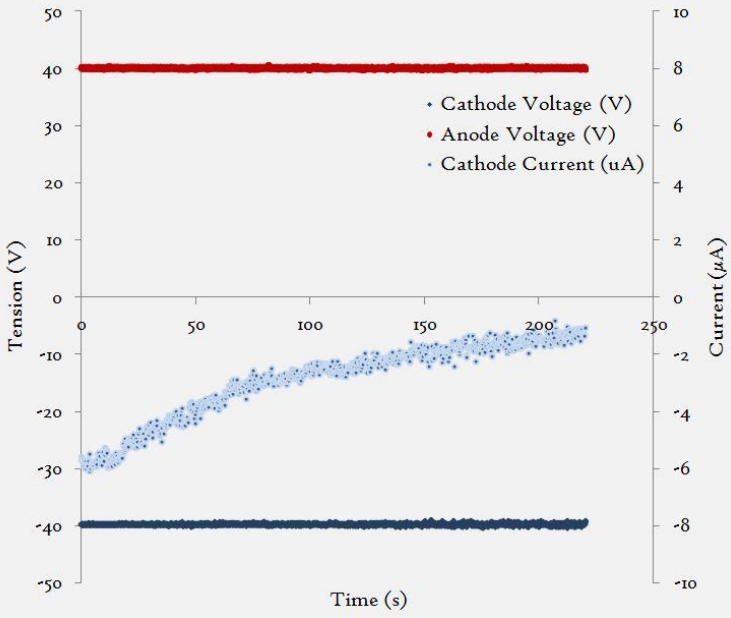

Figure 20. Monitoring of the current and intensity in the anode (DNA reservoir) and cathode (opposite reservoir) of a negative control without DNA in solution.

Current was first monitored in absence of DNA in the solution with a window free of PEGDA, the recorded intensity was about 20µA for a potential difference of 80V; the whole resistance was 4MΩ, which is consistent with theoretical calculations. Still in absence of DNA in the solution and with the membrane located at within the main channel, the current intensity was not higher than -10µA (Figure 20), meaning that the supplementary membrane resistance was higher than 4MΩ. Moreover, current intensity decreased slowly during the experiment. Without any large molecules like DNA in solution, a steric clogging of the membrane pores could not be responsible for this intensity decrease. PEGDA molecule is not charged, and the radical polymerization of PEGDA should not create charges inside the membrane. Charge exclusion by electrodialysis is not thus a valid hypothesis to explain this current intensity decrease which did not occurred without the membrane.

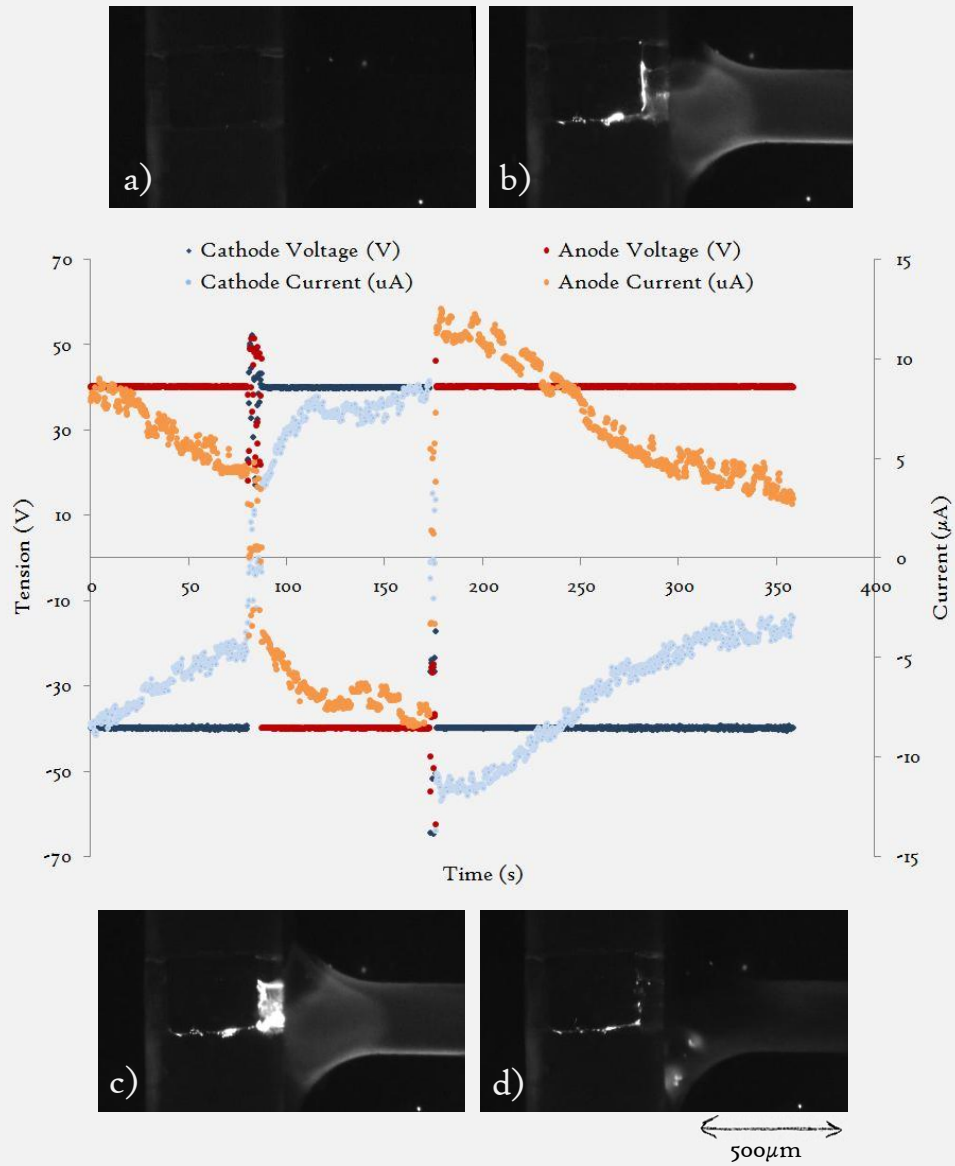

Figure 21. Monitoring of the current and intensity in the anode (DNA reservoir) and cathode (opposite reservoir) during alternative steps of preconcentration and release of 1ng of Lambda-DNA, and fluorescent pictures of the PEGDA membrane. **a)** Initial state before electrophoresis. **b)** Concentrated DNA against the membrane after 80s of preconcentration. **c)** Release of captured DNA, immediately after tension inversion and **d)** after 90s of release.

This current intensity variation along the course of experiments was also observed during preconcentration experiments with Lambda-DNA, as seen on the Figure 21. Voltage polarity was reversed after 80s of preconcentration to release DNA from the membrane, and re-inverted after 80s to demonstrate the reversible trapping of the biomolecules. During preconcentration steps, a clear zone with over-concentrated DNA appeared quickly before the membrane. Current decreased quickly after the preconcentration apparition and individual molecules completely stopped to move, even if the current was still higher than 5µA. As soon as the tension was inverted, most of the trapped DNA moved backward and current increased quickly, meaning that the membrane saturation was reversible.

After 80s of releasing, a small portion of DNA was still blocked between the NOA surface and the hydrogel, or against the PEGDA membrane. This could be explained by the residual presence of free radical, still activated after PEGDA polymerization, which chemically bound the DNA to the hydrogel[36].

Preconcentration and releasing of DNA was presented on Figure 22 with a ten times smaller DNA quantity (100pg). DNA preconcentration was still visible, even with a smaller quantity trapped. However, the concentration factor (calculated as the band minus NOA fluorescence over channel minus PDMS fluorescence) was around 25 after 2min of preconcentration. Releasing was more efficient than for the previous example, with no DNA blocked against the membrane, demonstrating the absence of entanglement and entrance of the Lambda-DNA inside the gel.

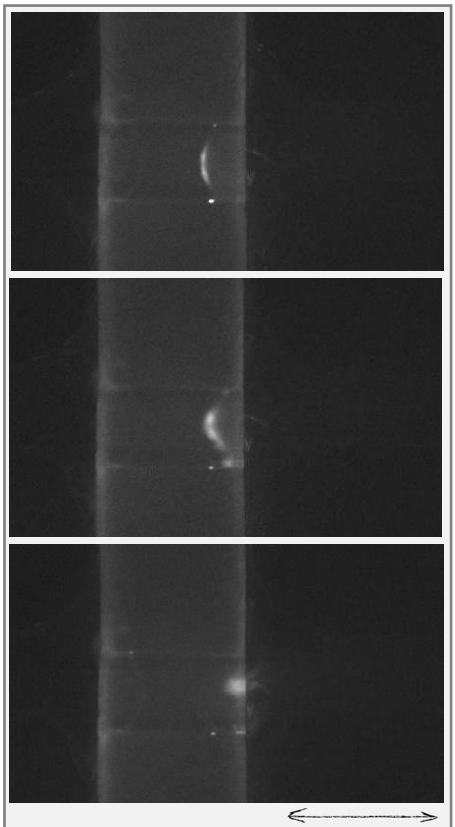

Figure 22. Time-lapse of the release of preconcentrated DNA from 100pg of Lambda-DNA. Duration from top to bottom: 5s.

DNA preconcentration has been successfully demonstrated in a sliding wall thanks to membrane polymerisation within the window. No leakage occurred during the experiment, even with a displacement of the moving structure between chip filling and the preconcentration experiment. The development of a glass-PDMS hybrid surface allowed the integration of the sliding wall in a system where glass surface was mandatory, for example for planar electrode integration. In addition, there is still place for improvements. The membrane composition and concentration could be tuned to improve the DNA concentration.

Because of the concave shape of the hydrogel, transport of molecules after trapping was also possible. This displacement of trapped objects could be especially useful for multiple treatments or when reagents have to be changed. Others object could easily be trapped. MDCK cells, a cell line from dog kidney, have been easily subjected to electrophoresis and trapped against a PEGDA membrane in the same microdevice. Unfortunately, difficult visualization of cells through the NOA wall did not allow a good imaging of the process.

5 Perspectives for the sliding wall toolbox

With these different proof-of-concepts, the sliding wall toolbox is already well stocked. We succeeded to demonstrate these different functions:

- Compartmentalization, with high aspect ratio chambers and quick mixing of the components.
- Valves, with planar metallic walls or 3D NOA walls which could resist up to 300mbars.
- Reconfigurable networks, with metallic walls, which enable the fabrication of microfluidic device with several fluidic paths, depending on the wall position.
- Trapping and concentration of biomolecules like DNA or objects like cells, with the integration of hydrogel membrane inside sliding walls.
- Displacement of analytes and solution between two locations of the microchip by moving a sliding wall containing a window did not encounter any difficulties.
- Integration of walls in a glass surface has been done with the incorporation of PDMS/glass hybrid surface.

Several material and fabrication protocol were used, including micro-milling for stainless-steel planar walls, soft-lithography for NOA wall and stereolithography for resin-based walls. New trials have just been done with a 3D printer with higher resolution in order to produce complex, smooth and leak proof walls with a simpler technique.

Moreover, the sliding wall toolbox did not show all its potential. New experiments are planned in order to demonstrate the use of planar walls for complex operations like multiplexing reaction, or to use pushing walls as syringes for pumping. Work has to be done on the wall lubrication to allow an automated displacement of walls with motors, or to install indentation in the wall and guiding duct to stop the sliding wall in planned locations. The integration of membrane into walls has proved to be easy and efficient, and was demonstrated for two different hydrogels. Tuning the membrane composition and addition of probing molecules during membrane polymerization could increase the specificity of the biomolecule trapping and be used for example in assay for cell secretion characterization.

Finally, sliding wall is a perfect tool for portable and minimally-instrumented microsystem. Manual actuation could be a great advantage for simple system. Moreover, the two developed component (microreactor and DNA preconcentration) do not require pressure controller or pumps, leading to an easier integration inside our DNA detection microdevice. Addition of these components into my main project has not been fully conducted. Bricks have been developed, like the microreactor for sequential reaction, which still need to be tested with a fully isothermal amplification-elongation reaction, or the DNA preconcentration in the optics of a single aggregate detection. Assembling the different parts together will be easier with the development of glass/PDMS hybrid surface for the integration of walls with planar electrodes.

References

1. Gao, Y. *et al.* A versatile valve-enabled microfluidic cell co-culture platform and demonstration of its applications to neurobiology and cancer biology. *Biomed. Microdevices* **13,** 539–548 (2011).

2. Zhou, Q. *et al.* Liver injury-on-a-chip: microfluidic co-cultures with integrated biosensors for monitoring liver cell signaling during injury. *Lab Chip* **15,** 4467–4478 (2015).

3. Yamada, A., Vignes, M., Bureau, C., Mamane, A., Venzac, B., Descroix, S. , Viovy, J-L., Villard, C., Peyrin J-M., and Malaquin, L. In-mold patterning and actionable axo-somatic compartmentalization for on-chip neuron culture. *Lab Chip* **16,** 2059–2068 (2016).

4. Yamada, A., Renault, R., Chikina, A., Venzac, B., Pereiro, I., Coscoy, S., Verhulsel, M., Parrini, M.C., Villard, C., Viovy, J-L. and Descroix, S. Transient microfluidic compartmentalization using actionable microfilaments for biochemical assays, cell culture and organs-on-chip. *Lab Chip* (2016). doi:10.1039/C6LC01143H

5. Schomburg, W. K., Fahrenberg, J., Maas, D. & Rapp, R. Active valves and pumps for microfluidics. *J. Micromechanics Microengineering* **3,** 216–218 (1993).

6. Unger, M. A., Chou, H. P., Thorsen, T., Scherer, A. & Quake, S. . Monolithic Microfabricated Valves and Pumps by Multilayer Soft Lithography. *Science (80-.).* **288,** 113–116 (2000).

7. Thorsen, T., Maerkl, S. J. & Quake, S. R. Microfluidic Large-Scale Integration. **298,** 580–584 (2002).

8. Araci, I. E. & Quake, S. R. Microfluidic very large scale integration (mVLSI) with integrated micromechanical valves. *Lab Chip* **12,** 2803–6 (2012).

9. Pitchaimani, K. *et al.* Manufacturable plastic microfluidic valves using thermal actuation. *Lab on a chip* **9,** 3082–7 (2009).

10. Hansson, J., Hillmering, M., Haraldsson, T. & van der Wijngaart, W. Leak-tight vertical membrane microvalves. *Lab Chip* **0,** 1–3 (2016).

11. Singh, R. K. *et al.* A novel helical micro-valve for embedded micro-fluidic applications. *Microfluid. Nanofluidics* **19,** 19–29 (2015).

12. Cooksey, G. a & Atencia, J. Pneumatic valves in folded 2D and 3D fluidic devices made from plastic films and tapes. *Lab Chip* **14,** 1665–8 (2014).

13. Hu, Z., Kwon, G. H., Kim, C. B., Kim, D. P. & Lee, S. H. Integration of movable structures in PDMS microfluidic channels. *Biochip J.* **4,** 117–122 (2010).

14. Sochol, R. D. *et al.* Microfluidic bead-based diodes with targeted circular microchannels for low Reynolds number applications. *Lab Chip* **14,** 1585 (2014).

15. Oskooei, A., Abolhasani, M. & Günther, A. Bubble gate for in-plane flow control. *Lab Chip* **13,** 2519 (2013).

16. Oh, K. W., Rong, R. & Ahn, C. H. Miniaturization of pinch-type valves and pumps for practical micro total analysis system integration. *J. Micromechanics Microengineering* **15,** 2449–2455 (2005).

17. Browne, A. W., Hitchcock, K. E. & Ahn, C. H. A PDMS pinch-valve module embedded in rigid polymer lab chips for on-chip flow regulation. *J. Micromechanics Microengineering* **19,** 115012 (2009).

18. Gu, W., Zhu, X., Futai, N., Cho, B. S. & Takayama, S. Computerized microfluidic cell culture using elastomeric channels and Braille displays. *Proc. Natl. Acad. Sci. U. S. A.* **101,** 15861–15866 (2004).

19. Weibel, D. B. *et al.* Torque-actuated valves for microfluidics. *Anal. Chem.* **77,** 4726–4733 (2005).

20. Sollier, E., Murray, C., Maoddi, P. & Di Carlo, D. Rapid prototyping polymers for microfluidic devices and high pressure injections. *Lab Chip* **11,** 3752 (2011).

21. Bartolo, D., Degré, G., Nghe, P. & Studer, V. Microfluidic stickers. *Lab Chip* **8,** 274–279 (2008).

22. Bhargava, K. C., Thompson, B. & Malmstadt, N. Discrete elements for 3D microfluidics. *Proc. Natl. Acad. Sci. U. S. A.* **111,** 15013–8 (2014).

23. Lim, J., Maes, F., Taly, V. & Baret, J.-C. The microfluidic puzzle: chip-oriented rapid prototyping. *Lab Chip* **14,** 1669–72 (2014).

24. Renaudot, R. *et al.* A programmable and reconfigurable microfluidic chip. *Lab Chip* **13,** 4517–24 (2013).

25. Silva, R. J., Bhatia, S. & Densmore, D. A reconfigurable continuous-flow fluidic routing fabric using a modular, scalable primitive. *Lab Chip* **16,** 2730–2741 (2016).

26. Konda, A., Taylor, J. M., Stoller, M. A. & Morin, S. A. Reconfigurable microfluidic systems with reversible seals compatible with 2D and 3D surfaces of arbitrary chemical composition. *Lab Chip* **15,** 2009–2017 (2015).

27. Du, W., Li, L., Nichols, K. P. & Ismagilov, R. F. SlipChip. *Lab Chip* **9,** 2286–2292 (2009).

28. Kühnemund, M., Witters, D., Nilsson, M. & Lammertyn, J. Circle-to-circle amplification on a digital microfluidic chip for amplified single molecule detection. *Lab Chip* **14,** 2983–92 (2014).

29. Stumpf, F. *et al.* LabDisk with complete reagent prestorage for sample-to-answer nucleic acid based detection of respiratory pathogens verified with influenza A H3N2 virus. *Lab Chip* **16,** 199–207 (2016).

30. Lee, C.-C. *et al.* Multistep synthesis of a radiolabeled imaging probe using integrated microfluidics. *Science* **310,** 1793–6 (2005).

31. Peyman, S. A., Iles, A. & Pamme, N. Rapid on-chip multi-step (bio)chemical procedures in continuous flow – manoeuvring particles through co-laminar reagent streams. *Chem. Commun.* 1220 (2008). doi:10.1039/b716532c

32. Striemer, C. C., Gaborski, T. R., McGrath, J. L. & Fauchet, P. M. Charge- and size-based separation of macromolecules using ultrathin silicon membranes. *Nature* **445,** 749–53 (2007).

33. Foote, R. S., Khandurina, J., Jacobson, S. C. & Ramsey, J. M. Preconcentration of proteins on microfluidic devices using porous silica membranes. *Anal. Chem.* **77,** 57–63 (2005).

34. Lu, J. C., Liao, W. H. & Tung, Y. C. Magnet-assisted device-level alignment for the fabrication of membrane-sandwiched polydimethylsiloxane microfluidic devices. *J. Micromechanics*

Microengineering **22,** 75006 (2012).

35. Mohamadi, R. M. *et al.* An integrated microfluidic chip for immunocapture, preconcentration and separation of β-amyloid peptides. *Biomicrofluidics* **9,** 54117 (2015).

36. Lee, H. S., Chu, W. K., Zhang, K. & Huang, X. Microfluidic devices with permeable polymer barriers for capture and transport of biomolecules and cells. *Lab Chip* **13,** 3389–97 (2013).

37. Luo, X., Wu, H. C., Betz, J., Rubloff, G. W. & Bentley, W. E. Air bubble-initiated biofabrication of freestanding, semi-permeable biopolymer membranes in PDMS microfluidics. *Biochem. Eng. J.* **89,** 2–9 (2014).

38. Luo, X., Vo, T., Jambi, F., Pham, P. & Choy, J. S. Microfluidic partition with in situ biofabricated semipermeable biopolymer membranes for static gradient generation. *Lab Chip* **16,** 3815–3823 (2016).

39. Puchberger-Enengl, D. *et al.* Microfluidic concentration of bacteria by on-chip electrophoresis. *Biomicrofluidics* **5,** (2011).

40. Dendukuri, D. & Doyle, P. S. The Synthesis and Assembly of Polymeric Microparticles Using Microfluidics. *Adv. Mater.* **21,** 4071–4086 (2009).

41. Cruise, G. M., Scharp, D. S. & Hubbell, J. A. Characterization of permeability and network structure of interfacially photopolymerized poly(ethylene glycol) diacrylate hydrogels. *Biomaterials* **19,** 1287–1294 (1998).

42. Pavesi, A. *et al.* How to embed three-dimensional flexible electrodes in microfluidic devices for cell culture applications. *Lab Chip* **11,** 1593 (2011).

43. Wu, J. *et al.* Inkjet-printed microelectrodes on PDMS as biosensors for functionalized microfluidic systems. *Lab Chip* **15,** 690–695 (2015).

44. Khosla, a. & Gray, B. L. Preparation, characterization and micromolding of multi-walled carbon nanotube polydimethylsiloxane conducting nanocomposite polymer. *Mater. Lett.* **63,** 1203–1206 (2009).

45. Lee, S. W. & Lee, S. S. Shrinkage ratio of PDMS and its alignment method for the wafer level process. *Microsyst. Technol.* **14,** 205–208 (2007).

Conclusion

Writing "conclusion" is a little bit artificial, as a research project did not seem to be concluded. The storyline of this study started in the nineties, with the discovery of the electrohydrodynamic instabilities as an artefact of DNA separation by capillary electrophoresis by Jean-Louis Viovy. Based on these observations, he postulated the possibility to detect long DNAs aggregated by this phenomenon inside a microfluidic chip, through conductometric detection several years later. A first proof-of-concept was demonstrated in 2012 by Youba Diakité during a previous PhD, despite unexpected complications due to electronic incompatibilities and interferences.

The main goal of the project was to obtain a portable, sensitive, label-free and optic-free system for the detection of bacterial DNA on the field. I had first to optimize the previous prototype in order to make it more sensitive and portable. The system would then be easily used for the detection of HRCA products - an apparently simple amplification reaction which was supposed to amplify and elongate short DNAs into a huge quantity of long DNAs. But research is never so simple and could not be written before experimental validations. The detection system by itself did not bring a lot of supplementary complications. Electronic was optimized with the help of Robert Breton (Kenium Company). The excitation module is now portable, supplied with battery, more stable and could still be more miniaturized. Besides, microchip design and microfabrication has also been modified to improve the reproducibility of the measure, along with the signal treatment which is now characterized and robust.

In contrary, development of the biomolecular reaction was way more unexpected. Based on a short collaboration with Ismail Cissé (ESPCI Paris), our first trials gave us good results concerning the compatibility between HRCA products and our detection method. We demonstrated the possibility to measure elongated products from a concentrated sample of short DNAs. But the HRCA did not work as expected regarding the amplification of the long DNAs produced from few short DNAs. Mechanism of the amplification reaction was then explored with the help of David Herthnek (Scilife Lab, Stockholm University) via real-time fluorescent experiments, which allowed us to highlight the sensitivity limitations of the first protocol (LOD: 100fM). However, the detection limit with our conductometric system was still around 10nM. Does the HRCA produce enough long DNAs? Thank to kinetics simulations of the HRCA, we learnt that the final number of long DNAs should be constant and large enough for our application, independently of the initial number of molecules. Long DNA production was not the problem. This model would also be interesting for the biochemist community, regardless our own questions. Lastly, a theoretical model of DNA diffusion inside a RCA coil gave us the main information: long products of HRCA could not escape the RCA coil by diffusion and are not available for aggregation and detection.

We thus had to change our strategy and to develop a two-step reaction: a first amplification of short DNA by SDA followed by a product elongation by HRCA. Thanks to this technique, we succeeded to detect by conductometry an initial concentration of 1pM (10 millions of molecules) of DNA corresponding to a MRSA gene. LOD was limited by the poor sensitivity of the SDA reaction, which, at this stage, could not be optimized further regarding the state-of-the-art level. With a simple RCA instead of the HRCA, the same initial concentration was detected by a visible change on the fluid

property, which became visco-elastic (formation of DNA hydrogel), which could be a simpler, alternative way to assess the amplification result.

In parallel, I developed several original and innovative microfabrication techniques using fibres and wires. Two projects, not described in this manuscript, led to one patent application and two collaborations with teams specialized in organ-on-chips and textile industry. Besides, Ayako Yamada, post-doc in the team, initiated with my help and these fibres another new technique for transient compartmentalization of microfluidic chambers, leading to two papers in Lab-on-Chip and a second patent application. Based on her initial approach, I developed a technology called "sliding walls", where 3D structures produced by 3D printing, micro-milling or soft-lithography were used as mobile components in microfluidic chips. Several functionalities were demonstrated, as compartmentalization, valves, reconfigurable microfluidics, membrane incorporation and DNA preconcentration, some of them produced by Yang Liu, an intern that I supervised. The sliding wall technology was also developed in order to integrate into a single microdevice the different steps of our instabilities–based DNA detection method: sample preparation, amplification and conductometric detection steps. Indeed, the SDA-HRCA reaction is a two-step protocol and necessitates the addition of reagents between the SDA and HRCA steps. We thus developed and demonstrated the functionality of our compartmentalization method enabling the quick mixing of large volume of fluid (above 1µl) at will, by opening communication between several chambers. In addition, to improve the method sensitivity, we also prepared a new preconcentration method for genomic DNA based on an electrophoretic migration of the molecules against a PEGDA membrane included inside a sliding wall.

Writing "conclusion" is a little bit artificial, simply because we hope that the different projects could continue as described in the always coupled "perspectives", or to follow their own stories. Our initial idea was to promote our system as a miniaturized and portable device. Looking at the review of industrialized and lab-based technologies on Chapter 1, we initially considered that it was still room for this type of system for bacteria detection. But our method finally suffers from the necessary complexity of the DNA amplification-elongation reaction. With some little improvements (optimization of the SDA and thermostable RCA), we believe that this step could become fully isothermal, with a sensitivity close to the clinical threshold, but the addition of new reagents could not be overcome. Our sliding wall toolbox could solve this problem, but the whole system would maybe become too complex compared to existing technologies. Another possible way to use our DNA detection system would be to couple it with the sliding wall-based DNA preconcentration. If only one aggregate could be detected, the direct detection of preconcentrated, digested genomic bacterial DNA could be possible without any amplification, after selective trapping of these bacteria.

We are convinced that the sliding wall technology will find interesting applications, both for research projects and portable devices. At a shorter term, the "sliding wall" toolbox will be tested for complex, manually-actuated and reconfigurable microfluidic system, where fluidic path could be changed during chip operation and fluid movement produced by syringe-like displacement of sliding structures. The trapping of molecules into membrane could also be a powerful tool for analytical applications. Lastly, we did not take profit yet of the possible displacement of sample or trapped analytes inside a wall window between several channels for sequential treatment, which could also benefit to a wide range of applications.

Without being the end of these projects, this last sentence is, at least, the conclusion of a manuscript describing 3 years and half of PhD.

Appendix

• Abbreviations

AIDS: Acquired ImmunoDeficiency Syndrome

ART: Antiretroviral Therapy

bp: base pairs

BSA: Bovine Serum Albumin

C2CA : Circle-to-Circle Amplification

CAD: Computer Assisted Design

CFU: Colony Forming Unit

DNA: Deoxyribonucleic acid

dsDNA: Double-stranded Deoxyribonucleic acid

ELISA: Enzyme-linked Immunosorbent Assay

EWOD: Electrowetting-on-dielectric

HDA: Helicase-dependent isothermal Amplification

HIV: Human Immunodeficiency Virus

HRCA: Hyper-branched Rolling-Circle Amplification

HV: High voltage

ICT: Immunochromatography Cassette

ITN: Insecticid-treated bed net

LAMP: Loop-mediated isothermal Amplification

LOD: Limit of Detection

MEMS: Microelectromechanical System

MTB: *Mycobacterium tuberculosis bacilli*

NI: National Instrument

nt: nucleotides

PAGE: PolyAcrylamide Gel Electrophoresis

PCR: Polymerase Chain Reaction

PDMS: polydimethylsiloxane

PEGDA: Polyethylene Glycol Diacrylate

PG-RCA: Primer Generation Rolling-Circle Amplification

PNA: Peptide Nucleic Acid

POC: Point-of-Care

QALY: Quality Adjusted Life Year

RCA: Rolling-Circle Amplification

RNA: Ribonucleic acid

RPA: Recombinase Polymerase Amplification

SDA: Strand-Displacement Amplification

SNP: Single Nucleotide Polymorphism

SSB: Single-stranded DNA Binding Protein

ssDNA: Single-stranded Deoxyribonucleic acid

Vpp: Volt peak-peak

WHO: World Health Organization

- # SDA-HRCA protocol

Here is presented the final protocol for the amplification-elongation reaction, based on two steps: SDA then HRCA. All the reagents were conserved at -20°C before use, and thermalized to room temperature before mixing, except for enzymes.

For the SDA protocol, the target is a synthetic oligonucleotide. No specific denaturation step is needed. The reactant, primer, target and enzyme mixes are prepared separately and mixed together in this order just before the incubation in a PCR tube at 56°C.

Negative controls are also performed with water instead of the ldh1 target.

SDA

Enzymes	conc	final conc	vol
Bst 2.0 WarmStart	8U/µl	800mU/µl	3,00
Nt.BbvCI	10U/µl	200mU/µl	0,60
		enzyme volume	3,60

Target	conc	final conc	vol
ldh1	X	X/10	3,00

Primers	conc	final conc	vol
Extension Primer 1	10µM	250nM	0,75
Extension Primer 2	10µM	500nM	1,50
Bump Primer 1	1µM	50nM	1,50
Bump Primer 2	1µM	50nM	1,50
		oligos volume	5,25

Reactants	conc	final conc	vol
dNTP	25mM	1mM	1,20
Cutsmart buffer	10X	1X	3,00
dH_2O	-	-	13,95
		reactant volume	18,15

vortex		total volume	30,00
56°C during 30min	80°C during 20min		

For HRCA, all the reagents are mixed together with the ligase at the end. Negative controls with water instead of the positive and negative SDA products were performed. Positive controls were also realised with the ldh1 + N 2 oligos (final concentration 100nM) instead of the SDA products. Final incubation could be reduced to 1h. SDA products could be kept at -20°C between the two steps during weeks if needed.

HRCA

Ligation

	conc	final conc	vol
SDA product	-	-	2,5
Circle Random	1µM	100nM	1
BSA	10%, 100µ/µl	1,25µ/µl	0,125
T4 ligase buffer	5X	0,75X	1,5
dNTP	25mM	1mM	0,4
T4 ligase	1U/µl	25 mU/µl	0,5
dH_2O	-	-	3,975
		mix volume	7,5
		total volume	10
37°C during 30 minutes	65°C during 10min		

Polymerization

	conc	final conc	vol
Ligated solution	-	-	10
HRCA Primer 1	20µM	1µM	0,5
HRCA Primer 2	20µM	1µM	0,5
Phi29 polymerase	10U/µl	500mU/µl	0,5
35°C during 3h, 65°C during 2min		total volume	11,5